Opaque Inertial Suspensions

Dash, A.

DOI
10.4233/uuid:f62e9c3c-934f-425a-870f-84b8f56f104e

Publication date
2022

Document Version
Final published version

Citation (APA)
Dash, A. (2022). *Opaque Inertial Suspensions*. [Dissertation (TU Delft), Delft University of Technology]. https://doi.org/10.4233/uuid:f62e9c3c-934f-425a-870f-84b8f56f104e

Opaque Inertial Suspensions

Opaque Inertial Suspensions

Dissertation

for the purpose of obtaining the degree of doctor
at Delft University of Technology,
by the authority of the Rector Magnificus Prof. dr. ir. T.H.J.J. van der Hagen,
chair of the Board for Doctorates,
to be defended publicly on

Thursday, 08 September 2022, at 1500 o'clock

by

Amitosh DASH

Master of Science in Mechanical Engineering,
Delft University of Technology, Delft, The Netherlands,
born in Ahmedabad, India.

This dissertation has been approved by the promotors.

Composition of the doctoral committee:

Rector Magnificus,	Delft University of Technology (*chairperson*)
Prof. dr. ir. C. Poelma,	Delft University of Technology (*promotor*)
Dr. ir. W.-P. Breugem,	Delft University of Technology (*promotor*)
Independent members:	
Prof. dr. S. Balabani,	University College London
Dr. ir. D.E. Rival,	Queen's University
Prof. dr. ir. N.G. Deen,	Eindhoven University of Technology
Prof. dr. ir. J.T. Padding,	Delft University of Technology
Prof. dr. ir. F.H.L.R. Clemens,	Norwegian University of Science and Technology
	Delft University of Technology / Deltares
Prof. dr. ir. R.A.W.M. Henkes,	Delft University of Technology (*reserve member*)

Funding:	European Research Council Consolidator Grant 725183
Printed by:	Gildeprint
Front & Back:	Ultrasound image of slurry being resuspended & Author collecting slurry samples
Keywords:	Suspensions, Inertial instabilities, Ultrasound Imaging
Nederlandse titel:	Ondoorzichtige Inertiële Suspensies

ISBN 978-94-6384-361-4

An electronic version of this dissertation is available at
http://repository.tudelft.nl/.

Preface

This thesis reflects most of the work performed by the author (and collaborators) from 01 September 2017 to 30 November 2021 as a doctoral candidate at the Laboratory for Aero- & Hydrodynamics, Mechanical, Maritime and Materials Engineering, Delft University of Technology.

There are four main chapters in this thesis. The common theme binding these chapters are that they are all concerned with measurements in suspensions, which are optically opaque. Moreover, the particles or the flows are inertial enough for interesting phenomena to occur. In Chapter 3, it is demonstrated that issues due to opacity can be circumvented by simply adding visualization flakes, especially in the context of Taylor-Couette flows. On the other hand, the contents of Chapter 4 and 5 attempt to tackle the opacity head-on with ultrasound imaging, with moderate success. In Chapter 6, an example of how fluid mechanical aspects can be potentially translated to something useful for practitioners in the slurry community is presented.

The scope of the topics covered in this thesis is broader than it is deeper. Moreover, the problems are mostly approached in what might be perceived as a top-down method (explaining observations based on fundamental theory) rather than a bottom-up method (going from a firm theory and hypothesis to observations that support said hypothesis). The breadth of topics covered in this thesis is reflected in the fact that researchers from different sub-domains of Fluid Mechanics could find select contents of this thesis interesting. Chapters 3 and parts of Chapters 4 and 5 will be of interest for one curious about the fundamental fluid mechanics of suspensions. Chapter 6 and parts of Chapters 5 will be of interest to one from the slurry community. Lastly, the reader interested in the application of ultrasound for suspensions is directed to Chapters 4 and 5.

The author and the research in this thesis were financially supported by the European Research Council Consolidator Grant (ERC-CoG) 725183 awarded to Prof. Christian Poelma in 2016. This dissertation has been written under the umbrella of a larger project "OpaqueFlows".

Amitosh DASH
Delft, July 2022

Contents

Preface v

Summary xi

Samenvatting xiii

1 More particles, more problems - Introduction 1
- 1.1 Flowing Suspensions: Inertia and Opacity . . . 3
- 1.2 OpaqueFlows . . . 4
- 1.3 Objectives and outline of this thesis . . . 5

2 A primer for suspension fluid mechanics and ultrasonics 9
- 2.1 Fluid Mechanics of Suspensions . . . 11
  - 2.1.1 Taylor-Couette flow . . . 11
  - 2.1.2 Pipe flow . . . 16
- 2.2 Ultrasound for monitoring flowing suspensions . . . 21
  - 2.2.1 Basics of ultrasound imaging . . . 22
  - 2.2.2 Interactions between ultrasound and suspensions . . . 24
  - 2.2.3 Existing acoustic/ultrasonic concentration profiling techniques . . . 28
  - 2.2.4 Existing studies on ultrasound based velocimetry outside cardiovascular flows . . . 29

3 Particle-laden Taylor-Couette flows 33
- 3.1 Introduction . . . 35
- 3.2 Experimental set-up and measurement procedure . . . 37
  - 3.2.1 Geometry of the Taylor-Couette facility . . . 37
  - 3.2.2 Preparation of the neutrally buoyant suspension . . . 38
  - 3.2.3 Rotation control and torque measurements . . . 39
  - 3.2.4 Temperature estimation . . . 40
  - 3.2.5 Experimental protocol . . . 40
  - 3.2.6 Flow visualization . . . 43
  - 3.2.7 Experimental uncertainties . . . 43
  - 3.2.8 Comparison of current experiments against recent, similar ones . . . 44
- 3.3 Global analysis of the experiments . . . 46
  - 3.3.1 Flow visualization . . . 46
  - 3.3.2 Torque measurements . . . 48

3.4 Lower-order transitions . . . 52
3.4.1 Dilute suspension: A detailed example . . . 52
3.4.2 Semi-dilute suspension: A detailed example . . . 54
3.4.3 Dense suspension: A detailed example . . . 56
3.4.4 Can coexisting regimes in ramp-up experiments be due to imperfect neutral buoyancy? . . . 57
3.4.5 Azimuthally localized wavy vortex flow: transient or a new regime? . . . 58
3.5 Higher-order transitions . . . 62
3.5.1 Dilute suspension: A detailed example . . . 63
3.5.2 Semi-dilute suspension: A detailed example . . . 64
3.5.3 Dense suspension: A detailed example . . . 66
3.6 Conclusions and Outlook . . . 67
3.6.1 Summary of key findings . . . 67
3.6.2 Possible future investigations . . . 68
3.A Validation in single-phase Taylor-Couette flows . . . 69
3.A.1 Regime classification per flow visualization . . . 69
3.A.2 Torque data . . . 75
3.B Simultaneous Ultrasound Imaging Velocimetry and Flow Visualization . . . 76
3.B.1 Flow regimes in Taylor-Couette: Pure inner cylinder rotation . . . 77
3.B.2 Experimental apparatus . . . 79
3.B.3 Data processing . . . 80
3.B.4 Application of UIV to single-phase Taylor-Couette flows . . . 81
3.B.5 Application of UIV to particle-laden Taylor-Couette flow . . . 85
3.B.6 Conclusion: UIV is a potential tool for particle-laden Taylor-Couette flows . . . 86

4 Ultrasonic particle volume fraction profiling 87
4.1 Introduction and scope . . . 89
4.2 Calibration in uniform suspensions . . . 91
4.3 Inversion for non-uniform suspensions . . . 95
4.3.1 Procedure 1: Stepwise reconstruction . . . 95
4.3.2 Procedure 2: Dual-frequency reconstruction . . . 97
4.3.3 Comparison of the two techniques with synthetic profiles 99
4.4 Limitations induced by multiple scattering . . . 101
4.4.1 Multiple scattering in gelatin models . . . 102
4.4.2 Characterizing the scattering behaviour . . . 104
4.4.3 An example of calibration and reconstruction . . . 105
4.5 Application to particle-laden pipe flows . . . 107
4.5.1 Background to radial migration in particle-laden pipe flows . . . 107
4.5.2 Experiments . . . 107
4.5.3 Calibration in uniform suspensions . . . 108

4.5.4 Reconstruction in dilute suspensions: comparison with particle counting . . . 109
4.5.5 Application of technique to higher volume fractions . . . 111
4.6 Conclusions and outlook . . . 113
4.A Recipe for the gelatin models . . . 114

5 Ultrasound Imaging Velocimetry in particle-laden flows 117
5.1 Introduction and scope . . . 119
5.2 Cross-correlation theory for UIV in particle-laden flows . . . 120
5.2.1 Cross-correlation theory for single-exposure, double-frame PIV . . . 120
5.2.2 Interaction between ultrasonic waves and suspensions . . . 121
5.2.3 Cross-correlation theory for UIV of particle-laden flows . . . 122
5.3 Experimental datasets: particle-laden pipe flows . . . 125
5.3.1 UIV at laboratory scale . . . 125
5.3.2 UIV at industrial scale . . . 126
5.3.3 Data processing . . . 127
5.4 Quality of cross-correlation results . . . 128
5.4.1 Effect of ensemble size and imaging depth with fixed bulk volume fraction . . . 129
5.4.2 Effect of bulk volume fraction . . . 132
5.5 Case studies . . . 134
5.5.1 Laminar-turbulent transition . . . 134
5.5.2 Effect of a 90° bend on slurry flow . . . 136
5.6 Conclusions and Outlook . . . 141
5.A Additional explanation for PIV processing . . . 142

6 Long-time-scale transients in a slurry pipeline 147
6.1 Introduction . . . 149
6.2 Experimental setup and procedures . . . 150
6.3 Results: unaltered inflow experiments . . . 152
6.3.1 Global characteristics: pressure drop and bulk velocity . . . 152
6.3.2 Local characteristics: velocity profiles . . . 155
6.4 Results: ramped inflow experiments . . . 157
6.5 Slowly settling behaviour . . . 159
6.6 Self-equilibrating behaviour . . . 161
6.7 Conclusions and Outlook . . . 164
6.A Slurry characterization . . . 169
6.A.1 Particle sizing . . . 169
6.A.2 Mass density . . . 169
6.A.3 Rheology . . . 170
6.A.4 Zeta potential . . . 172
6.A.5 Settling test . . . 172

6.B Relevant equations for non-Newtonian slurry flows 173
6.B.1 Laminar flow calculations 173
6.B.2 Turbulent flow model of Wilson and Thomas 173
6.B.3 Turbulent flow model of Slatter 174

7 Meten is weten - Conclusions, outlook, and impact **175**
7.1 Conclusions: what is new in this dissertation 177
7.1.1 Fundamental Fluid Mechanics 177
7.1.2 Applied Fluid Mechanics 178
7.1.3 Experimental Fluid Mechanics 178
7.2 Outlook: how to build on this dissertation 179
7.2.1 Fundamental Fluid Mechanics 180
7.2.2 Applied Fluid Mechanics 180
7.2.3 Experimental Fluid Mechanics 181
7.3 Impact: who benefits from this dissertation 182

References **185**

Summary

Opacity and inertia are two aspects that hinder and complicate progress in our complete understanding of flowing suspensions. This thesis *Opaque Inertial Suspensions* attempts to make a small contribution to this challenging subject. The overall research question of this dissertation is: **How and to what extent can state-of-the-art measurement techniques be leveraged, in particular ultrasound imaging, to gain novel insights into the fluid mechanics of opaque inertial suspensions?** The work in this thesis is firmly ingrained in experimental approaches to provide insights into fundamental and applied flows.

Experimental Fluid Mechanics

Ultrasound imaging is utilized to tackle the inherent opacity of suspensions. To characterize a suspension flow, two key desired quantities are velocity and concentration profiles of the dispersed phase. To retrieve these, physical aspects of ultrasonic propagation in suspensions are included in a lumped model, prior to evaluating the flows of interest. The work herein offers a framework to apply ultrasound imaging to suspension flows.

To determine concentration profiles, an empirical approach is formulated which lumps the interaction between ultrasonic waves and suspensions into two parameters - peak backscatter amplitude and amplitude attenuation rate. Calibration is necessary in homogeneous suspensions to determine these two parameters, following which inhomogeneous suspensions can be evaluated. The empirical approach is shown to have shortcomings as well, one of which is multiple scattering.

This lumped model is then incorporated into cross-correlation theory established for Particle Image Velocimetry. This modified theory heuristically explains how ultrasound imaging velocimetry performs for flowing suspensions while explaining the role of numerous factors (like particle volume fraction, imaging depth, particle size). Attenuation of sound waves limits the parameter space to which ultrasound imaging velocimetry remains functional. The limits for time-averaged velocity profiles can be pushed using ensemble correlation averaging. Retrieving time-resolved velocity profiles fails earlier. Determining the growth rate of the maximum peak height as function of ensemble size may provide indications on whether collecting more images might help.

Fundamental Fluid Mechanics

For fundamental fluid mechanics, it is not uncommon to study the flow of neutrally buoyant suspensions in canonical geometries. The presence of inertia at the particle level or the system level can complicate matters. The former would result in differing behaviours of the two phases while the latter could trigger hydrodynamic instabilities and/or turbulence. The work herein contributes to the growing field of "Fluid Mechanics of Suspensions".

The flow of suspensions in the Taylor-Couette geometry (pure inner cylinder rotation) is studied using flow visualization and torque measurements. It is seen that with increasing particle loading, the probability of observing axisymmetric Taylor vortices reduces while that of non-axisymmetric structures rises. One anomalous observation is that a hybrid form of axisymmetric Taylor vortices and non-axisymmetric wavy vortices – azimuthally localized wavy vortices – can exist in suspension laden systems. Analysing the frequency spectra of the flow structures beyond wavy vortices suggests that the route to chaos is altered. For densely-laden systems, a second, incommensurate frequency (related to modulation on wavy vortices) is not observed. Simultaneous torque measurements show that the scaling exponent between the torque and the rotation rate of the inner cylinder is independent of the particle loading.

In pipe flows, inertial migration of particles is captured under (semi-)dilute conditions. The degree of migration gets weaker with increasing Reynolds numbers, and is visible even at the commencement of intermittent flows. The imprint of inertial migration is weakly visible in the time-averaged velocity profiles. Like the time-averaged particle volume fraction profiles, the time-averaged velocity profiles of these suspensions become blunter with increasing Reynolds numbers.

Applied Fluid Mechanics

Suspensions are relevant in several industrial processes, with transport of slurries in pipelines being a conventional example. When the particulate phase is very small, the slurry is typically considered as a homogeneous non-Newtonian fluid. Even though this is a matured field with a vast database of experiments, insights have been typically gained from measuring integral quantities. The work in this thesis serves as a proof-of-concept on how looking into the flow non-intrusively with ultrasound imaging can provide added value.

The recovery of slurry flow beyond a 90° pipe bend is assessed in an industrial scale facility, by adjudging the streamwise momentum and (a)symmetry of the velocity profiles. It is seen that the recovery of the flow is swifter under a turbulent condition than a laminar one. This provides unique experimental data for validation of numerical models.

Revisiting the laminar-turbulent transition of a non-settling slurry yielded nuanced insights which have not been brought to the forefront yet. Two long-time-scale transients were observed - “slow settling” and “self-equilibration”, which can be captured in flow meter readings. The slow settling phenomenon is related to the sedimentation of particles over long time scales, which can cause an eventual shutdown. Self-equilibration is related to the gradual erosion of the bed of settled particles which leads to a rise in flow rates. The equilibrium phase is attained after complete resuspension of particles by intermittent turbulent structures. Both these transient phenomena can potentially be translated into useful guidelines for the operation of slurry pipelines.

While this thesis operates at low technological readiness levels, there is nevertheless potential for the work herein to contribute to immediate societal or environmental needs. For example, the non-Newtonian slurry considered herein mimics the rheology of concentrated domestic wastewater, whose transport is yet to properly accounted for in new, sustainable sanitation systems.

Samenvatting

Ondoorzichtigheid en inertie zijn twee aspecten die de vooruitgang in ons volledig begrip van stromende suspensies belemmeren en bemoeilijken. Dit proefschrift *Ondoorzichtige Inertiële Suspensies* probeert een kleine bijdrage te leveren aan dit uitdagende onderwerp. De algemene onderzoeksvraag van dit proefschrift is: **Hoe en in welke mate kunnen state-of-the-art meettechnieken, in het bijzonder ultrasone beeldvorming, worden ingezet om nieuwe inzichten te verkrijgen in de vloeistofmechanica van ondoorzichtige inertiële suspensies?** Het werk in dit proefschrift is stevig verankerd in experimentele benaderingen om inzicht te verschaffen in fundamentele en toegepaste stromingen.

Experimentele Stromingsleer

Ultrasone beeldvorming wordt gebruikt om de inherente ondoorzichtigheid van suspensies aan te pakken. Er zijn twee belangrijke grootheden om een suspensiestroom te karakteriseren: de snelheids- en concentratieprofielen van de gedispergeerde fase. Om deze te verkrijgen, worden fysische aspecten van ultrasone voortplanting in suspensies opgenomen in een model, alvorens de stromingen van belang te evalueren. Dit werk biedt een kader voor de toepassing van ultrasone beeldvorming op suspensiestromen.

Om concentratieprofielen te bepalen wordt een empirische benadering geformuleerd die de interactie tussen ultrasone golven en suspensies in twee parameters samenvat - piek backscatter amplitude en de dempingssnelheid van de amplitude. Kalibratie is nodig in homogene suspensies om deze twee parameters te bepalen, waarna inhomogene suspensies kunnen worden geëvalueerd. De empirische benadering blijkt ook tekortkomingen te hebben, waarvan meervoudige verstrooiing er één is.

Dit lumped model wordt vervolgens opgenomen in de cross-correlatietheorie die is opgesteld voor Particle Image Velocimetry. Deze aangepaste theorie verklaart heuristisch hoe ultrasound imaging velocimetry presteert voor stromende suspensies terwijl de rol van talrijke factoren (zoals deeltjesvolumefractie, beelddiepte, deeltjesgrootte) wordt verklaard. Verzwakking van geluidsgolven beperkt de parameterruimte tot welke ultrasound imaging velocimetry functioneel blijft. De grenzen voor tijd-gemiddelde snelheidsprofielen kunnen worden verlegd met behulp van ensemble correlatie gemiddelden. Het bepalen van tijd-opgeloste snelheidsprofielen zal eerder falen bij hogere concentraties. Bepaling van de groeisnelheid van de maximale piekhoogte als functie van de ensemblegrootte kan aanwijzingen opleveren over de vraag of het verzamelen van meer beelden zou kunnen helpen.

Fundamentele Stromingsleer

Voor fundamentele vloeistofmechanica is het gebruikelijk om de stroming van neutraal drijvende suspensies in canonieke geometrieën te bestuderen. De aanwezigheid van traagheid op deeltjesniveau of op systeemniveau kan de zaken compliceren. De eerste kan resulteren in verschillende gedragingen van de twee fasen, terwijl de tweede hydrodynamische instabiliteiten en/of turbulentie kan veroorzaken. Dit werk draagt bij tot het groeiende gebied van "Fluid Mechanics of Suspensions".

De stroming van suspensies in de Taylor-Couette geometrie (enkel rotatie van de binnenste cilinder) wordt bestudeerd met behulp van stromingsvisualisatie en koppelmetingen. Men ziet dat met toenemende deeltjesbelasting, de waarschijnlijkheid van het waarnemen van axisymmetrische Taylor wervelingen afneemt terwijl die van niet-axisymmetrische structuren toeneemt. Een afwijkende waarneming is dat een hybride vorm van axisymmetrische Taylor wervelingen en niet-axisymmetrische golvende wervelingen – azimutaal gelokaliseerde golvende wervelingen – kan bestaan in suspensies. Analyse van de frequentiespectra van de stromingsstructuren voorbij de wavy vortices suggereert dat de weg naar chaos veranderd is. Voor dicht beladen systemen wordt een tweede, incommensurabele frequentie (gerelateerd aan modulatie op wavy wervels) niet waargenomen. Gelijktijdige metingen van het koppel tonen aan dat de schalingsexponent tussen het koppel en de rotatiesnelheid van de binnenste cilinder onafhankelijk is van de deeltjesbelasting.

In buisstromingen wordt inertiële migratie van deeltjes waargenomen onder (semi-)verdunde omstandigheden. De mate van migratie wordt zwakker met toenemende Reynoldsgetallen, en is zelfs zichtbaar bij het begin van intermitterende stromingen. De afdruk van traagheidsmigratie is zwak zichtbaar in de tijd-gemiddelde snelheidsprofielen. Net als de tijd-gemiddelde deeltjesvolumefractieprofielen worden de tijd-gemiddelde snelheidsprofielen van deze suspensies afgevlakt naarmate de Reynoldsgetallen toenemen.

Toegepaste Stromingsleer

Suspensies zijn relevant in verschillende industriële processen, waarbij het transport van slurries in pijpleidingen een bekend voorbeeld is. Wanneer de deeltjesfase zeer klein is, wordt de slurry typisch beschouwd als een homogene niet-Newtoniaanse vloeistof. Hoewel dit een volwassen vakgebied is met een uitgebreide database van experimenten, zijn inzichten typisch verkregen door het meten van integrale hoeveelheden. Het werk in dit proefschrift dient als een proof-of-concept van hoe het niet-intrusief kijken in de stroming met ultrasone beeldvorming toegevoegde waarde kan hebben.

Het herstel van de slibstroom voorbij een 90° buisbocht wordt beoordeeld in een installatie op industriële schaal, door het beoordelen van het stroomwaartse momentum en (a)symmetrie van de snelheidsprofielen. Men ziet dat het herstel van de stroming sneller verloopt onder turbulente dan onder laminaire omstandigheden. Dit levert unieke experimentele gegevens op voor de validatie van numerieke modellen.

Het opnieuw bestuderen van de laminaire-turbulente overgang van een niet-bezinkend slib leverde genuanceerde inzichten op die nog niet eerder op de voorgrond waren geplaatst. Twee transiënten op lange termijn werden waargenomen - 'langzame bezinking'

en 'zelf-equilibratie', die kunnen worden vastgelegd in debietmeterstanden. Het fenomeen van langzame bezinking houdt verband met de sedimentatie van deeltjes over lange tijdschalen, die een uiteindelijke dichtslibbing kan veroorzaken. De zelf-evenwichtsfase houdt verband met de geleidelijke erosie van het bed van bezonken deeltjes, die leidt tot een toename van het debiet. De evenwichtsfase wordt bereikt na volledige resuspensie van de deeltjes door intermitterende turbulente structuren. Deze beide voorbijgaande fenomenen kunnen worden vertaald in nuttige richtlijnen voor de exploitatie van slurry pijpleidingen.

Hoewel deze dissertatie op een laag niveau van technologische gereedheid werkt, is er niettemin potentieel voor het werk hierin om bij te dragen aan onmiddellijke maatschappelijke of milieubehoeften. Bijvoorbeeld, de niet-Newtoniaanse slurry die in dit proefschrift wordt beschouwd, bootst de reologie na van geconcentreerd huishoudelijk afvalwater, waarvan het transport nog niet naar behoren in aanmerking wordt genomen in nieuwe, duurzame sanitaire systemen.

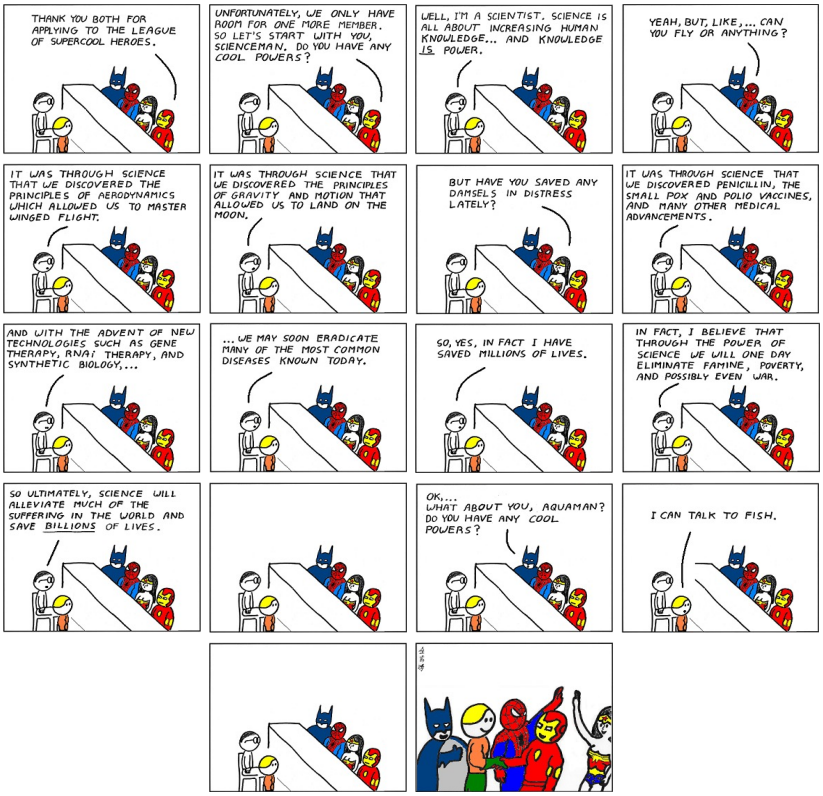

Source: Reshaped from "Science is Supercool" (*https://www.abstrusegoose.com/62*) - licensed under CC By 3.0

More particles, more problems: an introduction to this dissertation

Cross-fertilization is good for many living things and is equally good for scientific disciplines. *In the normal course of events fluid mechanics has been largely carried out in isolation in each of the disciplines that uses it, including meteorology, oceanography, mechanical engineering, chemical engineering, and many others. Learning something about meteorology and chemical engineering can on occasion be enormously productive for a mechanical engineer, for example.*

Meteorology has several times developed approaches that became common elsewhere in fluid mechanics only after a lapse of perhaps 20 years. For example, Lorenz was exploring chaos in meteorology in the late 1950s and early 1960s, but it did not really hit fluid mechanics until the work by Gollub and Swinney in the mid-1970s.

Smagorinsky was modeling the large-scale behavior of meteorological flows using simple closures in the mid-1960s, but large eddy simulation of turbulent flows in the rest of the fluid mechanics community did not take off until a decade later …

Leibovich (2003)

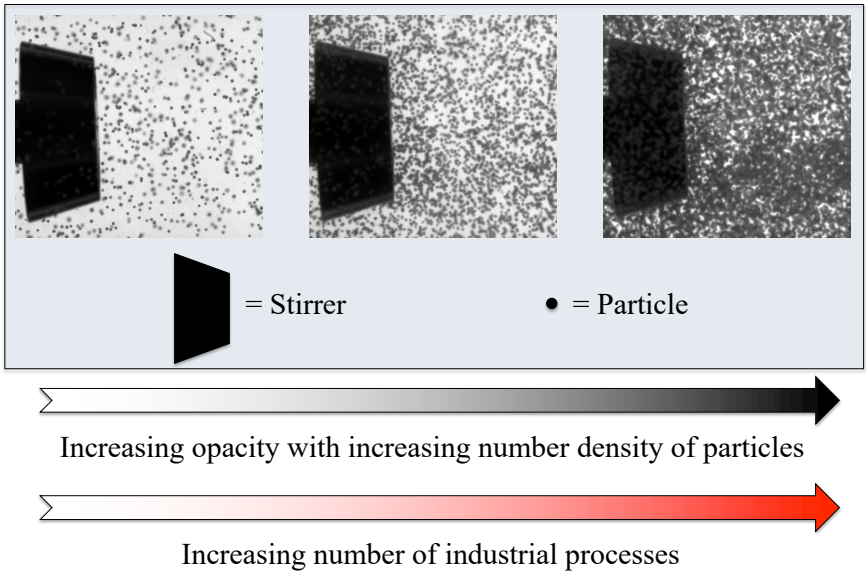

"More particles more problems" is an appropriate phrase to describe dispersed multiphase flows. By introducing more particles, problems are created in studying the flow with established optical measurement techniques. At the same time, by introducing more particles, one ends up studying problems more relevant to industrial processes.*

*Photographs are stills from videos recorded with the help of C. Çetın.

1.1. Flowing Suspensions: Inertia and Opacity

The Navier-Stokes equations have been identified as one of the "seventeen equations that changed the world" (Stewart, 2012). Established in 1845, these equations govern all flow related processes, be it in nature or in technology.

However, the equations have two terms that play contrasting roles: a non-linear advection term and a linear viscous diffusion term. The two terms commonly serve as proxies for inertial and viscous forces respectively. When the latter dominates, the system of equations can be simplified and often solved analytically. However, once inertial forces dominate, hydrodynamic instabilities and turbulence complicate the analysis.

Thus, once inertia is relevant, common practice is to solve the equations (or simplified derivatives thereof) on computers. To dispel any doubts on the solutions obtained by computational means, validation of the computed results with experiments is a crucial step. Over the past few decades, advances on computational and experimental fronts has significantly aided the Fluid Mechanics community in understanding and solving relevant problems. This also holds true for the various subdisciplines of Fluid Mechanics.

A specific subdiscipline of Fluid Mechanics is the flow of suspensions. A "suspension" refers to a multiphase system wherein insoluble solids are dispersed in a suspending liquid. The presence of multiple phases further complicates the physical understanding of such systems by introducing new parameters and phenomena. The adverse role played by the non-linear advection term for single-phase flows (continuous medium) is only exacerbated for suspensions (discontinuous medium). Inertia at the particle level means that the particle behaves differently than the carrier liquid, while inertia at the system level means that the flow may be prone to instabilities and turbulence. Moreover, if multiple particles are present, they can interact with one another as well. Again, once inertial forces dominate, the equations cannot be simplified and one has to resort to computational and experimental techniques, both of which have their own hurdles.

Unfortunately, matured experimental techniques that have been developed and refined for analysing transparent single-phase flows cannot be trivially applied to suspensions. The single biggest reason behind this is that suspensions are typically opaque, which necessitates one to resort to alternate measurement techniques which are either not as well developed or simply return data of inferior quality.

Thus, *"Opaque Inertial Suspensions"* is a difficult terrain of Fluid Mechanics to conquer. This dissertation attempts to make a dent herein by addressing two pertinent matters:

- From a fluid mechanical perspective, the focus is primarily on suspensions where inertia (of either the particles, the fluid, or both) is relevant.
- These suspensions are opaque. In order to study them experimentally, ultrasound imaging is the predominant weapon of choice in this dissertation.

This dissertation explores the Jekyll and Hyde nature of *"Opaque Inertial Suspensions"*. Suspensions are sure to show intriguing behaviour (Jekyll), but opacity and inertia (Hyde) will muddy the waters, pun intended. In the following sections, more detailed, yet general background information is offered in the framework of this dissertation.

1.2. OpaqueFlows

In order to address the issue of obtaining reliable experimental data in dispersed multiphase flows, a project proposal was approved in 2016 that tackles the issue head-on. The project is titled "Flows Unveiled: Multimodal Measurement in Opaque Two-Phase Flows" or "OpaqueFlows" in short (Poelma, 2018). Several early-career (post)doctoral researchers and students have contributed to this project with Christian Poelma (promotor of this thesis) as the principal investigator. The author of this thesis is one of the doctoral researchers. The official project objective is as follows:

Dispersed multiphase flows are encountered in nearly every process in nature and industry; examples include sediment in rivers, catalysts in reactors and blood flow. Despite their relevance, it is currently difficult to accurately and efficiently model these flows. The opacity of the flows, even at moderate volume fractions, renders the common optical flow measurement tools useless. As a result, very little high-quality data is currently available to develop (numerical) models.

In this project, I lift the veil that covers multiphase flows. I do this by bringing together four flow measurement modalities, based on ultrasound, magnetic resonance, X-ray and advanced optical imaging. These are each applied to three benchmark flows, impenetrable to common (optical) techniques. This project will be the first focused effort to systematically apply these techniques to the same three benchmark flows. These benchmarks are: (1) a turbulent flow with heavy particles, (2) a laminar flow with relatively large particles and (3) a laminar flow with small particles showing non-Newtonian behaviour. These three flows represent archetypical flows from nature and industry, each pertaining to particular open questions in the field of fluid mechanics. The combined velocity and concentration field data resulting from this set of experiments will be vital in assessing and improving each of the techniques: direct comparison will allow evaluation of the performance and show the effect of acquisition and processing parameters on the accuracy. Detailed simulations using the exact same conditions will serve as further reference. Combined with the multi-modal experimental data, this will give breakthrough insight in the underlying physics of each of the benchmark flows. This in turn will lead to better multiphase flow models, which are demanded by a wide range of application areas (e.g. process technology, dredging, food and cosmetics industry, and hemodynamics research).

A central tenet of this project is the ambition to combine multiple measurement techniques (multimodal measurement) to study a single flow in detail. Since each measurement technique has its own strengths and weaknesses, each modality would return useful but incomplete insights of the flow. However, together, information from the multiple modalities would help gain a more complete insight into the flow. This concept was likely inspired from the field of medical imaging diagnostics wherein different imaging modalities yield complementary information about the inner structure or functionality of the human body. While the concept of multimodality is commonplace in the medical imaging community, there are only select examples in the Fluid Mechanics community (Haavisto *et al.*, 2017).

Shown in Figure 1.1 is a schematic overview of the project as of November 2021. The original proposal seemingly hints at benchmark flows being centred around the choice of particles and the nature of the flow. However, the project has evolved differently with the benchmark flows being centred about the choice of geometry as well as the contents.

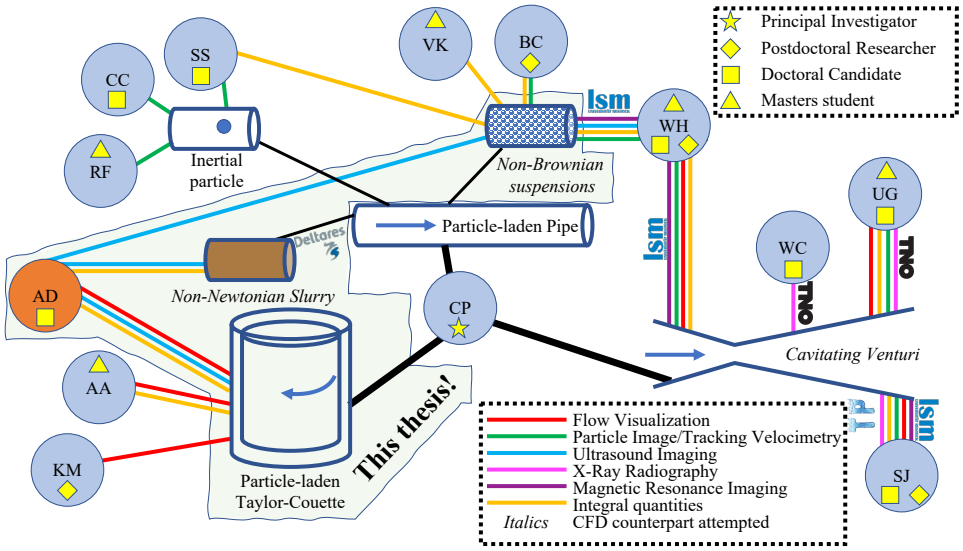

Figure 1.1: Global overview of contributors (initials shown), measurements (color-coded), and external collaborations (logos) under the umbrella of the OpaqueFlows project (November 2021).

Despite this detour, the key scientific questions put forth in the original proposal are being addressed. The three systems are 'cavitating venturi', 'particle-laden pipe flows', and 'particle-laden Taylor-Couette flows'. Within pipe flows, even further divisions can be made depending on the size, type, and quantity of particles present.

The global overview clearly shows that the "center-of-mass" is situated about the projects of non-Brownian suspension laden pipe flows and cavitating venturi. These two geometries have been probed the most thoroughly with numerous measurement techniques. All flow facilities except that of the non-Newtonian slurry belonged to the host laboratory. For this exception, the measurement apparatus was transported to the flow facility at the collaborator. Similarly, knowledge and equipment for all measurement techniques except X-Ray radiography and Magnetic Resonance Imaging were available within the lab. For the two exceptions, the flow loops were transported to the respective measurement equipment with the collaborator. In almost all cases, integral quantities (pressure drops, torque) were measured. In a few instances, comparison with Computational Fluid Dynamics has also been attempted.

1.3. Objectives and outline of this thesis

Given that this thesis is written under the umbrella of the "OpaqueFlows" project, the overarching objective of the research in this thesis is to tackle a variety of opaque flowing suspensions using experimental techniques, with a focus on ultrasound imaging. To formalize it, the objective of this dissertation is:

How and to what extent can state-of-the-art measurement techniques be leveraged, in particular ultrasound imaging, to gain novel insights into the fluid mechanics of opaque inertial suspensions?

Specific research questions are given in the list containing the chapter-by-chapter breakdown at the end of this chapter. In Figure 1.2, a schematic overview of the major contributions of this dissertation are illustrated. The contents of this thesis can be classified broadly into two categories: (i) Fluid Mechanics of inertial suspensions and (ii) Ultrasound imaging for tackling opaque flowing suspensions. This thesis touches upon topics that can be interesting to Fluid Mechanicians interested in fundamental phenomena, application-oriented research, and experimental techniques.

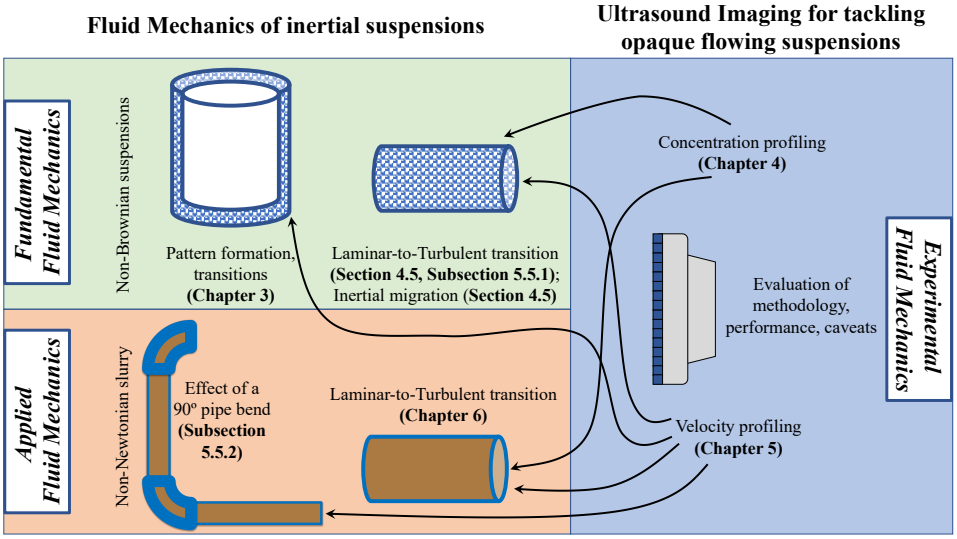

Figure 1.2: A visual guide to this thesis - major contributions and where to find them.

One of the central tenets of the "OpaqueFlows" project is the analysis of a single flow geometry with multimodal imaging techniques. In this thesis, ultrasound imaging, flow visualization, and integral quantity measurements (pressure drop and torque) are utilized. This thesis contributes to the development and better understanding of ultrasound imaging in particular, which can then serve as a matured modality in future experiments of flowing suspensions.

This thesis has four main chapters. For the most part, each chapter may be read individually. In the text below, an attempt is made to link the contents of each chapter to the contents of the "OpaqueFlows" project objective. The bold text below are research questions for each individual chapter. Prior to these main chapters, an overview of the state-of-the-art on the topics of suspension fluid mechanics and ultrasonics (for suspension fluid mechanics) is presented (**Chapter 2**).

1. **Particle-laden Taylor-Couette flows (Chapter 3):** The genesis of the "OpaqueFlows" project laid on the foundation that common optical flow measurement techniques failed under moderate particle loading, preventing the experimentalist from curating high-quality data. In this chapter, a counter-example is provided wherein the problem of opacity is circumvented by imaging the near wall flow in a Taylor-Couette geometry. This allows for the characterization of secondary motions and subsequently, a detailed study of pattern formation in dense, neutrally buoyant, non-Brownian suspensions. In the "OpaqueFlows" project objective, *common optical flow measurement tools* likely referred to velocimetry techniques and *high-quality data* likely referred to the internal structure of the flow (thus spatio-temporal velocity profiles or distribution of particles). However, flow visualization can also be viewed as a *common optical flow measurement tool*. The flow visualization measurements are complemented by torque measurements. This could already provide sufficient insights to validate numerical models. There are some studies that investigate the role of particle volume fraction and Reynolds number on the flow pattern observed in the Taylor-Couette geometry. However, all these studies are restricted to the first appearance of wavy Taylor vortices. In this chapter, the following questions are addressed:

What is the characteristic of the flow structures beyond the appearance of wavy Taylor vortices, particularly with an eye on the route to chaos? What additional information do the torque measurements provide? Can new structures be discovered in suspension Taylor-Couette flows?

2. **Ultrasonic particle volume fraction profiling (Chapter 4):** Another aspect of the "OpaqueFlows" project is to develop, assess, and improve measurement techniques with respect to obtaining velocity/concentration profiles. Using ultrasound to obtain velocity field data has penetrated the Fluid Mechanics community significantly over the past decades. However, ultrasound can also be used to obtain information on concentration field data. While other communities (primarily, coastal engineering) have been active in this field, this topic is yet on the fringes of the experimental fluid mechanics community. In this chapter, the methodology to obtain particle volume fraction profiles from ultrasonic data and associated caveats are described and assessed. As a case study, inertial migration of particles in optically inaccessible, neutrally buoyant, suspension-laden pipe flow is investigated. In this chapter, the following questions are addressed:

How can one profit from ultrasonic backscatter data to reconstruct particle volume fraction profiles? What are the possibilities and limitations in the context of ultrasonic particle volume fraction profiling? Can inertial migration of particles in a pipe flow be detected at optically inaccessible volume fractions?

3. **Ultrasound Imaging Velocimetry in particle-laden flows (Chapter 5):** While ultrasound has been utilized to obtain velocity data, it is often in homogeneous fluids

seeded with tracer particles. Ultrasound functions in a more complicated manner when used in particle-laden systems. In this chapter, the performance of ultrasound imaging velocimetry is assessed for two types of particle-laden pipe flows - at laboratory scale and at industrial scale. For the former, a neutrally buoyant, non-Brownian suspension is considered while for the latter, a non-Newtonian slurry. Correspondingly, two case studies are presented: laminar-turbulent transition for the laboratory scale flow and flow about a 90° bend for the industrial scale flow. The latter case study reaped more success. In fact, the non-Newtonian slurry serves as a proxy for concentrated wastewater and corresponding numerical simulations are being performed by external collaborators. These case studies are accompanied by a theoretical counterpart which sufficiently explains the performance of ultrasound imaging velocimetry in particle-laden flows. With respect to the "OpaqueFlows" project, the work in this chapter contributes to the maturation of ultrasound imaging velocimetry as a modality. In this chapter, the following questions are addressed:

What is the role of particles in the quality of velocimetry data? How can one gain the maximum out of the recorded images in the context of velocimetry? To what extent can ultrasound imaging velocimetry tackle flows in academic or industrial backdrops?

4. **Long-time-scale transients in a slurry pipeline (Chapter 6):** This chapter illustrates the added value of ultrasound imaging in explaining peculiar observations of integral quantities such as volumetric flow rate and pressure drops in a horizontal slurry pipeline. Even though the topic of laminar-turbulent transition of non-settling slurries has been studied for several decades, most studies are restricted to measurement of global quantities such as pressure drops. Moreover, there is seemingly little work reported on the role of the experimental protocol. As was intended to be the ultimate objective of the "OpaqueFlows" project, the work in this chapter works on translational research. Unique insights in the fundamental fluid mechanical aspects of slurry flows are brought to light with ultrasound, which bear consequence for applications. In this chapter, the following questions are addressed:

What is the role of the experimental protocol in the context of slurry pipe flows? What additional information does ultrasound imaging offer to the measurement of global quantities of slurry flows? Can understanding the underlying fluid mechanical processes provide inputs on practical guidelines to operate a slurry pipeline?

In the final chapter (**Chapter 7**) the novel contributions of this dissertation are summarized, suggestions for future work are offered, and the impact of the work herein is discussed.

2

A primer for suspension fluid mechanics and ultrasonics

Resolution of the open issues in suspension mechanics may result from development (and combination) of new – or creative application of existing – experimental, theoretical, and numerical tools. Some experimental tools, such as particle-image velocimetry (PIV) and particle tracking velocimetry (PTV), which are discussed below, have undergone extremely rapid evolution and wide dissemination, allowing more researchers to benefit from them …

On the experimental side, the greatest difficulty in suspension flows results from the fact that the medium is opaque, particularly when the particles are concentrated. The classical pure fluid techniques thus often cannot be used directly. However, techniques such as PIV and PTV which are now quite common can be applied either in dilute … suspensions or even to dense suspensions when index matching is applied. By index matching, we refer to the careful choice of liquid and solid having the same index of refraction. In general, it will be necessary to tag a few of the particles, or alternatively to tag the fluid using a fluorescent dye. Note that these direct imaging techniques are made all the more powerful by high-speed cameras which are now used in many laboratories. More involved and less broadly accessible methods may provide information that is difficult to access otherwise; these include magnetic resonance imaging (MRI), electrical impedance tomography (EIT), or X- or gamma-ray based techniques.

Guazzelli and Morris (2011)

Section 2.2.1, Section 2.2.2, and Section 2.2.3 are based on Appendices C, B, and A in Dash, Hogendoorn, and Poelma (2021).

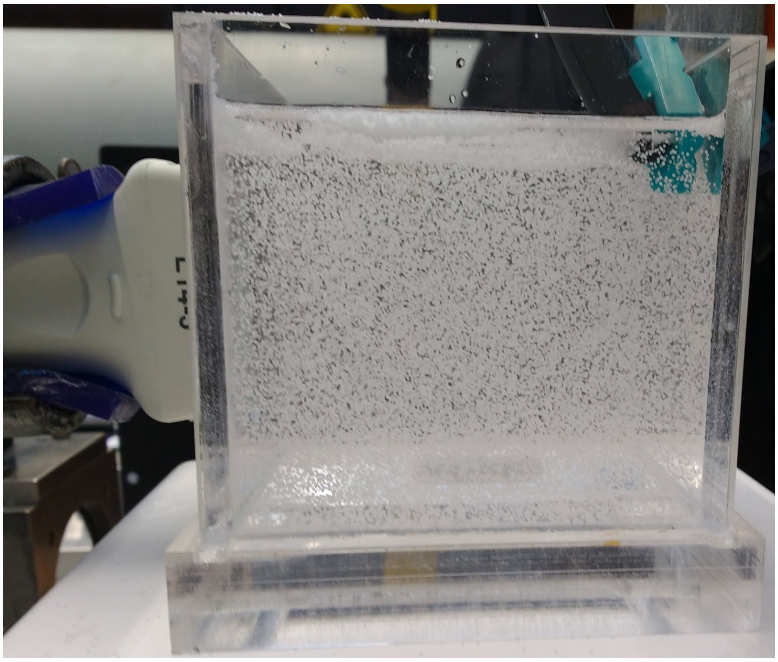

A bit surprisingly, ultrasound (sound waves with frequencies exceeding the human hearing range) is overlooked in the above quote. Sound can succeed where light fails. In the photo, an ultrasound transducer (on the left) is used to study the suspension.

2.1. Fluid Mechanics of Suspensions

A suspension refers to a mixture of solid particles dispersed in a liquid continuum. The phrase "fluid mechanics of suspensions" has been directly taken from the recent review article by Morris (2020). While an explicit definition for this phrase was not offered, Morris (2020) does state " ... *whereas the 'fluid mechanics of suspensions' remains a topic that is in its infancy – only a few of its features are becoming clear enough to define it as a subject.*" A related topic which is considered to be relatively mature is the rheology of suspensions, where the base flow is laminar (Guazzelli and Pouliquen, 2018). The topic "fluid mechanics of suspensions" probably encapsulates the collection of partially addressed open questions, including a couple that can be found in the epilogue of the book by Guazzelli and Morris (2011): *"alteration of existing instabilities: ... the presence of particles may alter instabilities known for pure fluids."* and *"Finite inertia and turbulence: This is a practically relevant topic, not only in industrial processes but also in natural phenomena ..."*. This is also reflected in the examples covered by Morris (2020). The above three references as well as the recent review article by Brandt and Coletti (2022), which focuses on the turbulent regime, serve as good starting points for one to get acquainted with the state-of-the-art on the fundamentals of flowing suspensions.

In order to understand the fundamentals of any flow, research is often carried out in so called canonical geometries. Two primary examples are the (vertical) Taylor-Couette geometry and the (horizontal) pipe flow. A key difference between the two is the driving mechanism of the flow. In the former, flow is generated by motion of the cylinders (walls) making it a shear-driven flow. In the latter, flow is generated by a pressure gradient making it a pressure-driven flow. In the following subsections, a few key physical concepts behind single-phase flows as well as particle-laden flows in these two geometries are presented. The literature is discussed in a broad manner with an aim to discuss key phenomena without necessarily stating all details or exceptions. As a result, not all relevant literature is cited.

2.1.1. Taylor-Couette flow

Single-phase flows

The Taylor-Couette geometry is the more abstract of the two geometries. This geometry has two concentric, independently rotating cylinders with the working fluid present in the gap. In this section, key developments in single-phase Taylor-Couette flow research, relevant to this dissertation, are highlighted. For pure inner cylinder rotation, the flow is typically characterized by the Reynolds number based on the radial gap width, inner cylinder speed, and the kinematic viscosity of the working fluid.

Studying the flow in the Taylor-Couette geometry began in the late 19th century with the independently executed experiments of Couette (1890) and Mallock (1896). These studies had the goal of estimating the viscosity of the working fluid. Based on the simplest particular integrals of the equations for fluid motion (Stokes equations), the measured torque was expected to be linearly related to the rotation rate of the cylinder. An observation common to these early studies was that there were scenarios when the flow was either "stable" (linear relation between torque and rotation rate) or "unstable" (non-linear

relation between torque and rotation rate).

The Taylor-Couette geometry was then chosen by Taylor (1923) as a geometry to study the onset of "unstable" flows. Compared to the infinite planar Couette geometry, this was a pragmatic choice. Taylor (1923) found an excellent agreement between experiments and linear stability theoretical calculations for the onset of "unstable flows" – a unique achievement, especially given that all calculations were performed without a computer. This was the first time one had successfully predicted the onset of instabilities theoretically. Prior to this, the likes of Kelvin, Rayleigh, Sommerfeld, Orr, Mises, and Hopf had attempted to solve this problem in a planar Couette flow, but were unsuccessful. The theoretical calculations rested on the no-slip boundary condition assumption, the success of which has apparently been considered *"as perhaps the most convincing proof of the correctness of the Navier-Stokes equations and of the no-slip boundary condition for the fluid at the cylinder walls"* (Donnelly, 1991). The theoretical work herein was a step further than the stability analysis of Rayleigh (1917) wherein the fluid was inviscid. A key outcome from the work of Taylor (1923) was the emergence of vertically stacked, axisymmetric structures (commonly known as Taylor vortices) when the flow became unstable under pure inner cylinder rotation (owing to centrifugal forces). The height of each vortex was equal to the radial gap between the cylinders, as also predicted theoretically. These Taylor vortices are referred to as secondary motions, and their appearance leads to a sharp rise in the torque needed to drive the inner cylinder (linear to non-linear relation between torque and rotation rate of cylinder). This landmark publication remains celebrated to this day*.

The next major insight on pattern formation in the Taylor-Couette geometry was provided by Coles (1965), a landmark paper summarizing a decade's worth of work. This work is synonymous with "wavy" Taylor vortices – a secondary instability, wherein azimuthally travelling waves appear atop the Taylor vortices. While earlier studies had observed wavy Taylor vortices, this was the first time it was recognized as a new feature of the flow. A key feature of these wavy vortices was its non-uniqueness. At any given Reynolds number, multiple stable flow states (sometimes as many as twenty) could be achieved, depending on the initial conditions and the history of the flow. Di Prima and Swinney (1985) remark *"In retrospect it is not surprising that there exist multiple stable states. Uniqueness of the solutions of the Navier-Stokes equations has been proved only for very small Reynolds number, and nonlinear systems often exhibit multiple stable solutions; nevertheless, we know of no other physical system for which the existence of multiple stable states has been so vividly demonstrated."*

Gollub and Swinney (1975) provided the next major breakthrough in this geometry. By means of analysing velocity spectra, the authors showed that the transition to turbulence occurred in finite steps. This work was later reported in detail by Fenstermacher, Swinney, and Gollub (1979). Wavy Taylor vortices are characterized by one fundamental frequency - related to their propagation speed (King *et al.*, 1984). Upon increasing the Reynolds number, a second, incommensurate frequency component appeared in the spectrum. The significance of the second incommensurate frequency would be later demonstrated by Gorman and Swinney (1982), that the second frequency corresponds to modulations on the wavy Taylor vortices. Further increase in the Reynolds number

*Kundu, Cohen, and Dowling (2012) report *"When asked, however, what gave him maximum satisfaction, Taylor singled out his work on the stability of Couette flow."*

saw the introduction of weak broadband component, and subsequent disappearance of the two incommensurate fundamental frequencies, one by one. The appearance of the weak broadband component was denoted as the onset of chaos. The key significance of the finding was in disproving the theory of Landau (1944) who claimed that turbulence occurs in infinite steps. The Landau picture stated that at each step, a new incommensurate frequency is added to the spectrum, until the spectrum looks *"complicated and confused"* (Swinney and Gollub, 1978). However, this finding supported the picture provided by Ruelle and Takens (1971) who postulated that turbulence occurs only after a finite number of transitions*. The movie by Gorman and Swinney (2009) offers a nice overview of the transitions in the Taylor-Couette flow†.

Perhaps the most well-known image related to the Taylor-Couette geometry is the regime map compiled by Andereck, Liu, and Swinney (1986). The regime map displays the pattern formed in the system as a function of the Reynolds number of the two cylinders. Koschmieder (1993) states *"The experimental stability diagram ... is based on one particular experimental procedure which was followed at all Reynolds numbers in order to obtain consistent results. That means that does not show the total complexity of Taylor vortex flow between two rotating cylinders ... This procedure does not permit the observation of hysteresis."* This work demonstrated how unpredictable the flow can be away from equilibrium, while at the same time showing the richness of beautiful flow patterns that could be observed in this simple geometry.

In recent years, one of the key lines of research in the Taylor-Couette geometry has been on highly turbulent flows‡, wherein the boundary layer is also fully turbulent. Some of the earlier works on this subject can be found in Wendt (1933), Lathrop, Fineberg, and Swinney (1992) and Lewis and Swinney (1999). One of the experimental facilities that greatly contributed to this line of research is the Twente turbulent Taylor-Couette facility (van Gils *et al.*, 2011; Lohse, 2011), which can reach Reynolds numbers of 2 million (pure inner cylinder rotation). This facility is accompanied by a 20 kW refrigerator to maintain a constant temperature of the fluid. From a practical viewpoint, there is an upper limit to the Reynolds number that can be studied here due to viscous dissipation, which scales approximately with the cube of the Reynolds number. Therefore, a tenfold increase in Reynolds number would mean that a thousand times stronger motor and cooling capacity would be required (production ≈ dissipation). Nevertheless, a key point is that at even at extremely high Reynolds numbers, Taylor vortex-like structures persist in the flow.

For a historical development of the flow in this simple apparatus, the article of Donnelly (1991) is a good read. The book of Koschmieder (1993) offers a more extensive overview of the developments in this geometry until 1992. The review by Fardin, Perge, and Taberlet (2014) offers a concise overview as well. For a more recent summary, focusing specifically on single-phase, highly turbulent Taylor-Couette flows, the review article by Grossmann, Lohse, and Sun (2016) is recommended. In contrast to the above ref-

*"*And Ruelle said: "You have seen evidence of behaviour described by a strange attractor." We didn't know what a strange attractor was, but that sounded good."* (Harry Swinney in Thiel *et al.*, 2010)

†Gorman, Reith, and Swinney (1980) also report long-lived flow states with three and four incommensurate frequencies.

‡One of the reasons behind this is that the Taylor-Couette flow shares several similarities with Rayleigh-Bénard convection (Prigent *et al.*, 2006). It is practically easier to obtain turbulence with mechanical driving than thermal driving. The two systems are sometimes also referred to as "the twins of turbulence research".

erences, the book of Chossat and Iooss (1994) approaches the Taylor-Couette flow as a problem of applied mathematics. While most of the Taylor-Couette research is dominated by fundamental aspects, this geometry also has numerous engineering applications, as highlighted in the review on Taylor-Couette reactors by Schrimpf *et al.* (2021).

Neutrally buoyant, non-Brownian suspensions of spherical particles

One of the earliest studies of neutrally buoyant suspensions in a Taylor-Couette geometry were the seminal experiments of Bagnold (1954), wherein only the outer cylinder was rotated and the system was filled with extremely dense suspensions. Two flow regimes were reported, which were dependent on the shear rate of the system. At low shear rates, viscous fluid stresses dominate ('macro-viscous' regime) and at high shear rates, grain collision stresses dominate ('grain-inertia' regime). The two regimes are separated by an intermediate regime. This led to the conception of a non-dimensional number to demarcate the two regimes, the Bagnold number. This work has since been critically reassessed by Hunt *et al.* (2002). A key conclusion drawn from this reassessment was that the apparatus used by Bagnold (1954) was relatively short and the results were likely influenced by the end plates of the system as well. Nonetheless, the work of Bagnold (1954) has been very influential and has been highly cited amongst the rheology and granular flows community.

The first reporting of shear-induced migration of particles is attributed to the experiments of Leighton and Acrivos (1987)*. It was observed that particles migrated from a region of high shear rate to a low shear rate of their facility†, which also helped explain the puzzling observations of Gadala-Maria and Acrivos (1980). Basically, Gadala-Maria and Acrivos (1980) noticed that the viscosity measured by their rheometer reduced significantly over the course of hours. Since then, numerous experiments have reported this migration phenomenon in Couette geometry (Abbott *et al.*, 1991; Chow *et al.*, 1994; Tetlow *et al.*, 1998; Ovarlez, Bertrand, and Rodts, 2006).

All of the above literature and associated phenomena have been primarily addressed by the rheology and granular flows community. Moreover, this shear-induced migration phenomenon is attributed to particle-particle interactions in dense suspensions. In dilute suspensions, with relatively large particles, fluid-particle interactions are responsible for the phenomenon of inertial migration. For example, Halow and Wills (1970a,b) report inertial migration in the Couette geometry wherein spheres migrate to an equilibrium position close to the midpoint of the system. This problem was recently revisited by Majji and Morris (2018), and provide clear visualizations of migration‡. When there is circular Couette flow (no secondary motions), the particles migrate to a location close to

*Another set of experiments performed in the Couette geometry was by Karnis, Goldsmith, and Mason (1966b), surprisingly in a counter-rotating system. One of the key findings was that with concentrated suspensions, the velocity profile would deviate significantly from the analytical solution for single-phase flows. The deviation becomes even more pronounced with increasing particle sizes. It is unclear whether these observations can be simply attributed to shear-induced migration effects.

†Strictly speaking, the experimental facility of Leighton and Acrivos (1987) differs from conventional annular Couette geometries. In their case the high shear region is the annular gap and the low shear region is a reservoir. In a conventional annular Couette geometry, the region of high shear is near the inner cylinder (bob) and the region of low shear is near the outer cylinder (cup).

‡The images of migration shown by Majji and Morris (2018) are not instantaneous snapshots, but are compositions of several images within the time period of a single rotation of the cylinder.

the midpoint of the annular gap. Upon the appearance of Taylor vortices, two types of particle behaviour is seen. When the vortices are weak, the particles are distributed nearly uniformly in the core with particle free regions in the boundaries. Once the vortices are sufficiently strong, the particles accumulate along a circular equilibrium region in each vortex, whose diameter grows with increasing Reynolds numbers. Once wavy vortices appear, particles are unable to reach an equilibrium position and the particles are uniformly distributed. Numerical work by Henderson and Gwynllyw (2010) studies the effect of particle size as well density ratio of the two phases on migration behaviour in the presence of Taylor vortices. They show that when the neutral buoyancy criterion is not perfectly satisfied, there exist retention zones (wherein particles are retained and eventually reach a limit cycle) as well as non-retention zones (wherein particles are influenced by gravity as they move vertically across the Taylor vortices). The authors show that the extent of the retention zones is higher with increasing satisfaction of the neutral buoyancy criterion, decreasing particle sizes, and increasing Reynolds numbers. The latter observation is also visible in the experiments of Majji and Morris (2018).

Yet another topic of interest combining neutrally buoyant suspensions and Taylor-Couette flow is the effect of the suspensions on the flow regimes and instabilities (with inner cylinder rotation). Ali *et al.* (2002) were perhaps the first to attempt this problem and studied extremely dilute suspensions experimentally and analytically (linear stability analysis). The experimental findings did not qualitatively match the predictions of decreasing critical Reynolds numbers for the onset of Taylor vortices. The paper of Majji, Banerjee, and Morris (2018) revived this subject. Basically, they showed that as the particle size increases, their effect on the flow regimes becomes more emphatic. For larger particles, it was shown how the appearance of Taylor vortices is diminished upon increasing the concentration of particles, and are replaced by non-axisymmetric structures such as spiral vortices and/or ribbon like structures. For smaller particles, observation of similar non-axisymmetric structures was subdued. For the larger particles, it was systematically shown that the critical Reynolds numbers at which the flow becomes unstable reduces with increasing particle loading. Both, Majji, Banerjee, and Morris (2018) as well as Gillissen and Wilson (2019) have attempted to predict experimental findings with the help of linear stability analysis, but this has proven challenging. Ramesh, Bharadwaj, and Alam (2019) looked closely into the effect of experimental protocol and demonstrate the presence of hysteresis in the flow regimes observed. One of the important findings was the presence of vertically segregated flow states wherein two differing flow features could coexist simultaneously in the system. Velocimetry measurements of the secondary motions corroborate their flow visualization observations while also allowing for characterizing the skeleton of the structures. Ramesh and Alam (2020) additionally provide examples on the existence of counter-propagating spiral vortices*. Baroudi, Majji, and Morris (2020) demonstrate how inertial migration in the system, as compared to a well mixed system, could significantly affect the flow regimes observed at a certain Reynolds number. Some of their results even suggest that the flow might never gain equilibrium. In a recent numerical work, Kang and

*While Ramesh and Alam (2020) refer to the flow state in Figure 3(a) of their work as interpenetrating spiral vortices, it might have been more appropriate to refer to it as counter-propagating spiral vortices, based on Figure 2 of Goharzadeh and Mutabazi (2010). Chossat and Iooss (1994) refer to counterpropagating spiral vortices as a regime with a defect (see Figure I.6 and Figure VII.12 therein) while hinting that it is metastable.

Mirbod (2021) use the Suspension Balance Model to investigate flow transitions in such a system. It is unclear whether the Suspension Balance Model is the most appropriate tool for a direct comparison with the experimental works. The authors themselves acknowledge that the Suspension Balance Model is focused on shear-induced migration rather than inertial migration. Despite this, the authors are able to recover several non-axisymmetric structures observed in experiments. The very recent experiments of Moazzen *et al.* (2022) add to the growing literature on this subject. To conclude, *"After just a few years of intensive study, the behavior of suspensions in TC flow is seen to be so rich that the range of behavior verges on bewildering"* (Morris, 2020).

2.1.2. Pipe flow

Single-phase flows

Compared to the Taylor-Couette geometry, the nature of transitions in a pipe flow are a lot "simpler" - that there is a direct, abrupt transition from laminar to turbulent flows*. In the Taylor-Couette geometry, increasing the Reynolds number causes the system to undergo a sequence of successive instabilities. Each instability increases the complexity of the dynamics in the system until turbulence is attained. In this context, Barkley (2016) remarks *"There is just one problem – this picture is essentially irrelevant to transition in pipe flow. One can end up wasting a lot of time trying to bend and contort this scenario to try to make it conform to what is observed in pipe experiments. In actuality, the route to turbulence in pipe flow is of a wholly different type, and requires a completely different perspective. If you have the above picture of transition in mind, you should forget it now. I cannot stress this enough."*

One of the earliest, influential works on the topic of pipe flows were the experiments of Poiseuille (1846)†. These experiments were performed in capillary tubes, and was key to the establishment of the (Hagen-)Poiseuille law‡. The Poiseuille law relates the pressure drop per unit length, volumetric flow rate, fluid viscosity and pipe diameter in laminar flows. Darcy (1857) was perhaps the first to show that the linear relation between pressure gradient and volumetric flow rate changes to a non-linear one, at high flow rates. This qualitative change was attributed to the appearance of disordered motions. However, Hagen (1854) might have been the first to describe laminar-turbulent transition, wherein sawdust was used for flow visualization (Rott, 1990).

All of these paved way to the celebrated (flow visualization) experiments of Reynolds (1883a,b), a topic covered in almost every undergraduate level course on Fluid Mechanics. These publications set up several key concepts that are relevant even today. The experiments recognized the phenomenon of laminar to turbulent transition of the flow. Around

*In the Taylor-Couette geometry, with pure outer cylinder rotation, the flow also undergoes a direct transition from laminar to turbulent state.

†This is a reference to the summary paper. Poiseuille had communicated his results in 1840-1841. See Sutera and Skalak (1993) for an extensive overview on the work and life of Poiseuille.

‡The work of Hagen (1839) was performed independently and published before those of Poiseuille. However, more often than not, the law is referred to as Poiseuille law. Sutera and Skalak (1993) write about the work of Hagen *"His results were similar to those of Poiseuille, but less extensive and less accurate. However, they included some entrance effects and observations of the differences between laminar and turbulent flows. "*

this transition, "flashes" of turbulence were reported. More importantly, based on extensive measurements in pipes of various diameters, flow velocities, fluid viscosities, a new non-dimensional number was conceived, what is now commonly known as the Reynolds number (Re). It was shown that the Reynolds number at which laminar-turbulent transition is nearly a constant, $Re \approx 2100$. Nevertheless, Reynolds did recognize the role of background disturbances and also demonstrated that this transition could also occur at $Re \approx 13000$. This observation is supportive of what is now known about pipe flows, that it is linearly stable (stable to infinitesimal disturbances) and finite-amplitude perturbations are necessary to trigger the transition to turbulence.

The overall understanding of the transition to turbulence in pipes has grown significantly since the experiments of Reynolds. The references in the following paragraph only cover a few, recent studies. There are numerous other relevant studies as well. For a broader overview on transition to turbulence in pipe flows, the review articles by Eckhardt *et al.* (2007), Mullin (2011), and Barkley (2016) can serve as good starting points. Figure 36 in Barkley (2016) succinctly illustrates the process of laminar-turbulent transition.

In recent years, it has been shown by Faisst and Eckhardt (2003) that alternative, exact solutions to the Navier-Stokes equations exist next to the Hagen-Poiseuille solution (parabolic velocity profile), which take the form of unstable travelling waves ($1250 \leq Re$). Signatures of the travelling waves were later experimentally observed by Hof *et al.* (2004) in puffs (intermittent turbulent structures in a laminar background). In controlled experiments, these puffs are typically generated by perturbing the flow with well-defined disturbances. Whether the puffs are sustained or not depends on the Reynolds number as well as the measurement location. At lower Reynolds numbers ($1775 \leq Re \leq 2050$), the puffs eventually decay, suggesting that the turbulence is a long-lived transient or metastable (Hof *et al.*, 2006). At slightly higher Reynolds numbers ($2050 \leq Re \leq 2500$), the timescale for the the decay of the puffs become higher than the timescale for them to split (Avila *et al.*, 2011; Hof, 2011). In these cases, turbulence proliferates by splitting. Based on the crossover of the timescales of these two processes, Avila *et al.* (2011) determine the critical Reynolds number for the onset of sustained turbulence as $Re = 2040 \pm 10$. At higher Reynolds numbers ($Re \geq 2500$), there is a transition from puff splitting processes to weak slug expansion. A slug is a structure wherein the the downstream front of the structure advects at a speed faster than the upstream front. When the downstream front advects faster than the laminar flow in front of it, the turbulent patch invades the laminar region, leading to an expansion. At even higher Reynolds numbers, strong slug expansion can be observed, wherein turbulence spreads at both fronts of the structure. When the fronts expand in this manner, fully turbulent flow arises (Barkley *et al.*, 2015).

Mullin (2011) remarks the following on the practical and philosophical relevance of transitional flows: *"The issue of transition to turbulence in pipe flow is both of deep scientific interest and of significant engineering importance. Transitional flows can involve large pressure variations as the pressure gradient required to drive laminar and turbulent flows may differ by an order of magnitude. Thus flows in oil and gas pipelines are sometimes run inefficiently turbulent to avoid the large pressure fluctuations found in the transitional regime. In addition, the control of turbulence is a dream of many practitioners, just as an understanding of turbulence is the desire of many scientists."*

Neutrally buoyant, non-Brownian suspensions of spherical particles

Some of the earliest works on this topic were performed in the 1960's (Cox and Mason, 1971; Leal, 1980). Research on this topic was likely motivated by rheology of blood as well as problems associated with paper making. Studying spheres offers more simplicity than rods, discs or ellipsoidal grains.

Among one of the major discoveries in this time was the observation of lateral migration of spherical particles in an initially uniform dilute suspension flowing in a tube (Segré and Silberberg, 1961). Basically, the particles arrive at an equilibrium at a location intermediate to the pipe axis and the pipe wall. This phenomenon goes by several names such as 'inertial migration' and 'tubular pinch effect'. Inertial migration is attributed to *"fluid-particle interaction within the confining geometry of a conduit"* (Guazzelli and Morris, 2011). An associated observation was the formation of long-lived chains of particles aligned along the streamwise direction, first noted by Segré and Silberberg (1962)*.

The next major advances on this subject were in the 2000's. A thorough investigation on inertial migration of a single sphere was performed by Matas, Morris, and Guazzelli (2004). At low Reynolds numbers, the migration phenomenon resembled what was reported by Segré and Silberberg (1961). As the Reynolds number was increased, the behaviour was modified with this annulus moving outwards, towards the wall. Another remarkable observation was that at high Reynolds numbers, yet another annulus emerged. This 'inner' annulus was located closer to the pipe axis than the 'outer' annulus originally reported by Segré and Silberberg (1961). In a related study, Matas *et al.* (2004) analyse the formation of particle trains (long-lived chains of particles aligned along the streamwise direction) in more detail†.

In recent years, further insights were gained in the phenomenon of inertial migration by the works of Morita, Itano, and Sugihara-Seki (2017) and Nakayama *et al.* (2019). In both cases, pipe facilities with high ratios between pipe length and inner pipe diameter were used. Morita, Itano, and Sugihara-Seki (2017) speculated that the "inner annulus" is a transient phenomenon and that the particles would eventually concentrate themselves on the "outer annulus". However, claiming this conclusively would require relatively long pipes, especially for high Reynolds number. The work of Nakayama *et al.* (2019) extended on this work by using a pipe with an even higher ratio between its length and inner diameter. Three regimes were demarcated. At low Reynolds numbers, particles were focused only on the "outer annulus", on both annuli for intermediate Reynolds numbers, and only on the "inner annulus" for higher Reynolds numbers.

The above studies are restricted to dilute suspensions. However, there are also numerous studies involving much more concentrated suspensions. Among the earlier studies on this subject are of experimental nature wherein velocity and concentration profiles were measured‡ (Karnis, Goldsmith, and Mason, 1966b,a). One of the key findings by Karnis,

*The authors call this structuring 'necklaces' and state *"These phenomena are here described for their intrinsic interest but were not followed up systematically."*

†Maude and Yearn (1967) also report on the presence of a 'wall peak' (high concentration of particles close to the tube wall) and that the particle trains form within this peak.

‡This was achieved by refractive index matching of both phases and only a few non-refractive index matched particles were used as tracers. Concentration profiles were obtained by simple counting and binning of tracers. For velocity profiles, the flowing suspensions were photographed through a microscope. The films were then analysed by projecting them onto a drafting table.

Goldsmith, and Mason (1966b) was that upon increasing the concentration of the suspension, the velocity profile went from a parabolic shape to a partial plug flow. In Karnis, Goldsmith, and Mason (1966a), the presence of a particle-free layers near the pipe wall were reported, which affect the velocity profile as well as reducing the measured pressure drops.

Since then, numerous studies have investigated this behaviour and refined the conclusions of Karnis, Goldsmith, and Mason (1966b)*. The blunting of velocity profiles for concentrated suspensions is attributed to the phenomenon of shear-induced migration, wherein particles move from a region of high shear to low shear. In laminar pipe flows, this translates to particles moving towards the axis, which has been captured experimentally (Sinton and Chow, 1991; Hampton *et al.*, 1997; Butler and Bonnecaze, 1999). Shear-induced migration is attributed to particle-particle interactions leading to a non-Newtonian rheology. In this sense, it differs from inertial migration which is attributed to particle-fluid interactions in a closed geometry. Han *et al.* (1999) provide a unique example wherein it is demonstrated that the two phenomena may occur concurrently.

Most of the above work is restricted to laminar flows. Another topic of interest is how the laminar-turbulent transition is affected by the addition of particles. The experiments of Matas, Morris, and Guazzelli (2003) established the role of particle sizes relative to the pipe diameter as well as particle volume fraction in either increasing or decreasing the critical suspension Reynolds numbers† at which the laminar-turbulent transition occurs. For relatively small particles, the suspension Reynolds number at which laminar-turbulent transition occurs is at nearly the same Reynolds number for single-phase flows, independent of particle concentration. For relatively larger particles, the critical suspension Reynolds number decreased with increasing particle loading. In the recent years, this subject has been revived. Hogendoorn and Poelma (2018) as well as Agrawal, Choueiri, and Hof (2019) independently reported how the laminar-turbulent transition undergoes a qualitative change. Basically, at higher volume fractions, intermittent structures are absent and the transition occurs via a globally fluctuating state. The latter is also referred to as 'particle-induced transition'. At intermediate volume fractions, both mechanisms can coexist. This change in the local spatio-temporal dynamics is complemented by a global change in the friction factor curves (skin friction coefficient as a function of Reynolds number). Flows wherein the route to turbulence is via spatio-temporal intermittency, the friction factor curves have an abrupt jump in the transitional region ("classical" transition). When the flow reaches turbulence via a globally fluctuating state, the friction factor plots are smooth and monotonic, even in transitional regions ("smooth" transition). More recently, it has also been demonstrated that the "smooth" transition via a globally fluctuating state can be obtained under (extremely) dilute conditions for relatively large particles (Leskovec, Lundell, and Innings, 2020; Hogendoorn, Chandra, and Poelma, 2021). Hogendoorn, Chandra, and Poelma (2022) lean on the concept of particle-induced perturbations to estimate the onset of turbulence and distinguish the qualitative nature of transitions.

*Karnis, Goldsmith, and Mason (1966b) report that the concentration profiles stayed uniform over the course of their experiments.

†A distinction is made between "Reynolds number" and "suspension Reynolds number". The latter uses an effective viscosity for the suspension while the former uses the viscosity of the continuous phase.

Homogeneous, non-settling, non-Newtonian slurries

It is not uncommon to see Fluid Mechanicians study neutrally buoyant suspensions in great detail. The absence of gravitational effects simplifies the analysis of the problem. In reality, however, neutrally buoyant suspensions are exceptions rather than the norm. A category of pipe flows that is much more grounded in reality is the flow of slurries.

A slurry is a mixture of particles and a liquid, much like the suspensions discussed previously. However, here, the densities of the two phases differ quite significantly. Depending on the settling velocity of the particles, the slurry may be classified as settling or non-settling. Typically, when the particulate phase is fine and the (hindered) settling velocity low, it is assumed that the slurry is homogeneous. In essence, this simplifies the otherwise two-phase flow problem to a single-phase flow problem. The difficulty, however, arises from the fact that such slurries of fine particles often display non-Newtonian behaviour, especially when the fraction of particles is high. The emergence of non-Newtonian behaviour is attributed to interaction between the fine particles at the level of surficial electrical charges.

The rheology of the slurry can be defined in several ways with power law, Bingham plastic, and Herschel-Bulkley models being the most common choices. The Herschel-Bulkley model (fluid with a yield stress and shear-thinning behaviour) is quite prevalent. Under homogeneous conditions, if the rheology of the slurry is known, the velocity profile and wall shear stresses can be derived analytically for laminar flows.

As a rule of thumb, most single-phase flows are turbulent in practice. However, if particles are added, the viscosity of the system can effectively rise, and the system might even end up in a laminar state. One of the key design parameters for a slurry transport pipeline is the critical velocity* at which the flow undergoes a transition from laminar to turbulent regimes. As Wilson *et al.* (2006) state *"for non-Newtonian flows there is a special interest in conditions near the laminar-turbulent transition. There are two reasons for this interest, one economic and the other based on reliability of operation"*. In laminar flows, a slight increment in the pressure gradient produces a certain increment in the bulk velocity. In turbulent flows, however, an identical degree of increment in the pressure gradient would produce a lower increment in the bulk velocity. For a non-settling slurry, operating on the laminar side of the transition will thus be economically favourable†. This is illustrated well in Figure 8(a) of Pullum, Boger, and Sofra (2018), where the minima for pumping energy as a function of particle loading, for a constant discharge, occurs at a transitional velocity. Thus, the transitional velocity is also considered to be the point with minimum specific energy consumption. In practice, it seems that a factor of safety is added and the slurry is transported at a "Minimum Allowable Transport Velocity" (Javadi, Pirouz, and Slatter, 2020).

There are numerous criteria and methods to predict the transitional velocity (summaries available in Slatter, 1995; Eshtiaghi *et al.*, 2013; van den Heever, Sutherland, and

*For Newtonian fluids, it is accepted that there is a range of velocities at which transitional flows occur. It seems that the slurry community treat transition often as a point rather than a range. Practically, it makes sense as the pipeline designer is primarily interested in predicting pressure losses.

†For slowly settling materials, laminar transportation can be adopted for short distances. In a long pipeline, pipeline blockage could be a serious risk under laminar conditions. Moreover, under laminar conditions, pipe wear might be reduced, leading to elongated pipe lifetimes (Javadi, Pirouz, and Slatter, 2020).

Haldenwang, 2014). Of these, the method proposed by Slatter (1995) seems to be amongst the widely accepted ones. Similarly, there are numerous models to predict the wall shear stresses for turbulent flows (summarized in Slatter, 1995; Vlasak and Chara, 1999; van den Heever, Sutherland, and Haldenwang, 2014; Mehta *et al.*, 2021). The methods by Wilson and Thomas (1985), Thomas and Wilson (1987), and Slatter (1995) are widely accepted.

Almost always, such homogeneous slurry flows are studied exclusively by means of pressure drop measurements and subsequent generation of friction factor curves. In contrast to Newtonian flows, the friction factor curves usually show a smooth transition from laminar to turbulent states rather than an abrupt one. This is visible even in the early work of Metzner and Reed (1955). One way to study the local features of such non-Newtonian flows is to create transparent, homogeneous non-Newtonian fluids, which can be readily diagnosed by state-of-the-art optical measurement techniques. Many such experiments have been performed, with a key outcome being that time-averaged velocity profiles are axisymmetric under laminar and turbulent conditions but non-axisymmetric under transitional flows (Escudier and Presti, 1996; Escudier *et al.*, 2005; Peixinho *et al.*, 2005; Güzel *et al.*, 2009; Wen *et al.*, 2017). Another interesting insight is that a "smooth" transition between the friction factor curves under laminar and turbulent conditions can coexist with spatio-temporal intermittency (Güzel *et al.*, 2009; Güzel, Frigaard, and Martinez, 2009). However, one must realize that slurry flows are two-phase flows unlike those of homogeneous, non-Newtonian fluids, and care must be taken in directly comparing them.

2.2. Ultrasound for monitoring flowing suspensions

A common complication while studying dispersed multiphase flows experimentally is the presence of multiple scattering interfaces which render state-of-the-art optical measurement techniques useless. Thus, the statement "more particles, more problems" is a valid viewpoint from the perspective of an experimentalist. To investigate what is going on inside the flow, researchers often resort to non-optical measurement techniques, intrusive probes, or circumvent opacity altogether by matching the refractive indices of the continuous and dispersed phase. Most of the non-optical, non-intrusive techniques have been inspired by the medical imaging field. Overviews of the different measurement techniques applied to multiphase flows can be found in numerous review articles (Powell, 2008; van Ommen and Mudde, 2008; Albion *et al.*, 2011; Nadeem and Heindel, 2018; Poelma, 2020). Thus, no attempt is made at summarizing the different measurement techniques here.

Ultrasound is one of the measurement techniques often touted as a neutralizer to tackle opacity. Ultrasound for flow monitoring comes in various forms of instrumentation and working principles. From the perspective of this thesis, the focus will lie on ultrasound imaging that is typically found in the medical field. While there is a lot of intricate physics and mathematics underlying the formation of ultrasound images, for the Fluid Mechanician, the images simply serve as a mean to an end. The images can be further processed to obtain information on the flow. Cross-correlation techniques originally developed for Particle Image Velocimetry (PIV), when applied to ultrasound images, can return velocity fields. This technique is commonly known as Ultrasound Imaging Velocimetry (UIV) or Echo-PIV. Similarly, intensity of the echoes can be used to comment on the contents of

the medium.

The key advantages of using ultrasound over other measurement techniques for particle-laden flows is that it is relatively inexpensive, safe, versatile, easy to use, and offers acceptable spatial and temporal resolution. Of course, using it presents challenges as well, usually related to quality and interpretation of the data, which will become evident over the course of this thesis. Ultrasound already finds numerous applications in flow monitoring, for example, among coastal engineers as well as in the process industry. To steal the phrase from Shook and Roco (1991), ultrasonic techniques might *"represent the ultimate in convenience"**.

One of the striking features of Fluid Mechanics is that it is often delivers visually appealing phenomena, so much so that annual competitions are held wherein numerous aesthetically pleasing visuals are submitted. In contrast to the beauty of Fluid Mechanics, Bushberg *et al.* (2012) state the following *"While medical images can have an aesthetic appearance, the diagnostic utility of a medical image relates both to the technical quality of the image and the conditions of its acquisition. Consequently, the assessment of image quality in medical imaging involves very little artistic appraisal and a great deal of technical evaluation. In most cases, the image quality that is obtained from medical imaging devices involves compromise ... and better ultrasound images result when the ultrasound power levels are large. Of course, patient safety and comfort must be considered when acquiring medical images; thus, excessive patient dose in the pursuit of a perfect image is not acceptable. Rather, the power and energy used to make medical images require a balance between patient safety and image quality"*. For the purpose of Fluid Mechanics, "patient safety" is irrelevant. However, there is a limit to which excessive ultrasound powers are acceptable. Using powerful ultrasonic waves could turn the measurement technique from a non-intrusive to an intrusive one, as the ultrasonic waves may start affecting the fluid/flow itself (for example, by acoustic streaming or acoustic cavitation).

For the reader with little to no knowledge on how ultrasound imaging works, the book of Bushberg *et al.* (2012) is a good read. The book of Szabo (2004) can be useful for one interested in more advanced concepts concerning the imaging technique. For one specifically interested in Fluid Mechanics related applications, the review articles of Thorne and Hanes (2002), Poelma (2017), Tan *et al.* (2021), and the book of Takeda (2012) can serve as nice starting points.

2.2.1. Basics of ultrasound imaging

Ultrasound imaging is based on the use of acoustic waves (longitudinal waves) as compared to electromagnetic waves (transversal waves) used in optical techniques. At the core of the instrumentation responsible for the generation/reception of ultrasonic waves (> 20 kHz, beyond the range of human hearing) lie piezoelectric elements (capable of converting electrical signals into pressure waves and vice versa).

The general principle behind ultrasound imaging can be summarized with the phrase "pulse-echo": the piezoelectric element is excited by electronic signals to generate pressure 'pulses' (characterized by central frequency and number of cycles) which traverse through the medium of interest as a beam. In a linear array transducer, several individual

*This phrase was originally used in the context of ultrasonic flowmeters.

piezoelectric elements can be simultaneously employed to customize beam profiles (for example, to focus the beam at a given depth or steer it in a desired direction). Presence of scatterers/heterogeneities in an otherwise uniform medium, whose acoustic properties deviate from the surrounding medium, are responsible for generating 'echoes' (reflection of acoustic waves towards the ultrasound transducer). These echoes are then received by the piezoelectric element and its mechanical vibrations are converted to electronic signals. Since the same transducer is used for transmitting and receiving the ultrasonic waves, it is also referred to as a transceiver.

The initial electronic waves received are typically referred to as pre-beamformed RF (Radio Frequency) data. These electronic signals then undergo a receive beamforming process to return post-beamformed RF data. Receive beamforming refers to the process of applying delays to the echoes received by an array of individual piezoelectric elements to account for differences in times-of-flight such that their sum originates from a focal point (see Szasz, 2016, Figure 2.3(b), for an illustrative example). This step improves the image quality and resolution.

The post-beamformed RF data are the most basic form of ultrasound data that can be used further. This RF data are an alternating sinusoid (as the transmitted pulse is sinusoid) whose amplitude and phase is changing. Information about the scatterers/reflectors is contained in the amplitude of the RF data. Thus, an amplitude demodulation step (which includes envelope detection) is performed to retain the amplitude while getting rid of the sinusoidal oscillations. This new signal is referred to as A-mode ('A' for amplitude). The A-mode data is seldom used in the medical field and is commonly log-compressed to obtain B-mode data ('B' for brightness), resulting in greyscale images, which can be used by physicians for diagnosis. The log-compression step reduces the dynamic range resulting in a better balanced histogram of image intensities.

The B-mode data are a concatenation of multiple 1-D signals to form a 2-D array/image. These 1-D signals are time series based on a sampling frequency. The sampling frequency differs from the aforementioned central frequency, in that the latter describes the properties of the transmitted pulse, while the former characterizes the rate at which the echoes are electronically sampled. These 1-D time series can be converted to depths by utilizing the speed of sound of the medium.

The two-dimensional array/image has two directions: the direction parallel to the array of transducer elements is referred to as the lateral direction and the one perpendicular as the axial direction. While ideally, it would be desirable to have a thin, rectangular field-of-view (like in Particle Image Velocimetry), the actual region insonified by the transducer has a much more complex geometry (see Poelma, 2017, Figure 2, for an illustrative example). Importantly, the beam profile also has a thickness in the third dimension, also known as the elevational direction, resulting in the beam profile having a certain thickness.

Another aspect is that the beam profile has two distinct regions: a near-field (where the beam converges) and a far-field (where the beam diverges). The pressure amplitude characteristics in the near-field are non-monotonic and complicated, in comparison to the far-field where the ultrasound intensity of the field decreases monotonically with distance. Thus, it is typically desirable to image in the far-field of the ultrasound transducer.

A sequence of images can be recorded, with each individual image referred to as a frame. The temporal separation between the frames determines the frame rate.

2.2.2. Interactions between ultrasound and suspensions

While ultrasound finds its most noteworthy applications in the field of medicine, it also has found applications in industrial settings. For example, ultrasound is utilized for systems involving (colloidal) suspensions and emulsions (Dukhin and Goetz, 2002). One specific example is in the food industry where ultrasound finds widespread application in monitoring as well as processing of food products (Awad *et al.*, 2012). It is thus unsurprising that very elaborate and rigorous theoretical models exist which describe the interaction between ultrasound and suspensions. The most well-known ones are ECAH (named after the authors' initials Epstein and Carhart, 1953; Allegra and Hawley, 1972) and coupled-phase models (Harker and Temple, 1988; Gibson Jr and Toksöz, 1989; Challis *et al.*, 2005). These theoretical models are commonly used in commercial products to estimate particle size distributions (Challis *et al.*, 2005). Below, the most relevant aspects concerning the interaction between ultrasound and suspensions are briefly discussed.

At a single-particle level, the interaction between the particle and a plane ultrasonic wave is governed by the relative wavelength, ka, the product of the wavenumber ($k = 2\pi/\lambda$, where λ is the ultrasonic wavelength) and scatterer radius (a). Mathematical investigations have been performed for cases where the scatterers are much smaller than the wavelength (Rayleigh, 1877) as well as where they are of comparable sizes (Faran Jr, 1951). For example, in the 'long wavelength regime' ($ka \ll 1$), the scattering is dependent on the ultrasonic frequency, while this does not hold true in the 'short wavelength regime' ($ka \gg 1$). In the 'intermediate wavelength regime' ($ka \sim 1$), it is known that single spherical particles return rather complicated ultrasonic images, with a single particle returning echoes longer than the particle size itself (see Baddour *et al.*, 2005, Figure 4(d), for an illustrative example).

A suspension is composed of a liquid continuous phase and a dispersed phase (rigid spherical particles). The continuous phase is usually homogeneous and primarily affects the acoustic waves by absorption (an irreversible process by which acoustic energy is dissipated into heat) whereas the dispersed phase can also affect the acoustic waves by other phenomena such as scattering (redirection of energy instead of dissipation). Both these mechanisms collectively lead to the extinction of the acoustic wave.

The absorption mechanism is typically associated with relaxation processes, where the medium returns to its original state after being exposed to a pressure variation induced by the sound wave (Bjørnø, 2017). On the other hand, several mechanisms can be identified for the interaction between sound waves and colloids (Dukhin and Goetz, 2002). For large particles ($ka > 1$), absorption mechanisms are negligible and the extinction of the acoustic waves may be attributed primarily to scattering processes. If relatively smaller particles were used (resulting in the long wavelength regime), the scenario would be the opposite, with negligible scattering and domination of absorption mechanisms.

Table 2.1: Overview of studies targeting ultrasonic particle volume fraction profiling in particle-laden flows. Six clusters have been made primarily on basis of the features of the technique.

Work(s)	Technique	Experiments
(I) *Techniques developed originally for estimation of suspended sediment concentrations in marine environments*		
Thorne and Hanes (2002), Hurther *et al.* (2011), Thorne, Hurther, and Moate (2011) and associated works	– Technique developed and refined over a span of decades – Meticulous inclusion of acoustical scattering theory into methodology	– Technique is typically used for mass concentrations of 1-10 kg/m^3 which corresponds to $\phi \sim 0.005$ – Technique constrained to fixed combination of particles and ultrasound transducer
(II) *Techniques for Acoustic Backscatter Systems applicable to arbitrary suspension flows*		
Admiraal and García (2000), Hunter, Peakall, and Biggs (2012), Rice *et al.* (2014), Bux *et al.* (2015), Rice *et al.* (2015) and associated works	– Semi-empirical approach (needs calibration) – Theoretical formulations adapted from cluster I extended to arbitrary suspensions	– Primarily applied to settling suspensions and pipe flows of heavy particles suspended in a liquid medium – Domain sizes ranging from ~ 4 to ~ 40 cm – Technique typically applied for $\phi_{\text{bulk}} < 0.03$

Continued on next page ...

Table 2.1 – continued from previous page

Work(s)	Technique	Experiments
(III) *Purely empirical techniques (calibration in uniform suspensions then exploited for non-uniform suspensions)*		
Furlan *et al.* (2012), Saint-Michel *et al.* (2017)	– Calibration parameters obtained in uniform suspensions – Non-uniform suspensions studied with help of calibration – Account for attenuation	– Experiments in pipe (2.5 cm) and Taylor-Couette geometry (0.2 cm) – Uniform suspensions, $\phi_{\text{bulk}} \leq 0.15, 0.40$ – Non-uniform suspensions, $\phi_{\text{bulk}} \leq 0.10, 0.15$
(IV) *Direct correspondence between echo intensity and particle volume fraction (empirical, but not accounting for attenuation)*		
Zou *et al.* (2014), Gurung *et al.* (2016), Stener *et al.* (2014), Stener *et al.* (2016), Hitomi *et al.* (2018), Saint-Michel, Gibaud, and Manneville (2018)	– Directly correlate (power spectral density of) backscattered echo intensity to local volume fraction – Do not account for attenuation – Calibration can be done in uniform suspensions	– Domain sizes varying from ~ 1 to ~ 40 cm – Maximum volume fractions studied between $0.01 \leq \phi_{\text{bulk}} \leq 0.10$

Continued on next page ...

Table 2.1 – continued from previous page

Work(s)	Technique	Experiments
(V) *Particle counting*		
Chemloul, Chaib, and Mostefa (2009), Lee, Boning, and Anthony (2018)	– Identify individual particles – No calibration needed	– Typically applicable to dilute suspensions $\phi_{\text{bulk}} < 0.02$
(VI) *Pair(s) of separate transmitter-receiver configuration (typically use relations for time-of-flight and attenuation)*		
Gunning *et al.* (1988), Wedlock, McConaghy, and Hawksworth (1993), Hoyos *et al.* (1994), Pinfield, Povey, and Dickinson (1996) and other works	– Traverse pair perpendicular to direction of wave propagation (non-intrusive) – Alternatively, install several pairs	– Usually applied to extremely slowly sedimenting/creaming flows (over days) – Volume fractions as high as $\phi_{\text{bulk}} \sim 0.6$ studied
Warsito *et al.* (1997), Vatanakul, Zheng, and Couturier (2004)	– Traverse pair through the flow in direction of wave propagation (intrusive)	– Often in context of three-phase flows – Domain sizes ~ 10 cm
Warsito *et al.* (1999), Utomo *et al.* (2001)	– Several pairs used (non-intrusive) – Computed Tomography algorithms used for reconstructing 2-D profiles	– In context of three-phase flows – Domain sizes ~ 10 cm

2.2.3. Existing acoustic/ultrasonic concentration profiling techniques

The topic of volume fraction profiling using ultrasound has already been the subject of several studies as evidenced by the summary in Table 2.1. In this table, the works have been categorized into six clusters (I-VI), primarily based on the nature of the technique. It is possible that a few studies may have been overlooked in this summary owing to the wide variety of fields where ultrasound finds application. Nevertheless, this table hopefully offers the reader a relevant reference depending on their application, field-of-view and apparatus at their disposal.

Works in cluster I can be considered to be very comprehensively developed methods with acoustical scattering theory at its heart. These have been specifically developed in the context of studying suspended sediment concentration profiles in marine environments, typically with the aid of bespoke Acoustic Backscatter Systems and/or Acoustic Concentration and Velocity Profilers. It must be noted that this topic is an independent field of research in itself, and there are several other papers that are not included here.

A simplified version of the key equations central to the works in cluster I is shown in Equation (2.1).

$$V(r) \propto M^{1/2} \exp\left(2 \int_0^r \xi(r') M(r') dr'\right) \tag{2.1}$$

This concisely elucidates the interaction between the measured, backscattered ultrasound signal, $V(r)$, and the desired quantity, the distribution of the suspended sediment, $M(r)$. Here, r is the depth, and ξ is the attenuation coefficient. In short, $V(r)$ is the rms of the voltage received, corresponding to the backscattered acoustic signal at a given depth r. This backscattered signal is proportional to the local mass fraction ($\propto M^{1/2}$) and also the net attenuation of sound until that depth (expressed by the integral). The exponential term indicates the exponential decay of the acoustic waves. It must be noted that the integral term also includes the local mass fractions, which complicates the equation.

At least three techniques to extract mass fraction profiles have been used (Hurther *et al.*, 2011) - the iterative implicit inversion method, the explicit inversion method and the dual-frequency inversion method. In fact, most of the techniques developed in clusters II, III may be considered to be generalized variants of the methods developed in cluster I. However, exact relations developed for cluster I are limited to marine sediment being sampled by an Acoustic Backscatter System with an eye towards application in field experiments. Moreover, the theory has been reported to be inapplicable beyond loadings of 2.5 g/L or a volume fraction of $\phi \sim 0.001$ (Hunter *et al.*, 2012), due to multiple scattering (scattering of sound waves between particles).

Thus, the group of works in cluster II overcome a few constraints of this theory and extend the above formulations as well as inversion techniques to arbitrary suspensions (i.e. suspensions other than sediments in marine environments), while using Equation (2.1) as basis. Their primary applications have been geared towards sediment flows/transport and in a recent endeavour, an array of acoustic backscatter systems was deployed in profiling a large-scale laboratory experiment (Hunter *et al.*, 2020). However, as argued by Saint-Michel *et al.* (2017), the validity of Equation (2.1) might breakdown at higher volume

fractions, due to multiple scattering, which means that the techniques in cluster II may be considered semi-empirical. Moreover, the expression cannot be directly applied to linear array transducers as the manner in which the beam spreads would be different, and could also be a function of various imaging settings. In this spirit, the works in cluster III can be considered to be the most generalized and completely empirical methods which lump the acoustical scattering behaviours into a couple of calibration parameters (obtained in uniform suspensions). These may be applied to arbitrary suspensions with arbitrary beamforms. Moreover, such an approach can accommodate wall-bounded flows, as walls can be difficult to account for in the approach based on cluster I (Admiraal and García, 2000). It must be noted that this step of calibration is also necessary in procedures involving cluster II.

Other methods based on echo intensity in cluster IV, and particle detection in cluster V, have also been proposed. While the latter technique is best used for dilute suspensions, the works based on echo intensities often do not compensate for attenuation of the sound in the reconstruction. Finally, works in cluster VI employ a separate transmitter and receiver. If only one pair is used, profiles can be determined by traversing the pair perpendicular to the direction of sound propagation at a fixed separation (non-intrusively) or parallel to it (intrusively). However, by using multiple pairs, Computed Tomography algorithms can be employed for reconstructing an entire cross-section. These studies are often performed in the context of gas-liquid flows (Hoyle, 1996), with fewer examples involving solid particles.

2.2.4. Existing studies on ultrasound based velocimetry outside cardiovascular flows

Ultrasound has various modalities that is applied to study flows. Below, a few examples are listed wherein ultrasound has provided insights into flows apart from cardiovascular ones. The division has been made primarily on basis of the nature of the measurement apparatus/technique. It is possible that a few relevant studies have not been referred to, owing to the wide range of applications where ultrasound is used for flow monitoring.

Acoustic/Ultrasonic Doppler Velocity Profiler (ADVP/UDVP)

The measurement apparatus here consists of a single piezoelectric element and provides velocity information along a single line with a high spatio-temporal resolution. Unlike the linear array transducer, this instrument has been specifically created for studying fluid motion at length scales of $\mathcal{O}(0.5\text{ m})$, exceeding that of a human body.

The book of Takeda (2012) compiles numerous and diverse range of examples wherein such an apparatus (UDVP) can be used (for example, liquid metals, in-line rheometry, gas-liquid flows, turbid flows). In combination with a pipe geometry, it is common to install the transducer at a non-normal angle with respect to the pipe wall. This device (ADVP) is also used in marine environments to study small-scale sediment transport, by measuring (instantaneous) velocity as well as suspended sediment concentration profiles (Thorne and Hanes, 2002). There seem to be no discernible technical differences between UDVP and ADVP, and the names might be specific to the respective field of application. For the sake

of brevity, readers are encouraged to visit the above two references and associated works in order to gain a complete overview of these measurement techniques and applications.

With a single transducer, the technique can return one velocity component along one dimension (1D1C, where D refers to dimension and C refers to component). By using two transducers, the technique can be extended to 1D2C and to 1D3C with three. Temporal resolution is usually high, except while accessing deep locations.

Ultrasound Array Doppler Velocimeter (UADV)

A drawback of the previous device is that the measurement is 1D1C with a single probe. However, by arranging several transducers in an array, the technique is extended to 2D1C and by using multiple arrays (placed orthogonally), the technique can be extended to (dual-plane) 2D2C (Franke *et al.*, 2013; Büttner *et al.*, 2013; Nauber *et al.*, 2016). This development has mainly been driven by researchers in Dresden who have created custom transducers. This has allowed them to study unsteady flows of liquid metals with typical velocities of $\mathcal{O}(1\ \mathrm{cm/s})$ in domain sizes of $\mathcal{O}(5 \times 5\ \mathrm{cm}^2)$. In recent years, these researchers have seemingly shifted towards using UIV for liquid metal flows (Weik *et al.*, 2021).

Diffusing Acoustic Wave Spectroscopy (DAWS) + Dynamic Sound Scattering (DSS)

These two techniques were likely first introduced by Cowan, Page, and Weitz (2000), with an aim to obtain information on the dynamics of strongly scattering systems. These were directly inspired from analogous light scattering techniques, and are typically performed using single-element transducers. Information on velocity fluctuations is recovered, usually in densely-laden suspensions and under the absence of any turbulence or secondary motions. Measurements are typically performed with a single element transducer.

Diffusing Acoustic Wave Spectroscopy (DAWS) relies on describing the multiple scattering of ultrasonic waves under the "diffusion approximation". Cowan *et al.* (2002) explain the theoretical foundations behind this technique in depth. In short, the temporal autocorrelation function is related to the motion of the scatterers. This way, information on local relative velocity and strain rate of the suspended particles can be extracted.

Dynamic Sound Scattering (DSS), on the other hand, relies on singly scattered waves. Cowan *et al.* (2016) explain the theoretical foundations behind this technique in depth. In short, the temporal autocorrelation function is related to the mean square velocity fluctuations of the scatterers. Of the two techniques, DSS seems to have most relevance to fluid flows, especially for investigating the complex dynamics of particulate suspensions at high volume fractions. For example, DSS has been used to study fluidization and sedimentation of suspensions (Kohyama, Norisuye, and Tran-Cong-Miyata, 2009) as well as dynamics of neutrally buoyant suspensions in a Couette cell (Strybulevych *et al.*, 2019).

Ultrasonic Speckle Velocimetry coupled with rheometry (Rheo-USV)

Here, a specific body of studies performed by researchers based in France over the past couple of decades are referred to. An ultrasonic sensor is coupled to a Taylor-Couette geometry whose gap (~ 1-2 mm) is filled with complex fluids, and excellent temporal

resolution is maintained (with respect to desired flow velocities). Typically, velocities of $\mathcal{O}(0.1$ m/s) are studied, but flows up to 1 m/s have been studied as well (Saint-Michel *et al.*, 2017). This has allowed the researchers to gain significant insights into the spatio-temporal dynamics of shear banding in complex fluids (Manneville, 2008; Divoux *et al.*, 2016) among other physical phenomena.

While earlier studies were 1D1C in nature (see Manneville, Bécu, and Colin, 2004, Figure 4 therein), these evolved to 2D1C with newer equipment (see Gallot *et al.*, 2013, Figure 1 therein). Much like UIV, a cross-correlation analysis is performed, albeit along one dimension of the image only (explaining the "1C" nature of measurements). The axial direction of the ultrasonic sensor is inclined with an angle ψ with respect to the azimuthal velocity in the Couette cell. This means that the measured velocity, v, has multiple contributions in it: $v = v_\theta + \frac{v_r}{\tan\psi}$, where v_θ and v_r represent velocities in the azimuthal and radial directions (Fardin *et al.*, 2014). Typically in rheometry, flow is unidirectional along the azimuthal direction, meaning $v_r = 0$ or $v \approx v_\theta$. In the presence of secondary motions, the two velocity components can be segregated by performing two measurements wherein the flow has identical shear rates but opposite directions. This way $v_+ = v_\theta + \frac{v_r}{\tan\psi}$ and $v_- = v_\theta - \frac{v_r}{\tan\psi}$ are measured (Perge, Fardin, and Manneville, 2014). Using these two measurements, 2D2C information is recovered for the time-averaged velocity profile.

Quite curiously, the 1D1C measurements were preceded by 2D1C (Sandrin, Manneville, and Fink, 2001) and even 2D2C (Manneville, Sandrin, and Fink, 2001) measurements of a vortex. The 2D2C measurements were performed with two orthogonally placed linear array transducers (similar to UADV) with 1D cross-correlation analysis performed on images recorded by each transducer. Such an orthogonal configuration, while universally inapplicable, provides velocity information with uniform resolution in both directions (unlike UIV). The authors hinted at studying turbulent flows with ultrasonic speckle velocimetry in the future, but it has seemingly not been pursued. About the same time as the above two works, Carlson and Ing (2003) applied a similar approach (1D cross-correlation along each line of an image), allowing for the reconstruction of the streamwise velocity profile in the cross-section of a particle-laden pipe flow.

Ultrasound Imaging Velocimetry (UIV)

Similar to how PIV was preceded by laser speckle velocimetry (Adrian, 1984), UIV/echo-PIV was preceded by speckle tracking (Bohs *et al.*, 2000). The move from speckle to particle velocimetry (higher to lower seeding density) technique was necessitated since speckle is highly sensitive to flow gradients and out-of-plane motion.

A key advantage of UIV over Doppler techniques is its lack of dependence on the angle of imaging, while also being intrinsically 2D2C. UIV measurements are typically performed with commercially available linear array transducers (unlike in UADV and rheo-USV, which had custom-made transducers). Moreover, unlike UADV and rheo-USV, instantaneous 2D2C measurements can be made with a single transducer.

One of the earlier studies in the context of applying UIV to particle-laden flows was that of Crapper, Bruce, and Gouble (2000) which was used as a proof-of-concept to demonstrate the feasibility of combining of ultrasound imaging and PIV algorithms.

Thereafter, there have been several studies that investigated particle-laden flows.

UIV has been applied to particle-laden pipe flows in Delft to study turbulence (Gurung and Poelma, 2016), in-line rheometry (Gurung *et al.*, 2016) and transition-to-turbulence (Hogendoorn and Poelma, 2018; Thota Radhakrishnan *et al.*, 2021). In these studies, the imaging depths were between 1-4 cm with velocities < 0.65 m/s being studied.

The aforementioned researchers at Dresden (see UADV) have also been active in applying UIV to flows. In the work of Kupsch *et al.* (2019), it was determined that UIV was robuster than Doppler based techniques, at least in the context of suspensions. Kupsch *et al.* (2019) recognize the effect of ultrasonic attenuation in suspensions which can increase the uncertainty in the velocimetry results, especially with increasing imaging depths. Here, flows up to 0.01 m/s and imaging depths of 1.5 cm were accessed in a suspension with a volume fraction of 0.08.

Researchers at Chicago have also been recently active in applying UIV to study phenomena related to dense suspensions, namely dynamic jamming (Han, Peters, and Jaeger, 2016; Majumdar *et al.*, 2017; Han *et al.*, 2019). The suspensions are typically placed in small vessels. Imaging depths of up to 2 cm and velocities up to 0.2 m/s are studied. These works utilize fast ultrasound imaging to capture the dynamics of jamming. In fact, Han *et al.* (2019) set the ultrasound transducer on an optical stage to reconstruct an averaged three dimensional flow field.

There have also been examples wherein ultrasound contrast agents have been added to the flow of suspensions. Following filtering of the raw data in the frequency domain, particle tracking is performed at superior spatial resolutions (Kupsch *et al.*, 2021) or velocity information of the carrier and dispersed phases are separated (Najjari, Zhang, and Rival, 2021). In the latter study, suspensions with volume fractions as high as 0.40 were studied, without suffering from any effects of attenuation. This might be attributed to their use of water-absorbing polymeric beads being dispersed in water, minimizing scattering losses.

Finally, a relatively more exotic example is the use of an acoustic camera (sonar apparatus) to perform velocimetry measurements of bubbles in turbid environments (field measurements). Young, McFall, and Bryant (2018) demonstrate the use of such a device in order to obtain 2D2C velocity information in a much larger areal domain with dimensions of $\mathcal{O}(80 \times 60\ \text{cm}^2)$ for velocities of $\mathcal{O}(0.05\ \text{m/s})$.

Particle-laden Taylor-Couette flows: higher-order transitions and evidence for azimuthally localized wavy vortices

Those not involved in rotating cylinder flow might well inquire what all the fun is about. That question is not hard to answer: Rotating cylinder flow is easy to produce, beautiful to observe and as profound a subject in fluid dynamics as there is.

Donnelly (1991)

We extend upon the known flow transitions in neutrally buoyant particle-laden Taylor-Couette flows by accessing higher suspension Reynolds numbers ($Re_{\mathrm{susp}} \sim O(10^3)$) in a geometry with radius ratio $\eta = 0.917$ and aspect ratio $\Gamma = 21.67$. Flow transitions for several particle volume fractions ($0 \leq \phi \leq 0.40$) are investigated by means of flow visualization experiments, in a flow driven by a rotating inner cylinder. Despite higher effective ramp rates, we observe non-axisymmetric patterns, such as spirals, in the presence of particles. A novel observation in our experiments is the azimuthally localized wavy vortex flow, characterized by waviness present on a fraction of the otherwise axisymmetric Taylor vortices. The existence of this flow state suggests that in addition to the already established, destabilizing effect of particles, they may also inhibit the growth of instabilities. Flow topologies corresponding to higher-order transitions in particle-laden suspensions appear to be qualitatively similar to those observed in single-phase flows. A key difference, however, is the visible reduction in the appearance of a second,

This chapter has been published in Dash, Anantharaman, and Poelma (2020). 'We' in this chapter refers to the three authors - Amitosh Dash, Arjun Anantharaman, and Christian Poelma. Section 3.A was included as online supplementary material of the publication while Section 3.B was part of conference proceedings in Dash *et al.* (2019).

incommensurate frequency at higher particle loadings, which could have implications for the onset of chaos. Simultaneous torque measurements allow us to estimate an empirical scaling law between the Nusselt number (Nu_ω), the Taylor number (Ta) and the relative viscosity (χ^e): $Nu_\omega \propto Ta^{0.24}\chi^{e\,0.41}$. The scaling exponent of Ta is non-trivially independent of the particle loading. Apparently, particles do not trigger a qualitative change in the nature of angular momentum transfer between the cylinders.

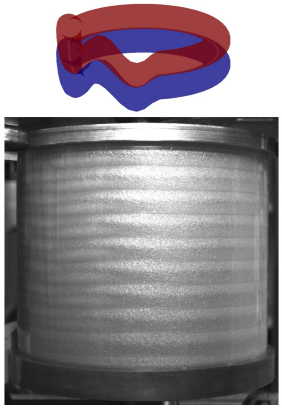

Azimuthally localized wavy vortex flow*- unique flow state that can exist in particle-laden Taylor-Couette flows. The schematic on the top illustrates two counter-rotating Taylor vortices, atop which wavy features are azimuthally localized. The snapshot in the bottom shows a realization of this flow state. The vortices are toroidal on the right side whereas on the left additional wavy undulations are evident.

*The author of this thesis proposed a colloquial name, *een koosnaampje*, for this flow state - azimuthon, an amalgamation of 'azimuthal' and 'soliton'. It turns out that the term 'azimuthon' is popular in other fields of physics.

3.1. Introduction

The Taylor-Couette system, a canonical flow geometry, has been bestowed upon with honorifics such as 'hydrogen atom of fluid dynamics' Tagg (1994) as well as 'Drosophila' (van Gils *et al.*, 2012). This is with good reason, as it has served as a very simple system to address fundamental problems in physics such as: instabilities, nonlinear dynamics, pattern formation, spatio-temporal chaos and turbulence (Grossmann, Lohse, and Sun, 2016). Furthermore, this flow apparatus is also of interest to application-oriented research, primarily concerning chemical processing (see Table 1 in Zhu and Vigil (2001) for numerous examples). This geometry also forms the skeleton of the contemporary rheometer, and is commonly used for measuring dynamic viscosities of fluids (Guazzelli and Pouliquen, 2018).

While the initial Taylor-Couette apparatus were dedicated to the determination of fluid dynamic viscosity (Couette, 1890; Mallock, 1896), the now near-century old, seminal contribution of Taylor (1923) laid the foundation for future work in this field. The work of Taylor (1923) established the critical conditions necessary for the appearance of secondary flow structures, subsequently known as Taylor vortices (pair of counter-rotating vortices, stacked axially), when the flow is driven by a rotating inner cylinder. The critical conditions are commonly quantified by means of a Reynolds number, or even a Taylor number. Further increase in the rotational velocity of the cylinder leads to additional instabilities, such as the appearance of wavy vortices (Coles, 1965), modulated wavy vortices (Gorman and Swinney, 1982; Zhang and Swinney, 1985), before the onset of chaos (Gollub and Swinney, 1975; Fenstermacher, Swinney, and Gollub, 1979) and turbulence (Koschmieder, 1979; Lathrop, Fineberg, and Swinney, 1992; Lewis and Swinney, 1999). Initial studies primarily involved the usage of Newtonian fluids, and this alone provided a plethora of intriguing flow phenomena, by either varying the flow geometry or the nature of the cylinder rotation (i.e. inclusion of outer cylinder rotation). Consequently, an extensive study of the various flow patterns has resulted in the comprehensive flow regime map compiled by Andereck, Liu, and Swinney (1986). Contemporary single-phase Taylor-Couette flows have been predominantly geared towards understanding high-Reynolds-number turbulence (Grossmann, Lohse, and Sun, 2016), where the bulk flow as well as the two boundary layers are turbulent in nature.

In the century since Taylor's seminal work, the studied phenomena within this simple flow geometry have branched significantly. Newer forms of instabilities and flow phenomena have been uncovered by simply changing the fluid within the Taylor-Couette geometry. Along this line, the study of unusual flow patterns in a neutrally buoyant, non-Brownian, particle-laden suspension, arising due to inertial effects, has recently gained traction. This is exemplified in the recent works of Majji, Banerjee, and Morris (2018) and Ramesh, Bharadwaj, and Alam (2019), where both studies successfully uncover novel flow patterns stemming from the additional presence of solid particles. Majji, Banerjee, and Morris (2018) were the first to report the occurrence of non-axisymmetric flow structures (ribbons and spirals) as primary instabilities. An experimental protocol with decreasing inertia in time was preferred over one with increasing, as axial non-homogeneities in the particle distribution were observed for the latter. Ramesh, Bharadwaj, and Alam (2019) extended on this by also considering an experimental protocol with increasing inertia,

which gave rise to the so-called 'coexisting states' (presence of axially segregated flow states, such as the combination of wavy and Taylor vortices or Taylor and spiral vortices). More recently, Ramesh and Alam (2020) also reported the existence of interpenetrating spiral vortices in such flows.

Changes in the nature of the suspension was also the theme of one of the pioneering works in the field of non-Brownian particle-laden flows, namely the experiments of Bagnold (1954) (later re-examined by Hunt *et al.*, 2002). Torque measurements of neutrally buoyant particle-laden suspensions in a Taylor-Couette geometry driven by a rotating outer cylinder yielded two distinct flow regimes which were characterized on the basis of their respective scaling law behaviours. Thus, besides flow visualization techniques, torque measurements are capable of providing complementary, global information of the flow topology, as also evidenced in several single-phase, turbulent Taylor-Couette flow studies (Wendt, 1933; Lathrop, Fineberg, and Swinney, 1992; Eckhardt, Grossmann, and Lohse, 2007).

The flow visualization studies of Majji, Banerjee, and Morris (2018), Ramesh, Bharadwaj, and Alam (2019) and Ramesh and Alam (2020) restrict their studied range of flow topologies up to the appearance of wavy Taylor vortices. To the best of our knowledge, there are no systematic studies explicitly pursuing the development of flow regimes beyond the appearance of wavy vortices for neutrally buoyant, non-Brownian particle-laden suspensions in a Taylor-Couette geometry driven by inner cylinder rotation. Studying these higher-order transitions can provide insight into the phenomena leading to the transition to turbulence.

To this end, the current study aims to add on to the existing body of work, in an existing Taylor-Couette facility (Ravelet, Delfos, and Westerweel, 2010), with the chapter addressing the following issues.

1. We study the lower-order transitions in our Taylor-Couette geometry (i.e. until the first appearance of wavy vortices), in order to verify whether the current experiments also yield non-axisymmetric flow patterns. Differences from previous studies could be expected since the current experiments are performed under different conditions (discussed later in Section 3.2.7).

2. We also pursue flow transitions beyond the appearance of Wavy vortices, i.e. higher order transitions. We investigate whether there is a qualitative change in these transitions as compared to single-phase flows.

3. We assimilate the effect of flow inertia and particle loading on the required torque to sustain the flow, into an empirical scaling law.

The above points are addressed experimentally by means of simultaneous flow visualization and torque measurements. The remainder of the chapter is structured as follows: In Section 3.2 the finer details of the experimental set-up, the measurement procedure as well as experimental uncertainties are described. Hereafter, a global overview of our experimental results is presented in Section 3.3, focusing on flow visualization (Section 3.3.1) as well as torque measurements (Section 3.3.2). For the torque measurements, we derive an empirical scaling law relating the measured torque, the driving force and the particle

loading. Three detailed flow visualization examples for different particle volume fractions are then used to illustrate the nature of lower- as well as higher-order transitions in Section 3.4 and Section 3.5, respectively. Among the lower-order transitions, special attention is given to a novel flow state, 'azimuthally localized wavy vortex flow' in Section 3.4.5. We summarize our key findings in Section 3.6, while also specifying possible future directions that can be undertaken to consolidate/expand upon our findings.

3.2. Experimental set-up and measurement procedure

Details of the experimental set-up and the various measurement techniques employed are presented in this section. Readers interested in further details of the experimental set-up and procedures are referred to Anantharaman (2019). The chief components of the set-up are illustrated in Figure 3.1. Note that the torque measurements and the flow visualization recordings were performed simultaneously.

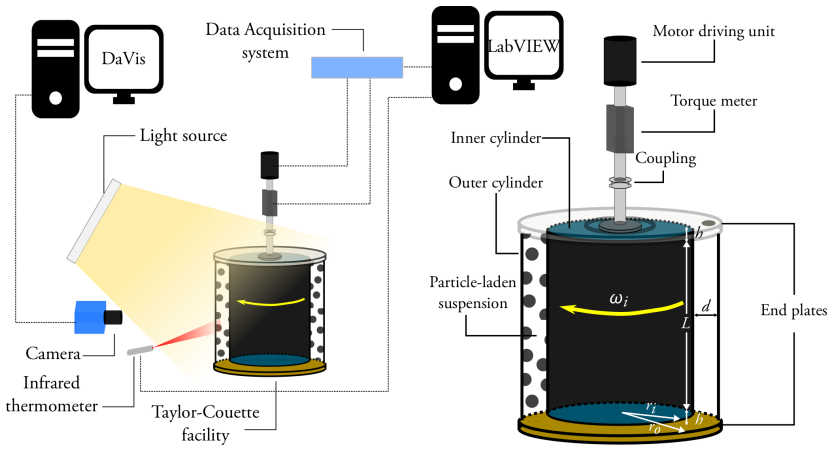

Figure 3.1: Schematic of the experimental set-up and measurement equipment involved. Objects are not drawn to scale. (*Left*) Experimental set-up and measurement apparatus.*(*Right*) A close-up of the Taylor-Couette geometry.

3.2.1. Geometry of the Taylor-Couette facility

The Taylor-Couette facility used in the current investigation is composed of two vertical, coaxial, concentric and independently rotatable cylinders. The inner cylinder has a radius (r_i) of 11 cm, and the outer cylinder has a radius (r_o) of 12 cm. This leads to the current

*Ultrasound images were simultaneously recorded for each experiment for volume fractions up to 0.15. The measurements were in a azimuthal-radial plane near the mid-height of the Taylor-Couette geometry. However, the data was not processed. If processed the results from these measurements would contain information from the PMMA particles as well as the visualization flakes. However, the results would be specific to the structure present in the measurement plane. As shall be shown in this chapter, the lower-order transitions can have strong axial segregations. Examples of ultrasound imaging for single-phase flows can be found in Section 3.B.

system having an annular gap width ($d = r_o - r_i$) of 1 cm and a radius ratio ($\eta = r_i/r_o$) of 0.917. The inner cylinder has a height (L) of 21.67 cm, while the outer cylinder has a height of 22.21 cm, leading to the formation of two end gaps, each with a height of 2.70 mm. Thus, the present geometry has an aspect ratio ($\Gamma = L/d$) of 21.67. The present system may thus be categorized as a narrow gap ($1 - \eta \ll 1$) and relatively tall ($\Gamma \geq 20$). In the current experiments, the outer cylinder is held at rest, while the inner cylinder has a rotational velocity, ω_i, which is determined by the desired rotational frequency, $f_i = \omega_i/(2\pi)$. The inner cylinder velocity $U_i = \omega_i r_i$ is the source for the shear and the apparent shear rate can be defined as the ratio between the inner cylinder velocity and the gap width, $\dot{\gamma}_{\text{app}} = U_i/d = (\omega_i r_i)/d$.

With the help of these parameters, several non-dimensional control parameters can be defined. For a working fluid with a density, ρ, and dynamic viscosity, μ (thus, kinematic viscosity $\nu = \mu/\rho$), the inner cylinder Reynolds number is defined as $Re = (\omega_i r_i)d/\nu = \dot{\gamma}_{\text{app}} d^2/\nu$. Alternatively, the Taylor number, $Ta = KRe^2$ may also be used, where the prefactor $K = (1 + \eta)^6/(64\eta^4) = 1.0971$ is related to the geometry of the Taylor-Couette facility via the geometric Prandtl number (Eckhardt, Grossmann, and Lohse, 2007).

Surfaces of both the cylinders are made of polymethylmethacrylate (PMMA), facilitating optical access. However, the inner surface of the hollow, inner cylinder (thus, not in contact with the fluid) is painted black to avoid reflections from the structural metal bars present inside the inner cylinder. The inner cylinder is sealed shut by means of PVC discs (which rotate with the inner cylinder), whereas the outer cylinder has end plates made of a PMMA base with a brass ring (bottom) and aluminium (top), both of which would rotate together with the outer cylinder.

3.2.2. Preparation of the neutrally buoyant suspension

The Taylor-Couette facility was filled with a nearly neutrally buoyant suspension consisting of rigid PMMA particles in an aqueous glycerol solution (~ 67.6% v/v), with a density of 1187.7 kg/m^3 and a dynamic viscosity of 28.7 mPa·s at 20°C. The continuous phase was prepared by mixing appropriate quantities of demineralized water with an aqueous glycerol solution with a specific gravity of 1.23 (Boom BV, The Netherlands). The two components were mixed together, while stirring and warming the mixture simultaneously, before adding a small quantity of Tween-20 (0.1% by volume), a surfactant, which aids in suspending hydrophobic particles. The effect of the surfactant on properties such as density and viscosity was neglected, since it is added in a very small amount.

Rigid PMMA particles (PMMA powder - acrylic, injection moulding grade, Goodfellow USA) were used as the dispersed phase. A sieving procedure was used to narrow the distribution of particle sizes. An inspection of a small sample of particles (~ 675) under a microscope, equipped with a Nikon objective M × 1.0/0.4 lens, yielded the following information. The majority of the particles are smooth spheres with a few of them possibly having voids within, which are clearly visible as PMMA is optically transparent. The median particle diameter (commonly referred to as $d_{p,50}$, but as d_p in this chapter) was found to be 599 μm. This results in a gap width to particle diameter ratio (d/d_p) of approximately 16.7.

The sieved particles were then dispersed in the aqueous glycerol mixture by means of

a magnetic stirrer. After mixing for a few minutes, the suspension was allowed to rest for about 20 minutes. It was observed that there is a thicker layer of particles creaming to the top as compared to those which sediment to the bottom. These creaming particles could possibly be light because of the presence of internal voids, which are removed before the batch is introduced into the flow.

Suspensions are commonly characterized by an effective suspension viscosity (Guazzelli and Pouliquen, 2018). Of the several existing viscosity laws, we utilize fits of the nature proposed first by Eilers (1941), $\mu_{\text{susp}}/\mu = [1 + 1.25\phi/(1 - \phi/\phi_c)]^2$, where ϕ_c is the volume fraction of particles beyond which the suspensions cease to flow, which is usually lower than the random close packing (≈ 0.64). We have chosen a value of $\phi_c = 0.614$ (verified with torque measurements as a reasonable choice). The subscript 'susp' is henceforth utilized when the effective suspension viscosity is used instead of that of the continuous phase.

3.2.3. Rotation control and torque measurements

The inner cylinder is driven by a Maxon DC motor, via a shaft and flexible coupling mechanism. The cylinder can be rotated (in both directions) up to a rotational frequency of 10 Hz with an absolute resolution of 0.01 Hz. Furthermore, to verify whether the desired rotational frequency matches the actual rotational frequency of the inner cylinder, a TTL frequency counter returns a pulse every 36° rotated by the inner cylinder, i.e. 10 pulses for a complete rotation. The frequency determined by the TTL frequency counter is subsequently used for estimating the apparent shear rates and Reynolds numbers. The input to the motor is controlled by a custom-made LabVIEW program via a data acquisition (DAQ) block (NI PCI-6035E) and a 12-bit DAQ board (NI BNC-2110).

The same data acquisition system is also used to record the torque, T, experienced by the entire inner cylinder, via a torque meter (HBM T20WN, 2Nm) attached to the shaft of the inner cylinder. This meter can measure torques up to 2 Nm with an absolute resolution of 0.01 Nm, and is sampled at a frequency of 2 kHz in the current study.

The relative motion between the end plates of the two cylinders may also be likened to a von Kármán swirling flow. This motion would contribute to additional torque, while also spawning vortices due to the so-called Ekman pumping, commonly referred to as end effects. Since the torque measurements also include contributions from the von Kármán flow, the torque is simply halved, in line with previous studies in the same facility (Ravelet, Delfos, and Westerweel, 2010). This assumption was later verified by Greidanus *et al.* (2015) to be analytically valid for laminar flows in the current facility. We assume that this is also valid for non-laminar, particle-laden flows. A fragmented inner cylinder design (Lathrop, Fineberg, and Swinney, 1992; van Gils *et al.*, 2011) would be needed to eliminate the influence of the ends on torque measurements.

The torque can then be modified into several non-dimensional variants, such as dimensionless torque, $G = T/(L\rho\nu^2)$, friction coefficient, $c_f = T/(\pi\rho r_i^2 L U_i^2)$ and the Nusselt number, $Nu_\omega = T/(2\pi L\rho J^\omega_{lam})$, where $J^\omega_{lam} = 2\nu r_i^2 r_o^2 \omega_i/(r_o^2 - r_i^2)$ is the azimuthal flux of the angular velocity between the two cylinders for purely laminar flow. The above three quantities are related to each other (Grossmann, Lohse, and Sun, 2016).

3.2.4. Temperature estimation

The current facility lacks a temperature control system, which would ideally alleviate the negative effect of heating of the fluid by viscous dissipation. As a consequence, the dynamic/kinematic viscosity of the fluid may undergo significant changes. Previous studies in the same facility have sought solutions such as ensuring that the temperature did not vary by more than 0.5 °C (Tokgoz *et al.*, 2012), or by running the system for a few hours prior to the measurements, ensuring a stable temperature thereafter (Gul, Elsinga, and Westerweel, 2018). Such measures were not applicable for the current investigation due to the nature of the experimental protocol and, thus, an *ad-hoc* approach to estimate the varying temperature throughout the experiments is adopted (similar to Greidanus *et al.*, 2015; Benschop *et al.*, 2018).

Before and after each experiment, a PT-100 sensor is inserted into the system through an opening on the top end plate attached to the outer cylinder, to measure the fluid/suspension temperature (under the assumption of isothermal conditions). Since the above intrusive method is not feasible during the experiment, an infrared thermometer (Calex PyroPen) measures the temperature of the outer surface of the outer cylinder at a sampling rate of 1 Hz. The emissivity constant in the proprietary software, CalexSoft, responsible for these measurements, is set as 0.86 (corresponding to the PMMA surface). Combining the above temperature measurements (PT-100 + infrared thermometer), 'instantaneous' temperatures of the suspension, and, thus 'instantaneous' Reynolds numbers for the flow, can be estimated. This is extremely handy as the viscosity of an aqueous Glycerol solution is very sensitive to temperature changes ($\approx 5\%\ ^{\circ}C^{-1}$ at temperatures around 20°C for the current composition of the solution). Typical temperature variations in the current experiments were in the order of 5°C, necessitating this *ad-hoc* technique for temperature estimation. The estimated temperatures were then utilized to compute the instantaneous physical properties of the fluid by an open source, freely available Matlab script (based on Cheng, 2008; Volk and Kähler, 2018).

3.2.5. Experimental protocol

In this chapter we distinguish suspension Reynolds number (Re_{susp}) from the Reynolds number (Re). The former is based on an effective suspension viscosity while the latter only on the viscosity of the continuous liquid phase*. We cover a wide range of suspension Reynolds numbers ($Re_{\text{susp}} \sim O(10^1 - 10^3)$) for a wide variety of volume fractions ($0 \leq \phi \leq 0.40$). Moreover, it is desired that these large ranges of Reynolds numbers are sampled fine enough to have a clear picture of the transitions between various flow regimes. Recent experiments of Majji, Banerjee, and Morris (2018) and Ramesh, Bharadwaj, and Alam (2019) were performed for a similar range of volume fractions, but for a lower range of Reynolds numbers ($Re_{\text{susp}} \sim O(10^2)$). These two studies utilized slowly accelerating/decelerating ramp protocols, i.e. $dRe/d\tau \ll 1$. Here, $\tau = t/(d^2/\nu)$ is dimensionless time where the time t is normalized by a time scale based on viscous diffusion

*These two options represent two different points-of-view. Using Re_{susp} inherently implies that the suspension is viewed as an effective fluid. Using Re views the suspension as a two-phase flow where the behaviour of the particles is allowed to be independent from that of the carrier fluid. For a neutrally buoyant suspension, inertial and shear migration represent phenomena where the suspension loses its homogeneity.

(d^2/ν).

Dutcher and Muller (2009) showed that the critical Re at which the flow transitions from laminar Couette flow to Taylor vortex flow was a function of the ramp rate, and define a critical ramp rate (ramp rate below which the critical Re is in good agreement with linear stability theory) of $\mathrm{d}Re/\mathrm{d}\tau = 0.68$ for their experiments ($\eta = 0.912, \Gamma = 60.7$). Moreover, they report a low deviation in the critical Reynolds number with varying ramp rates for higher-order transitions such as wavy vortex flow and modulated wavy vortex flow for $0.18 < \mathrm{d}Re/\mathrm{d}\tau < 2.93$, while also finding no effect of the ramp rate on the onset of turbulent Taylor vortices for $\mathrm{d}Re/\mathrm{d}\tau < 27.2$*. In a similar vein, Xiao, Lim, and Chew (2002) ($\eta = 0.894, \Gamma = 94$) report an absence of dependence of the characteristics of the wavy vortex flow regime for ramp rates $\mathrm{d}Re/\mathrm{d}\tau < 11.2$. Of course, a caveat is that the above statements are valid for single-phase flows and whether the same would be directly applicable for suspensions is unknown.

For the current experiments, following a ramp rate of $|\mathrm{d}Re/\mathrm{d}\tau| \ll 1$ would require an unreasonable amount of time to cover the entire span of control parameters (Re, ϕ), and thus a compromise is reached, which ensures a practical approach (similar to Cagney and Balabani, 2019). The apparent ramp rate is maintained at $|\mathrm{d}Re/\mathrm{d}\tau| < 3$. We define the apparent ramp rate as the ratio between the net differential change in Reynolds number and the net differential change in dimensionless time. These net differential changes are the difference between the values at the start and end of the protocol, making the apparent ramp rate a global measure of our experimental protocol. Of course, it must be noted that if the effective suspension viscosity is taken into account for the Re as well as τ, i.e. $|\mathrm{d}Re_{\mathrm{susp}}/\mathrm{d}\tau_{\mathrm{susp}}|$, the apparent ramp rates will drop sharply with increasing ϕ. For example, for $\phi = 0.10$, a reduction with a factor of 1.75 will occur, whereas for $\phi = 0.30$, this factor shall be about 9. In conclusion, we expect that our choice of ramp rate may affect the accurate determination of precise transition boundaries for dilute suspensions. However, the chosen ramp rate is not expected to affect the flow topologies themselves, which is acceptable for the present study.

Two types of experimental protocols are followed: the Reynolds number of the inner cylinder is slowly raised (reduced, respectively) with time by increasing (decreasing) the apparent shear rate. We change $\dot{\gamma}_{\mathrm{app}}$ in steps of 3.5 s^{-1} for $\dot{\gamma}_{\mathrm{app}} \leq 69.1$ s^{-1} and steps of 6.9 s^{-1} for $\dot{\gamma}_{\mathrm{app}} > 69.1$ s^{-1}. Maximum shear rates of 414.7 s^{-1} are achieved for all suspensions with $\phi \leq 0.20$. For suspensions with $0.25 \leq \phi \leq 0.35$, the maximum shear rate studied is 380.1 s^{-1} and 276.5 s^{-1} for $\phi = 0.40$, in order not to exceed the maximum torque acceptable for the torque meter. In summary, the shear rate is ramped up (down) in a quasi-static manner with non-infinitesimal steps. At each step, the shear rate is held constant for a period of 90 s and between two steps, the flow is accelerated (decelerated) at a rate of 3.5 s^{-2} (thus, $|\mathrm{d}Re/\mathrm{d}\tau| \sim 90$ between two steps, which is a local measure of the ramp rate unlike the apparent ramp rate). These protocols are henceforth referred to as: 'ramp-up'

*There seems to be no explicit mention of the criterion of $\mathrm{d}Re/\mathrm{d}\tau \ll 1$ being a necessity by the authors. In fact the lowest value accessed by the authors is a value of ~ 0.18. Moreover, the use of $\mathrm{d}Re/\mathrm{d}\tau$ might be mostly relevant for the transition from circular Couette flow to a flow regime with secondary motions. Once secondary motions appear, the conventional definition of $\mathrm{d}Re/\mathrm{d}\tau$ could be considered too strict. τ is a time scale based on viscous diffusion. However, once secondary motions appear, angular momentum is transported not only by viscous diffusion, but also by the secondary motions whose influence is much higher. This is also evident in torque measurements as there is a sharp rise in the torque value once secondary motions appear.

('ramp-down'). Please note that these two experiments are done separately, like Ramesh, Bharadwaj, and Alam (2019). A few experiments were repeated on different days, and sufficient repeatability was observed.

Before the ramp-up experiments, the flow is sheared for a few minutes at a high shear rate, homogenizing the dispersed phase as well as the visualization flakes (see Section 3.2.6) across the system. After allowing the system to be at rest for about twenty minutes, facilitating the decay of residual motions, the experiments are started. For the ramp-down experiments, the flow is accelerated to the highest desired shear rate at a rate of 3.5 s^{-2} ($|dRe/d\tau| \sim 90$, a local measure of the ramp rate unlike the apparent ramp rate) and sheared for five minutes before starting the actual measurements.

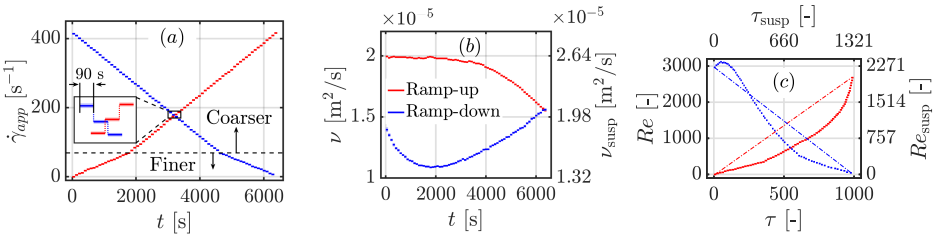

Figure 3.2: Example of the temporal variation of the control parameters for ramp-up and ramp-down protocols ($\phi = 0.10$). (*a*) Apparent shear rate. (*b*) Estimated kinematic viscosity of the working fluid/suspension. (*c*) The estimated (suspension) Reynolds number. The dash–dotted lines in (*c*) are representative of the apparent ramp rate.

A typical example of the realized experimental protocol is illustrated in Figure 3.2 for $\phi = 0.10$. While the apparent shear rates are in line with expectations (Figure 3.2(*a*)), the considerable change in the kinematic viscosity (Figure 3.2(*b*), on occasions up to 20% variations) manifests itself in non-linear profiles between the Reynolds number and non-dimensional time (Figure 3.2(*c*)). In the ramp-up experiments the viscosity decreases monotonically, as the magnitude of viscous heating only increases with time. In contrast, for the ramp-down experiments, the viscosity profile is often non-monotonic in time. The initial reduction in viscosity is driven by the temperature rise due to viscous heating, while later, the increase in viscosity (thus lowering of temperature) may be attributed to heat loss mechanisms dominating heat generated by viscous dissipation. These profiles also suggest that solely relying on temperature measurements before and after experiments could be misleading for a ramp-down experiment - even though the net change might not be much, the viscosity would have varied quite significantly over the course of the experiment. Ultimately, in the ramp-down experiments the Reynolds numbers profile may also appear non-monotonic (reduction in viscosity dominates reduction in apparent shear rates, initially). The apparent ramp rate, $|dRe/d\tau|$, for the ramp-down experiment in this example is $\sim |(0-3000)/(1000-0)| \sim 3$. If suspension viscosity is considered, $|dRe_{susp}/d\tau_{susp}|$, then the apparent ramp rate becomes $\sim |(0-2271)/(1321-0)| \sim 1.7$.

3.2.6. Flow visualization

For the classification of flow regimes, the well-established technique of flow visualization is employed. To this end, a small quantity of Iriodin 100 silver pearl (Merck KGaA, Darmstadt, Germany) is added to the suspension, 0.1% by mass. The size of these anisotropic flakes is specified by the manufacturers to be between 10-60 μm with a density between 2800-3000 kg/m^3. Given the low volume fraction of these flakes present, and their relative smaller size (by an order of magnitude, compared to the dispersed phase as well as the geometry), their effect on the flow behaviour is assumed to be negligible. The anisotropic flakes align themselves with the stream surfaces (Savaş, 1985) and any reflected light is attributed to the rotational motion of these flakes (Gauthier, Gondret, and Rabaud, 1998).

The light source illuminating the flakes is an LED panel, which is mounted at an oblique angle, above the flow facility, to minimize specular reflections onto the camera. The light reflected back by the flakes is recorded by a LaVision Imager sCMOS 16-bit camera equipped with a Nikon 35 mm lens ($f_\# = 4$). The pixel pitch of the camera is 6.5 μm and images with sizes up to a maximum of 2560 × 2160 pixels can be captured. This covers a field-of-view of about 28.1 × 23.7 cm^2 in the current experiments, while providing a resolution of 0.11 mm pixel^{-1} along the axial direction. Images are recorded with an exposure time of 1500 μs and a frame rate of 50 Hz. In order to record at higher frame rate of 100 Hz, the sensitive region of the camera was cropped in one direction to yield images of sizes 2560 × 200 pixels. The camera is focused onto the outer surface of the outer cylinder by means of a custom-made calibration target. No special measures are implemented on the set-up to circumvent the imaging artefacts that would arise due to the curvature of the outer cylinder (such as non-uniform resolution). Accurate quantitative analysis is thus restricted to the section of the geometry parallel to the camera sensor. Images of the calibration target nevertheless allow for making quantitative estimates of the flow structures along the azimuthal/streamwise direction (for example, streamwise wavelengths), albeit with higher uncertainty.

The full field-of-view images have been utilized for qualitative purposes in this study, while the cropped ones are further processed into space–time plots (i.e. concatenating together a column of pixels from consecutive images). While creating space–time plots from the flow visualization images, we compensate for the non-uniform illumination by means of a simple intensity gradient correction, along the axial direction. All space–time plots cover an axial extent of 20 cm or 20d, while most of them are based on recordings lasting 30 s. The space–time plots are further processed by means of simple fast Fourier transform analyses to extract information on axial periodicities as well as temporal frequencies.

3.2.7. Experimental uncertainties

The current experiments also entail a few uncertainties that may affect the interpretation of the results. The issue regarding temperature variations due to viscous heating is tackled with the help of an infrared thermometer. Thus, we can make a reasonably accurate estimate of the Reynolds number at any given step of the ramp protocol. A single value for the Reynolds number for each step is assumed, but in practice we do observe changes in the estimated temperature even in a single step, with maximum r.m.s. values in the order of 0.15 °C, which would correspond to a 0.8% uncertainty in viscosity as well as

Reynolds number. Similarly, maximum r.m.s. values for the apparent shear rate were found to be of the order 0.3 s^{-1}, which might be significant for lower Reynolds numbers (~1% uncertainty), but not so much for higher ones (~0.1% uncertainty). In all, we can estimate the Reynolds numbers up to an accuracy of 2% for each step. However, the finite size in the steps between consecutive shear rates translates to finite steps between consecutive Reynolds numbers, ~17.5 for finer steps and ~35 for the coarser steps. This has a detrimental implication on the accurate estimation of critical Reynolds numbers for transitions between flow states.

The temperature variation in time, due to viscous heating, also has a subtle impact on the fluid density, which can be estimated. For example, the density of the continuous phase reduces by 0.5% when the temperature is raised from 20°C to 30°C. In contrast, the density of PMMA (the dispersed phase) seemingly increases with increasing temperature, changing by 0.3% as the temperature is raised from 20°C to 30°C (see Rudtsch and Hammerschmidt, 2004, Table II). This contrast would drive the suspension to one with 'slightly heavier' particles. Moreover, a batch of particles often has a heterogeneous distribution of densities (for example, Bakhuis *et al.* (2018) report a near 0.5% density heterogeneity in their particles). Another subtle factor that may affect the neutral buoyancy of the suspension is the water absorption by the particles, which is specified as 0.2% increase in weight over 24 hours. With all these uncertainties in mind, we believe that our suspension can be considered to be nearly neutrally buoyant, with a weak bias towards slightly heavier particles. Assuming a discrepancy of 0.5% in the densities of the particles and the fluid, the settling/creaming velocity of a single particle in a quiescent system (at 25 °C) would be about 52 μm/s or it would take about 190 seconds for the particle to travel one gap width.

3.2.8. Comparison of current experiments against recent, similar ones

For a small range of Reynolds numbers, we primarily compare our flow visualization results against two existing similar works (Majji, Banerjee, and Morris, 2018; Ramesh, Bharadwaj, and Alam, 2019). For this reason, we first compare the present experimental parameters against the salient experiments of the reference articles, in Table 3.1. Subscripts 'f' and 'p' refer to corresponding properties of the fluid and particle, respectively.

Adding particles to a single-phase flow introduces new complexities to the analysis, in terms of additional non-dimensional parameters, including the particle volume fraction, ϕ, as well as the ratio between the annular gap width and particle diameter, d/d_p. One other number is the particle Reynolds number, which provides insight into the inertia of the fluid. We define $Re_p = \rho_f d_p^2 \dot{\gamma}_{\text{app}}/\mu_f = Re(d_p/d)^2$. Commonly, the viscosity is of the continuous phase and not of the suspension. It must be noted that the choice of particle radius instead of the diameter as the appropriate length scale is a common choice in literature too, which can cause discrepancies up to a factor of four, while comparing with other works. Key differences in the current experiments, compared to those by Majji, Banerjee, and Morris (2018) and Ramesh, Bharadwaj, and Alam (2019) include the ratio between the particle diameter and the gap width, as well as relatively higher particle Reynolds numbers, which suggests that particles in the current study could be

Parameter	Present	Majji, Banerjee, and Morris (2018)	Ramesh, Bharadwaj, and Alam (2019)
	Taylor-Couette geometry		
Radius ratio (η)	0.917	0.877	0.914
Aspect ratio (Γ)	21.7	20.5	11
	Suspension characteristics		
Gap width to particle diameter ratio (d/d_p)	16.7	30	37.5
Suspension Reynolds numbers (Re_{susp})	$\in [O(10^1)\ O(10^3)]$	$\in$ [80 160]	$\in$ [60 180]
Estimated particle Reynolds number (Re_p)	$\in$ [0.17 10]	$\in$ [0.1 0.63]	$\in$ [0.04 0.38]
Particle volume fractions (ϕ)	$\in$ [0 0.40]	$\in$ [0 0.30]	$\in$ [0 0.25]
	Experimental protocol		
Ramping rates	$\lvert dRe/d\tau\rvert \sim O(1)$	$\lvert dRe_{\text{susp}}/d\tau_{\text{susp}}\rvert \ll 1$	$\lvert dRe_{\text{susp}}/d\tau_{\text{susp}}\rvert \ll 1$
Directions	Separate ramp-down and ramp-up	Ramp-down only	Separate ramp-down and ramp-up

Table 3.1: Comparison of experimental parameters in related studies where non-Brownian suspensions are sheared in a Taylor-Couette facility by means of pure inner cylinder rotation. Please note that only the most salient cases from the works of Majji, Banerjee, and Morris (2018) and Ramesh, Bharadwaj, and Alam (2019) are listed in this table. The particle Reynolds numbers reported here differ significantly from those reported in Ramesh, Bharadwaj, and Alam (2019), their table 1. These numbers have been corrected after private correspondence with Prof. Meheboob Alam.

more inertial.

However, a better indicator of particle inertia is the Stokes number. The Stokes number for a particle in a simple shear flow, accounting for added mass effects, may be defined as $St = \dot{\gamma}_{\text{app}}\tau_p = (\rho_p + 0.5\rho_f)d_p^2\dot{\gamma}_{\text{app}}/(18\mu_f)$. Here, τ_p is the relaxation time for a particle. Under neutrally buoyant conditions, this expression simplifies to $St = Re_p/12$. This definition, however, is more suitable for flows with no secondary motions. Of course, alternative definitions of the Stokes number could be used for flows with Taylor rolls i.e. secondary structures. For example, $St_{\text{roll}} = \tau_p/\tau_{\text{roll}}$, where τ_{roll} can be estimated as the time needed for a roll to make a complete revolution. The characteristic length scale of a roll is $O(d)$, while a typical velocity scale may be approximated as $O(0.05 - 0.1\omega_i r_i)$ (based on Wereley and Lueptow, 1998, figure 3), i.e. $\tau_{\text{roll}} \approx 0.05-0.1\dot{\gamma}_{\text{app}}$ or $St_{\text{roll}} \approx 10-20St \approx Re_p$. This sets a tighter constraint on the suitability of the particles as faithful tracers of the surrounding fluid. Under such a constraint, all the studies tabulated in Table 3.1 may include effects of particle inertia.

Yet another relevant non-dimensional number is the Bagnolds number (Bagnold, 1954) defined as $Ba = \rho_p d_p^2\dot{\gamma}_{\text{app}}\lambda^{1/2}/\mu_f$ $(= Re_p\lambda^{1/2}$, under neutrally buoyant conditions), where $\lambda = 1/[(\phi_c/\phi)^{(1/3)} - 1]$ is referred to as a linear concentration. For our experimental parameters, $Ba < 40$ implying that we are always in the so-called macro-viscous regime, where the flow behaves like a Newtonian fluid. This also holds true for the studies of Majji, Banerjee, and Morris (2018) and Ramesh, Bharadwaj, and Alam (2019).

3.3. Global analysis of the experiments

In this work we use the conventions used by Dutcher and Muller (2009) to differentiate between lower-order transitions (from circular Couette flow to the first appearance of wavy vortices) and higher-order transitions (all transitions beyond the first appearance of wavy vortices). An exhaustive validation of single-phase flow experiments in our facility with the aid of simultaneous flow visualization and torque measurements can be found in Section 3.A.

3.3.1. Flow visualization

We present a consolidated regime map of all our experiments in Figure 3.3. The different flow regimes are a function of volume fraction as well as the suspension Reynolds number (normalized by the experimentally determined critical Reynolds number for single-phase flows, $Re_{c,\phi=0} = 142$). For simplicity, we make a crude classification by not distinguishing between the various wavy flow states such as laminar/modulated/turbulent wavy vortices. Instead, we only classify the wavy states as periodic (one distinct peak in the spectrum, excluding harmonics) and quasi-periodic (multiple, incommensurate peaks in the spectrum). To distinguish between these two, we use a mix of qualitative (visual inspection of space–time plot) and quantitative conventions. We define the quantitative approach as follows: let p_1 be the tallest peak, p_2 be the second tallest one and p_b be the median of the spectrum + 10×median average deviations. If the quantity $(p_1 - p_b)/(p_2 - p_b) < 10$ then we classify the flow as quasi-periodic.

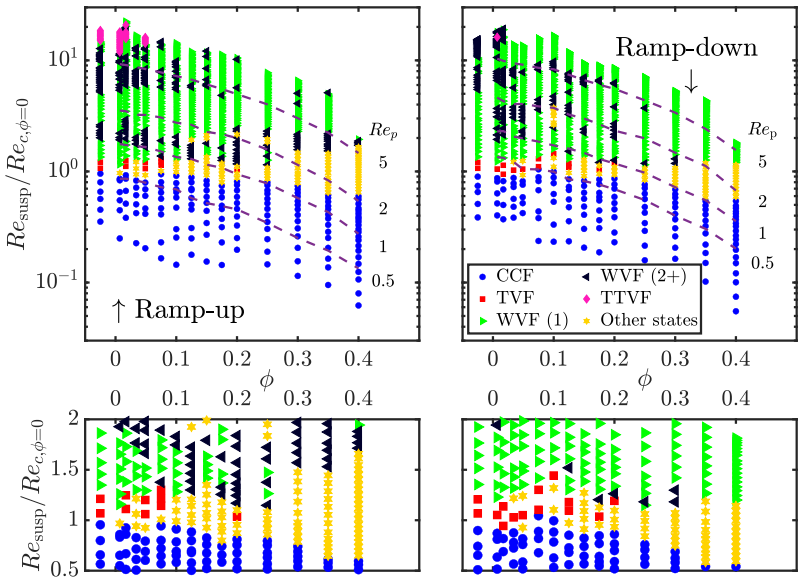

Figure 3.3: (*Top*) A consolidated regime map as a function of particle volume fraction as well as suspension Reynolds number (normalized by the experimentally determined critical Reynolds number for single-phase flows, $Re_{c,\phi=0} = 142$). In the legend, WVF (1) and WVF (2+) refer to periodic (single, distinct peak in the spectrum) and quasi-periodic (at least two, distinct, incommensurate peaks in the spectrum) wavy vortex flows, respectively. The single-phase flow case has been offset to aid better comparison. The purple dashed lines are approximate isolines for various particle Reynolds numbers. (*Bottom*) Zoomed-in portion of the consolidated regime map corresponding primarily to the lower-order transitions.

This global overview already allows us to draw a few preliminary conclusions. In general, the critical suspension Reynolds number for the flow to display secondary structures decreases with increasing volume fraction of the solid particles, independent of the ramp direction. This observation is in agreement with recent experiments (Majji, Banerjee, and Morris, 2018; Ramesh, Bharadwaj, and Alam, 2019) as well as theoretical linear stability analysis (Ali *et al.*, 2002; Gillissen and Wilson, 2019). This premature destabilization has been attributed to the anisotropy in the suspension microstructure, with neighbouring spheres interacting in the compressive direction of the base flow (Gillissen and Wilson, 2019).

The major addition to the regime map is that the suspensions introduce what has been marked as 'other states', which usually precedes the wavy vortex flow (WVF) regime. These refer to the collection of states reported in recent literature, among others (wavy) spiral vortex flows (reported first by Majji, Banerjee, and Morris, 2018) as well as coexisting states (reported first by Ramesh, Bharadwaj, and Alam, 2019). Moreover, the range of Reynolds numbers over which these states are observed increase with increasing volume fraction for both ramp protocols. This results in increasing separation between circular Couette flow (CCF) and wavy vortex flows. This observation seems to be in agreement with the regime map of Ramesh, Bharadwaj, and Alam (2019), but not with that of Majji,

Banerjee, and Morris (2018), who seemingly have the opposite trend.

There is a diminished appearance of axisymmetric Taylor vortex flow (TVF) as a standalone state, with increasing volume fraction, irrespective of our experimental protocol. This observation is in contrast to, both, Majji, Banerjee, and Morris (2018) and Ramesh, Bharadwaj, and Alam (2019). While Ramesh, Bharadwaj, and Alam (2019) observe Taylor vortices over a finite range of Reynolds numbers, irrespective of the particle volume fraction ($\phi < 0.25$), Majji, Banerjee, and Morris (2018) observe that the range of Reynolds numbers over which Taylor vortices are obtained diminishes with increasing volume fraction ($\phi < 0.2$), while not observing the state altogether for $\phi = 0.30$. One possible reason for our lack of observation of Taylor vortices, as compared to other works, might be the nature of our experimental protocol, which has higher effective acceleration rates, as well as the limited amount of time spent at a constant Reynolds number. Majji, Banerjee, and Morris (2018) do observe in their transient studies that coexisting flow states that initially appear to have axial segregation, eventually develop into fully formed Taylor vortices after 5-10 minutes (see $Re = 116.9, 119.0$ in figure 15 of Majji, Banerjee, and Morris (2018)). The diminished appearance of Taylor vortices in our experiments prevents us from verifying the observation of Ramesh, Bharadwaj, and Alam (2019) whether the transition from Taylor vortices to wavy vortices is subcritical or not.

As far as higher-order transitions are concerned, the implications of the addition of particles are subtler. For example, the first appearance (or last, for ramp-down experiments) of wavy vortices may also be quasi-periodic, but a clear trend is not observed for the same. Moreover, as shall be seen later, the onset of chaos is delayed and the nature of transitions is seemingly qualitatively different from its single-phase flow counterpart. These flow regimes are explored in more detail by examining three volume fractions corresponding to different regimes of a suspension.

3.3.2. Torque measurements

The flow visualization measurements were complemented by global measurements of torque, which are often used to characterize flow regimes, be it from the perspective of rheology (Bagnold, 1954) or from turbulence (Eckhardt, Grossmann, and Lohse, 2007). In Figure 3.4 we show the consolidated $Nu_\omega - Ta$ plot for all our ramp-up experiments. We note that between the suspension experiments and the single-phase flow experiments, the experimental set-up was dismantled and reassembled. For this reason, we do not consider the single-phase flow results in the empirical fitting. We emphasize that we do not account for effective suspension viscosity in either Nu_ω and Ta, as this allows us to easily interpret drag increase/reduction as an effect of the addition of particles.

In Figure 3.4 we distinguish the flow regimes into three: (*i*) CCF; (*ii*) intermediate states (corresponding to all points between CCF and WVF (1/2+) in Figure 3.3, often TVF and 'other states'); and (*iii*) WVF onwards (all points from the first appearance of WVF, irrespective of the nature of the spectrum).

We first consider points corresponding to those classified under circular Couette flow (all crosses × in Figure 3.4). For all suspensions with $\phi \leq 0.20$, we observe that Nu_ω is independent of Ta. In rheological terms this simply means that the viscosity is independent of the shear rate, i.e. the flow behaviour is Newtonian. However, for $\phi \geq 0.25$, at higher

Ta (in the laminar regime), there is an increase in the scaling exponent which might be indicative of shear-thickening like effects. Picano *et al.* (2013) attributed the 'inertial' shear-thickening to the presence of anisotropy in the microstructure of the non-colloidal suspension flow ($Re_p \in [0.4, 40]$). This effect was caused by the presence of a shadow region, and the authors account for it by means of an 'effective volume fraction' (volume fraction after excluding the shadow regions).

From the onset of wavy vortices (all pluses + in Figure 3.4), it was observed that Nu_ω scaled approximately with $Ta^{0.23}$. This is especially true for the dilute and semi-dilute suspensions. Only for the densest suspensions ($\phi \geq 0.25$) it was observed that the scaling exponent fluctuated in the range ±0.03, without any clear trend. In a global sense, the exponent was 0.226 ± 0.014 (correspondingly, $\alpha = 1.45 \pm 0.03$ in $G \propto Re^\alpha$). Nevertheless, these fluctuations are subtler than the changes observed upon the onset of the fully developed turbulence regime characterized by a transition from laminar to turbulent boundary layers. For this transition, the coefficients are expected to gradually change from ~0.25 to ~0.38.

A similar observation was made in the experiments of Bakhuis *et al.* (2018) ($\eta = 0.716$, $\Gamma = 11.7$), albeit at extremely high Reynolds numbers ($O(10^6)$) and lower volume fractions ($\phi \leq 0.08$), where only minimal changes in the scaling exponent were observed in their relation $Nu_\omega \propto Ta^{0.40}$. On the other end of the particle loading spectrum, the torque measurements of Savage and McKeown (1983) ($\eta = 0.627$, $\Gamma = 5.08$) showed that the particle size had a greater impact on the scaling between shear stress and apparent strain rate than particle loading itself ($\phi > 0.4$, $Re \sim O(10^3)$). While not discussed explicitly, their measured shear stresses and apparent strain rates appear to be related by $\tau \propto \dot{\gamma}_{app}^{1.2-1.4}$ (i.e $Nu_\omega \propto Ta^{0.1-0.2}$; see figure 7 in Savage and McKeown (1983)). The relatively lower scaling exponents for Savage and McKeown (1983) may be a result of the relatively small aspect ratio. While not reported explicitly by the authors, the exponent for the Taylor number appears to be a function of the particle volume fraction in the work of Ramesh, Bharadwaj, and Alam (2019) (see their figure 27), in contrast to our findings. For example, in their ramp-down experiments for $180 \geq Re_{\text{susp}} \geq 150$, it appears that $Nu_{\omega,\text{susp}} \propto Ta_{\text{susp}}^{0.26}$ for $\phi = 0.10$ and $Nu_{\omega,\text{susp}} \propto Ta_{\text{susp}}^{0.35}$ for $\phi = 0.20$.

Another telling observation in the current results is the nature of the curves itself or, more specifically, how the curve transitions from $Nu_\omega \propto Ta^0$ to $Nu_\omega \propto Ta^{0.23}$. For the dilute suspensions, there is a relatively sharp shift between the two scaling exponents. However, for the densest suspensions, especially $\phi \geq 0.35$, the shift between the two scaling regimes is visibly gradual. Similar observations were visible in skin friction coefficient plots of recent particle-laden pipe flow experiments, and have been attributed to the presence/absence of turbulent puffs (Hogendoorn and Poelma, 2018; Agrawal, Choueiri, and Hof, 2019). Similar behaviour for particle-laden channel flows was demonstrated by Lashgari *et al.* (2014), by means of streamwise velocity fluctuations, which was attributed to inertial shear-thickening effects. Moreover, Ramesh, Bharadwaj, and Alam (2019) too observe this behaviour in their Taylor-Couette flow experiments ($\phi = 0.10, 0.20$). In the current case, this observation may be correlated with the separation between CCF and WVF (thus, all dots in Figure 3.4). As shown previously in Figure 3.3, the separation between CCF and WVF seemingly increased with increasing volume fraction of the particles, which may lead to the smoothness of the transition. Since correlation does not

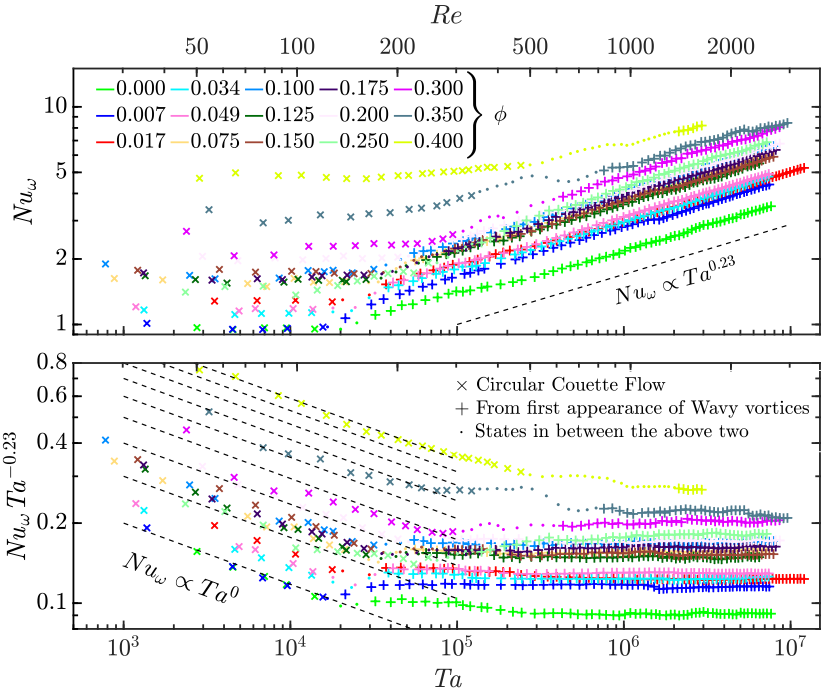

Figure 3.4: (Compensated) $Nu_\omega - Ta$ scaling for all ramp-up experiments.

necessarily mean causation, this correlation should be revisited in the future.

As a final step in the torque data analysis, we assimilate our data into an empirical fit of the nature: $Nu_\omega = BTa^k \chi^{e\,n}$. Here, χ^e is the relative viscosity (Eilers' fit:$\mu_{\text{susp}}/\mu = [1 + 1.25\phi/(1 - \phi/0.614)]^2$).

We assume that drag augmentation in our experiments is brought upon solely by a rise in the effective viscosity. With the above expression, we implicitly neglect drag increase due to the formation of a particle-wall layer that has been observed in turbulent, particle-laden channel flows (Costa *et al.*, 2016). Such an assumption may be valid since the investigated flows in the current study are not turbulent, and, thus, the existence of a particle-wall layer may be questioned. Nevertheless, it must be noted that Sarabian *et al.* (2019) report particle layering near both the cylinder walls in the circular Couette flow regime for $0.20 \leq \phi \leq 0.50$ in their experiments with non-Brownian suspensions. The relative contributions of particle-wall layering and rise in effective viscosity to drag augmentation should be explored in the future.

We fit data corresponding to all particle-laden flows from the onset of wavy vortices (thus, all the pluses in Figure 3.4, except $\phi = 0$). We neglect the single-phase case for the fitting due to the aforementioned arbitrary correction employed, and this correction is expected to primarily affect the prefactor B, which is not of much interest. The results are tabulated in Table 3.2. The fitted exponent for the Taylor number for the ramp-up

Protocol	B	k	n	R-square of fit
Ramp-up	0.1373 (0.1276, 0.147)	0.2258 (0.221, 0.2306)	0.3996 (0.3898, 0.4095)	0.964
Ramp-down	0.0784 (0.0686, 0.0882)	0.2634 (0.2551, 0.2717)	0.4159 (0.4021, 0.4297)	0.924

Table 3.2: Coefficients (95% confidence bounds in parentheses) obtained by a surface fit of data (all the pluses in Figure 3.4, except $\phi = 0$) to the equation $Nu_\omega = BTa^k \chi^{e\,n}$, as well as the corresponding R-square.

experiments, k, is ~ 0.23, in accordance with the visual observation of the scaling, $Nu_\omega \propto Ta^{0.23}$. The fitted exponents for the ramp-down experiments do not deviate significantly from the ramp-up ones.

The scaling exponent of 0.23 corresponds to $\alpha \sim 1.46$ ($G \propto Re^\alpha$). Eckhardt, Grossmann, and Lohse (2007) provide an explanation for the physical origin of these scaling exponents for single-phase flows. An exponent of $\alpha \sim 1.5$ is attributed to the dominance of boundary layer and hairpin contributions to the transport of angular velocity, as compared to that from the bulk and the background. The authors also propose relationships for the thickness of the boundary layers, for the azimuthal velocity as well as axial velocity, relative to the gap width. For the range of Reynolds numbers studied here, it may be expected that the boundary layers are thick and occupy a large fraction of the annular gap width. The absence of deviation in the scaling exponent between Nu_ω and Ta across all the volume fractions might suggest that the particles do not influence the nature of the angular momentum transfer between the cylinders (at least for the parameters studied here).

Another relevant non-dimensional number is the Bagnold number (Bagnold, 1954). The Bagnold number is the ratio between grain collision stresses to viscous stresses and, for all our experiments, it is found to be $Ba < 40$, implying that all our experiments were in the so-called 'macro-viscous regime'. Beyond $Ba > 450$, the grain collision stresses also play a major role and can shift the nature of the torque scaling significantly. Thus, despite our experiments spanning a wide range of suspension topologies, we do not notice a major impact on the scaling exponent, probably because all our experiments were in the 'macro-viscous regime'. But again, it has also been reported that the Bagnold number is insufficient to distinguish contributions from turbulence and particles (Lashgari *et al.*, 2014), which highlights the complexity of explaining the observation.

In the end, even though the results are not completely unambiguous, we can still report an approximate empirical scaling law from our observations, which approximately reads as $Nu_\omega \propto Ta^{0.24} \chi^{e\,0.41}$. Alternatively, this scaling behaviour may also be written as $G \propto Re^{1.49} \chi^{e\,0.41}$ or $c_f \propto Re^{-0.51} \chi^{e\,0.41}$. We reiterate that the above terms are defined using the fluid viscosity and not the suspension viscosity, except χ^e, and that this scaling is valid beyond the first appearance of wavy vortices.

3.4. Lower-order transitions: From Circular Couette Flow to the first appearance of wavy vortices

In this section we coarsely traverse the flow regimes studied exhaustively by Majji, Banerjee, and Morris (2018), Ramesh, Bharadwaj, and Alam (2019) and Ramesh and Alam (2020). All these studies performed their experiments at a very low ramp rate, in contrast to our experiments. We primarily intend to verify the existence of non-axisymmetric flow structures and coexisting states in our flow facility, which appear in the presence of particles. Thus, we perform a qualitative comparison with the findings in the above works. We also tested slower ramp rates in the limited range corresponding to the lower-order transitions, which are known to be especially sensitive to ramping protocols. This gave results similar to those obtained using ramp rates corresponding to our experiments.

As a reference, in single-phase flows, the flow transitions from circular Couette flow to laminar wavy vortex flow via Taylor vortex flow. By the first appearance of wavy vortices, we only consider patterns where the wave travels solely in the azimuthal direction and not axially. Thus, wavy spiral vortices are not considered as the demarcation between lower- and higher-order transitions.

3.4.1. Dilute suspension: A detailed example

In general, the nature of the lower-order transitions for the dilute suspensions did not vary significantly from that of single-phase flows, in both experimental protocols. The first significant appearance of anomalies in our experiments occurs at $\phi = 0.034$, slightly lower in comparison to $\phi = 0.05$ reported in other similar experiments (Majji, Banerjee, and Morris, 2018; Ramesh, Bharadwaj, and Alam, 2019), possibly owing to the difference in experimental protocols as well as higher particle Reynolds numbers.

Select regions of flow transitions for $\phi = 0.034$ are shown in Figure 3.5, primarily to demonstrate the differences from single-phase flow. In the ramp-up experiments the flow from CCF ($Re_{\text{susp}} = 118$) transforms to a state with a presence of mildly visible spirals with Taylor vortices towards the ends ($Re_{\text{susp}} = 134$). Hereafter, the flow transforms to a state with Taylor vortices barring a defect at the mid-height of the Taylor-Couette system ($Re_{\text{susp}} = 151$), which has a trident like shape on a space–time plot. We conjecture that there is a competition between the Taylor vortices arriving from the top and the bottom, and that this could possibly be a transient state. Hereafter, we observe a flow state seemingly developing into a fully wavy vortex flow ($Re_{\text{susp}} = 172$). This is visible in the space–time plot as a small portion of the Taylor vortices eventually transforms into wavy vortices ($Re_{\text{susp}} = 185$).

The route for the ramp-down experiments is very similar to the ramp-up ones. We observe wavy vortex flow ($Re_{\text{susp}} = 187$) devolve into Taylor vortex flow ($Re_{\text{susp}} = 146$) via a partially wavy vortex flow ($Re_{\text{susp}} = 173$). While in the ramp-up experiment it was observed that the waviness of the vortices grew in time, the same is observed here, while one might expect a slow devolution into a state entirely occupied by Taylor vortices. A possible reason is that the waviness (even partially occupying the system) may be considered as a destabilizing perturbation, which allows the wave to grow. The Taylor vortices are then suppressed upon reducing the shear rate ($Re_{\text{susp}} = 124$), and the flow is

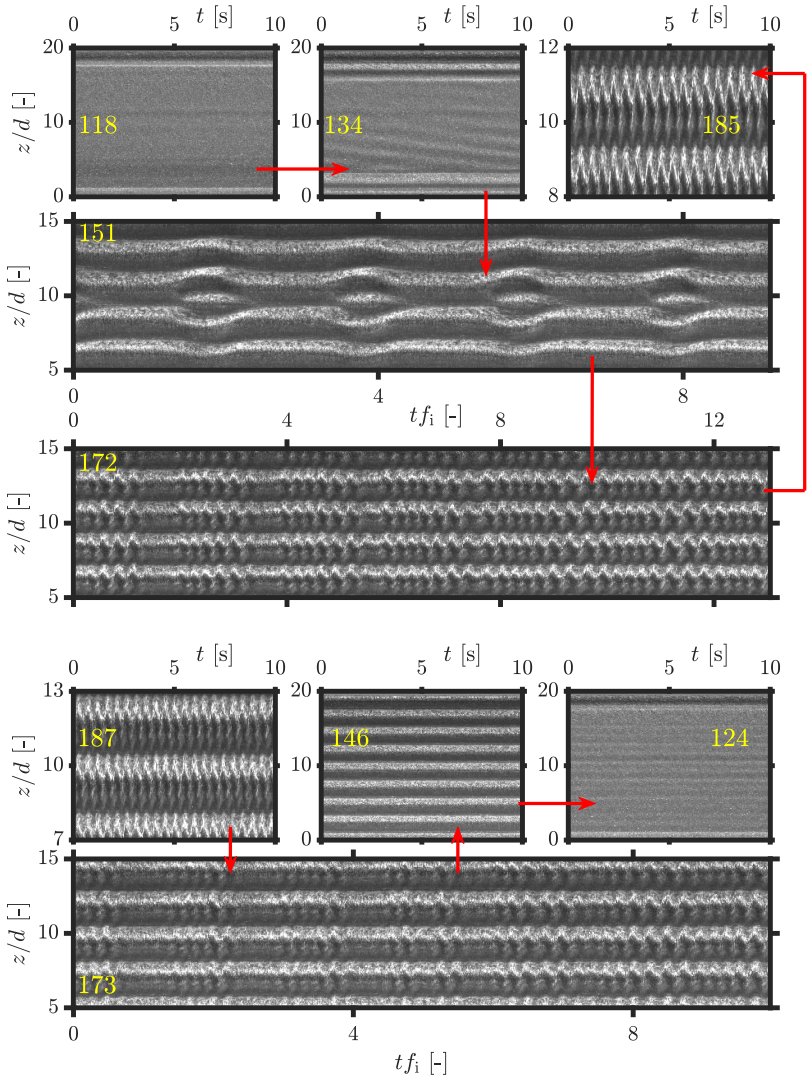

Figure 3.5: Lower-order transitions for a dilute suspension (ϕ = 0.034). Only for the stretched space–time plots, the x-axis is time normalized by the time period of the inner cylinder rotation. The numbers in the figures represent the suspension Reynolds numbers, Re_{susp}. (*Top*) Ramp-up experiments. (*Bottom*) Ramp-down experiments.

nearly free of secondary structures thereafter. It must be noted that the developing wavy vortices have not been reported either by Majji, Banerjee, and Morris (2018) or Ramesh, Bharadwaj, and Alam (2019). We revisit the flow state with developing wavy vortices in Section 3.4.5.

3.4.2. Semi-dilute suspension: A detailed example

With increasing particle loading, it was noted in Figure 3.3 that the gap separating CCF and WVF grew. We look into the example of a semi-dilute suspension, by considering the case of $\phi = 0.15$. Examples of the lower-order transitions are shown in Figure 3.6 for both experimental protocols.

In the ramp-up experiments CCF ($Re_{\text{susp}} = 117$) transforms into a state with a sharp distinction between the topologies in the top and bottom halves ($Re_{\text{susp}} = 132$). The top half has axisymmetric Taylor vortices, whereas the bottom half has non-axisymmetric spiral vortices. This flow topology is very reminiscent of the coexisting states reported recently by Ramesh, Bharadwaj, and Alam (2019). Upon increasing the shear rate ($Re_{\text{susp}} = 144, 152$), the overall flow topology remains unchanged, but the following can be observed. A very low-frequency waviness appears along the spiralling structure, accompanied by a crest on the Taylor vortices at the corresponding azimuthal location. A similar flow state was achieved in the transient evolution experiments of Majji, Banerjee, and Morris (2018) for their $Re_{\text{susp}} = 107.6$, a particle loading of $\phi = 0.10$ and particle diameter of $d_p = 230\ \mu\text{m}$, which they describe as 'a combination of spirals and Taylor vortices with azimuthal waviness'. Upon increasing the shear rate further, the segregation still persists, but a high-frequency waviness is now evident as well, with the inclination of the spirals slowly reducing ($Re_{\text{susp}} = 164, 178, 192$), until they are completely horizontal ($Re_{\text{susp}} = 201, 211$), with the absence of any structures travelling axially. The signature of the crests/defects appearing at lower Reynolds numbers ($Re_{\text{susp}} = 152$) are also the possible reason for the wavy vortices initially appearing distorted ($Re_{\text{susp}} = 201$). We observe wavy spirals at volume fractions as low as $\phi = 0.10$. This is in contrast with other similar experiments. For example, while Majji, Banerjee, and Morris (2018) begin to observe these structures only from $\phi \geq 0.20$, Ramesh, Bharadwaj, and Alam (2019) do not observe this flow regime altogether. Moreover, the wavy spirals observed by Majji, Banerjee, and Morris (2018) seemingly do not have any visible higher-frequency waviness, observed in the current experiments.

The ramp-down experiments, in contrast, shows a relatively different behaviour. Wavy vortex flow ($Re_{\text{susp}} = 197$), upon a reduction of shear ($Re_{\text{susp}} = 181$), devolves into a state similar to the developing wavy vortices also observed for $\phi = 0.034$. Upon further reduction of shear ($Re_{\text{susp}} = 166$), we observe a state with a mix of inclined vortices (with opposite inclinations either side of the mid-height), with wavy vortices occupying the circumference partially, possibly at the same locations of the partially developed wavy vortex flow state. Further reduction of the shear rate ($Re_{\text{susp}} = 155, 144$) led to a segregated state, wherein the region around the mid-height had spiralling structures while the ends had Taylor vortices. Similar observations have been made in counter-rotating, single-phase flow as well, with spirals existing between rotating defects (Hoffmann, Lücke, and Pinter, 2005). This served as a precursor to the formation of ribbons ($Re_{\text{susp}} = 130$), albeit fainter than those observed by Majji, Banerjee, and Morris (2018). We do not regularly observe ribbons structures, unlike Majji, Banerjee, and Morris (2018), possibly due to the pace of our experimental protocol, as well as the limited regions over which this flow state is found to be stable. The lowest volume fraction we observed ribbons was at $\phi = 0.075$. Then, the flow reaches CCF at $Re_{\text{susp}} = 117$.

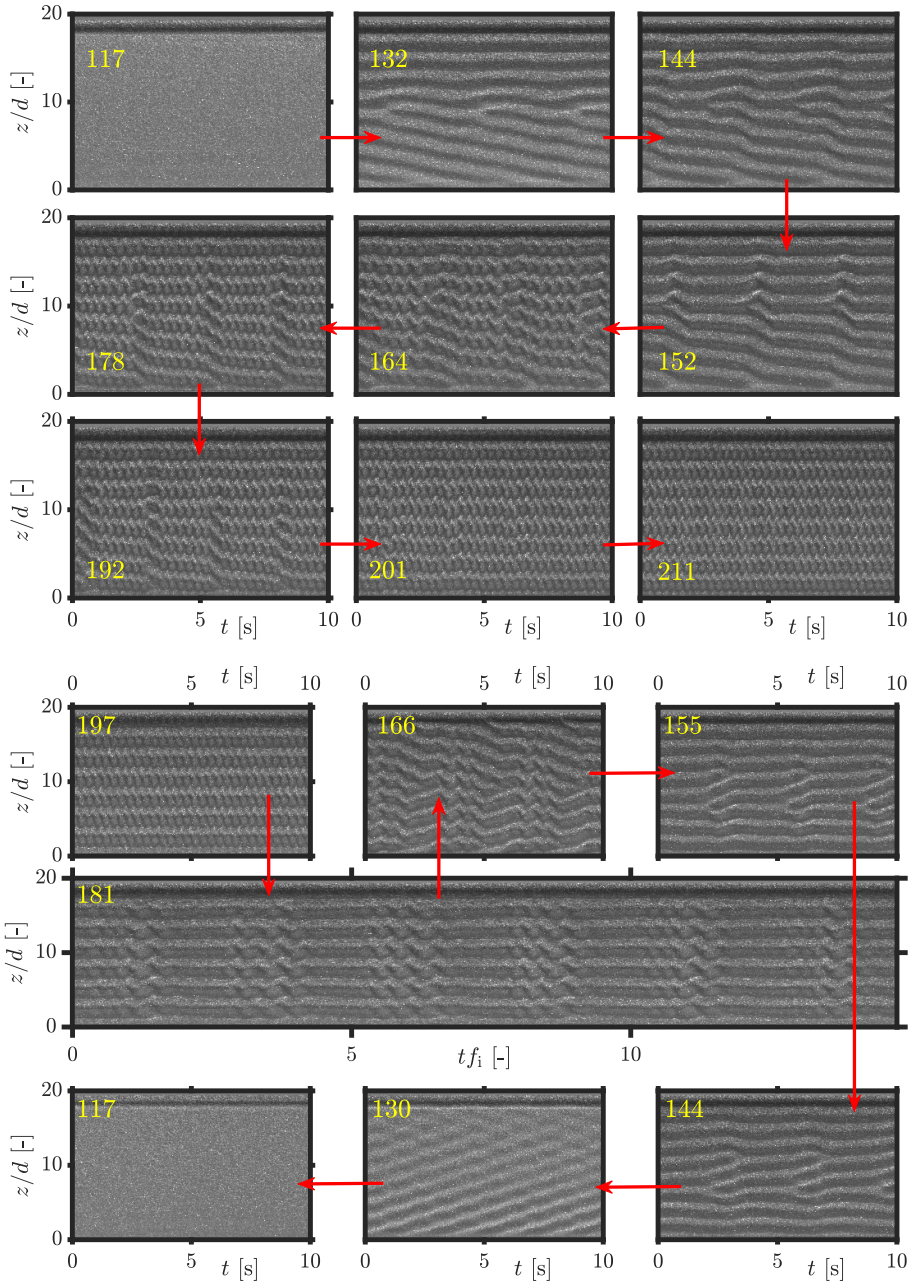

Figure 3.6: Lower-order transitions for a semi-dilute suspension (ϕ = 0.150). See caption of Figure 3.5 for other details.

3.4.3. Dense suspension: A detailed example

Finally, we consider an example of a dense suspension, namely $\phi = 0.30$. It must be noted that the image quality begins to deteriorate with increasing volume fractions, and at the highest volume fractions studied ($\phi = 0.40$), visual analysis becomes less straightforward, possibly because the dispersed phase begins to block the optical path. Examples of lower-order transitions for $\phi = 0.30$ are shown in Figure 3.7.

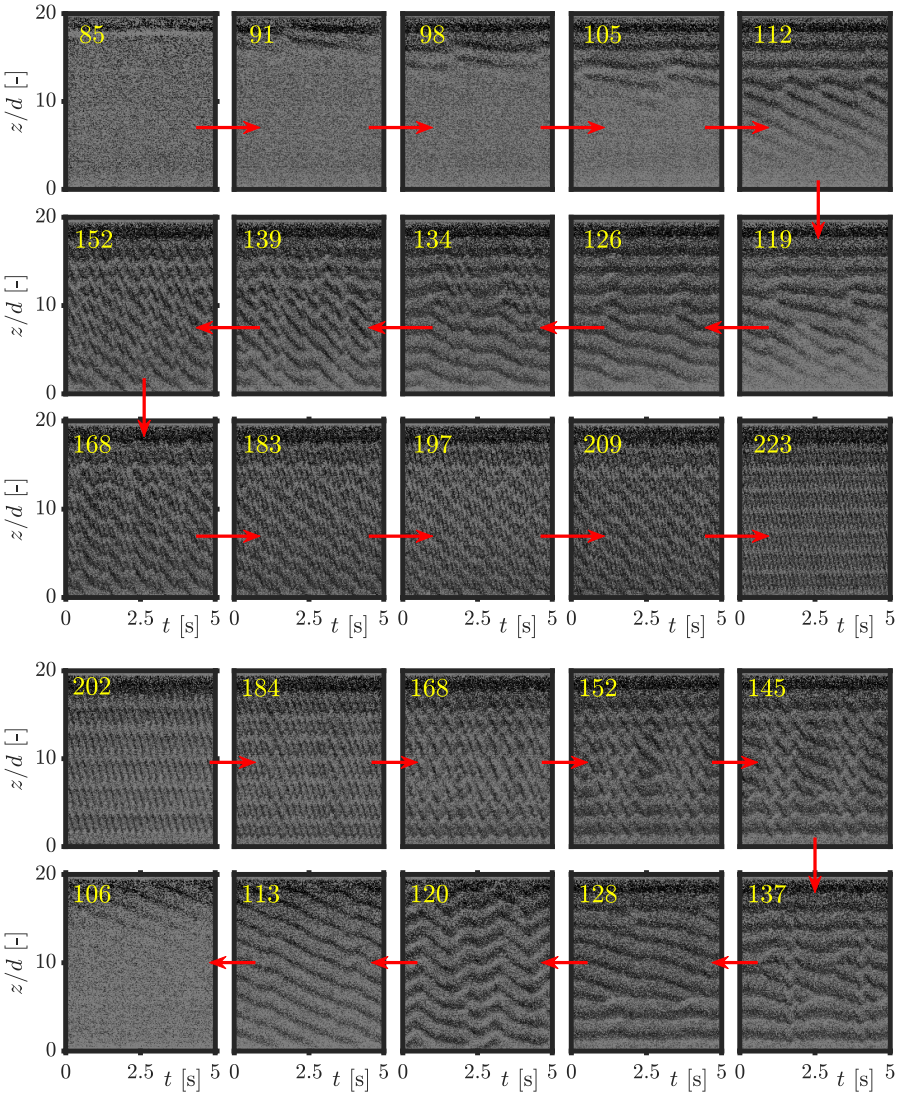

Figure 3.7: Lower-order transitions for a dense suspension ($\phi = 0.30$). An image adjustment procedure has been employed to enhance the contrast. See caption of Figure 3.5 for other details.

The flow topologies for the ramp-up experiments qualitatively resemble the observations for $\phi = 0.15$. The flow is azimuthal to begin with ($Re_{susp} = 85$), and the flow topology slowly evolves ($Re_{susp} = 91, 98, 105, 112$) until the secondary structures occupy the entire axial extent of the system ($Re_{susp} = 119, 126$). There are two noteworthy observations: firstly, a coexisting flow state is formed with Taylor vortices at the top and spiral vortices at the bottom, and secondly, that the flow requires a lot more time in order to go from a purely circular state to a flow with secondary structures. The latter might imply that the presence of particles in such large quantities suppresses the development rate of the flow state in time. Upon increasing the Reynolds number further ($Re_{susp} = 134, 139, 152, 168, 183, 197, 209$), we observe that the spiralling structures swallow one of the Taylor vortices, while also developing waviness. The Taylor vortices too display waviness simultaneously. Eventually, the wavy vortex flow state is obtained ($Re_{susp} = 223$). Majji, Banerjee, and Morris (2018) do not observe the wavy vortex flow regime for $\phi = 0.30$ and also mention that they observe only a sequence of non-axisymmetric flow states. While the latter observation is true for the present experiments too, the former observation may be attributed to the lower suspension Reynolds numbers ($Re_{susp} \approx 140$) achieved by Majji, Banerjee, and Morris (2018), compounded with our observation that the separation between CCF and WVF grows with increasing ϕ. The reduced speed in the formation of structures also makes it less straightforward to demarcate whether the flow state should be considered as CCF or not.

The ramp-down experiments show a devolution also not drastically different from that seen for $\phi = 0.15$. The initially wavy vortex flow state ($Re_{susp} = 202$) begins to show amplifications on the waves, at least partially ($Re_{susp} = 184$), and the amplifications occupy the entire circumferential extent upon further reduction of the shear rate ($Re_{susp} = 168$). This is followed by the appearance of spiralling structures near the mid-height of the set-up accompanied by a damping of the waviness ($Re_{susp} = 152, 145, 137$), and eventually, we obtain a state with spiral vortices in the center surrounded by Taylor vortices at both ends ($Re_{susp} = 128$). At $Re_{susp} = 120$ an interesting flow state is observed which might appear to be wavy vortex flow at first sight, but actually is a state with competing spirals (left winding versus right winding). These structures appear to be visually similar to cross-spirals (Altmeyer and Hoffmann, 2010). Further reduction in the Reynolds number ($Re_{susp} = 113$) yields a flow state with spirals spanning the entire axial extent, and then subsequent disappearance of secondary structures $Re_{susp} = 106$.

3.4.4. Can coexisting regimes in ramp-up experiments be due to imperfect neutral buoyancy?

The following discussion is primarily heuristic in nature and stems from the observation that the ramp-up experiments display more radical axial segregation of flow regimes than the ramp-down ones. Similar observations are visible in the experiments of Ramesh, Bharadwaj, and Alam (2019), where their ramp-up experiments yielded the coexisting states, while the ramp-down experiments did not (see figures 5, 12-14 in their article). An exception to this trend was found in the experiments of Ramesh and Alam (2020) who reported axially segregated states in their ramp-down experiments too. Majji, Banerjee, and Morris (2018) circumvent this conundrum altogether by sticking to a ramp-down proto-

col, as they observed migration of particles towards the axial boundaries (see section 3.2 of their article) in the event of following a ramp-up protocol. Moreover, a common assumption in all relevant experiments (Majji, Banerjee, and Morris, 2018; Ramesh, Bharadwaj, and Alam, 2019; Ramesh and Alam, 2020), including the present work, is that particles are homogeneously distributed.

Shown in Figure 3.8 is a contour plot of times needed for a homogeneous suspension to settle/rise by one gap width of the annulus, in a finite container. This is done so by calculating the settling velocity of a homogeneous suspension in a confined vessel $v_{s,b} = v_t(1-\phi)^n$, where $v_t = (\rho_p/\rho_f - 1)(g d_p^2/(18\nu))$ is the terminal velocity of a single particle (Richardson and Zaki, 1954). For the range of density difference uncertainties in the current experiment, the particle terminal velocity based Reynolds number $\ll 0.2$, so $n = 4.65 + 19.5(d_p/d) = 5.82$. While estimating the settling velocities, we have taken the extreme scenario of using the highest observed temperature for determining the kinematic viscosity.

For our ramp-up experiments, the flow was sheared at a very high rate before being left to rest for about 20 minutes prior to the commencement of experiments. After starting the experiments, typical durations before the flow developed any secondary structures were in the order of 5-10 minutes. Neglecting the influence of CCF on particle resuspension, the suspension gets about 30 minutes or 1800 seconds to non-homogenize. Since the estimated settling/rising velocities for marginal density differences are typically much smaller than velocities of secondary flow structures, the settling/rising effect may be neglected once secondary flow structures appear.

Assuming that the various uncertainties (including effect of temperature as well as particle density distribution) cause a density difference of 0.005 (0.5%), then the suspension is able to axially migrate 3 gap widths, before the flow can develop secondary structures for $\phi = 0.15$, and about 0.8 gap widths for $\phi = 0.30$, for example. These are relatively large distances and can result in inhomogeneous distribution of suspension Reynolds number across the axial direction. This in turn could cause different instability mechanisms across the axial direction, triggering the formation of axially segregated coexisting states.

In conclusion, it may be said with the help of the above estimates that the existence of 'coexisting states' with radical axial segregation of flow states could be affected by marginal density differences between the two phases. In virtually all experiments using large quantities of particles, these imperfections may be unavoidable. However, conclusively (dis)proving whether subtle density differences play a significant role would require simultaneous measurements of particle volume fractions along the axial direction.

3.4.5. Azimuthally localized wavy vortex flow: transient or a new regime?

A question that can be raised is whether the flow structures observed in the detailed examples here were spawned by our experimental protocol, which involves higher ramp rates ($|\mathrm{d}Re/\mathrm{d}\tau| \sim O(1)$) as well as limited durations over which a constant Reynolds number was maintained (90 s). The transient evolution experiments of Majji, Banerjee, and Morris (2018) serve as a good reference for this matter (see figure 15 of their article). Over the short term (~ 5 minutes), several of their experiments display coexisting states (axially seg-

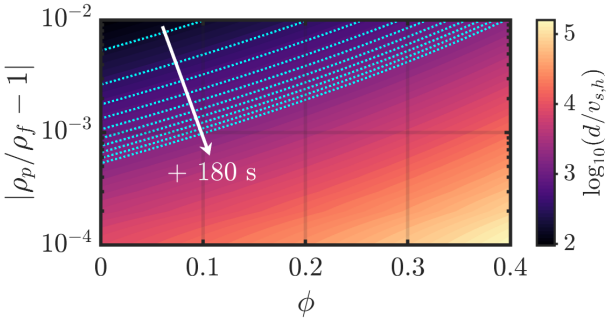

Figure 3.8: Estimated time duration needed for a homogeneous suspension to settle/rise by one gap width in a quiescent Taylor-Couette (for the current geometry) as a function of particle volume fraction and density mismatch. Each dotted blue line represents an isoline with increments of 180 s from 180 s to 1800 s.

regated), and a few of these even survive for up to 30 minutes. Thus, these experiments do suggest that flows with axial segregation and/or defects may survive for extended periods of time. Even Chossat and Iooss (1994) state in their book, 'For instance, for values of the parameters where spiral waves are expected, one actually sees a flow with 'defects', and one has to wait quite a long time before these defects disappear'. Thus, the same may be applicable to our experiments, and that a few of our reported flow states may be transients while a few of them might survive for an extended period of time.

One of the most intriguing flow states observed in our experiments was the developing/intermittent/localized wavy vortex flow ($Re_{\mathrm{susp}} = 172$, ramp-up in Figure 3.5; $Re_{\mathrm{susp}} = 173$, ramp-down in Figure 3.5; $Re_{\mathrm{susp}} = 181$, ramp-down in Figure 3.6). This state primarily differs from the flow states with defects, in the sense that there are no sinks/sources, and that any segregation occurs in the azimuthal direction (a fraction of the circumferential span has waviness on the otherwise axisymmetric Taylor vortices). These structures were observed in both the ramp-up as well as ramp-down experiments, ruling out any path dependence. The space–time plot on its own does not clarify whether this flow state is a combination of Taylor vortices and wavy vortices, coexisting at separate azimuthal sectors, or if the Taylor vortices become wavy for a short period of time before returning to the axisymmetric form.

In order to unveil the nature of these developing/intermittent/localized wavy vortex flows, additional experiments were performed. The rotational frequency of the inner cylinder was manually adjusted until the desired flow state was achieved. Hereafter, the rotational frequency or the Reynolds number was kept constant (thus, $|\mathrm{d}Re/\mathrm{d}\tau| = 0$). Imaging is performed with the help of three cameras (GoPro Hero 7 Black), simultaneously recording separate circumferential sectors of the Taylor-Couette system. Synchronization of the three cameras is done in the post-processing stage by identifying the time instant of a distinct sound source. Classical methods of visualizing the entire circumference of the Taylor-Couette system typically involves using multiple mirrors and a single camera (Gorman and Swinney, 1982; Prigent and Dauchot, 2000). However, these were not pursued due to space constraints around our facility.

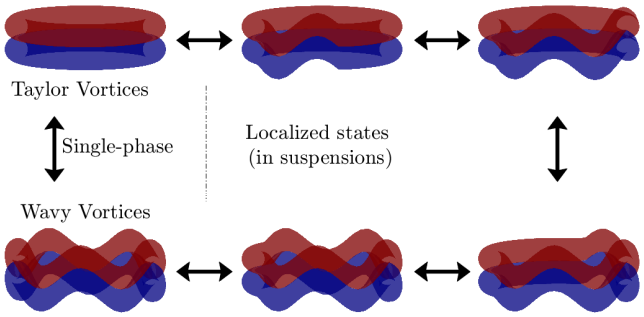

Figure 3.9: Schematic representation of flow topologies when Taylor vortices transform into wavy vortices via a localized growth in a suspension-laden system. The red and blue (wavy) tori represent a pair of counter-rotating vortices with opposing azimuthal vorticity. For suspensions, it is also possible for the flow to stabilize at an intermediate state.

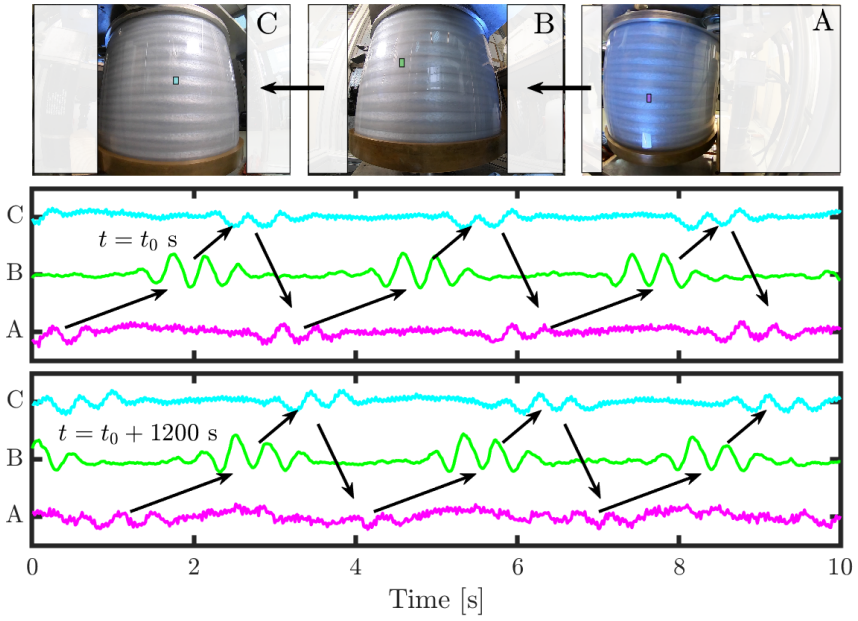

Figure 3.10: An example of a sustained version of localized wavy vortex flow in a suspension with $\phi = 0.10$. Coloured patches in the top panel indicate the locations, where the scattered light intensity is sampled. The bottom panels are time series of the light intensity at three locations, close to the mid-height, recorded on the three individual cameras. Arrows in the bottom panel indicate the propagation of the localized wave along the circumference. The time series in the bottom panels are separated by 20 minutes. Our longest observation of this flow state has been in a suspension with $\phi = 0.15$ for about $t \approx 5$ hours. This corresponds to $tf_i \approx 15000$ or $t\dot{\gamma}_{\text{app}} \approx 1 \times 10^6$.

Shown in Figure 3.9 is a schematic of the process depicting the transition between Taylor vortices and wavy vortices in suspension-laden systems. Intermediate states, i.e. waves only present partially across the circumference, are visible in two forms: a stable and an unstable form (see supplementary movies accompanying Dash, Anantharaman, and Poelma, 2020). In our experiments this flow state is primarily observed in the transition process between Taylor vortex flow and wavy vortex flow. On multiple instances, we have observed this flow topology lasting for longer than an hour. Our longest observation of this flow state in a stable form has been in a suspension with $\phi = 0.15$ for about 5 hours (about 15000 inner cylinder rotations). Towards the end of its lifetime, the wavy fraction slowly decayed to leave behind axisymmetric Taylor vortices. We have also observed scenarios where the wavy fraction grew in extent to occupy the entire circumference. It is also common to normalize the time with an advective time scale, $\dot{\gamma}_{app}^{-1}$, while studying transient structures (Borrero-Echeverry, Schatz, and Tagg, 2010). In such a case, the lifetime of the structure is $\approx 1 \times 10^6$. The longevity of this flow state can be better tested in a temperature controlled facility, which truly allows for $|dRe/d\tau| = 0$.

In Figure 3.10 we present an example of a stable version of the azimuthally localized wavy vortex flow state. The two bottom panels prove the existence of the localized flow state for at least 1200 s. We estimate the wave speed to be approximately half the speed of the inner cylinder. The recipe to achieve a stable form of the localized wavy vortex flow state is still an open question. From our experience, an unstable version is easily achieved by setting a constant shear rate which corresponds to a Reynolds number slightly above the critical value needed to obtained wavy vortices. The stable version has usually been achieved by arbitrarily varying the shear rate at the boundary between Taylor and wavy vortices, crossing it on multiple occasions. The stable version shown here was attained at $Re_{susp}/Re_{c,\phi=0} \approx 1.54$ for $\phi = 0.10$. For reference (see Figure 3.3), the transition between wavy vortex flow and the preceding (succeeding, alternatively) flow state occurs between $1.20 \leq Re_{susp}/Re_{c,\phi=0} \leq 1.28$ ($1.60 \geq Re_{susp}/Re_{c,\phi=0} \geq 1.44$) for the ramp-up (ramp-down) experiments.

To the best of our knowledge, this specific flow state has not been reported in the past, even though similar observations have been made. We note that Ramesh, Bharadwaj, and Alam (2019) do identify a coexisting state with Taylor vortices and wavy vortices in suspension-laden flows, however with axial segregation. Moreover, Abshagen *et al.* (2012) report a flow state with an axial localization of an azimuthally rotating wave in single-phase flows. While the localized wavy vortex flow from our experiments appears to be similar to the 'very short wavelength bursts' reported by Carey, Schlender, and Andereck (2007), the latter appears much beyond the onset of wavy vortex flow in high radius ratio systems. Wiener and McAlister (1992) also observed a solitary wave travelling across a system with axisymmetric Taylor vortices, but in the axial direction, while also reflecting off the end caps. Finally, an extremely similar flow state was reported in numerical studies on a rotating planar Couette flow by Salewski, Gibson, and Schneider (2019). A localized slug of wavy vortex flow emerged in a background of Taylor vortices via a modulational sideband instability. However, the localization occurred along the spanwise direction (axial direction in Taylor-Couette geometry) rather than the streamwise direction (azimuthal direction in Taylor-Couette geometry).

The transition between Taylor vortex flow and wavy vortex flow in single-phase flows

has been attributed to the 'self-sustaining process' also known as the 'regeneration cycle' (Martinand, Serre, and Lueptow, 2014; Dessup *et al.*, 2018). Recent numerical work by Wang, Abbas, and Climent (2018) shed light on the regeneration cycle for the flow of (semi-)dilute suspensions comprised of neutrally buoyant, finite-size, spherical particles in a planar Couette flow as well as channel flow. A key conclusion was that the spatial distribution of the particles was decisive, whether they are predominantly present in the streamwise rolls or the streaks. We thus conjecture that the particles interfere with the self-sustaining process in our experiments, giving birth to this localized flow state, but proving this requires further investigation.

In conclusion, based on our observations, we can conclude that the azimuthally localized wavy vortex flow state might be either a stable state or a long-lived transient. Since we are unable to conclusively claim that this flow state has an infinite lifetime, there is a possibility that it may be a long-lived transient. We can nonetheless propose that finite-sized particles, which are known to cause premature destabilization of the flow, are also capable of inhibiting the growth of instabilities.

3.5. Higher-order transitions: From the first appearance of wavy vortices

In this section we discuss the nature of higher-order transitions in particle-laden flows. For the sake of simplicity, we classify the flows only as periodic or quasi-periodic, depending on the number of incommensurate peaks appearing in the spectrum. A periodic flow has a single, distinctly identifiable peak in the spectrum, while a quasi-periodic flow has multiple, incommensurate, distinctly identifiable peaks in the spectrum. As a reference, in single-phase flows the flow transitions roughly in the following order with increasing Reynolds number: laminar wavy vortex flow (periodic), modulated wavy vortex flow (quasi-periodic), chaotic wavy vortex flow (quasi-periodic), turbulent wavy vortex flow (periodic), turbulent Taylor vortex flow (aperiodic). The flow patterns including and beyond chaotic wavy vortex flows additionally feature small-scale structures. A caveat, however, is that the exact nature of higher-order transitions is not set in stone. Section 3.A includes a detailed example for single-phase flows, and provides an in-depth explanation of the terminology.

The primary tool we employ in this section is a simple spectral analysis along the time axis of the space–time plots. The spectra along each axial location are averaged to return a single spectrum. The averaging is not expected to be detrimental as fundamental frequencies have been found to be independent of the axial location (Fenstermacher, Swinney, and Gollub, 1979), even though this might not hold true for the amplitudes. Peaks in the spectra are identified as follows. All points at least ten median average deviations away from the median of the spectrum are marked as 'potential peaks'. Hereafter, only the 'potential peaks' that are local maxima in the neighbourhood of five points are retained as true peaks. After isolating the true peaks, we use a mix of qualitative (visual inspection of the space–time plot) and quantitative conventions to classify the flow as either periodic or quasi-periodic. The quantitative approach is as follows: let p_1 be the tallest peak, p_2 be the second tallest one and p_b be the median of the spectrum + 10×median average deviations.

If the quantity $(p_1 - p_b)/(p_2 - p_b) < 10$ then we classify the flow as quasi-periodic. The frequencies in the spectra are normalized by the rotational frequency of the inner cylinder (f_i). Thus, all peaks close to $f/f_i = 1$ may be associated with the system itself. We also do not perform an extremely detailed, quantitative analysis of the spectra (for example, identifying the significance of different peaks, and identifying all the linear combinations), as it is not trivial (as evidenced by Gorman, Reith, and Swinney, 1980; Takeda *et al.*, 1993, in table 3 and figure 2 respectively) while also going beyond the scope of the current study.

While a similar spectral analysis can also be performed along the space axis to yield axial wavenumbers, we restrict our discussion to the (de)generation of vortex pairs (also referred to as vortex pinching/splitting processes by King and Swinney (1983)). Given that our system has two fixed end plates, which fix the boundary conditions for the flow, the (de)generation of vortices in the axial direction only occurs in pairs. If the total integer number of waves encompassing the circumference, m, is known with absolute certainty, then the wave speed (normalized with the inner cylinder speed) can be estimated as $\bar{c} = (f/f_i)/m$ (King *et al.*, 1984). We can estimate m by extrapolating from the full field-of-view snapshots. However, this approach is suspect to errors, which could affect the accurate determination of the wave speeds.

3.5.1. Dilute suspension: A detailed example

Firstly, we consider the example of $\phi = 0.034$ in Figure 3.11 to qualitatively probe the nature of the higher-order transitions in dilute suspensions. In the ramp-up experiments 'other states' are observed between $1.03 \leq Re_{susp}/Re_{c,\phi} \leq 1.32$. This is followed by wavy vortex flow for $1.42 \leq Re_{susp}/Re_{c,\phi} \leq 1.84$. Hereafter, between $1.92 \leq Re_{susp}/Re_{c,\phi} \leq 2.20$ the azimuthal waves undergo distortion, resulting in noisier spectra, and pave way for a new flow state with different axial/azimuthal wavenumbers at $Re_{susp}/Re_{c,\phi} = 2.36$. This behaviour is similar to that observed in single-phase flows. This new wavy state with a single frequency component of $f/f_i \approx 3.8$ is sustained in the region $2.36 \leq Re_{susp}/Re_{c,\phi} \leq 6.16$. This is followed by flow states similar to modulated wavy vortex flow and/or chaotic wavy vortex flow for $6.46 \leq Re_{susp}/Re_{c,\phi} \leq 8.80$, characterized by the appearance of finer structures in the flow (suggesting presence of chaos) as well as spectra with multiple peaks. The flow then returns to a state characterized by a single, dominant frequency, while also displaying chaotic elements for $9.18 \leq Re_{susp}/Re_{c,\phi} \leq 13.03$ (barring $Re_{susp}/Re_{c,\phi} = 11.94$, when there is a shift in azimuthal wavenumbers), reminiscent of the wavy turbulent vortex flow in single-phase flows. The flow undergoes a spectral cascading process between $13.42 \leq Re_{susp}/Re_{c,\phi} \leq 14.1$, leading to a shift in the azimuthal wavenumber from $f/f_i \approx 2.3$ to $f/f_i \approx 1.9$. From $Re_{susp}/Re_{c,\phi} = 15.31$ to $Re_{susp}/Re_{c,\phi} = 15.61$, there is a sudden shoot-up in the frequency component from $f/f_i \approx 1.9$ to $f/f_i \approx 3.8$, which is sustained until the highest Reynolds number ($Re_{susp}/Re_{c,\phi} = 18.21$). A similar observation was made in our single-phase flow experiments, and could be likened to the 'fast azimuthal wave'. Originally, this structure resembling the 'fast azimuthal wave' was reported to appear only after the appearance of turbulent Taylor vortices (Takeda, 1999). In this sense, our observations may be likened to the findings of Imomoh, Dusting, and Balabani (2010), who also observed this structure before the appearance of turbulent Taylor vortices.

The ramp-down experiments initially return a flow state akin to the wavy turbulent

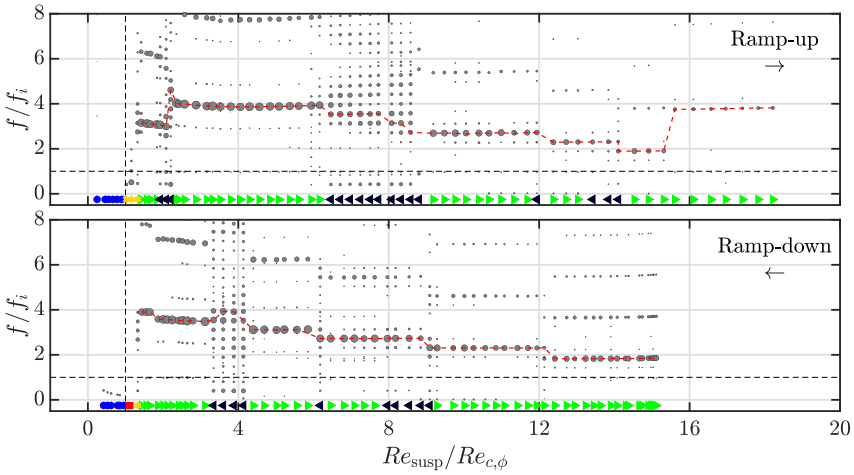

Figure 3.11: Compilation of frequency spectra for a dilute suspension ($\phi = 0.034$). Here $Re_{c,\phi}$ is the highest suspension Reynolds number at which circular Couette flow is identified. The size of the markers are proportional to their prominence in the spectrum. The dashed red lines approximately represent the primary frequency. A sudden drop (rise, respectively) in the dashed red line suggests a decrease (an increase) in the number of azimuthal waves. The coloured markers at the bottom correspond to the flow regimes shown in Figure 3.3.

vortex flow, characterized by a single, dominant frequency in the spectrum and fine-scale structures in the flow between $15.11 \geq Re_{susp}/Re_{c,\phi} \geq 9.29$ (with the disappearance of a vortex pair at $Re_{susp}/Re_{c,\phi} = 12.14$). This is followed by a flow state with multiple, incommensurate frequencies in the spectra between $9.09 \geq Re_{susp}/Re_{c,\phi} \geq 7.97$, with the flow still displaying smaller-scale structures. This is then followed by wavy vortex flow between $7.63 \geq Re_{susp}/Re_{c,\phi} \geq 4.40$, characterized by a single dominant frequency (except $Re_{susp}/Re_{c,\phi} = 6.18$, when the azimuthal wavenumber undergoes a shift) and a gradually diminishing presence of finer flow features. Between $4.14 \geq Re_{susp}/Re_{c,\phi} \geq 3.34$, the flow appears to be similar to the early modulated wavy vortex flow and also precedes the appearance of wavy vortex flow with a new azimuthal state (from $f/f_i \approx 3.1$ to $f/f_i \approx 3.5$) as well as an axial one (reduction of a vortex pair). The flow then is wavy in nature for $3.12 \geq Re_{susp}/Re_{c,\phi} \geq 1.44$. A surprising observation is the creation of two vortex pairs between $1.87 \geq Re_{susp}/Re_{c,\phi} \geq 1.65$. This is then followed by an 'other state' ($Re_{susp}/Re_{c,\phi} = 1.33$) and Taylor vortex flow ($Re_{susp}/Re_{c,\phi} = 1.12$), before becoming purely circular.

3.5.2. Semi-dilute suspension: A detailed example

Next, we consider the example of a semi-dilute suspension using the case $\phi = 0.15$ in Figure 3.12. As seen in the section describing the lower-order transitions, proper wavy vortices are not observed in the ramp-up experiments until $Re_{susp}/Re_{c,\phi} = 1.63$ with $f/f_i \approx 3.5$, and this flow state persists until $Re_{susp}/Re_{c,\phi} = 1.87$. Between $1.87 \leq Re_{susp}/Re_{c,\phi} \leq 2.62$, the flow transitions to a state with wavy vortices, albeit with a different azimuthal wavenumber (reflected in $f/f_i \approx 3.8$), and with the loss of a vortex pair. This transition oc-

curs with the appearance of distortion on parts of the waves (at $Re_{\text{susp}}/Re_{c,\phi} = 2.06$), which then give rise to a flow state with dislocations appearing in the form of wavy spiral vortices. Even for single-phase flows, splitting/merging of vortex pairs in the axial direction occurs by means of spiralling structures. Thus, it is fathomable that these spiralling structures are in fact intermediate states, and if more time were spent at each of the Reynolds numbers, the spiral might not have survived. Nevertheless, this observation throws weight behind our proposition that the presence of particles could lead to a reduction in the growth rate of instabilities. Hereafter, the flow states primarily sustain their waviness even until the highest Reynolds numbers we achieved $2.62 \leq Re_{\text{susp}}/Re_{c,\phi} \leq 13.91$. Moreover, the waviness usually has a single dominant frequency and quasi-periodicity is primarily observed when there is a shift in the azimuthal wavenumber. While not shown here, the spectra begin to appear noisier beyond $Re_{\text{susp}}/Re_{c,\phi} \geq 7.89$, while the flow also appears to display finer structures beyond $Re_{\text{susp}}/Re_{c,\phi} \geq 9.69$. Thus, the transition to chaos appears more vague compared to single-phase flows as it is not preceded by a flow state with two distinct, incommensurate frequencies. It may be concluded that the presence of higher number of particles can inhibit the appearance of the second, incommensurate frequency.

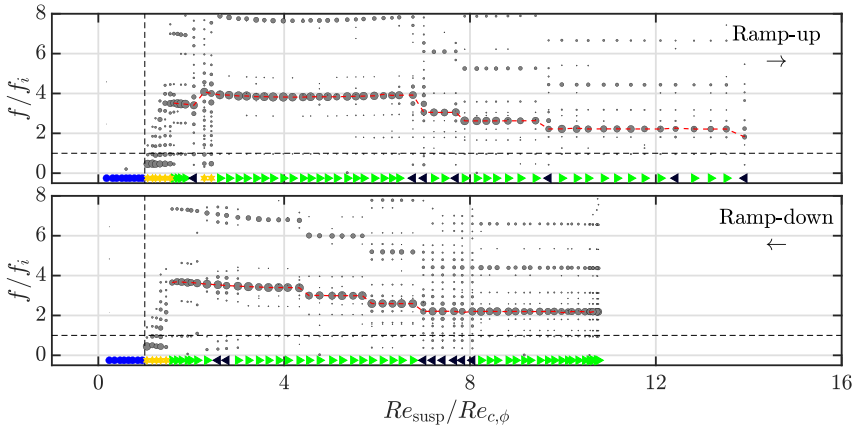

Figure 3.12: Compilation of frequency spectra for a semi-dilute suspension ($\phi = 0.15$). See caption of Figure 3.11 for other details.

The ramp-down experiments start of with a flow state with waviness, characterized by a spectrum with a single, dominant frequency ($f/f_i \approx 2.2$) while also being amply noisy. The flow itself appears to have smaller-scale structures, and, thus, the flow may initially be chaotic. We note that in the ramp-down experiments, the Reynolds number initially increases from $Re_{\text{susp}}/Re_{c,\phi} = 10.65$ to a maximum of $Re_{\text{susp}}/Re_{c,\phi} = 10.77$, despite decreasing shear rates. This is caused by sharp reductions in the viscosity arising from viscous heating. Nevertheless, this wavy flow state is sustained for $Re_{\text{susp}}/Re_{c,\phi} \geq 8.24$. Between $8.05 \geq Re_{\text{susp}}/Re_{c,\phi} \geq 7.00$, the spectrum has multiple peaks, reminiscent of the chaotic wavy vortex flow state in single-phase flows. We note that such a flow state was not observed in the corresponding ramp-up experiments. Between $6.77 \geq Re_{\text{susp}}/Re_{c,\phi} \geq 1.59$, the flow is wavy, predominantly with a single frequency component ($2.5 \leq f/f_i \leq 3.7$), with the exception of $Re_{\text{susp}}/Re_{c,\phi} = 2.76, 2.57$, where the space–time plots appear similar

to the early modulated wavy vortex flow seen for single-phase flows. The 'other states' are obtained between $1.46 \geq Re_{\text{susp}}/Re_{c,\phi} \geq 1.05$, before the flow becomes purely circular in nature.

3.5.3. Dense suspension: A detailed example

Finally, we consider an example of a dense suspension, $\phi = 0.30$ in Figure 3.13. The lower-order transitions, as shown previously, consisted primarily of the 'other states' ($1.06 \leq Re_{\text{susp}}/Re_{c,\phi} \leq 1.99$), before wavy vortices are obtained. However, as can be noticed from the compilation of spectra from the ramp-up experiments, the initial appearance of wavy vortices is accompanied by the presence of a secondary frequency ($f/f_i \approx 1.25$). This behaviour persists for $2.12 \leq Re_{\text{susp}}/Re_{c,\phi} \leq 2.92$. Moreover, between $2.80 \leq Re_{\text{susp}}/Re_{c,\phi} \leq 2.92$, additional apparent modulations are clearly visible on the space–time diagrams (visible as additional peaks in the spectra, near the primary peak $f/f_i \approx 4$), which then give way to a wavy vortex flow regime characterized by a single peak for the remainder of the experiments ($3.10 \leq Re_{\text{susp}}/Re_{c,\phi} \leq 8.88$), with the exception of locations where the flow transitions from one wavy state to another ($Re_{\text{susp}}/Re_{c,\phi} = 5.53, 6.62$). Curiously, between $5.69 \leq Re_{\text{susp}}/Re_{c,\phi} \leq 8.88$, a peak with a low amplitude (relative to the primary peak) is persistently present at $f/f_i \approx 3$. This also appears to be independent of the value of the primary frequency which varies from $3.1 \geq f/f_i \geq 2.3$. A key difference here from the single-phase flows is the lack of an extended region with a second, incommensurate frequency, which also has implications for the onset of chaos. A similar behaviour was also observed for $\phi = 0.15$. Thus, it indeed appears that the presence of particles inhibits the appearance of the second, incommensurate frequency. The peak at $f/f_i \approx 3$ seems to be the sole feature that may insinuate the appearance of a second frequency component, but we disregard it given its lack of strength. Of course, the studied range of Reynolds numbers ($Re_{\text{susp}}/Re_{c,\phi} \leq 8.88$) disallows us from drawing a firm conclusion on this matter, and can be a topic of interest in the future. In our single-phase flow experiments, the wavy turbulent vortex flow state was attained at $Re/Re_c = 9.00$, preceded by flow regimes with apparent chaos. Thus, even though the presence of particles causes a premature appearance of secondary flows, their presence possibly delays the onset of chaos.

The ramp-down experiments produce even less complicated transitions, and the dominant flow state is the wavy vortex flow between $7.16 \geq Re_{\text{susp}}/Re_{c,\phi} \geq 1.92$. The flow eventually transitions back to 'other states' via wavy flow states with multiple incommensurate frequencies ($1.75 \geq Re_{\text{susp}}/Re_{c,\phi} \geq 1.60$). This is clearly visible in the space–time plots for $Re_{\text{susp}} = 178, 162$ in Figure 3.7. Similar to the ramp-up experiments, an extremely weak peak is also present at $f/f_i \approx 3$ for $7.16 \geq Re_{\text{susp}}/Re_{c,\phi} \geq 4.31$. However, its significance remains unclear.

In conclusion, based on the three detailed examples considered here, we can claim that higher-order transitions in dilute suspensions are not qualitatively different from single-phase flows. However, with increasing particle volume fractions, there is evidence for the suppression of a second, incommensurate frequency. This frequency is commonly observed in single-phase flows (usually implying modulated waves) and serves as a precursor to the arrival of chaos (Gollub and Swinney, 1975; Fenstermacher, Swinney, and Gollub, 1979). The inhibition of the second, incommensurate frequency implies that at higher

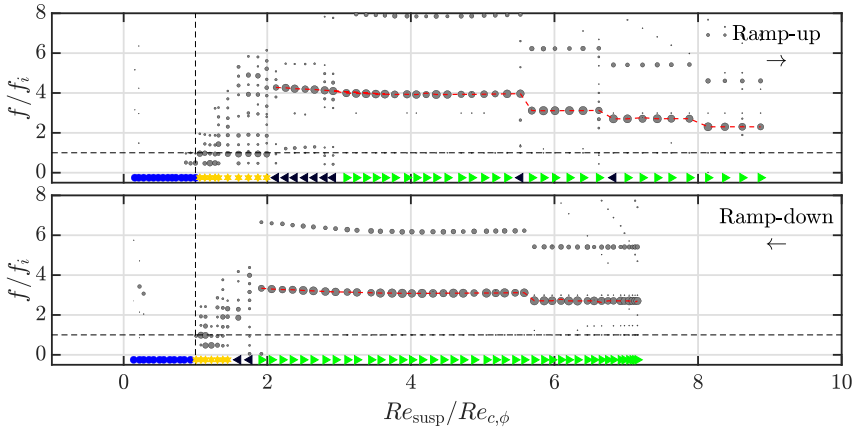

Figure 3.13: Compilation of frequency spectra for a dense suspension (ϕ = 0.30). See Figure 3.11 for other details.

particle loadings, the route to chaos is altered.

3.6. Conclusions and Outlook

In this section we summarize the key findings and their implications in Section 3.6.1 and propose possible future investigations to extend upon the current study in Section 3.6.2.

3.6.1. Summary of key findings

We set off with the target of addressing the following: previously unreported anomalies in lower-order transitions; nature of higher-order transitions; and the possibility to derive an empirical scaling law for the torque measurements. All these targets were in the context of experimentally studying neutrally buoyant, non-Brownian, particle-laden suspensions (solid spheres dispersed in a liquid) in a vertical Taylor-Couette geometry, driven by a rotating inner cylinder. The varied parameters include particle loading ($\phi \in [0\ 0.40]$), the (suspension) Reynolds number (up to $O(10^3)$, by varying the apparent shear rate) as well as experimental protocol (increasing and decreasing Reynolds numbers). The key findings are listed below.

1. Despite higher acceleration/deceleration rates (Table 3.1), previously reported non-axisymmetric flow regimes (such as spirals and ribbons) as well as 'coexisting states' (constituted of two separate states axially segregated) are observed in the particle-laden flows. These are observed as a part of the lower-order transitions for suspensions (Figure 3.5-Figure 3.7). Moreover, we identify that particle-laden flows are likelier to display 'defects' .

2. We speculate in Section 3.4.4 that 'coexisting states' (axial segregation of flow states) could potentially arise due to imperfect satisfaction of the neutral buoyancy. This

stemmed from the observation that experiments with increasing Reynolds numbers in time, display radical segregation in flow states more often. Conclusively (dis)proving the above proposition would require accurate measurements of particle volume fraction profiles along the axial direction.

3. A novel flow regime is reported in the form of an azimuthally local wavy vortex flow, with a fraction of the circumference composed of Taylor vortices and the remainder being wavy (see Figure 3.9, Figure 3.10). It may be considered as a 'coexisting state', with segregation in the azimuthal direction. Based on our observations, it is either a stable state or a long-lived transient.

4. Based on the increased appearance of defect-laden flow patterns as well as an example of a sustained azimuthally localized wavy vortex flow, we propose that the presence of a dispersed phase, which is known to trigger premature destabilization, is also capable of inhibiting the growth rate of instabilities. This is also proposed in the framework of the particles interfering with the self-sustaining process.

5. The gap between circular Couette flow and the appearance of wavy vortices clearly increases with increasing particle loading (Figure 3.3). Moreover, the first appearance of wavy vortices is sometimes quasi-periodic in nature, predominantly for dense suspensions undergoing ramp-up experiments.

6. Flow topologies corresponding to higher-order transitions in dilute suspensions are qualitatively similar to those observed in single-phase flows (Figure 3.11). At the higher particle loadings, though, there are indications that the route to chaos is altered. This is based on the absence of a clear, second, incommensurate frequency (Figure 3.12, Figure 3.13). This at least holds for the range of Reynolds numbers studied here.

7. We obtain an empirical scaling law from our torque measurements, which reads as $Nu_\omega \propto Ta^{0.24}\chi^{c\,0.41}$ (Figure 3.4 and Table 3.2). This is valid for all our measurement points beyond the first appearance of wavy vortices, or for higher-order transitions in our study.

3.6.2. Possible future investigations

Given that the study of inertial instabilities in neutrally buoyant, non-Brownian, particle-laden Taylor-Couette flow is in a relatively nascent phase, a wide variety of questions can still be addressed experimentally in the future. This chapter focused on characterizing flow transitions by evaluating global quantities, such as torque and classifying the flow regimes based on flow visualization. Commonly, changes in global quantities are intimately linked with changes in the microstructure of the flow. This alludes to the need for understanding the microstructure of the flow, which would consist of the velocities of the two phases as well as inhomogeneities in the spatial distribution of the dispersed phase. In fact, advances along this line have recently been made in understanding the internal properties of the flow structures (Ramesh, Bharadwaj, and Alam, 2019), enhanced mixing by particles

(Dherbécourt *et al.*, 2016; Rida *et al.*, 2019) as well as radial migration of particles (Majji and Morris, 2018; Sarabian *et al.*, 2019).

Even though this study aimed at expanding the studied parameter space, there still are several uncharted territories. For example, even higher Reynolds numbers ($Re_{susp} \sim O(10^4)$) can be accessed, in order to assess the effect of particles on the onset of ultimate turbulence. Moreover, rotating the outer cylinder should also be a tantalizing prospect, given that counter-rotating single-phase Taylor-Couette flows are known to have non-axisymmetric modes arising as primary instabilities (Krueger, Gross, and Di Prima, 1966). Torque measurements can also allow for determining 'optimal' conditions, characterized by the ratio between the rotation rates of the two cylinders at which the transport of angular momentum between the cylinders is maximized (van Gils *et al.*, 2012).

On the other hand, state-of-the-art, fully resolved numerical simulation techniques for particle-laden flows (de Motta *et al.*, 2019) can complement measurements by state-of-the-art experimental techniques (Poelma, 2020) and provide a deeper understanding of the underlying physical mechanisms.

Acknowledgements

We would like to thank A. Greidanus for accelerating the start-up of this project as well as J. Graafland, E. Overmars and J. Ruijgrok for their technical assistance with the experiments. Furthermore, we are grateful to W.-P. Breugem, G. Elsinga and W. van de Water for their valuable comments on an earlier version of the chapter.

3.A. Validation in single-phase Taylor-Couette flows

Here, we extensively validate single-phase flow results. The flow generated in the present facility by the motion of the inner cylinder has been validated in the past for single-phase flows, albeit only with the aid of torque measurements in the study by Ravelet, Delfos, and Westerweel (2010). The system has since then been primarily utilized in studies pertaining to highly turbulent flows (thus Reynolds numbers > 10^4), with the exception of Alidai *et al.* (2016) who studied turbulent patches for pure outer cylinder rotation. Since the focus of the current study is on inner-cylinder driven, non-turbulent flow regimes, we validate the single-phase flow regimes in our system, primarily with the aid of flow visualization in Section 3.A.1 and briefly with torque measurements in Section 3.A.2.

3.A.1. Regime classification per flow visualization

As emphasized in the chapter, single-phase flows in the Taylor-Couette geometry have been studied in much detail previously. For the purpose of this study, we classify the flow regimes into two domains: lower order transitions and higher order transitions. The former is associated with flow regimes appearing between laminar Couette flow and the first fully-formed laminar wavy vortices along the circumferential direction, whereas the latter is associated with flow transitions and flow states that appear beyond. A similar

distinction was made by Dutcher and Muller (2009).

Lower order transitions: From Laminar Couette Flow to Wavy Vortex Flow

The lower order transitions are pretty well studied and for single-phase flows, the flow undergoes a transition from purely circular, Couette flow to Wavy Vortex Flow via the regime of Taylor Vortex Flow. We observe this expected behaviour, as exemplified by the images in Figure 3.14.

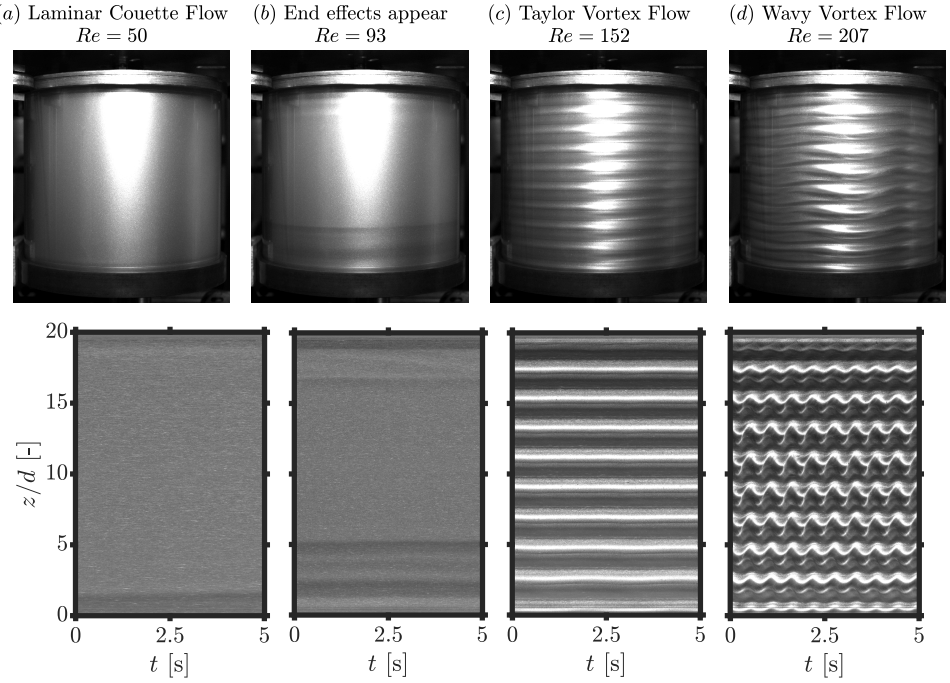

Figure 3.14: Lower order transitions for single-phase flows. (*Top*) Full field-of-view snapshots (inner cylinder rotates from right to left) (*Bottom*) Corresponding space-time plots (*a*) Circular Couette Flow (CCF). (*b*) Appearance of vortices due to Ekman pumping. (*c*) Taylor Vortex Flow (TVF). (*d*) Wavy Vortex Flow (WVF). Examples belong to the ramp-up experiment and the Reynolds numbers are not indicative of critical values for transition.

The flow initially is circular, which is free of any distinct features (Figure 3.14(*a*)), owing to the fact that the flow is purely along the azimuthal direction. Beyond a critical *Re*, we observe the presence of the Taylor Vortex Flow regime (Figure 3.14(*c*)), where the Taylor vortices appear as steady bands. This regime is often preceded by a regime where bulk of the flow is laminar but vortices due to Ekman pumping are prominent at the ends of the setup (Figure 3.14(*b*)). We observe a more persistent presence of these end vortices in the ramp-up experiments as compared to the ramp-down ones.

In the ramp-up (alternatively, ramp-down) experiments, we observe the first (last) appearance of weak/developing Taylor vortices at $Re = 136$ ($Re = 128$), while they first (last)

appear fully developed at $Re = 152$ ($Re = 152$). These are comparable to critical Reynolds numbers predicted by linear stability theory (Di Prima and Swinney, 1985, table 6.2) or other analytic expressions (Esser and Grossmann, 1996, equation 7), $Re \sim 145$ for a similar geometry. The finite step size in our experimental protocol prevents us from finding the exact boundary of the transition between flow regimes, and for now, we take the critical Reynolds number as $Re_c = 142 \pm 12$. With this, we also believe that the finite length of the cylinders do not significantly impact the critical Re at which the Taylor vortices appear, and this postulation is also in line with the findings of Cole (1976), who did not observe an effect of the aspect ratio on the critical Reynolds number ($\eta = 0.914, 1.23 \leq \Gamma \leq 61$). One critical difference between the two protocols is the axial wavelength of the vortices. For the ramp-up experiments, pairs of vortices appear to be separated by a distance of $\approx 2.1d$, which deviates slightly from the theoretically expected value of $\approx 2d$. The slight discrepancy may be attributed to the limited resolution in imaging ($\approx 0.14d$) as well as the influence of the end vortices. In contrast, the ramp-down experiments showed the Taylor vortex flow state to have a higher axial wavelength ($\approx 2.32d$), corresponding to a reduction by one Taylor vortex pair. Another factor that could play a role in our observations is the time needed for the onset (alternatively, decay) of Taylor vortices which are estimated to be $Ld/\nu = 50$ s ($10d^2/\nu = 108$ s for decay) by Czarny and Lueptow (2007), compared with the time we spend at a constant shear rate i.e. 90 s. However, these time scales are more appropriate when the Reynolds number under consideration is extremely close to the critical value, which is not applicable to our results owing to the finite step sizes taken.

The critical Reynolds number for transition between Taylor Vortex Flow and Wavy Vortex Flow is found to be between $172 \leq Re \leq 191$ ($192 \geq Re \geq 171$) for the ramp-up (ramp-down) experiments, which suggests that the flow hysteresis does not have a strong influence on the critical point for this transition. We approximate the critical Reynolds number for this transition to be around $Re = 181.5 \pm 10.5$ or $Re/Re_c = 1.28 \pm 0.07$. This is slightly higher than the value of $Re/Re_c = 1.17 \pm 0.02$ reported by Dutcher and Muller (2009) for their system ($\eta = 0.912, \Gamma = 60.7$). This discrepancy may be attributed to the the lower aspect ratio in the current facility. Cole (1976) showed that a reduction in the aspect ratio led to an increase in the critical Reynolds number for the transition between Taylor Vortex Flow and Wavy Vortex Flow, due to the damping provided by the ends (Jones, 1985).

Higher order transitions: From Laminar Wavy Vortices to Turbulent Taylor Vortices

The higher order transitions in single-phase Taylor-Couette flow are also well established and we adopt the conventions of Dutcher and Muller (2009) as the basis for our classification. The following flow regimes are identified on the basis of the temporal spectrum: Wavy Vortex Flow, when the spectrum shows a single, distinctly identifiable peak; Modulated Wavy Vortex Flow, when the spectrum shows multiple, incommensurate, distinctly identifiable peaks in the spectrum; Chaotic Wavy Vortex flow, when the spectrum also has multiple peaks and the flow also shows small-scale structures; Wavy Turbulent Vortex Flow, when the flow appears to have small-scale structures but the spectrum has a single, dominant peak, and; Turbulent Taylor Vortex Flow, when the Taylor vortices appear to be completely turbulent and the spectrum has no distinct peaks. The Chaotic Wavy

Vortex Flow regime has also been referred to as "weakly turbulent" (Fenstermacher, Swinney, and Gollub, 1979) and "Turbulent modulated wavy vortices" (Lueptow, Docter, and Min, 1992).

Examples of the different flow regimes and their corresponding spectra can be seen in Figure 3.15. The primary tool we employ is a simple spectral analysis along the time-axis of the space-time plots. The spectra along each axial location are averaged to return a single spectrum. The averaging is not expected to be detrimental as fundamental frequencies have been found to be independent of the axial location (Fenstermacher, Swinney, and Gollub, 1979), even though this might not hold true for the amplitudes (see Figure 3.14(d), for example). Peaks in the spectra are identified as follows: All points at least ten median average deviations away from the median of the spectrum are marked as "potential peaks". Hereafter, only the "potential peaks" that are local maxima in the neighbourhood of five points are retained as true peaks. The frequencies in the spectra are normalized by the rotational frequency of the inner cylinder (f_i). Thus, all peaks close to $f/f_i = 1$ may be associated with the system itself (Dutcher and Muller, 2009). We do not perform an extremely detailed, quantitative analysis of the spectra (for example, identifying the significance of different peaks, and identifying all the linear combinations), as it is not trivial (as evidenced by Gorman, Reith, and Swinney, 1980; Takeda *et al.*, 1993, in table 3 and figure 2 respectively) while also going beyond the scope of the current study.

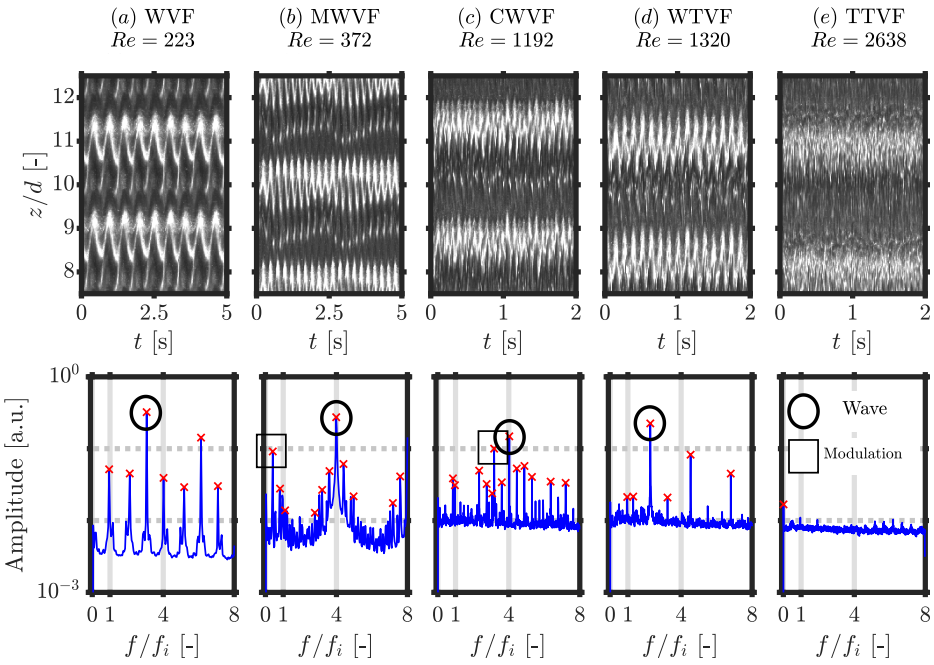

Figure 3.15: Higher order transitions for single-phase flows. (*Top*) Detailed portions of space-time plots. (*Bottom*) Corresponding amplitude spectra. (*a*) Wavy Vortex Flow (WVF) regime. (*b*) Modulated Wavy Vortex Flow (MWVF) regime. (*c*) Chaotic Wavy Vortex Flow (CWVF) regime (*d*) Wavy Turbulent Vortex flow (WTVF) regime (*e*) Turbulent Taylor Vortex Flow (TTVF) regime. The examples here belong to the ramp-up experiment.

While a similar spectral analysis can also be performed along the space-axis to yield axial wavenumbers, we restrict our discussion from the perspective of (de)generation of vortex pairs (also referred to as vortex pinching/splitting processes by King and Swinney (1983)). Given that our system has two fixed end plates, which fix the boundary conditions for the flow, the (de)generation of vortices in the axial direction only occurs in pairs. Azimuthal wavenumbers can be estimated with the help of full field-of-view snapshots, with the knowledge that only integer number of waves may be present along the circumference, as well as the ansatz that wave speeds do not change significantly upon a small variation in the Reynolds number (see King *et al.*, 1984, figure 7).

A comprehensive summary of the flow regimes for our experiments is shown in Figure 3.16. The maximum Reynolds numbers achieved are $Re/Re_c = 18.58$ and 15.42 for the ramp-up and ramp-down protocols respectively. In general, it can be seen that the flow states achieved in the two protocols are not the same, implying the presence of hysteresis for the higher order transitions. We only address the key points here in the text.

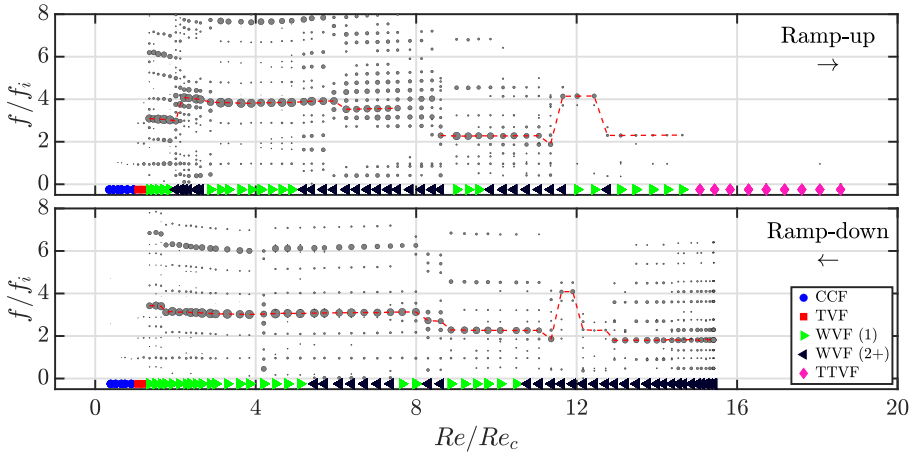

Figure 3.16: Compilation of frequency spectra for single-phase flows. The size of the markers are proportional to their amplitude in the spectrum. The coloured markers at the bottom correspond to the flow regimes shown in Figure 3.3 of the chapter. In the legend, WVF (1) and WVF (2+) refer to periodic (single, distinct peak in spectrum) and quasi-periodic (at least two, distinct, incommensurate peaks in spectrum) Wavy vortex flows respectively.

For the ramp-up experiments, the first appearance of Wavy Vortex Flow is characterized by the presence of six azimuthal waves and nine vortex pairs. Even though the first non-axisymmetric mode should ideally have one azimuthal wave, and progressively rise, we do not observe it due to our finite step sizes. For example, Krueger, Gross, and Di Prima (1966) theoretically show for $\eta \to 1$ that the flow goes from Taylor vortex flow to Wavy vortex flow with five waves by $Re \approx 1.05 Re_c$. The amplitude of these waves progressively increase with increasing Reynolds numbers (especially in the bulk), and the flow eventually appears to be in a mixed-mode state ($Re/Re_c = 2.01$). The mixed-mode state appears to be similar to the observations of Donnelly *et al.* (1980) "irregularities in the roll and wavy structure" and King and Swinney (1983) "distorted wave patterns". The

mixed-mode manifests itself in the spectrum by the appearance of a peak corresponding to the azimuthal state with nine waves, which also happens to be a feature of the next flow state ($2.12 \leq Re/Re_c \leq 2.22$). At $Re/Re_c = 2.12$, a vortex pinching process is simultaneously incepted and is completed at $Re/Re_c = 2.22$. This pinching process is visible in the space-time plots as spiral defects/dislocations (not shown).

For $2.22 \leq Re/Re_c \leq 2.62$, we observe a distinct low-frequency component in the spectrum ($f/f_i < 1$), which Dutcher and Muller (2009) refer to as an "early-modulated wavy flow" region. While they mention that such modulations were never reported for flows with a static outer cylinder, these low-frequency components appear to be very similar to "transient mode" identified by Fenstermacher, Swinney, and Gollub (1979). We nevertheless stick with the convention of Dutcher and Muller (2009) and classify it as a modulated wavy vortex flow (see Figure 3.15(*b*)). The range of Reynolds numbers over which this regime is observed by us is much narrower than that of Dutcher and Muller (2009) ($1.43 \leq Re/Re_c \leq 3.56$), and we speculate that it could be attributed to the shorter aspect ratio of our system.

At $Re/Re_c = 2.87$, yet another vortex pair degenerates, and the low-frequency component disappears from the spectrum as well. The spectrum has a single, dominant frequency between $2.87 \leq Re/Re_c \leq 4.90$, and we classify it as a Wavy Vortex Flow. This second appearance of the Wavy Vortex Flow was also observed by Dutcher and Muller (2009) ($3.56 \leq Re/Re_c \leq 5.20$), and implicitly by Fenstermacher, Swinney, and Gollub (1979). Between $5.20 \leq Re/Re_c \leq 5.68$, a second frequency component ($f/f_i > 1$) appears, what we classify as a Modulated Wavy Vortex Flow. Dutcher and Muller (2009) too observe this regime with $f/f_i > 1$. Hereafter, the region of $5.95 \leq Re/Re_c \leq 8.61$ is characterized by the presence of a spectrum with multiple peaks and making a clear classification cannot be done until a systematic distinction between the significance of the different peaks is performed. However, we do observe that beyond $Re/Re_c = 7.85$, the flow appears to have a visible presence of small-scale structures and the flow may then be considered to be in the Chaotic Wavy Vortex Flow regime (see Figure 3.15(*c*)).

At $Re/Re_c = 9.00$, we observe the Wavy Turbulent Vortex Flow (compared to $Re/Re_c = 7.85$ reported by Dutcher and Muller (2009)), which is characterized by the presence of a single, dominant peak in the spectrum, while the flow displays small-scale structures. The 'turbulence' is also evident in the noise floor of the amplitude spectrum (see Figure 3.15(*d*)). Between $11.06 \leq Re/Re_c \leq 11.35$, a shift in the azimuthal state occurs via a spectral cascade. However, between $11.66 \leq Re/Re_c \leq 12.44$, a peculiar shift in the temporal frequencies is observed. The frequency peak corresponding to the Wavy Turbulent Vortex Flow disappears suddenly, and is replaced by a high frequency component ($f/f_i > 4$). At first sight, this regime seems to qualitatively resemble the 'Fast Azimuthal Wave' (Walden and Donnelly, 1979; Takeda, 1999). However, a key difference is that the fast azimuthal wave appears only once the Turbulent Taylor Vortex Flow has set in, usually $Re/Re_c \geq 23$ (Takeda, 1999). The Wavy Turbulent Vortex Flow then returns for $12.77 \leq Re/Re_c \leq 14.63$, before giving way to Turbulent Taylor Vortex Flow for $15.07 \leq Re/Re_c \leq 18.58$ with an axial wavelength of $\approx 2.78d$. Dutcher and Muller (2009) report the onset of Turbulent Taylor Vortex flow at $Re/Re_c = 15.4$. It must be noted that Dutcher and Muller (2009) also report the appearance and subsequent disappearance of second temporal frequencies beyond the wavy Turbulent vortex Flow. Such an ob-

servation is indicative of the fact that the exact nature of higher order transitions is not necessarily set in stone, and the analysis may thus be subjective.

The ramp-down experiments evidently show a different behaviour (see Figure 3.16). One key observation is that we do not access the Turbulent Taylor Vortex Flow regime. Possible reasons for this may include: we accessed relatively lower Reynolds numbers owing to higher temperatures, and the high acceleration rate to reach the highest shear rate may delay the critical Reynolds number (see Dutcher and Muller, 2009). Instead, at the highest Reynolds number of $Re/Re_c = 15.41$, we observe a Wavy state with at least two incommensurate frequencies. Since the flow also shows distinct small-scale features, we classify it as a Chaotic Wavy Vortex Flow regime. This behaviour continues for the range $15.41 \geq Re/Re_c \geq 12.94$ with the exception of $Re/Re_c = 13.21$, where the frequency of the second wave appears to be different. A vortex pair disappears at $Re/Re_c = 12.72$ and between $12.72 \geq Re/Re_c \geq 12.16$, the nature of the flow remains Chaotic Wavy, but where the frequencies involved are markedly different, with drastically reduced amplitudes in the spectrum. This then gives way to a regime ($11.90 \geq Re/Re_c \geq 11.62$) resembling the 'Fast Azimuthal Wave' ($f/f_i > 4$) that was also observed in the ramp-up experiments.

Between $11.36 \geq Re/Re_c \geq 7.99$, the flow goes from Chaotic Wavy Vortex Flow to a Modulated Wavy Vortex Flow state via a couple of transitions in the azimuthal state ($11.36 \geq Re/Re_c \geq 11.06$ and $8.87 \geq Re/Re_c \geq 7.99$). The Modulated Wavy Vortex Flow between $7.65 \geq Re/Re_c \geq 5.46$ is characterized by a very low-frequency component. Hereafter, the Wavy Vortex Flow is recovered for the region $5.11 \geq Re/Re_c \geq 1.76$, accompanied by the destruction of a vortex pair at $Re/Re_c = 4.20$. Between $1.76 \geq Re/Re_c \geq 1.64$, the Wavy Vortex Flow gains a vortex pair and is the final higher order transition.

In summary, on the basis of our ramp-up experiments, we can confidently claim that our Taylor-Couette system can reproduce flow states corresponding to higher order transitions, in agreement with those reported in literature. The results of the ramp-down experiments (in comparison to the ramp-up experiments), unsurprisingly, hint at the non-uniqueness of the flow states attained at a given Reynolds number, even from a purely topological perspective. This is unsurprising, in light of the seminal work of Coles (1965).

3.A.2. Torque data

Torque measurements provide insight into the global behaviour of the flow, since it refers to an integral quantity. For the range of Reynolds numbers considered in this study, the primary insights attainable from the torque measurements are the critical Reynolds number where the flow veers away from purely azimuthal flow. For a purely azimuthal flow, an analytical solution may be easily derived relating the skin friction coefficient and the Reynolds number as $c_{f,\text{lam}} = \frac{4}{\eta(1+\eta)}/Re$ (derivations available in Wendt, 1933; Koeltzsch *et al.*, 2003).

In Figure 3.17(*a*), the reduced skin friction coefficient ($c_f/c_{f,\text{laminar,analytical}} - 1$) is plotted against the normalized Reynolds number. The deviation of the skin friction coefficient from its laminar value can also be used an indicator of the onset of Taylor vortices. Without any prior knowledge of the flow regime, one might over-predict Re_c by about 20%. This can be inferred by selecting the Re above which there is a monotonic rise in the reduced skin friction coefficient. Possible reasons for this over-prediction include the

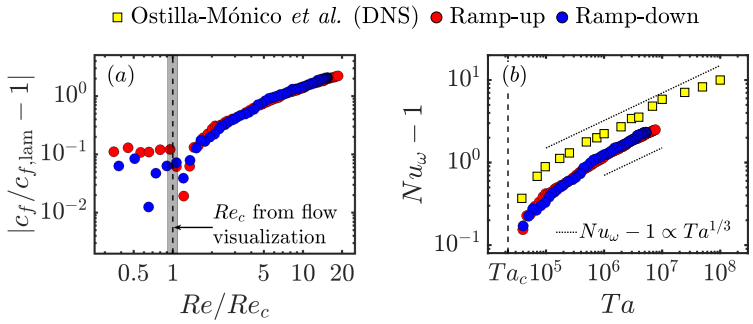

Figure 3.17: Torque measurements for both protocols are compared against numerical simulations (data from Ostilla-Mónico *et al.*, 2014, figure 4(*a*), $\eta = 0.909$). (*a*) Reduced skin friction coefficient versus reduced Reynolds number. (*b*) $Nu_\omega - 1$ versus Ta.

finite step sizes in the shear rates, as well as the measured torque values being close to the absolute resolution of the system (0.01 Nm). For this reason, the reduced skin friction coefficient does not converge to zero for $Re/Re_c < 1$ either.

To check the fidelity of the torque measurements for higher Reynolds numbers, we compare our results against those obtained in the direct numerical simulations of Ostilla-Mónico *et al.* (2014), albeit with $\eta = 0.909, \Gamma = 2\pi$. A clear difference is visible in the comparison of $Nu_\omega - 1$ versus Ta, in terms of the absolute values, but the profile shapes appear to be very similar. The differences in the absolute values may be attributed to differing boundary conditions (the numerical simulations do not simulate end plates), as well as the difference in axial wavelengths of the Taylor rolls. For the numerical work, it has been shown that up to 20% variation in Nu_ω can be observed by changing the axial wavelength of the Taylor vortices, especially at low Ta (Ostilla *et al.*, 2013, their section 3.4). Moreover, for $Re > 400$, the global scaling behaviour of $G \propto Re^{1.47}$ (alternatively, $G \propto Re^{1.49}$) was seen for the ramp-up (ramp-down) experiments. The scaling exponents are in close agreement with the exponent of 1.5 available in the empirical correlations of Wendt (1933). The value of 1.5 is attributed to the dominance of boundary layer and hairpin contributions (Eckhardt, Grossmann, and Lohse, 2007). In summary, our results suggest that our torque measurements are reliable for commenting on global scaling behaviours.

3.B. Simultaneous Ultrasound Imaging Velocimetry (UIV) and Flow Visualization in Taylor-Couette flows: Validation of UIV in single-phase flows

Ultrasound Imaging Velocimetry (UIV) is applied to a Taylor-Couette flow, for the case of pure inner cylinder rotation. By imaging a radial-azimuthal plane, two velocity components are obtained simultaneously in a two-dimensional plane. For the single-phase flow studies, Iriodin flakes (commonly used for visualizing flow structures) are used as "flow

tracers" for the backscatter of ultrasound. This allows for a simultaneous mapping of the flow regime, via flow visualization, as well as extracting quantitative velocity information in the radial gap. After validating UIV against the analytically well-defined laminar Circular Couette flow as well as turbulent Taylor-Couette flow, other regimes are probed as well, in particular, the Wavy Vortex flow. Finally, the application of UIV to a particle-laden Taylor-Couette flow (particle volume fraction, $\phi \sim 0.01$) is considered, under the conditions of oscillatory pure inner cylinder rotation. The results presented here serve as a proof-of-concept for the application of UIV to the Taylor-Couette flow and will be applied to denser particle-laden flows ($\phi \sim 0.05$) in the future.

3.B.1. Flow regimes in Taylor-Couette: Pure inner cylinder rotation

The Taylor-Couette flow is a canonical flow system that has been widely studied over the last century. It is a simple system where the fluid is contained between two co-axial, independently rotating cylinders, a schematic interpretation of which is shown in Figure 3.18. This simple, yet well-defined flow geometry facilitates the investigation of instabilities, non-linear dynamics and spatiotemporal chaos, pattern formation and turbulence (Grossmann, Lohse, and Sun (2016)).

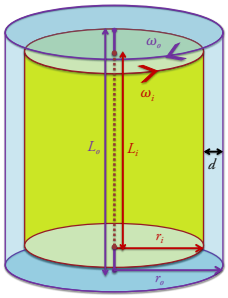

Figure 3.18: Schematic interpretation of the Taylor-Couette geometry

Early work, such as the famous study by Taylor (1923), established the transition of Circular Couette Flow (pure azimuthal motion of fluid) to axisymmetric Taylor Vortex Flow. Since then several studies have built up and established knowledge and features of the several flow regimes that exist owing to the multiple instabilities (Coles (1965), Fenstermacher, Swinney, and Gollub (1979), Gorman and Swinney (1982), King *et al.* (1984), Marcus (1984)). Andereck, Liu, and Swinney (1986) summarized the different flow regimes that can be observed in the case of a pure inner cylinder rotation as: Circular Couette Flow (CCF) → Taylor Vortex Flow (TVF) → Wavy Vortex Flow (WVF) → Modulated Wavy Vortex Flow (MWVF) → Turbulent Taylor Vortex Flow (TTVF).

Regime classification in single-phase Taylor-Couette flows is often performed by means of adding foreign elements into the working fluid, for example Kalliroscope, pearlescent pigments or rheoscopic fluids (Borrero-Echeverry, Crowley, and Riddick (2018)). These elements allow for a clear visualization of the topology of the flow structures. However,

the amount of quantitative information extractable from snapshots of such flows is usually limited to characteristics of the flow features (for example, wavelengths, wave frequencies, structure orientation etc.). Over the course of time, hot wire/film anemometry (Smith and Townsend (1982), Lewis and Swinney (1999)), Laser Doppler Anemometry (Fenstermacher, Swinney, and Gollub (1979), Burin, Schartman, and Ji (2010)) as well as Particle Image Velocimetry (Tokgoz *et al.* (2012), Huisman *et al.* (2013)) have been deployed to study the velocity profiles in single-phase Taylor-Couette flow.

The aforementioned experimental techniques have matured and are very suitable for studying highly turbulent single-phase flows. However, applying these optical techniques to non-dilute particle-laden flows ($\phi > 0.01$) can already be complicated due to data drop-out (Deen, Westerweel, and Delnoij (2002), Poelma, Westerweel, and Ooms (2006)). Refractive Index Matching is a potential solution and it even allows the investigation of extremely dense suspensions (Wiederseiner (2010)). However, a major limitation of this technique is the additional constraint imposed on the particle-fluid combination, disallowing the study of systems in their natural state.

Ultrasound based velocimetry is an alternative technique that can be applied to study, both, single-phase as well as particle-laden flows. This modality appears in various variants, such as Ultrasound Doppler Velocimetry (Takeda (1986)), Ultrasonic Speckle Velocimetry (Manneville, Bécu, and Colin (2004)) and Ultrasound Imaging Velocimetry (Poelma (2017)).

Of the above three variants, Ultrasound Doppler Velocimetry was developed the earliest and provides possibilities to record a single component of velocity along a single line. Similarly, Ultrasound Speckle Velocimetry can extract a single component of velocity on a two-dimensional plane, following a calibration. For rheometric applications, for which USV was originally developed, a single velocity component is usually sufficient. Ultrasound Imaging Velocimetry (UIV), also known as "echo-PIV", applies the principles of Particle Image Velocimetry (PIV) to ultrasound images. An advantage of UIV over its other ultrasonic velocimetry counterparts is that it offers potential to measure two components of velocity simultaneously on a two-dimensional plane, and can also derive turbulence statistics (Gurung *et al.* (2016)). It should be noted that UIV does not require a calibration procedure, except for an accurate estimate for the speed of sound in the medium.

In this study, we initially revisit the classical single-phase Taylor-Couette flow, under the conditions of pure inner cylinder rotation, by combining simultaneous measurements via UIV and flow visualization. After validating the laminar velocity profile in the Circular Couette Flow regime as well as Turbulent Taylor Couette flow, UIV is combined with flow visualization to study the dominant peak frequencies occurring in the Wavy Vortex Flow regime. Finally, as a proof-of-concept, we apply UIV to a particle-laden Taylor-Couette flow (particle volume fraction, $\phi \sim 0.01$), wherein the inner cylinder undergoes a sinusoidal motion. In the future, UIV will be applied to dense particle-laden flows (particle volume fraction, $\phi \sim 0.05$), along with simultaneous flow visualization and torque measurements.

3.B.2. Experimental apparatus

Three major components were involved in the experiments: the Taylor-Couette system, the apparatus to perform UIV and the apparatus to perform flow visualization. Each of these components is described in the following subsections.

Taylor-Couette geometry

The geometry of the Taylor-Couette system used in the current experiments is summarized in Table 3.3. The aspect ratio of the setup is 21.67, which is considered to be high and allows for the reduction of end-effects (disturbances induced by secondary flows created by the von-Kárman gaps between the end-plates of the inner and outer cylinder). The two cylinders can be rotated independently via two Maxon DC motors. Each cylinder can rotate up to a maximum of 10 Hz with a resolution of 0.01 Hz. A torque meter (HBM T20WN, 2Nm) is used to record the torque at a sampling rate of 2 kHz. Further details of the setup can also be found in Tokgöz (2014).

Table 3.3: Specifications of the Taylor-Couette geometry for the current experiments.

Specification	Measure [units]
Inner cylinder radius (r_i)	0.11 [m]
Outer cylinder radius (r_o)	0.12 [m]
Gap width ($d = r_o - r_i$)	0.01 [m]
Radius ratio ($\eta = r_o/r_i$)	0.917 [-]
Inner cylinder length (L_i)	0.2167 [m]
Outer cylinder length (L_o)	0.2221 [m]
Aspect ratio ($\Gamma = L_i/d$)	21.67 [-]

Ultrasound Imaging

Ultrasound imaging is performed via a SonixTOUCH Research (Ultrasonix/BK Ultrasound) system coupled with a linear array transducer (L14-5/38). The array has 128 elements that span ~3.9 cm. The imaging depth is maintained at 2 cm, allowing for a frame rate (rate at which ultrasound images are recorded) of 130 Hz. Higher frame rates, up to 400 Hz, can be obtained by reducing the imaging width/sector (lateral field-of-view) as well as reducing the line density (i.e. resolution in the lateral direction). The emitted ultrasonic pulse has a central frequency of 10 MHz and is one cycle long, while the received echo is sampled at a frequency of 40 MHz. The central frequency and the pulse cycle length determine the axial resolution of the image ($\mathcal{O}$(0.1 mm)) while the sampling

frequency (along with the speed of sound in the imaged medium) determines the axial spacing in the image ($\mathcal{O}(10\,\mu m)$). This implies that the image can be downsampled/decimated in the axial direction without loss of relevant information. Raw RF signals were acquired and processed externally. In order to visualize the single-phase flow, Iriodin flakes are used as scatterers of sound, whereas the particles in the particle-laden flow act as scatterers in the two-phase flow measurements.

Flow visualization

To visualize the flow structures in an aqueous glycerol solution (56% v/v), Iriodin 100 silver pearl (Merck KGaA, Darmstadt, Germany) was added 0.1% by mass. The combination of an LaVision Imager s-CMOS camera and a Nikkon 105mm f/2.8 FX AF MICRO-NIKKOR 105 mm lens ($f_\# = 5.6$) is used at a fixed imaging rate of 32.5 Hz, with the camera focussed at the surface of the outer cylinder. Illumination is provided by means of a halogen lamp mounted above the camera. The field-of-view is a window of 10.2 × 12.08 cm^2 (axial × lateral) with the resolution in the axial direction of 21 pixels/mm. The field-of-view is located sufficiently in the centre along the axial direction in order to minimize the end effects due to the von-Karman gaps, formed between the end plates of the inner and outer cylinder (Greidanus *et al.* (2015)).

3.B.3. Data processing

Three types of measurements are performed on the Taylor-Couette flow: measurement of the torque required to maintain the desired rotation speed of the inner cylinder, ultrasound imaging for UIV and recording images to identify the flow regime. Results from only the latter two are presented in this paper. The procedure for processing the data is explained in brief in the following subsections.

UIV

The recorded ultrasound images were downsampled in the axial direction by a factor of four in order to reduce the inherent resolution mismatch in the imaging plane (the lateral resolution is an order of magnitude worse). This results in an image of size 228 × 128 pixels. A temporal high-pass filter is used to reduce reflections near the walls of the cylinders (Sciacchitano and Scarano (2014)). For time-averaged information, correlation-averaging multi-pass PIV is performed, with a final window size of 8 × 16 pixels with 50% overlap between the windows. The resulting spatial resolution of the velocity vectors is thus 0.7 × 4.8 mm^2. The normalized median test (Westerweel and Scarano (2005)) is used for removing outliers in space, followed by a correction to compensate for beam sweep effects (Zhou *et al.* (2013)). To study transient flows, a sliding moving average over 10 frames is used, resulting in effective temporal resolutions as low as 25 ms.

Flow visualization

Space-time plots are generated by stacking the scattered light intensities profiles along the centre of the image in time. Due to a skewed illumination, an intensity normalization

correction is performed along the axial direction following which power spectra are then extracted from these space-time plots. The spectra are especially useful in determining the characteristic frequencies in the Wavy Taylor Vortex Flows.

3.B.4. Application of UIV to single-phase Taylor-Couette flows

Before applying UIV to particle-laden flows, it is applied to single-phase flows, which has been studied rigorously over the past decades. As a first step, the fidelity of UIV is checked on laminar Circular Couette flow as well as the Turbulent Taylor Couette flow. Hereafter, it is applied to a well defined flow regime, the Wavy Taylor Vortex regime. Here, results from UIV are also compared with those from flow visualization.

Validation: Circular Couette Flow

UIV is first applied to a low-speed laminar flow. For the Taylor-Couette system, the Couette flow velocity profile is analytically defined (Koschmieder (1993)). For pure inner cylinder rotation, the azimuthal velocity can be expressed as per Equation (3.1). The other velocity components (axial and radial) are expected to be zero.

$$v_\theta(r) = \left(\frac{\omega_i r_i}{1-\eta^2}\right)\left(\frac{r_i}{r} - \eta^2 \frac{r}{r_i}\right) \tag{3.1}$$

The results obtained by UIV on a laminar flow are shown in Figure 3.19. The inner cylinder had a rotation speed of approximately 7.6 cm/s leading to the inner cylinder Reynolds number ($Re_i = \frac{\omega_i r_i d}{\nu}$) of about 63. In Figure 3.19(a), the time-averaged velocity vectors are displayed, which are typical of a smooth, laminar, purely azimuthal flow. Two coordinate axes are shown: one based on the imaging plane (origin at one end of the ultrasound transducer), and the other based on the center of the Taylor-Couette system (i.e. cylindrical coordinates). It can be qualitatively seen that the vectors near the location $x_{cylinder} = 0$ are of better quality than those at the edges. Thus, for a quantitative analysis, vectors in a small sector near this area are considered.

The mean azimuthal and radial velocities for this flow are shown in Figure 3.19(b). The measured azimuthal velocities are in good agreement with the expected analytical profile until $(r - r_i)/d > 0.15$. Closer to the inner cylinder, velocities are miscalculated due to curvature effects, and also relatively higher particle displacements. The PIV grid is rectangular, and near the cylinder walls, part of the interrogation window lies outside the system. This leads to an underestimation of the particle displacements, and thus the velocities. A possible solution is performing cross-correlation on a conformal grid (Nguyen *et al.* (2010), Park *et al.* (2015)). Maximum mean radial velocities of up to 1% of the inner cylinder velocity are observed even though these are expected to be zero. This is an indication of the maximum accuracy of the technique with respect to the mean radial velocities.

The instantaneous azimuthal and radial velocities were also computed for this flow, which allowed the calculation of their respective standard deviations, plotted in Figure 3.19(c). For a pure laminar flow, these quantities should be zero. However, this is not observed and the deviations serve as an indicator for the maximum accuracy of the technique for

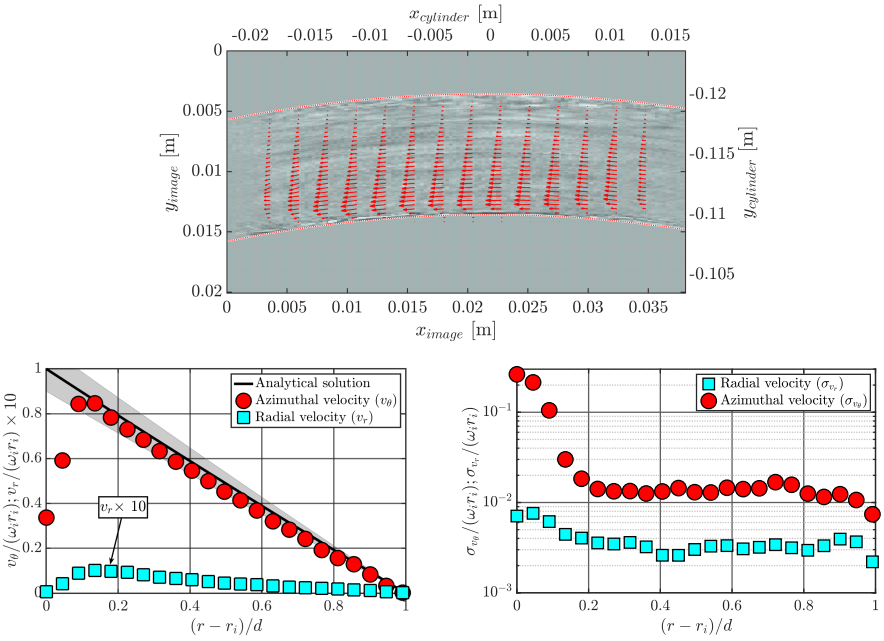

Figure 3.19: Velocities obtained in a laminar Circular Couette Flow at $Re_i \sim 63$. (a) Time-averaged velocity vectors. The dotted red lines indicate the cylinder walls. (b) Mean azimuthal and radial velocities (normalized by the inner cylinder velocity). Note that absolute values have been plotted. Solid black line represents the analytical solution whereas the patch is ±10% deviation from the analytical solution. (c) Standard deviation of the azimuthal and radial velocities (normalized by the inner cylinder velocity). Note that the statistics corresponding to the radial velocity components are multiplied by a factor of ten for better visualization.

temporally varying flows. Variations up to 2% and 0.5% of the inner cylinder velocity are observed for the azimuthal and radial velocity components in the bulk of the flow. A possible reason for this might be the disparity in the spatial resolution in the two directions. This also implies that the fluctuations of the radial velocity component would be a better indicator for the level of turbulence in the flow.

Validation: Turbulent Taylor Couette Flow

Following the study of the laminar Circular Couette Flow, other flow regimes obtainable at higher Re_i are considered. Higher Reynolds numbers are obtained here by increasing the speed of the inner cylinder rotation, as well as reducing the viscosity of the working fluid. It is known that UIV performed on images acquired by traditional beamforming can typically resolve velocities up to 0.8 m/s (Poelma (2017)). Thus, one might anticipate that this would impose an upper bound on the maximum resolvable azimuthal velocities. However, it is also known that in non-laminar flows, a relative flattened profile for the azimuthal velocity is obtained in the bulk, and is typically ~50% of the inner cylinder velocity (Wereley and Lueptow (1994)). This fact allows for studying flows driven by even higher inner cylinder velocities, at least in the bulk.

For validation at higher velocity ranges, as well as a higher Reynolds number, a measurement was performed in a flow where the inner cylinder was rotated at a speed of 1.46 m/s resulting in $Re_i = 1.46 \times 10^4$. The azimuthal velocities are compared with those measured by Ravelet, Delfos, and Westerweel (2010) in the same facility using Stereoscopic PIV at a flow with a comparable Reynolds number ($Re_i = 1.4 \times 10^4$).

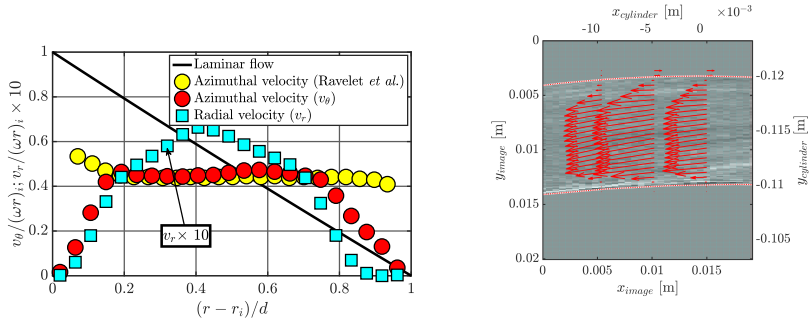

Figure 3.20: Velocities obtained in a turbulent Taylor Couette Flow at $Re_i \sim 1.4 \times 10^4$. Current results are compared with the PIV measurements of Ravelet, Delfos, and Westerweel (2010). Note that the statistics corresponding to the radial velocity components are multiplied by a factor of ten for better visualization. (a) Mean azimuthal and radial velocities (normalized by the inner cylinder velocity). Note that absolute values have been plotted. (b) Time-averaged velocity vectors. The dotted red lines indicate the cylinder walls.

It can be seen in Figure 3.20(a) that there is a good agreement between the two measurements of azimuthal velocities in the central region ($0.2 \leq (r - r_i)/d \leq 0.75$). However, there is a significant deviation in the regions closer to the cylinder walls. There are a few possible reasons for this. The PIV results have been averaged over an axial distance, as compared to the UIV results which correspond to a local axial location. This also means that the current UIV measurements are sensitive to the axial placement of the transducer with respect to a single Taylor roll as well as the Reynolds number of the flow. The Taylor rolls may change their location with changing Reynolds numbers and thus, it would be cumbersome to place the transducer consistently at the center, inflow or outflow of a Taylor roll. For example, the time-averaged velocity vectors in Figure 3.20(b) indicate that the transducer is located relatively closer to an inlet of the Taylor roll (due to the inward motion of the fluid). The measured radial velocity component profile is qualitatively typical of profiles measured in other studies, albeit with differing flow geometries (Bilson and Bremhorst (2007)).

Comparison with Flow Visualization: Wavy Taylor Vortex Flow

Next, we compare results from UIV as well as flow visualization, whose measurements were performed simultaneously. We focus on the Wavy Taylor Vortex Flow regime which is characterized by waves travelling in the azimuthal direction. Power spectra of the light intensity (recorded at a fixed axial location via flow visualization) and radial velocity fluctuations (measured via UIV) are computed. In the wavy vortex flow regime, a distinct peak (f_{peak}) is present in the power spectra, which corresponds to the periodicity of the

travelling waves (Fenstermacher, Swinney, and Gollub (1979)). These peak frequencies (normalized by the rotational frequency of the inner cylinder, f_i) measured by the two techniques are then compared for varying inner cylinder Reynolds numbers.

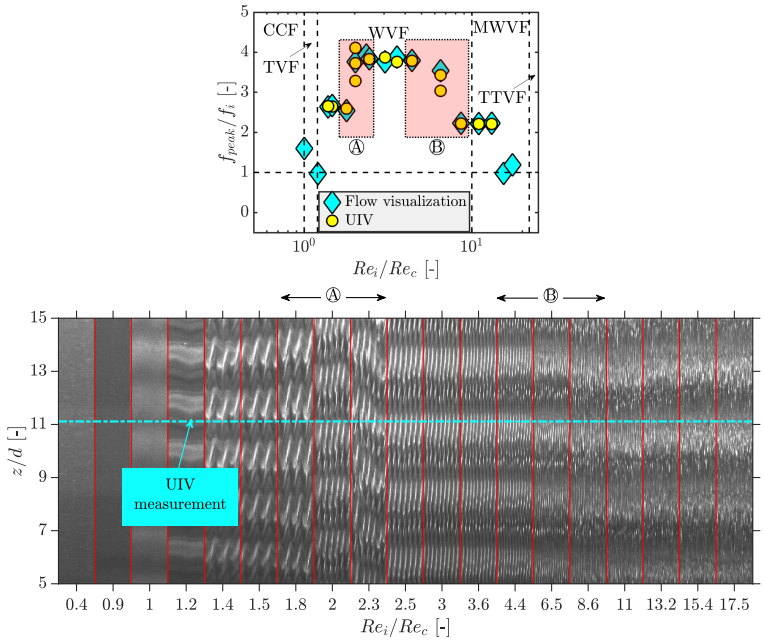

Figure 3.21: Transition within the Wavy Vortex Flow regime as captured by flow visualization and UIV. (a) Comparison of the peak frequencies measured by the two techniques. Regime demarcation is based on the measurements of Fenstermacher, Swinney, and Gollub (1979). (b) Space-time plots of the scattered light intensity for various Reynolds numbers.

This comparison can be seen in Figure 3.21(a). Shown also are demarcation of flow regimes observed by Fenstermacher, Swinney, and Gollub (1979) in their measurements, albeit for a system with $\eta = 0.877$. The critical Reynolds number Re_c is the Reynolds number at which the first instability occurs (CCF → TVF), which in the current case is ≈ 134, as seen by flow visualization. This is 8% lower than the analytically predicted value by Esser and Grossmann (1996). Both measurement techniques reveal a similar behaviour of the peak frequencies. A sudden shift in the plateau for f_{peak}/f_i can be seen around $Re_i/Re_c \sim 2$ and ~ 6.5 (denoted by Ⓐ and Ⓑ respectively in Figure 3.21(b)). The first transition Ⓐ represents a shift in the spatial state of the system, in the axial direction, i.e. there is an increase in the number of Taylor rolls in the axial direction. The second transition Ⓑ possibly represents the scenario in which there is a change in the number of waves along the azimuthal direction. Both measurement techniques provide similar results, which is in accordance with Gorman, Reith, and Swinney (1980) who showed that different methods of probing resulted in similar power spectra. Currently, we have not detected a secondary peak in out power spectra that would be expected in the MWVF regime. This will be looked into in more detail in future studies.

3.B.5. Application of UIV to particle-laden Taylor-Couette flow

Finally, we apply UIV to a particle-laden Taylor-Couette flow in which Polystyrene spheres (diameter ~ 530 ± 75 μm, specific gravity ~ 1.04) were added to an aqueous Glycerol solution (specific gravity ~ 1.23) to form a suspension with a volume fraction of 1%. UIV has previously been successfully applied to such particle-laden flows (Gurung and Poelma, 2016; Hogendoorn and Poelma, 2018). In the suspension studied here, a significant effect of buoyancy is expected on the particles, leading to an expected rise velocity of approximately 0.43 mm/s. This rise velocity, however, is not expected to cause a significant out-of-plane motion of particles between two consecutive frames. The focus of the current measurements is to check the fidelity of UIV by measuring the azimuthal velocity.

The inner cylinder is oscillated, while the outer cylinder is kept fixed. This leads to an inner cylinder velocity profile $U_i(t) = U_{base} + U_{ampl} \cdot \sin(\frac{2\pi t}{T})$. The inner cylinder velocity (U_i) is defined by a base velocity (U_{base}), an amplitude (U_{ampl}) and a time period (T). For the current case, we consider the case with $T = 3s$ and $U_{base} = U_{ampl} = 0.17m/s$. The instantaneous Reynolds numbers thus vary between 15 ± 15, which implies under single-phase flow conditions the flow would always remain laminar for which an analytical solution for the azimuthal velocity profile can be calculated (Verschoof *et al.* (2018)). This flow is thus more challenging to measure than a pure Circular Couette Flow, and at the same time has a well-defined theoretical velocity profile. This is in contrast with flows with Taylor vortices, where a clear quantitative reference for the velocities is not easily available.

For the current studies, the Womersley number (ratio between the unsteady inertial forces and viscous forces), $Wo \sim \mathcal{O}(1)$. Under these conditions, it is expected that the working fluid perfectly follows the modulations created by the inner cylinder (Verschoof *et al.* (2018)). Since the particle Stokes number $\ll 0.1$ (characteristic time scale of fluid $\sim d/U_{base}$, since the flow is laminar), it can also be expected that the particles more or less respond to the accelerations/decelerations of the fluid. It should be noted that UIV returns the velocities of the dispersed phase and not the fluid carrying the particles.

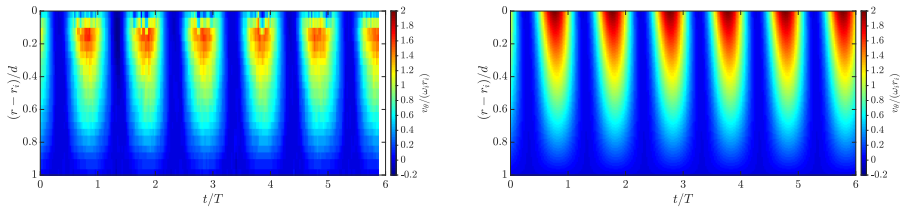

Figure 3.22: Application of UIV to a particle-laden Taylor-Couette flow. The inner cylinder is modulated with a time period of $T = 3s$. (a) Azimuthal velocities measured by UIV. (b) Azimuthal velocities calculated analytically.

Space-time plots of the azimuthal velocity obtained experimentally and analytically are plotted in Figure 3.22(a) and Figure 3.22(b) respectively. A good qualitative agreement is visible between the plots, especially for $(r - r_i)/d > 0.15$. The relatively low Womersley number implies that the Stokes boundary layer thickness is much larger than the gap

width d. This is also visible in the space-time plots as the peak velocities of the cylinder are propagated almost immediately over the gap.

3.B.6. Conclusion: UIV is a potential tool for particle-laden Taylor-Couette flows

In this paper, we applied UIV to single-phase Taylor-Couette flows driven by pure inner cylinder rotation and validated the mean velocity fields under both, the laminar and turbulent regime. It is also indicated that the radial velocity fluctuations are more appropriate for studying the turbulent characteristics of the flow. A good correlation was observed in the qualitative behaviour of the peak frequencies calculated from the power spectra of the radial velocity fluctuations (UIV) and the scattered light intensity (flow visualization). Finally, as a proof-of-concept, UIV was applied to a particle-laden flow (volume fraction 0.01) with the inner cylinder modulated sinusoidally. The velocity profiles obtained were also in-line with those expected analytically. In the future, UIV shall be applied with simultaneous flow visualization and torque measurements to particle-laden flows with higher volume fractions, to extract information about the flow regime and velocity profiles simultaneously similar to the recent studies by Majji, Banerjee, and Morris (2018) and Ramesh, Bharadwaj, and Alam (2019).

4

Ultrasonic particle volume fraction profiling: an evaluation of empirical approaches

Quality of the exam is extremely operator dependent, and of all medical imaging modalities, ultrasound can be considered an "art" and the operator must have extensive knowledge and understanding of the underlying basic physics to be considered a true "artist".

Bushberg *et al.* (2012)

We discuss empirical techniques to extract quantitative particle volume fraction profiles in particle-laden flows using an ultrasound transducer. A key step involves probing several uniform suspensions with varying bulk volume fractions from which two key volume fraction dependent calibration parameters are identified: the peak backscatter amplitude (acoustic energy backscattered by the initial layer of the suspension) and the amplitude attenuation rate (rate at which the acoustic energy decays with depth owing to scattering losses). These properties can then be used to reconstruct spatially varying particle volume fraction profiles. Such an empirical approach allows circumventing detailed theoretical models which characterize the interaction between ultrasound and suspensions, which are not universally applicable. We assess the reconstruction techniques via synthetic volume fraction profiles and a known particle-laden suspension immobilized in a gel. While qualitative trends can be easily picked up, the following factors compromise the quantitative accuracy: (1) initial reconstruction errors made in the near-wall regions can propagate and grow along the reconstruction direction, (2) multiple scattering can create artefacts which may affect the reconstruction, and (3) the accuracy of the reconstruction is

This chapter has been published in Dash, Hogendoorn, and Poelma (2021). 'We' in this chapter refers to the three authors - Amitosh Dash, Willian Hogendoorn, and Christian Poelma.

very sensitive to the goodness of the calibration. Despite these issues, application of the technique to particle-laden pipe flows shows the presence of a core with reduced particle volume fractions in laminar flows, whose prominence reduces as the flow becomes turbulent. This observation is associated with inertia-induced radial migration of particles away from the pipe axis and is observed in flows with bulk volume fractions as high as 0.08. Even transitional flows with low levels of intermittency are not devoid of this depleted core. In conclusion, ultrasonic particle volume fraction profiling can play a key complementary role to ultrasound-based velocimetry in studying the internal features of particle-laden flows.

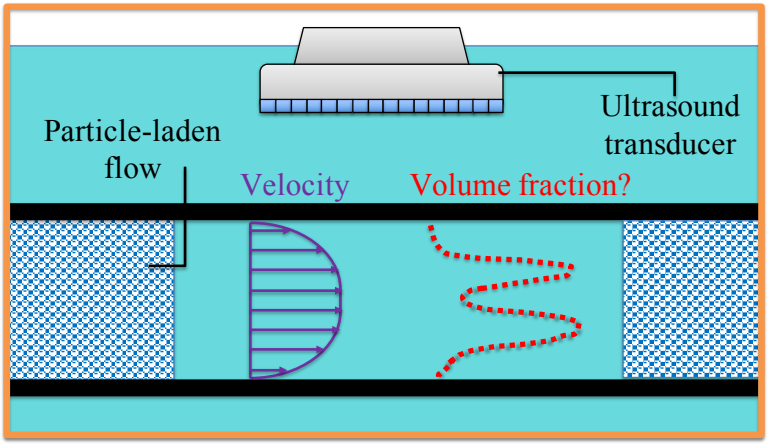

Can ultrasound also be used to quantify particle volume fraction profiles in particle-laden flows? This information can complement velocity measurements.

4.1. Introduction and scope

Dispersed multiphase systems are notoriously difficult to access by optical means. The major reason behind this is the presence of numerous scattering interfaces (between the continuous and dispersed phase) which leads to a quick extinction of light, for example in dense sprays (Coghe and Cossali, 2012), fluidized beds (van Ommen and Mudde, 2008) or bubbly flows (Mudde, 2005). This proves problematic for the application of established optical techniques for monitoring purposes.

Due to the complexity in visualizing opaque flows, various measurement techniques for diagnosing such flows have been developed. These techniques have been well summarized and compared in the context of fluidized beds (van Ommen and Mudde, 2008), granular mixing (Nadeem and Heindel, 2018) as well as dispersed multiphase flows (Poelma, 2020). The adoption of acoustical techniques (over X/γ-ray computed tomography, magnetic resonance imaging, electrical capacitance tomography or radioactive particle tracking) offers several advantages: ease of deployment, lower costs and lower health/safety risks. Moreover, it is completely non-destructive and non-invasive.

Ultrasound based velocimetry is relatively well matured (Takeda, 2012; Poelma, 2017). However, in dispersed multiphase systems, another key quantity of interest is the particle volume fraction (or concentration) profile. Simultaneous measurement of velocity and volume fraction profiles could be instrumental in addressing the micro-structural physics of such flows. The profiling that is discussed in this chapter should not be confused with commercially available sensors which provide a global/integrated measure of solid volume fractions (Bamberger and Greenwood, 2004).

Determination of particle concentration profiles via acoustics is *not* a novel topic and several communities have explored this aspect. We have summarized these efforts in Section 2.2.3. One of the communities that has made significant progress on this subject is of sediment transport processes in marine environments (Thorne and Hanes, 2002; Hurther *et al.*, 2011; Thorne, Hurther, and Moate, 2011). In fact, even plug-and-play open source software are being introduced (Fromant *et al.*, 2020). A key feature of their approach is their reliance on meticulously developed theoretical models, while being geared towards specific single-element transducers. The starting point of these models is the scattering induced by a single particle, which is then extended to an ensemble of scatterers. In the end, an equation is obtained between the measured backscattered acoustic signal and the characteristics of the system (distribution of particles, particle sizes, ultrasonic frequency etc.), which is solved to obtain the concentration profile. A brief overview of the interaction between ultrasound and suspensions can be found in Section 2.2.2.

The theoretical models often have limitations, especially in terms of maximum volume fractions that can be accurately accommodated (Hunter *et al.*, 2012). This has led to the development of more generalized approaches over the past decade and can be broadly categorized into: semi-empirical (Hunter, Peakall, and Biggs, 2012; Rice *et al.*, 2014; Bux *et al.*, 2015; Rice *et al.*, 2015) and empirical (Furlan *et al.*, 2012; Saint-Michel *et al.*, 2017).

A step common to both these generalized approaches involves calibration in a uniform suspension, where the dispersed phase is uniformly distributed across the region of interest. A key difference, however, is how data from calibration tests are used. Semi-empirical approaches integrate the calibration data in the aforementioned rigorous, theo-

retical scattering models, i.e. the equation between the backscattered acoustic signal and the characteristics of the system. Whereas in empirical methods, the calibration data are used directly to quantify volume fraction profiles in non-uniform suspensions (which is assumed to be composed of multiple, tiny, contiguous regions of uniform suspensions), without the aid of any theoretical scattering model. Empirical approaches offer the advantage of versatility and freedom (for example, the use of linear array ultrasonic transducers or flow configurations with walls) which are not incorporated in the aforementioned rigorous theoretical models.

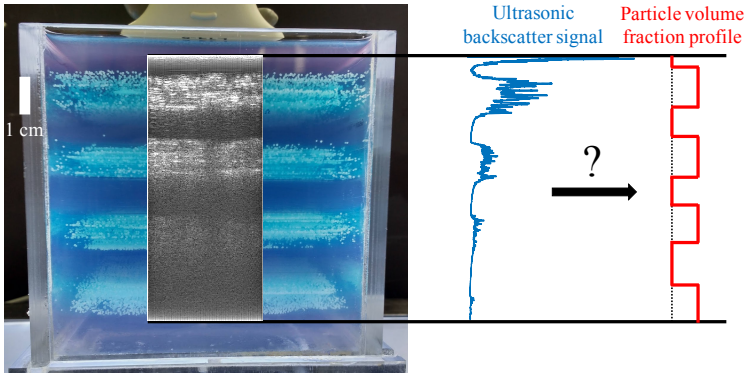

Figure 4.1: Example of a gelatin model to illustrate the core concept of ultrasound based concentration profiling. Multiple horizontal segments are present - either with or without particles arrested in their position. An ultrasonic image is overlaid.

The focus of the present work is on a detailed assessment of empirical approaches. We outline the general framework as well as address the goodness of the reconstruction. Factors that compromise the quantitative accuracy of the inversion techniques are also highlighted. Our work is performed with linear array transducers (commonly used for medical diagnoses), while the dispersed phase in the studied suspensions have sizes comparable to the ultrasonic wavelength (~ 0.2 mm). A reader unfamiliar with ultrasound imaging may find Section 2.2.1 useful, where the basics of the imaging technique and terminology are described. The approaches presented here are best applicable to (semi-)dilute suspensions and for size domains in the order of a few centimetres (laboratory-scale experiments and small/medium-scale industrial flows).

In this chapter, we describe the key ideas behind an empirical approach, which includes calibration in uniform suspensions (Section 4.2) followed by the application of inversion approaches in profiling non-uniform suspensions (Section 4.3). We explore the applicability of an inversion technique in a model composed of solid particles immobilized in gelatin (Section 4.4). An example of such a model is shown in Figure 4.1. These gelatin models help identify a limitation of the technique, namely, multiple scattering (scattering of sound waves between particles, discussed later in more detail). As a case study, we apply the technique to (semi-)dilute particle-laden pipe flows, focusing primarily on radial migration in neutrally buoyant suspensions (Section 4.5). We end by summarizing our key findings and discussing possible directions that can build up on the work presented

here (Section 4.6).

4.2. Calibration in uniform suspensions

Before proceeding to the profiling of non-uniform suspensions, a necessary step in an empirical technique would be the characterization of uniform suspensions. Characterization of uniform suspensions can be useful in monitoring the global volume fraction of the system. Unlike the transceiver apparatus (i.e. a single device for transmission and receiving of sound) employed here, uniform suspensions may also be monitored by means of a transmitter and a receiver placed at a fixed separation. The change in speed of sound or attenuation of sound due to the particles in between the two may then be used characterize the suspension and this has been done in previous studies (for example, Stolojanu and Prakash, 2001).

For the current experiments, a transceiver is used for measurements, which necessitates the use of different means to characterize the suspensions. The time-of-flight or extinction-of-sound like measurements used in separated transmitter-receiver configurations can not be used. Thus, the technique proposed by Weser *et al.* (2013a,b, 2014) is adapted and a schematic elucidating this process is shown in Figure 4.2.

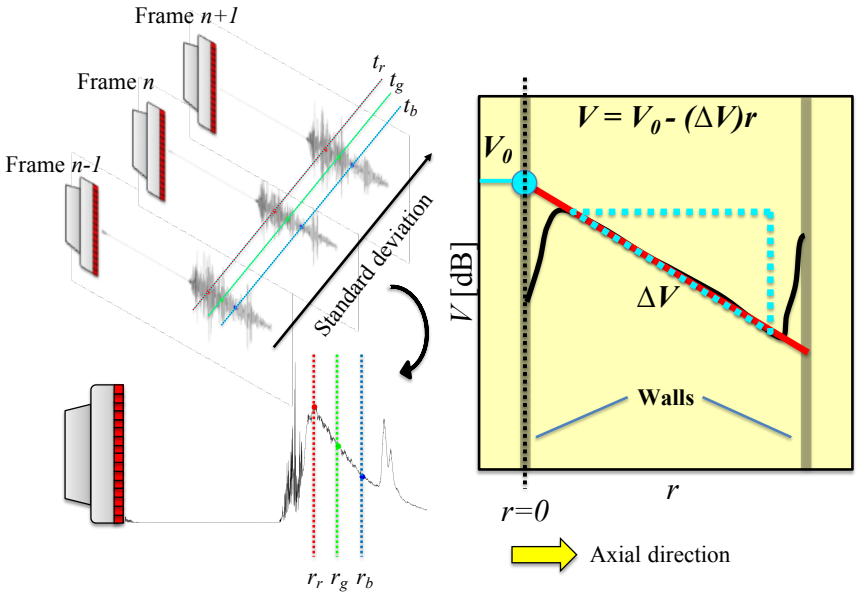

Figure 4.2: Backscatter amplitude and characterizing a uniform suspension. (*Top left*) Backscattered signals (post-beamformed RF data) recorded by the transducer in multiple frames. (*Bottom left*) Derivation of the backscatter amplitude profile. (*Right*) A simplified schematic of the backscatter amplitude (now in dB) with a linear fit (solid red straight line between walls) through it. This linear fit returns the peak backscatter amplitude (y-intercept) and the attenuation rate (slope) corresponding to the uniform suspension being characterized.

The procedure is as follows: Every frame in the entire ensemble of measurements is a

time series consisting of post-beamformed RF data. We emphasize that 'frame' is used in the current context to refer to an individual time series (for example, frame $n-1, n, n+1$ in Figure 4.2) and should not be confused with the time instant within a frame at which the backscattered signal is received (for example, $t_r/t_g/t_b$ in Figure 4.2). Then, a new series is created out of the data at a fixed time instant across all frames (for example, all the dots of three different colors - red, green and blue - in the top left panel in Figure 4.2 form a new series each). The standard deviation of each of these new series is converted to a new time series and thus, a new signal is born. This new signal is referred to as the backscatter amplitude (V) henceforth, and it displays an exponential decay with increasing distance, due to attenuation (fixed percentage of sound energy is lost for the depth propagated). In a medium with speed of sound c_0, time can be converted to space as $r = 0.5c_0t$*. Upon converting the magnitude of the backscatter amplitude into decibels, the exponential decay is converted into a linear decay. Of course, for a flow with extreme temporal fluctuations of the particle volume fraction, the conversion of magnitude to decibels could incur errors for the time-averaged signal due to the inherent non-linearity of the transform. However, this is not an issue for the present study, as the flow is steady in nature. An alternative approach is to use the mean (instead of the standard deviation, respectively) of the A-mode data (instead of the post-beamformed RF data). It must be noted that if the frame is a B-mode image (instead of post-beamformed RF/A-mode data), then the process of converting the backscatter amplitude to decibels is unnecessary. This arises from the fact that the log-compression step in generating the B-mode image is mathematically similar to that of converting a magnitude into decibels.

A straight line may be fitted through this decay profile and two parameters can be obtained: the y-intercept and the slope. For wall-bounded flows, these fits are usually done on the signal corresponding to the central region of the geometry, i.e. away from the walls. This is done so since the backscatter amplitude profile near the walls is less reliable. It has been shown that the y-intercept and the slope show good correspondence with theoretical backscattering coefficients and experimentally measured attenuation respectively (Weser *et al.*, 2013a,b, 2014). Thus, the y-intercept and the slope of this fitted line are referred to as the peak backscatter amplitude (V_0) and the attenuation rate (ΔV) respectively. Note that we consider the attenuation rate as a positive quantity, by fitting the following profile: $V(r) = V_0 - \Delta V r$.

In order to understand the influence of particle volume fraction on the backscatter amplitude characterization, the schematic in Figure 4.3 is considered. On the left is a a more dilute suspension, while a denser suspension is present on the right. When a fixed amount of acoustic energy is sent into the suspensions by the transducer, the denser suspension initially scatters the sound back to the transducer more intensely, due to the presence of more particles. This leads to higher peak backscatter amplitudes (V_0) for denser suspensions. However, as sound propagates through, the denser suspension scatters relatively more sound away from the transducer as well, in comparison to the diluter suspension. This leads to a quicker loss of acoustic energy, i.e. the attenuation rate (ΔV) is higher as well for denser suspensions.

A sample calibration performed in a pipe flow, as a function of particle volume fraction, is shown in Figure 4.4. The calibration was performed in a pipe with an internal diameter

*This relationship is referred to as space-time reciprocity

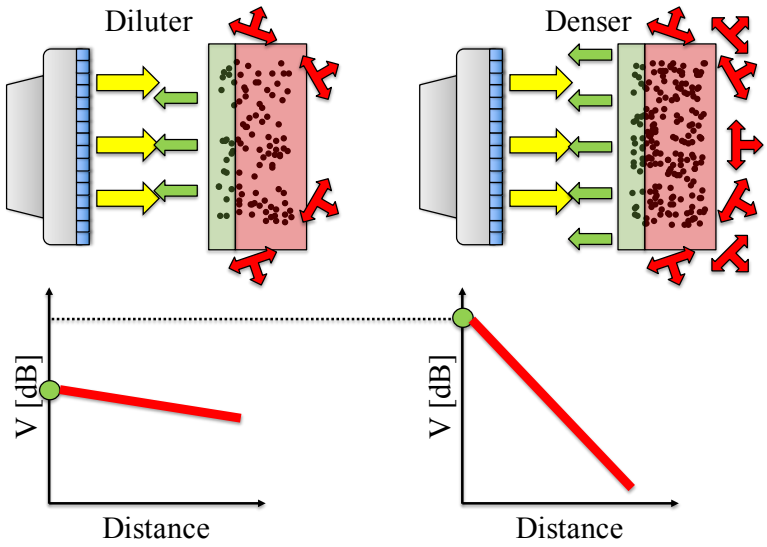

Figure 4.3: Effect of particle loading on backscatter amplitude. For a fixed insonification (yellow arrows pointing away from transducer), increasing the particle volume fraction in a uniform suspension increases the peak backscatter amplitude (green arrows pointing towards transducer in top panel and green circle in bottom, V_0) as the number of scattering interfaces are increased. However, the amount of scattering in the non-backscatter direction increases, leading to a quicker attenuation (groups of three red arrows originating from a node in top panel and solid red straight line in bottom, ΔV) of the backscatter amplitude.

of 10.00 mm, while the particle diameters were 530 ± 75 μm. The suspension is comprised of polystyrene spheres suspended in saline water. A uniform suspension was obtained by having a neutrally buoyant system as well as turbulent flow conditions. For the present experiments, it is expected that the particles possess finite inertia. Fiabane *et al.* (2012) have shown that neutrally buoyant particles are homogeneously distributed in turbulence, unlike heavy particles, which tend to cluster. Thus, we expect that the calibrations in the present study are not significantly affected by the phenomenon of turbophoresis - the preferential accumulation of inertial particles in regions of low turbulence intensity (Caporaloni *et al.*, 1975; Reeks, 1983).

Data acquisition is performed via a SonixTOUCH Research (Ultrasonix/BK Ultrasound) system coupled with a linear array transducer (L14-5/38). The transducer is immersed in a water bath surrounding the pipe, to improve the acoustic coupling. Straight line fits were performed on the backscatter amplitudes corresponding to the central parts of the pipe and the length used for the fit varied from 0.75 - 0.84 cm. Profiles of the peak backscatter amplitude and the attenuation rate from measurements at two central frequencies (1 MHz and 10 MHz, $ka \sim 1.1$ and 11, respectively; both with one cycle long pulses) are presented. While there is a minor difference between the results at the two central frequencies, the overall trends for the peak backscatter amplitude and the amplitude attenuation rate are in agreement with the expectations illustrated in Figure 4.3.

The peak backscatter amplitude in Figure 4.4 displays a power-law behaviour with

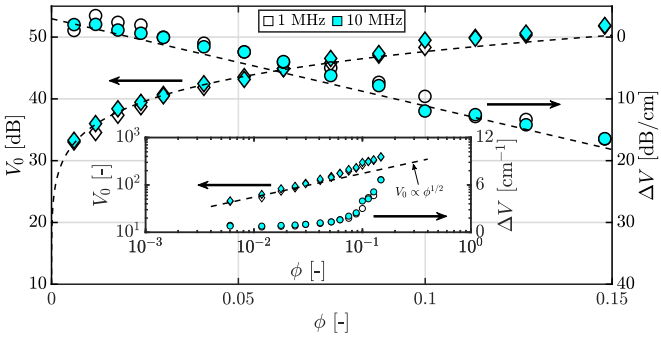

Figure 4.4: Sample calibration data obtained in a pipe flow with a uniform suspension. Characterization in decibels, but in arbitrary units for inset. Inset in log-log axes for peak backscatter amplitude and semi-log axes for amplitude attenuation rate. Diamonds represent the peak backscatter amplitude and circles represent the amplitude attenuation rate.

increasing volume fraction and can be characterized by means of an empirical power-law fit, $V_0 = a\phi^n$ with $n < 1$. This also means that the peak backscatter amplitude is more sensitive to volume fraction changes for lower volume fractions ($\frac{dV_0}{d\phi} = an\phi^{n-1}$). Plotting the peak backscatter amplitude on a log-log scale shows that the theoretical relation, $V_0 \propto \phi^{1/2}$ (Thorne and Hanes, 2002), is valid until $\phi \sim 0.04$ for the present suspension (see inset of Figure 4.4). This further strengthens the argument for the need for empirical methods. While not explored here, it has been shown for other suspensions (typically in the long wavelength regime) that the peak backscatter amplitude profile shows non-monotonic behaviour with a maximum attained between volume fractions of 0.10 - 0.30 (Chen and Zagzebski, 1996; Wang and Shung, 1997; Baddour and Kolios, 2005; Franceschini and Guillermin, 2012), which would impose a limit to the range of volume fractions that can be studied by the inversion techniques discussed later.

The attenuation shows a very linear behaviour with volume fraction, on the decibel scale, something that was also observed by Weser *et al.* (2014) for glass beads. The attenuation is characterized by a linear fit $\Delta V = m\phi + c$. An interesting observation is that the attenuation rate has a negative value at lower volume fractions, i.e. the backscattered energy *increases* with depth. A possible reason for this is the complex three-dimensional shape of the ultrasonic beam, which is commonly characterized by a focal point. The beam typically converges until the focal point and diverges thereafter. Another global property that is a function of particle volume fraction, is the speed of sound. However, for polystyrene suspensions in (saline) water, the speed of sound changes by only about 3% for volume fractions up to 0.15 (Kuster and Toksöz, 1974), and its effect can be neglected for the range of volume fractions studied here.

While we have chosen these two functions (power fit for peak backscatter amplitude and linear fit for amplitude attenuation rate) based on our observations, other functions may be chosen as well in order to attain a better fit. This encapsulates the spirit of the empirical nature of the measurement technique. It should be noted that performing ex-

situ calibration in a different geometry is not recommended as the flow geometry could also influence the propagation of the sound waves, and thus potentially, the characteristics of the backscatter amplitude profiles. In case a uniform suspension cannot be generated in the system (for example, due to the flow itself), calibration in a 1:1 mock-up could be considered. Moreover, beamform settings should remain unaltered throughout, for a valid comparison. Image settings such as multiple transmit foci is discouraged as this generates artificial discontinuities in the backscatter amplitude profile. The calibration data from Figure 4.4 will later be used to create synthetic backscatter amplitude profiles in Section 4.3.3.

4.3. Inversion to obtain particle volume fraction profile in non-uniform suspensions

In this section, we discuss two potential inversion techniques in Sections 4.3.1 and 4.3.2, before applying these to synthetically generated signals in Section 4.3.3.

4.3.1. Procedure 1: Stepwise reconstruction

The first technique that can be used to invert the backscatter amplitude signal to obtain the particle volume fraction profiles is the stepwise reconstruction technique. As the name suggests, the reconstruction is performed in a stepwise manner, beginning from the transducer and propagating in the initial direction of the acoustic waves. The reconstruction technique can be understood via the schematic in Figure 4.5. The time-averaged backscatter amplitude signal, V, is divided into a certain number of bins, each with a fixed length, Δr. It is assumed that the particle volume fraction is homogeneous within this bin. Each bin has a representative backscatter amplitude value (the bin average).

The reconstruction starts at the bin located closest to the ultrasound transducer. Let us consider the data point closest to the transducer in Figure 4.5. For the first bin, the bin-averaged backscatter amplitude, $V_{0,1}$, can be directly compared with the calibration curve of the peak backscatter amplitude (solid red non-linear calibration curve, V_0 versus ϕ) which returns an estimate for the particle volume fraction for that bin (ϕ_1). However, due to the particles present in this first bin, the backscatter amplitude signal will be attenuated due to scattering. Thus, as a next step, the signal in the following bins are adjusted to compensate for this loss by attenuation (shown by the group of six black arrows originating from the same node). This compensation is the product of the attenuation due to the local particle volume fraction (the solid green linear calibration curve, ΔV versus ϕ) and the bin size, $\Delta V_1 \Delta r$.

Following this, when the second bin is considered, the peak backscatter amplitude, $V_{0,2,c} = V_{0,2} + \Delta V_1 \Delta r$ is thus appropriate for estimating the local particle volume fraction. Then, the signal attenuation for the second bin, $\Delta V_2 \Delta r$, is accounted for in the following bins, i.e. the third bin onwards. This way, the time-averaged particle volume fraction profile, $\phi(r)$, is reconstructed in a stepwise manner.

The stepwise reconstruction process may be expressed with Equation (4.1).

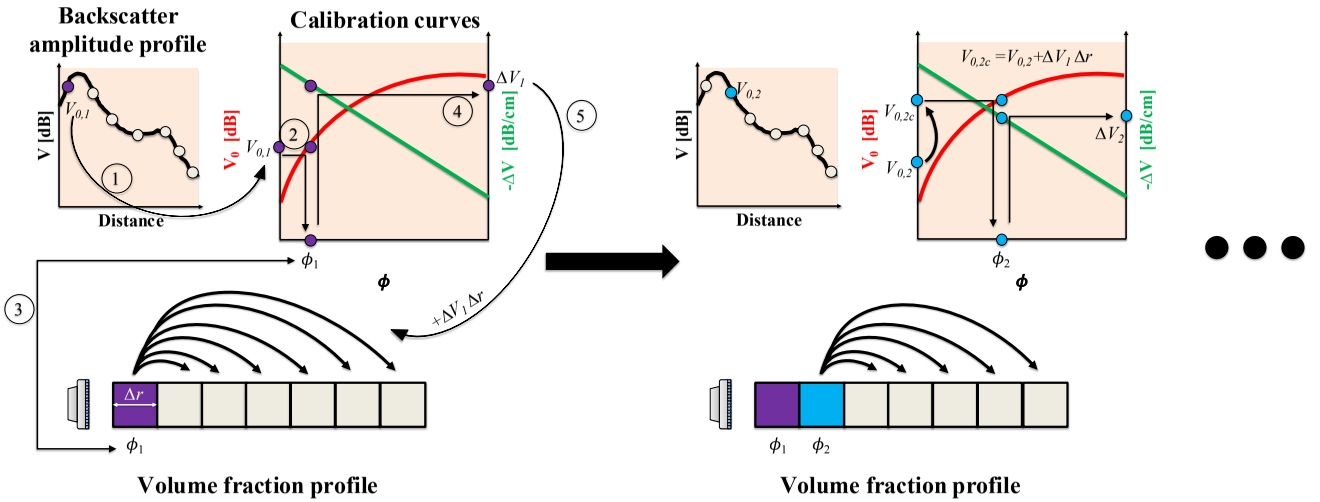

Figure 4.5: The stepwise reconstruction process for obtaining the particle volume fraction profile. (*Left*) Estimation of volume fraction in first bin: use $V_{0,1}$ to estimate ϕ_1 (steps 1-3) which can then be used to find ΔV_1 (step 4) that will be used in the compensation step (step 5). (*Right*) Estimation of volume fraction in second bin: estimate $V_{0,2c} = V_{0,2} + \Delta V_1 \Delta r$; use $V_{0,2c}$ to estimate ϕ_2 which can then be used to find ΔV_2. In the next step (not shown), estimate $V_{0,3c} = V_{0,3} + \Delta V_2 \Delta r + \Delta V_1 \Delta r$, use $V_{0,3c}$ to estimate ϕ_3 and so forth.

$$V(r) = \underbrace{V_0(\phi(r))}_{1} - \underbrace{\int_0^r \Delta V(\phi(r'))\mathrm{d}r'}_{2} \tag{4.1}$$

While the continuous form of the equation is shown, it can be discretized into bins of finite sizes, in order to solve the inverse problem. This equation can be considered as a simplified, lumped version of the semi-empirical formulations used in determining suspended sediment concentrations, (see Equation (2.1)). However, the above formulation allows more freedom in characterizing non-dilute suspensions, where scattering of sound may not be trivially expressed with theoretical formulations.

The nature of quantifying particle volume fractions with the stepwise reconstruction bears a strong similarity with the method used in Furlan *et al.* (2012). However, a key difference is their usage of spectra instead of our definition of backscatter amplitude. While spectra contain much more information, the much simpler backscatter amplitude is sufficient for the current purpose. Both these methods can also be likened to the iterative implicit technique used in the marine sediment transport community (see cluster I, Section 2.2.3).

The stepwise reconstruction is also very similar to the approach put forth by Saint-Michel *et al.* (2017), with one key difference. They acknowledge simplifying the reconstruction by not employing a space-dependent attenuation coefficient. In our terminology, their approach would transform Equation (4.1) into $V(r) = V_0(\phi(r)) - r\Delta V(\phi(r))$, which is free of the integral, allowing them to reconstruct the entire profile in one step.

4.3.2. Procedure 2: Dual-frequency reconstruction

As can be seen, the integral on the right hand side of Equation (4.1) turns the stepwise reconstruction technique into a set of implicit equations, which is susceptible to errors during inversion (Hurther *et al.*, 2011). The implicit nature of the set of equations for the stepwise reconstruction technique (Equation (4.1)) can prove troublesome in the reconstruction process due to numerical instabilities. A solution that was devised for this issue was the usage of the ultrasonic transducer at two different central frequencies (Hurther *et al.*, 2011). By changing the central frequency of the ultrasonic wave, the relative wavelength would be changed as well. This in turn affects the interaction of the acoustic wave with the particle/suspension.

This inversion technique has so far been used by theoretical (Hurther *et al.*, 2011) as well as semi-empirical approaches (Rice *et al.*, 2014). Here, we rearrange Equation (4.1) with the aid of the calibration curve fits, Equation (4.2). For each frequency, the coefficients a, n, m and c would have different values. The below forms for the curve fits are based on the data in Figure 4.4.

$$\begin{aligned} V_0 &= a\phi^n \\ \Delta V &= m\phi + c \end{aligned} \tag{4.2}$$

For the above characterization, upon combining Equations (4.1) and (4.2) followed

by a rearrangement of terms, Equation (4.3) is obtained*.

$$\frac{V(r) - a\phi^n(r) + cr}{m} = \underbrace{-\int_0^r \phi(r')dr'}_{\text{constant}} \tag{4.3}$$

The term on the right hand side is a constant for a stationary flow, allowing the elimination of the integral term. This is beneficial, as the left hand side of this equation, for the two frequencies may be equated directly, to create a system of explicit equations, as shown in Equation (4.4).

$$\frac{V_1(r) - a_1\phi_1^n(r) + c_1 r}{m_1} = \frac{V_2(r) - a_2\phi_2^n(r) + c_2 r}{m_2} \tag{4.4}$$

This technique has been shown to have been robuster for sediment transport studies (Thorne, Hurther, and Moate, 2011) as it is less susceptible to errors arising from numerical instabilities. The process is summarized in Figure 4.6 and as it suggests the entire profile can be reconstructed in a single iteration. Such a technique can also be extended to add measurements at a third central frequency of the transducer, which has been shown to further reduce the uncertainty in the estimated concentration profiles (Thorne and Hurther, 2014).

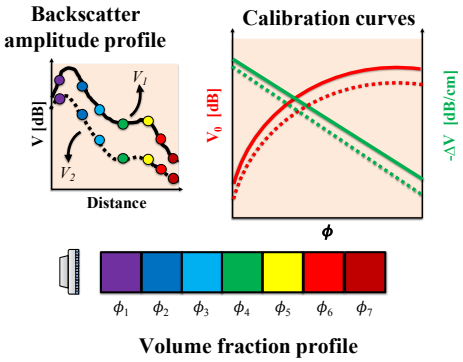

Figure 4.6: The dual-frequency reconstruction process for obtaining the particle volume fraction profile. (*Top left*) The backscatter amplitude signal measured at the two frequencies. (*Top right*) Calibration curves for the two frequencies. (*Bottom*) Reconstruction of the void fractions using Equation (4.4). The solid and the dashed lines correspond to measurements at the two frequencies.

In general, it would be desirable to have a calibration function for attenuation where the volume fraction can be trivially separated from the calibration constants. This is not the case when a second order polynomial is used for the amplitude attenuation rate as a function of particle volume fraction. In such a scenario, it would be challenging to formulate an equation resembling Equation (4.3), where a constant quantity ($\int_0^r \phi(r')\mathbf{d}r'$) was isolated.

*In the online manuscript, there is an additional = $-\phi_{\text{bulk}}$ on the right hand side, which is incorrect.

4.3.3. Comparison of the two techniques with synthetic profiles

Given the two proposed inversion techniques, a natural question that might arise is which of the two techniques is better. Here, we perform a comparison of the two techniques based on synthetic signals, generated from the experimental data in Figure 4.4 and the equation forms in Equation (4.2).

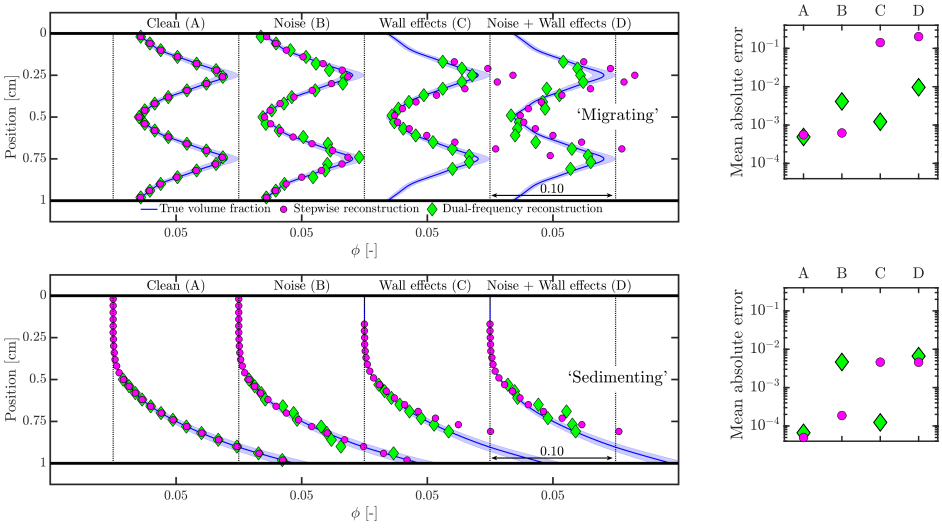

Figure 4.7: Performance of the two inversion techniques are judged by means of synthetic signals. Panels on the left show the reconstructions while those on the right show the corresponding mean absolute errors of the reconstructions with respect to the true volume fractions.(*Top*) Profiles mimicking inertial migration of particles. (*Bottom*) Profiles mimicking transport of heavy particles.

A particle volume fraction profile is assumed and the corresponding synthetic signal or 'forward problem' is generated with the help of Equation (4.1). Coefficients of the curve fits used to characterize the uniform suspensions are summarized in Table 4.1. This signal is basically a hypothetical backscatter amplitude as a function of distance from the transducer, conforming to the flow/measurement geometry used in the calibration (Figure 4.4). Since the calibration coefficients have similar values, it was seen that the separation between the constructed synthetic signals, $|V_{1\ \mathrm{MHz}}(r) - V_{10\ \mathrm{MHz}}(r)|$, is not separated by a large magnitude.

Table 4.1: Coefficients for curve fits used in synthetic signal generation. See Equation (4.2) for the curve fitting characteristic equations.

Frequency	a	n	m	c
1 MHz	65.12	0.1313	129.3	- 3.677
10 MHz	64.70	0.1328	141.1	- 2.971

Two assumed profiles and their corresponding reconstructions are shown in Figure 4.7. Two cases are considered: one where the particle volume fraction profile resembles the radial migration of neutrally buoyant particles away from the axis ('migrating') and the other where the profile resembles the transport of dispersed particles heavier than the fluid ('sedimenting'). While the migrating profile has a non-monotonic shape, the sedimenting one is monotonic. Furthermore, for each of the two cases, two undesirable, but unavoidable experimental effects are considered. For example, noise fluctuations are added to the backscatter amplitude signal, which can be expected in any realistic measurement. In the other case, wall effects are considered by corrupting the backscatter amplitude signal near the wall regions. The latter artefact is more relevant to wall-bounded flows, and have also been reported in other works (Wang *et al.*, 2003; Saint-Michel *et al.*, 2017).

First, the reconstruction of a 'clean' backscatter amplitude signal (without any noise or wall effects) is considered. It can be seen that both the inversion techniques perform equally well, which is also a verification that the inversion techniques have been implemented properly. The dual-frequency reconstruction technique is unable to estimate a volume fraction for positions between 0 and 0.5 cm. A possible reason for this is that the local volume fractions is very low (≈ 0) which would make Equation (4.4) difficult to solve.

Next, white Gaussian noise (signal-to-noise ratio of 15) is added to the backscatter amplitude signals. From the reconstructions, it is evident that the stepwise reconstruction technique performs slightly better than the dual-frequency technique. This happens as the fluctuations induced by noise on the backscatter amplitude signal are of similar order-of-magnitude as the separation of the backscatter amplitude signals recorded at the two frequencies. Nevertheless, both techniques provide satisfactory solutions, certainly at a qualitative level.

Hereafter, wall effects are considered. This is done by altering the backscatter amplitude signals near the wall regions, making these regions less reliable for reconstruction. Basically, the backscatter amplitude profile is manipulated in the near-wall region so that it deviates significantly from what would be expected from Equation (4.1). The inversion is then performed only between the regions of 0.15 - 0.85 cm. It is clear that the dual-frequency technique is the robuster one here. This is because of the explicit nature of the system of equations. In the stepwise reconstruction technique, an error is made in the particle volume fraction estimation at the first bin itself (at 0.15 cm). No information of the volume fraction profile is calculable before the first bin (< 0.15 cm), and an assumption needs to be made, i.e. the profile is homogeneous until the first bin. This assumption leads to an initial error which then propagates in an additive manner as the reconstruction moves away from the transducer. The behaviour of the error propagation is different for the two profiles. In both cases, the estimated volume fraction profiles behave in a similar fashion as the actual ones. However, for the 'sedimenting' profile, the absolute value of the estimation error is monotonic owing to the monotonic nature of the actual volume fraction profile. The stepwise reconstruction solution beyond a distance of 0.75 cm is not computed as the volume fraction estimate already exceeds 0.15, more than the maximum volume fraction in the calibration. Nevertheless, the stepwise reconstruction technique still provides a good qualitative insight.

Finally, both techniques are compared with Gaussian white noise (signal-to-noise ratio

of 5) as well as wall effects. Neither of the two techniques provide acceptable estimates at a quantitative level. This also shows that both artefacts, noise and wall effects, can affect the goodness of the reconstruction.

The discussion above pertained to the extraction of time-averaged profiles. The performance of the two reconstruction techniques are summarized in Table 4.2. While the effect of noise may be reduced by longer measurements, the quality of the data near the walls can be improved (also while removing the effects of fixed artefacts), with the help of tools such as a temporal high pass filter (Sciacchitano and Scarano, 2014).

Sometimes time-averaged profiles may not be sufficient and for dynamic processes, time-resolved monitoring might be desired. The stepwise reconstruction technique would be more appropriate for this purpose. Depending on the relevant time-scales of the flow processes, higher rates of signal acquisition might be required, for example, by means of plane-wave imaging (Tanter and Fink, 2014). In order to employ dual-frequency reconstruction, a high rate of signal acquisition in tandem with the possibility to quickly alternate between two central frequencies of the transducer are needed, which is not straightforward. This would also mean that if simultaneous measurements of velocity and particle concentration fields are desired with a single transducer, the stepwise reconstruction technique would be the more appropriate approach, and such measurements have been demonstrated by Saint-Michel *et al.* (2017).

Table 4.2: A summary comparing the two reconstruction techniques. Comparison based on synthetic signals.

Characteristic	Stepwise	Dual-frequency
System of equations	Implicit	Explicit
Handles noise well?	For low noise levels	If $\lvert\Delta V\rvert >> V_{\text{noise}}$
Handles wall artefacts?	Initial error occurs which grows in the reconstruction direction	Robust
'Instantaneous' concentration profiles	Possible with appropriate hardware	Requires multiple transducers

4.4. Limitations induced by multiple scattering: tests in gelatin models

While empirical reconstruction techniques have been developed and applied, in previous studies (Furlan *et al.*, 2012; Saint-Michel *et al.*, 2017), the techniques were not validated with a known particle volume fraction profile. In principle, such a system can be created, wherein a box is divided into multiple partitions by means of vertical walls. However, preliminary experiments with such a system showed that the presence of the walls created

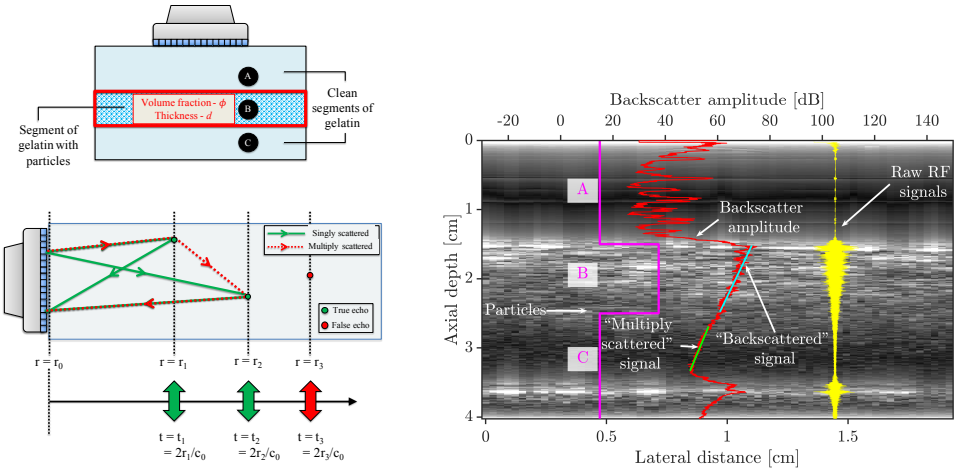

Figure 4.8: Evidence for the presence of multiple scattering. (*Top left*) Schematic of the gelatin based model. Particles are present only in segment B. (*Bottom left*) Simplified schematic of single and multiple scattering of sound propagating in a medium with a speed of sound c_0. (*Right*) Overlaid on the B-mode image is the profile of particle distribution. Shown also are the entire ensemble of raw RF signals as well as the backscatter amplitude. The backscatter amplitude signal can be further divided into the 'backscattered' signal (segment B) and 'multiply scattered' signal (segment C). The bottom wall of the gelatin model is located at an axial depth of about 3.6 cm.

additional issues, as they are not acoustically transparent. A possible solution would be to create walls with same acoustic impedances as the surrounding fluid (Ramotowski, 2012), but this is not trivial and thus was not pursued. Gelatin based models were thus utilized, which are also commonly used in the field of medicine as low-cost phantoms to mimic tissue (Bude and Adler, 1995; Culjat *et al.*, 2010). In Section 4.A, we provide further details on the practical intricacies involved in constructing these models. Moreover, only the stepwise reconstruction technique is considered for validation.

It must be noted that the nature of experiments in this section (particles immobilized in gelatin) is also central to the work of Fay, Brendel, and Ludwig (1976). However, they investigate such models with the aim of recognizing inhomogeneities in the context of medical diagnostics. We also note that similar experiments with immobilized suspensions to quantify particle volume fractions have also been performed in the context of optical measurement techniques (Knowles and Kiger, 2012; Liu and Kiger, 2016) as well as magnetic resonance imaging (Borup, Elkins, and Eaton, 2018).

4.4.1. Multiple scattering in gelatin models

In the present work, we use gelatin as a medium to immobilize particles, allowing for construction of known particle volume fraction profiles. This allows us to employ ultrasound in a controlled environment where the particle volume fractions are known. A schematic of such a gelatin based model is shown in Figure 4.8. The particle volume fraction profile in this schematic resembles a step function, composed of two clean segments of gelatin (segments A, C) with a particle-laden segment (segment B) sandwiched in between. Each segment may be characterized by its thickness, while the particle-laden segment may

additionally be characterized by the volume fraction of the particles.

A major reason for venturing into the gelatin models was to have an environment without the presence of any walls that could contaminate the signal. These models also allowed for the detection of "multiple scattering", depicted in Figure 4.8. Multiple scattering is the phenomenon where a sound wave is scattered off multiple interfaces instead of a single interface. This leads to the sound wave covering a longer path and is received by the transducer at a later time. While the issue of multiple scattering is well known in various sub-domains of ultrasound/acoustic community (Tourin, Fink, and Derode, 2000; Anugonda, Wiehn, and Turner, 2001; Jia, 2004; Snieder and Page, 2007), this aspect has not been entirely addressed in the context of particle volume fraction profiling. The use of gelatin models provides easy access to isolate and visualize this phenomenon.

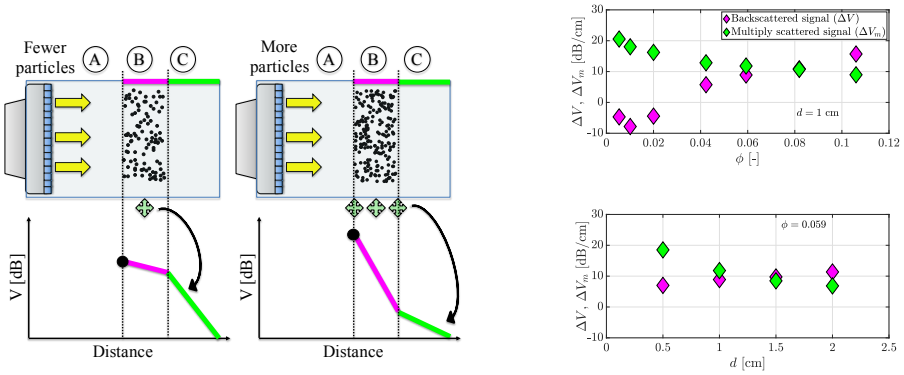

Figure 4.9: Characterization of the multiply scattered signal. (*Left*) Schematic for the behaviour of the backscatter amplitude profile as a function of the number of particles in a system corresponding to the schematic shown in Figure 4.8. (*Right*) Characteristics of the backscatter amplitude profile ($\Delta V, \Delta V_m$) as a function of volume fraction (ϕ) and thickness (d) of the particle-laden segment B.

The right image in Figure 4.8 provides strong evidence for the existence of this phenomenon in the gelatin system. The case considered resembles a step function, i.e. a particle-laden segment is sandwiched between two clean segments of gelatin. Shown in the background is a B-mode image. What is clearly visible in the B-mode image is the axial depth at which the particle-laden layer begins (about 1.5 cm) and the bottom of the gelatin model (about 3.6 cm). However, it is not very clear from the B-mode image where the particle-laden layer ends. Also shown is an ensemble of RF signals, as well as the backscatter amplitude profile, both of which provide clear evidence on the presence of multiple scattering. The multiply scattered tail is also referred to as 'coda' by seismologists (Snieder and Page, 2007).

Three regions can be identified. The first region, segment A (axial depth between 0 and 1.5 cm), has no particles present which, per expectations, results in corresponding RF signals with low strength (due to a lack of scatterers) and a fluctuating backscatter amplitude profile. The second region, segment B (axial depth between 1.5 and 2.5 cm), has particles present in it. The RF signals too indicate the presence of scatterers in this region. Similarly, the backscatter amplitude profile can be characterized pretty well by means of a linear fit (to reiterate, actually exponential decay, but linear in decibel units),

which is expected from a uniform suspension. The third region, segment C (axial depth between 2.5 and 3.6 cm), is again one without any particles. However, the RF signals indicate the presence of scatterers in this region and the backscatter amplitude profile also suggests that a uniform mixture may be present here, which is not the case. Thus, the observations from the third region confirm the existence of multiple scattering and it can be expected to cause issues in the volume fraction profile reconstruction if it is not accounted for. It must be noted that Fay, Brendel, and Ludwig (1976) do not observe such a behaviour. A possible explanation for this is that they might have used lower volume fractions of particles in their experiments, which they have not reported explicitly.

4.4.2. Characterizing the scattering behaviour

A disadvantage of gelatin models as compared to agitated suspensions is that the latter allows for a better ensemble averaging due to the inherent motion of the scatterers (Hall *et al.*, 1997). It must be noted that only three measurements were made with 64 lines in each measurement. In order to obtain sufficient convergence in the backscatter amplitude data, each line from each measurement was utilized resulting in 192 'effective' measurements. A shortcoming of these gelatin models is a lack of flow, which necessitates moving the transducer in order to probe more particles to reach statistical convergence.

Two straight line fits can be identified in the backscatter amplitude profile (Figure 4.8) which are referred to as the "Backscattered" and the "Multiply scattered" signal, corresponding to segments B and C, respectively. A question that may be raised is how the characteristics of these fits behave as a function of the number of particles in the system. The number of particles can be modified by changing either the volume fraction of the particle-laden layer or its thickness. The results are illustrated in Figure 4.9.

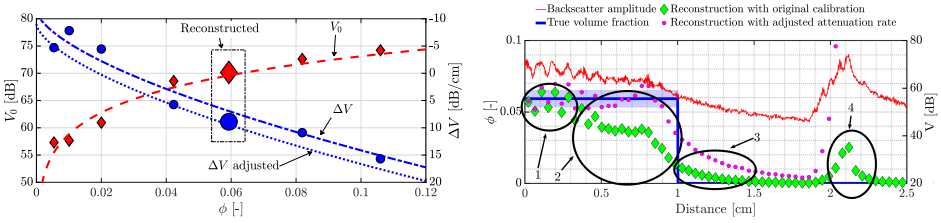

Figure 4.10: Reconstruction of a step particle volume fraction profile. (*Left*) Calibration curves for the Gelatin models, based on segment B. The larger symbols represent the characteristics of the case on which we apply stepwise reconstruction. (*Right*) Application of the stepwise reconstruction process to the phantom (segments B and C). For the reconstruction with the above calibration, the following can be noticed: 1 – Accurate reconstruction; 2 – Error due to undercompensation; 3 – Error due to multiple scattering; 4 – Detection of container bottom.

The slope of the backscattered signal as a function of the volume fraction is in line with the expectations (Figure 4.3). The slope of the multiply scattered signal is seen to decrease with both the particle volume fraction as well as the layer thickness. This can be understood by means of the schematic in Figure 4.9. The presence of more particles leads to the presence of more scattering events. The acoustic wave travels a tortuous path resulting in the transducer receiving signal for a longer period of time, i.e. appearance of

particles beyond the particle layer via space-time correspondence. Thus, the rate at which the signal decays is slower when more particles are present. In fact, similar observations have been reported by Tourin, Fink, and Derode (2000).

However, the result that is most puzzling is that the slope of the backscattered signal consistently rises with the thickness of the layer, albeit weakly. That a trend exists is not surprising since multiple scattering would start affecting the signal beyond a certain thickness. This observation could also have implications on the accuracy of the stepwise reconstruction process. Calibration is usually performed over the entire size of the flow geometry, while the reconstruction is done on a much smaller region, which may lead to signal overcompensation while accounting for the attenuation losses. Javanaud and Thomas (1988) state that the critical depth beyond which single scattering theories become invalid in the intermediate wavelength regime can be approximated by $\sim a/\phi$. For a suspension with $\phi = 0.0593$ and $a = 265\ \mu$m, the critical depth would be 0.45 cm. Thus, the effect of multiple scattering can be inhibited by imaging a small field-of-view, similar to Saint-Michel *et al.* (2017).

A caveat of these gelatin models is that attenuation due to absorption effects (see Section 2.2.2) are expected to be much higher than in a liquid. However, there seems to be sufficient evidence that this does not afflict the present interpretation of data. For example, the backscatter amplitude profile in the the region 0 – 1.5 cm in Figure 4.8 does not display a consistent attenuation behaviour. Moreover, the "multiply scattered" signal is not an artefact of this absorption since it is clearly dependent on the thickness and volume fraction of the particle-laden layer.

The above characterization implies that the presence of multiple scattering will complicate the accurate reconstruction of the volume fraction profiles. This would pose limitations on the critical depths and volume fractions that can be investigated while minimizing the influence of multiple scattering.

4.4.3. An example of calibration and reconstruction

The first demonstration of the performance of the reconstruction technique is done by means of a step function profile for the particle volume fraction. Seven cases were available where the particle-laden segment had the same thickness (of 1 cm), while the particle volume fraction differed. Data corresponding to the particle-laden segment of 1 cm was then used for the generation of calibration curves (Figure 4.10). Using the calibration data, an attempt was made to profile the particle volume fraction in one of the seven gelatin models ($\phi = 0.059$), in the regions corresponding to segments B and C. Power-law fits were used for characterizing both the peak backscatter amplitude, as well as the amplitude attenuation rate, based on the signal corresponding to segment B.

The reconstruction attempt for a particle volume fraction profile having the shape of a step function is shown in Figure 4.10. Shown also is the corresponding backscatter amplitude profile, which displays a clear periodicity in its shape. This is attributed to the method of preparation of these gelatin models where the particle-laden segment was created by individually immobilizing a 0.1 cm layer. Moreover, since only three frames were recorded, the periodicity is not suppressed. This periodicity is also transferred into the reconstructions. However, the periodicity seems to be diminished in the "multiply

scattered" section of the signal. Two reconstruction curves are considered, both of which were extracted by the stepwise reconstruction approach.

The first reconstruction (green diamonds) is based on the calibration curves in Figure 4.10. Four distinct regions can be identified for this reconstruction. In the first region, the reconstruction seems to work pretty accurately, apart from the periodic fluctuations (mean absolute error = 5.3 $\times 10^{-3}$, or 9% in a relative sense). This happens as the peak backscatter amplitude for this case (large red diamond in Figure 4.10) nearly coincides with the curve fit (dashed red line). However, problems begin to arise in the compensation step of the stepwise reconstruction technique. As can be seen in the calibration curves, the amplitude attenuation rate for the phantom (large blue circle) is higher than predicted by the curve fit (for the volume fraction of the phantom, dash-dotted blue line). Due to this, the attenuation losses are undercompensated, which further leads to an underestimation of the volume fraction. Furthermore, this error propagates monotonically. This issue is highlighted in the second region. The error in the initial underestimation propagates slowly (0.4 – 0.8 cm), while it accelerates after a certain point (0.8 – 1.0 cm). This difference is caused by the different gradients in the calibration curve for the peak backscatter amplitude. The peak backscatter amplitude is more sensitive to volume fraction changes at lower volume fractions than for higher ones. The negative consequence of multiple scattering on the volume fraction profile reconstruction is visible in third region. Despite the absence of particles, a volume fraction profile is calculated, whose effect persists for approximately 0.4 cm. Finally, in the fourth region, an artefact caused by the bottom wall of the container becomes visible in the volume fraction profile.

The second volume fraction profile (magenta circles) is also built up using the stepwise reconstruction approach. However, in this case, the calibration curve for the attenuation rate has been artificially increased (by 2.5 dB/cm) so that the attenuation rate predicted by the curve fit nearly coincides with the attenuation rate of the phantom (dotted blue line). The reconstruction that follows resembles the step function much better. The mean absolute error for this reconstruction over regions 1 and 2 is 6.4×10^{-3} (11% in a relative sense) as compared to 18.2×10^{-3} (31% in a relative sense) for the previous one. This is due to the absence of errors caused by under/over-compensation for attenuation losses. However, in this case, the effect of multiple scattering lingers on much deeper into the model (> 1 cm).

This example already provides two major conclusions. Firstly, multiple scattering can contaminate the volume fraction profile reconstruction, and can blur gradients. Secondly, the goodness of the calibration curve fits is critical for the accuracy of the reconstruction. In these gelatin models, the quality of the calibrations were lower owing to the limited number of measurements, as well as the absence of moving particles. However, if calibration is performed in a suspension with moving particles (as will be done in the next section), the quality of the statistics is expected to improve. It is unmistakable that the quality of the backscattered signal in the gelatin model and the subsequent reconstruction is noisy. In our experience, despite careful, repeated attempts, such issues persist in the gelatin models, highlighting a shortcoming of the models themselves. Nevertheless, these models also help appreciate the limitations of the entire process in obtaining an accurate volume fraction profile.

4.5. Application to particle-laden pipe flows

4.5.1. Background to radial migration in particle-laden pipe flows

A very common application of ultrasonic particle volume fraction profiling is studying the flow of heavy particles (see Section 2.2.3). This is typically accompanied with monotonically increasing particle concentration with depth. Here, we apply the technique to particle-laden pipe flows of a neutrally buoyant suspension, which is accompanied by a non-monotonic concentration profile. A practical application of this specific flow can be found in solid-liquid food flows (Lareo, Branch, and Fryer, 1997; Lareo, Nedderman, and Fryer, 1997).

This non-monotonicity is associated with the phenomenon of inertial migration/focusing, especially observed for a suspension with large particles in laminar flows. The reader interested in a detailed understanding of the phenomenon is directed to the seminal works of Segré and Silberberg (1962), Matas, Morris, and Guazzelli (2004) as well as the recent works of Morita, Itano, and Sugihara-Seki (2017) and Nakayama *et al.* (2019). As summarized by Nakayama *et al.* (2019) for a dilute suspension: at low Reynolds number, particles are focused at the so called - Segré-Silberberg annulus, approximately 0.3 pipe diameters away from the pipe axis. Upon increasing the Reynolds number, this annulus moves towards the wall, while another annulus concentrated with particles begins to appear closer to the pipe axis, the so called inner annulus. At even higher Reynolds numbers, the Segré-Silberberg annulus ceases to exist, and particles aggregate only at the inner annulus. Moreover, this phenomenon requires an extremely long development length (over a thousand pipe diameters).

The above is valid for dilute suspensions ($\phi \sim 10^{-4}$) with non-existent particle-particle interactions, where the suspensions were studied by standard optical means. The migration of particles away from the axis is attributed to fluid-particle interactions. Endeavours at studying this phenomena at higher volume fractions ($0.06 \leq \phi \leq 0.45$), albeit at much lower Reynolds numbers have also been made, with techniques such as refractive index matching (Koh, Hookham, and Leal, 1994), electrical impedance tomography (Butler and Bonnecaze, 1999), as well as magnetic resonance imaging (Hampton *et al.*, 1997; Han *et al.*, 1999). A common qualitative observation, at least for $\phi \geq 0.20$, was the migration of particles towards the pipe axis, which is attributed to particle-particle interactions. As a consequence of this migration towards the pipe axis, the velocity profile changes from a parabolic shape to a blunted one.

4.5.2. Experiments

We apply the stepwise reconstruction technique to particle-laden pipe flows for a wide span of Reynolds numbers and bulk volume fractions (laminar, intermittent as well as turbulent regimes for $0 \leq \phi_{\text{bulk}} \leq 0.09$). All experiments are performed in a plexiglass pipe with an internal diameter of $D = 10.00$ mm with a neutrally buoyant suspension composed of Polystyrene particles (diameters, $d_p = 530 \pm 75$ μm) in a salt-water solution, resulting in $D/d_p \approx 18.9$. The flow is gravity-driven with the flow entering the tube from a reservoir via an inlet chamber and measurements are performed $195D$ downstream of the inlet. A

slightly adapted version of this facility was also utilized in the study of Hogendoorn and Poelma (2018).

A different ultrasonic apparatus is used in the experiments shown below, namely a Verasonics Vantage 128 in combination with a linear probe (L11-5v). This transducer too has 128 individual piezoelectric elements spanning ~ 3.9 cm. The ultrasound transducer is immersed in a water bath surrounding the pipe, to aid acoustic coupling. Imaging is performed with an ultrasonic central frequency of 10.5 MHz. Data are sampled at 62.5 MHz with a 14-bit resolution. This apparatus provides an alternative to the conventional ultrasound imaging techniques: plane-wave imaging. This change is warranted by the fact that turbulent flows are extremely dynamic processes involving small time-scales. In order to study such flows, the plane-wave imaging technique offers the possibility to acquire images in the kilohertz range and accurately quantify the turbulent characteristics of the flow (Hogendoorn and Poelma, 2019). The post-beamformed RF data were further converted to B-mode images, which were then utilized for the volume fraction profiling. B-mode images are more readily accessible and are commonly used for velocimetry analyses. For each experiment, at least four separate measurements were made consisting of 10000-20000 images recorded at 400-4000 frames per second. For the calibration cases, all recordings were at 4000 frames per second. In order to assess the repeatability, the flow was stopped and restarted between each of the four ensembles.

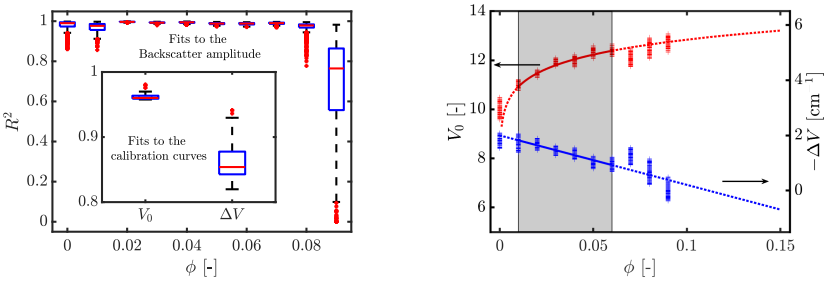

Figure 4.11: Characteristics of the empirical fits for particle-laden pipe flow. (*Left*) Coefficient of determination for linear fits to the backscatter amplitude profile. The values in the inset are the coefficients of determination for the fits to the peak backscatter amplitude and the amplitude attenuation rate. (*Right*) Calibration curves–power law for the the peak backscatter amplitude and first order polynomial for the amplitude attenuation rate. Individual markers represent the individual 128 piezoelectric elements and the lines are based on the mean value.

4.5.3. Calibration in uniform suspensions

Before applying the technique to non-uniform suspensions, calibration parameters (peak backscatter amplitude and amplitude attenuation rates as a function of bulk volume fraction) were estimated for each of the 128 transducer elements, as shown in Figure 4.11. The scatter in the estimated coefficients suggests that using a calibration for each individual element instead of a global statistic such as a mean/median would improve the accuracy of the reconstruction. For the present discussion, calibration fits are performed only for $0.01 \leq \phi \leq 0.06$ by fitting a power law for the peak backscatter amplitude and a first order polynomial to the amplitude attenuation rate. These curves are extrapolated to the range

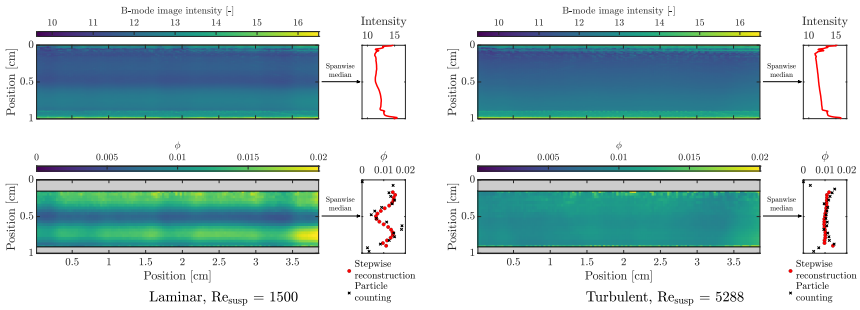

Figure 4.12: Comparison of time-averaged B-mode intensity images and reconstructed particle volume fraction profiles from the calibration. Two cases are considered, both for $\phi_{bulk} = 0.01$ – a laminar ($Re_{susp} = 1500$) and a turbulent one ($Re_{susp} = 5288$).

of $0 \leq \phi \leq 0.15$. The coefficients of determination for the linear fits to the backscatter amplitude profiles are mostly acceptable, however, this does not hold true for the calibration curves, especially for the amplitude attenuation rate. As a consequence, it can be expected that errors due to an imperfect compensation for the attenuation could accumulate/propagate and result in erroneous quantification of the volume fractions. Another observation is that the attenuation is negative and this arises due to the usage of time gain compensation (see Bushberg *et al.*, 2012, figure 14-27, for an illustrative example) which electronically increases the backscatter amplitude in depth.

4.5.4. Reconstruction in dilute suspensions: comparison with particle counting

First, we consider the reconstruction of the volume fraction profile in a dilute suspension ($\phi_{bulk} \sim 0.01$). Under such conditions, individual particles are still discernible in the image. In order to validate the stepwise reconstruction technique, a comparison of the reconstructed volume fraction was done against that from the particle counting technique. Particle counts were then converted to a volume fraction in an ad-hoc manner by assuming the bulk volume fraction of the turbulent case to be 0.01, verified as a reasonable choice by collecting a sample of the suspension.

Two representative cases are considered in Figure 4.12: one under laminar flow conditions and the other under turbulent conditions. By considering the B-mode images, a qualitative difference between the two is visible in the form of an abnormal intensity gradient under laminar conditions in the vicinity of the pipe axis (~ 0.5 cm), which becomes more evident in the spanwise median intensity profile. Such an abnormality is absent under turbulent conditions and the spanwise median intensity profile is characterized by a straight line, which is an indication of the uniformity of the dispersion that is exploited for calibration.

These differences in the image intensities translate into differences in the volume fraction reconstructions. It is vividly clear that the phenomenon of inertial migration is present under laminar conditions. Very similar profiles have been recorded in ultrasonic backscattering measurements of laminar blood flow, and has been called “black hole”

(Yuan and Shung, 1989; Qin, Durand, and Cloutier, 1998). The comparison of the reconstruction to the particle counting technique helps in the verification of this phenomenon and that it is not an artefact of the reconstruction. The mean absolute difference between the estimates by the two techniques, for these two examples, is approximately 1.5×10^{-3} (or 15% relative difference, with respect to the mean bulk volume fraction), confirming good performance by the stepwise reconstruction. In comparison, the turbulent flow has a relatively uniform distribution of particles. Thus, qualitative information about particle volume fraction profiles may also be extracted from the local echo intensity/amplitude (for example, see cluster IV in Section 2.2.3). However, for quantification purposes, the attenuation would have to be accounted for appropriately.

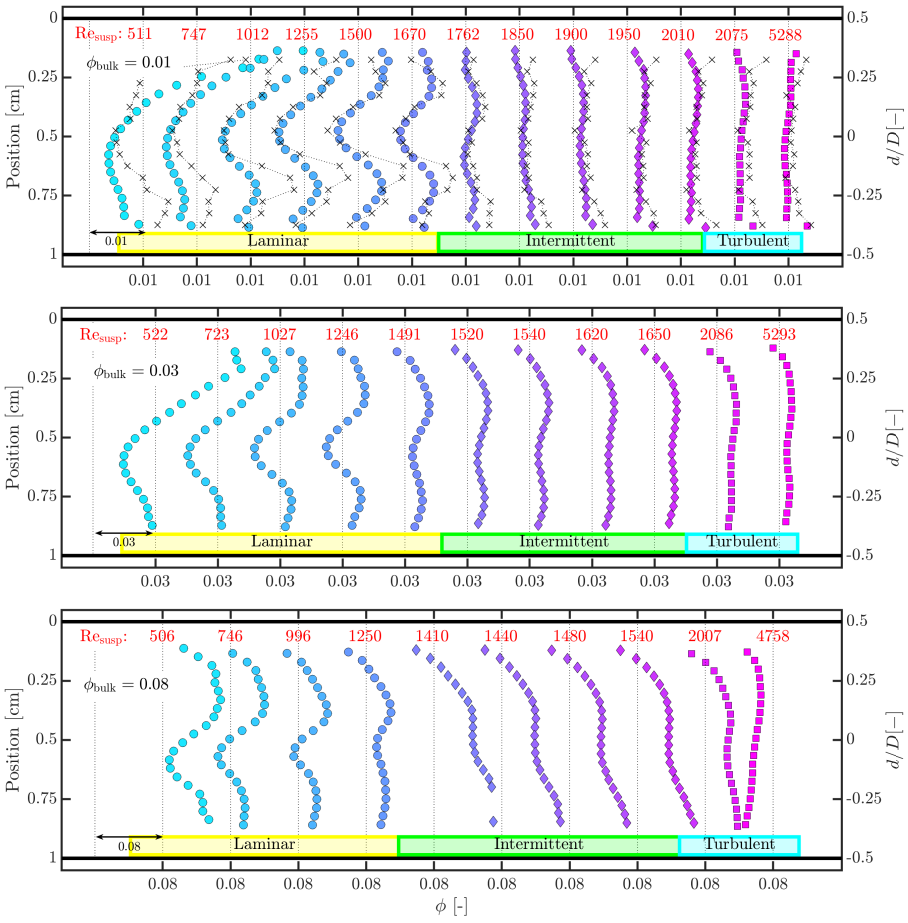

Figure 4.13: Compilation of reconstructed time-averaged particle volume fraction profiles for flows with bulk particle volume fractions of 0.01, 0.03 and 0.08. Missing markers indicate that estimated volume fraction is outside the range $0 \leq \phi \leq 0.15$. For $\phi_{\text{bulk}} = 0.01$, results based on particle counting are also shown (dotted line with crosses).

4.5.5. Application of technique to higher volume fractions

Finally, we apply the stepwise reconstruction technique to higher volume fractions, as well as to several Reynolds numbers. A detailed compilation of constructed volume fraction profiles for three bulk volume fractions is shown in Figure 4.13. The Reynolds numbers considered the entire span of flow regimes: laminar, intermittent and turbulent. These reconstructions are performed on the median intensity along the spanwise direction of the B-mode image, with help of the mean of the fitting coefficients for the 128 individual line elements. Only volume fractions in $0.01 \leq \phi \leq 0.06$ are used for characterizing the uniform suspensions, implying that all reconstructions with $\phi > 0.06$ are extrapolations (dashed lines in the right image of Figure 4.11). In the current context, all the Reynolds numbers reported here are based on the bulk velocity (U_b), pipe diameter (D), kinematic viscosity of the suspending fluid (ν_f) and relative viscosity ($\chi^e = (1+1.25\phi/(1-\phi/0.64))^2$) incorporated in them. The relative viscosity quantifies the effective viscosity of the suspension with respect to the suspending fluid and is based on a formulation first proposed by Eilers (1941). The appropriateness of this fit for the current suspension has been shown by Hogendoorn and Poelma (2018), and the Reynolds number is defined as $\mathrm{Re}_{\mathrm{susp}} = U_b D/(\nu_f \chi^e)$.

Three bulk volume fractions are considered ($\phi_{\mathrm{bulk}} = 0.01, 0.03, 0.08$), all of which may be considered in the dilute/semi-dilute regime. In the semi-dilute regime, particles are also able to interact with each other by means of hydrodynamic forces (Guazzelli and Pouliquen, 2018). Reconstruction of the volume fraction profiles for all the three cases can be characterized with a common observation. Laminar flows typically show a deficit in the volume fraction near the pipe axis with local peaking off-axis. This behaviour of reduced particle volume fractions near the pipe axis persists even for flows with low levels of intermittency (defined as fraction of flow with puffs). With increasing levels of intermittency and eventually entering the turbulent flow regime, the non-uniformity gradually diminishes, especially for $\phi_{\mathrm{bulk}} = 0.01$. While the profile for the highest Reynolds number for $\phi_{\mathrm{bulk}} \sim 0.01$ appears rather uniform, there still appears to be a weak non-uniformity for $\phi_{\mathrm{bulk}} \sim 0.03$.

The most noteworthy observation common to all three cases is the gradual disappearance of the distinct core with reduced volume fractions, upon increasing the Reynolds number. Prior to interpreting the physical significance of this observation, it is worth considering whether or how it could be affected by the various sources of error. Fortunately, the flow inherently allows us to sample more unique instances in comparison to a static gelatin model. Among the sources of error identified earlier in the chapter, the chief are: untrustworthy signal in the near-wall region, imperfect calibrations as well as multiple scattering. Errors caused by imperfect calibrations could exacerbate any errors generated by the untrustworthy signal in the near-wall region.

We start with multiple scattering. This phenomenon plays a stronger role with increasing volume fractions, and can primarily blur gradients. Thus, for $\phi_{\mathrm{bulk}} = 0.08$, the gradients may appear smoother than in reality, while this phenomenon is expected to only minimally affect the reconstructions for $\phi_{\mathrm{bulk}} = 0.01, 0.03$. The independent effect of an imperfect calibration is best visible in the reconstruction for $\phi_{\mathrm{bulk}} = 0.08$ and $Re_{\mathrm{susp}} = 4758$. This is the data used for calibration. The deviation of the actual measurement points from the extrapolated calibration curve (right subfigure in Figure 4.11)

induces an error in the reconstruction. The attenuation is overcompensated for, which leads to a gradually decreasing estimation of the particle volume fraction. For $\phi_{\text{bulk}} \sim 0.08$, $1410 \leq \text{Re}_{\text{susp}} \leq 2007$, the volume fraction profiles are accompanied with a linear trend. These could arise from an initial error in the estimation of the volume fraction, generated by the untrustworthy signal, in tandem with an inappropriate compensation of the attenuation, with the error compounding with depth. Notwithstanding this linear trend, a local minimum in the volume fraction profile appears, albeit a weak one.

As a final step to convince that the ultrasonic reconstructions are qualitatively sound, particle volume fraction profiles estimated by particle counting are also presented for $\phi_{\text{bulk}} = 0.01$. There is a good agreement between the two reconstructed profiles suggests that while there are quantitative discrepancies, reconstructions using ultrasound are qualitatively accurate. As was emphasized in Section 4.5.4, there is a direct correlation between the reconstructed volume fraction profile and the corresponding B-mode image intensities. Of course, for the lower Reynolds numbers, there is a sharp rise in the local volume fraction, which could also deteriorate the accuracy of the particle counting technique. In short, we feel that despite the various sources of error which quantitatively affect the reconstruction to varying degrees, the gradual disappearance of the distinct core with reduced volume fractions upon increasing the Reynolds number is physical.

This behaviour of the distinct core with reduced volume fractions is likely the signature of radial inertial migration of particles that have been observed in extremely dilute suspensions, under laminar conditions. Han *et al.* (1999) have observed similar concentration profiles in their magnetic resonance imaging measurements for $\phi = 0.06, 0.10$, albeit at very low Reynolds numbers (see figures 6(a), 8(a) therein*). Maude and Yearn (1967) too report a similar behaviour (see figure 9 therein†) for comparable experimental parameters ($D/d_p \approx 21.7$, $\text{Re}_{\text{susp}} \approx 480$, $\phi \approx 0.07$), but at a much lower streamwise location. In this context, it is also worthwhile to mention that such a depleted core has also been observed in numerical simulations of particle-laden laminar, channel flows for $\phi \leq 0.1$ (Kazerooni *et al.*, 2017). A key difference, however, is that the numerical simulations suggest a complete depletion unlike the present reconstructions. Of course, it must be noted that the reconstructed volume fraction profiles considered here are at a fixed distance of $195D$ downstream of the inlet. It would be worthwhile to make measurements at several locations in a longer pipe, in order to conclude whether the velocity *and* particle concentration profiles are fully developed or not.

In contrast, there are far fewer studies that explicitly report particle volume fraction profiles in the transitional‡ or turbulent flow regime for comparable experimental parameters. Our reconstructions suggest that the distinct core even persists into the transitional flow regime. Studying these regimes with multiple measurement techniques as well as fully-resolved simulations will be required for a complete understanding of the flow.

*In the online manuscript, this has been incorrectly changed to figure 7(a), 9(a)
†In the online manuscript, this has been incorrectly changed to figure 10
‡Matas, Morris, and Guazzelli (2004) in fact report *"It is also surprising to observe that the inner annulus is robust enough to survive even into the intermittent regime ..."*. This statement, however, is in the context of an extremely dilute suspension.

4.6. Conclusions and outlook

The aim of this chapter was to address the possibility to extract information on particle volume fraction profiles in dispersed multiphase flows by means of ultrasonic waves. We focused specifically on empirical approaches wherein the reliance upon theoretical models describing the interaction between ultrasound and suspensions is circumvented. Such techniques can be advantageous for studies where an available theoretical model may not be readily applicable (for example, when using linear array transducers or while investigating flow geometries with walls).

We discuss two possible ways to extract quantitative particle volume fraction profiles: stepwise reconstruction (Section 4.3.1) and dual-frequency inversion (Section 4.3.2). Both these techniques are reliant on a calibration procedure, which is performed in uniform suspensions (Section 4.2), yielding two key volume fraction dependent parameters: the peak backscatter amplitude and the amplitude attenuation rates (Figures 4.3 and 4.4). We explore the applicability of these empirical methods by, first, testing the inversion techniques on synthetically generated data (Section 4.3.3) and identify that errors generated in the near-wall regions are likely to inhibit the quantitative performance of the reconstructions, especially for the stepwise reconstruction technique.

Because of the detrimental effect of the walls, we next applied the stepwise reconstruction technique to a particle-laden gelatin model (Section 4.4). This helped appreciate the need for a prudent choice for calibration curves as well as isolate the presence of multiple scattering (Figures 4.8 and 4.10). The phenomenon of multiple scattering limits the imaging depth as well as particle loading, while also reducing the accuracy of the technique, especially for concentration gradients. Our introduction of gelatin models in the context of particle volume fraction profiling using ultrasound can be useful. However, despite careful attempts, it proved challenging to obtain good quality data.

Lastly, we apply the stepwise reconstruction technique to particle-laden pipe flows with bulk volume fraction as high as 0.08 (Section 4.5, Figure 4.13). We unveil the presence of a core with a deficit of particles, most likely associated with the phenomenon of inertial migration. This core becomes less pronounced with increasing Reynolds number, yet persisting into the intermittent flow regimes while there is also weak evidence of it sustaining into the turbulent flow regime.

The techniques presented here also have potential for being improved further. Dedicated acoustic simulation software exist (primarily from the medical field) that can be used to generate ultrasonic images. Examples include Field II (Jensen, 1997) and k-Wave (Treeby and Cox, 2010). While the former is restricted to point scatterers, the latter can also accommodate volume occupying spheres with custom properties such as mass density and speed of sound. The latter could thus serve as a possible tool for generating realistic synthetic images relevant for particle-laden flows, which could prove useful in assessing the accuracy of the particle volume fraction reconstruction techniques. Another issue that needs to be tackled is a practical manner to overcome issues arising from multiple scattering. In fact, advances along this line have already been made for static media (Aubry and Derode, 2009). And, while the profiling techniques presented here may be extended also to emulsions, bubbly flows would warrant alternative approaches (Murai *et al.*, 2009). Finally, the shape of the ultrasound beam can also be assimilated into the analysis to improve

the estimated volume fraction profiles.

In closing, this chapter highlights possible empirical approaches for quantifying/assessing particle volume fraction profiles in particle-laden flows, while also elaborating upon limiting factors that compromise the quantitative accuracy. In any case, ultrasound particle volume fraction profiling, especially in tandem with ultrasound based velocimetry, can be instrumental in unravelling the local characteristics of particle-laden flows.

4.A. Recipe for the gelatin models

As mentioned in Section 4.4, the use of gelatin as a tissue mimicking substance is a common choice. Thus, there are several works which have their own "recipe" for creating a gelatin based phantom. Below, we describe our approach and experiences concerning the procedure for creating the gelatin models.

Commonly, we start with a certain quantity of a solvent (water or aqueous glycerol) and adding food-grade gelatin powder (Dr. Oetker GmbH) in a ratio of 20 grams per litre of solvent. Supposedly, gelatin is insoluble in glycerine, and if aqueous glycerol is used as a solvent, the resulting mixture may be characterized as "a very fine gelatin sponge containing glycerine in its pores" (Ridout, 1879). The system is allowed to stay at rest for several minutes to allow the gelatin particles to swell. Hereafter, the system is stirred with the aid of a magnetic stirrer while simultaneously warming it from underneath (temperatures typically between 50 and 90 °C). The process of warming and stirring is continued until the gelatin particles dissolve and a clear, transparent solution is obtained. A few drops of Tween-20 are also added to aid the wetting of the particles that shall be introduced later. It is recommended to stir the solution at moderate rates, otherwise at higher rates air bubbles could get entrained into the solution, which can be difficult to get rid of, if the solution is highly viscous. On one occasion 50 grams of gelatin per litre of solvent was tested, which resulted in a longer waiting period for the dissolution of gelatin as well as the solution retaining a yellowish tinge, both of which are undesirable. However, this would increase the stiffness of the resulting model.

Once the solution is prepared, the desired particle-laden model can be prepared. Typically, we build up the model in thin sheets. Basically, only a very small volume of solvent is mixed with the appropriate amount of particles (based on desired volume fraction) and is added to the container corresponding to a sheet with a thickness of about 1–1.5 mm. An exception to this is the bottom clean segment, or segment C, in Figure 4.8 which is created in one iteration. The boundaries between the sheets are sometimes clearly visible in the ultrasound images, implying marginal acoustic impedance variations across the sheets. A few drops of food color can also be introduced to create an easy visual reference of the model (Figure 4.1). Hereafter, this sheet of solution is allowed to gel by placing the container in a refrigerator (~ 5°C). The sol-gel transition temperature has been found to be in the range of 20–30 °C (Parker and Povey, 2012). One thing that could occur, while adding the solution, especially with a syringe or pouring from a height, is the entrapment of air bubbles. Thus, it is recommended to introduce the new batch of solution as gently as possible. In case it is difficult to remove any bubbles, they are pushed to one of the walls and eliminated with the help of a spatula. The temperature of the to-be-added solvent should be optimal (60–70 °C in our experience). If it is too low, it is highly viscous

and does not spread readily over the gel surface and gels quickly, resulting in an uneven surface. On the other hand, if the new solution is too hot, it could erode the gel surface underneath. Typically, the transition of the newly introduced solution to gel would take only a few minutes for thin sheets. If insufficient time is allowed for this solidification process, particles can move across sheets of solutions, in case there are density differences between the particles and the gelatin solution.

Often, we prepared several containers, with varying profiles, simultaneously. As a result, it is not uncommon that this process lasted over days. The warm solution is stored overnight in a refrigerator which turns into a gel and is warmed back into a solution the following day, prior to recommencing with the construction of these gelatin models. Thus, all equipment, such as beakers and syringes, that have been contact with gelatin solution, are washed and soaked overnight to deter the accumulation of gelatin clumps. It must be noted that these models have a lifetime in the order of a few weeks (if refrigerated regularly, while not in use) as gelatin is susceptible to microbial growth. The gelatin surface that shall be in direct contact with the ultrasound transducer is most prone to erosion and in the worst case scenario, fissures may appear in the models, which is further exacerbated after the model is cooled in the refrigerator. Once the model has been used or microbial growth appears, it is disposed off in the gel state.

The above process can be optimized further. For example, if an extremely accurate construction of models is desired, then the physical properties of the gelatin, such as mass density and speed of sound, as a function of gelatin concentration as well as temperature can be accounted for (Davis and Oakes, 1922; Parker and Povey, 2012). Moreover, the lifetime of these models can be increased further by additives that could prevent bacterial invasion, such as p-methyl and p-propyl benzoic acid. Alternative techniques can be developed as well, with totally different ingredients (Culjat *et al.*, 2010). In fact, we also attempted to create similar models by suspending particles in ultrasound transmission gel (Aquasonic). An advantage of using ultrasound transmission gel over gelatin would be the lower absorption of sound. While the particles could be immobilized due to the high viscosity of the ultrasound transmission gel ($\approx 10^5$ times higher than water), the model is not stiff and is easily eroded upon contact with the transducer. Finally, the constructed gelatin models can be imaged in X-ray CT scanners to assess the construction and the true distribution of particles (for example, it is not uncommon to have more particles accumulate in the bulk rather than nearby the container walls).

5

Ultrasound Imaging Velocimetry in particle-laden flows: counteracting attenuation with correlation averaging

Ultimately, the experimenter only needs to make measurements that are "good enough" to answer the questions posed, and the quest for an optimum measurement can often stop short of the true optimum.

Adrian and Westerweel (2011)

Ultrasound imaging velocimetry (UIV) refers to the technique wherein ultrasound images are analysed with 2D cross-correlation techniques developed originally in the framework of particle image velocimetry. Applying UIV to opaque, particle-laden multiphase flows has long been considered to be an attractive prospect. In this study, we demonstrate how fundamental differences in acoustical imaging, as compared to optical imaging, manifest themselves in the 2D cross-correlation analysis. A chief point of departure from conventional particle image velocimetry is the strong variation in the intensity profile of the acoustic wavefield, primarily caused by the attenuation of ultrasonic waves in particle-laden flows. Attenuation necessitates using a larger ensemble of correlation planes to obtain satisfactory time-averaged velocity profiles. For a given combination of imaging and flow conditions, attenuation sets upper limits on volume fraction, penetration depth, as well as temporal resolutions that may be accessed confidently. This behaviour is evident in two experimental datasets and is also supported by a

An abridged version of this chapter has been published in Dash *et al.* (2022). 'We' in this chapter refers to the four authors - Amitosh Dash, Willian Hogendoorn, Gosse Oldenziel, and Christian Poelma.

modified cross-correlation theory. The modification is brought about by incorporating a lumped model of ultrasonic backscattering in suspensions into existing spatial cross-correlation analysis. The two experimental datasets correspond to two distinct particle-laden pipe flows: (1) a neutrally buoyant non-Brownian suspension in a laboratory scale flow facility, wherein particle sizes are comparable to the ultrasonic wavelength and (2) a non-Newtonian slurry in an industrial scale flow facility, wherein particle sizes are much smaller than the ultrasonic wavelength. We illustrate how and to what extent correlation averaging can counteract the adversity caused by attenuation. The work herein offers a template for one to evaluate the performance of UIV in particle-laden flows.

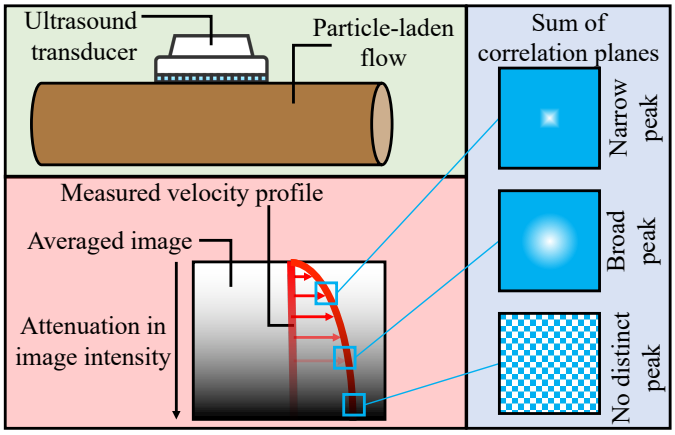

Ultrasound imaging velocimetry has limits to which it remains functional for particle-laden flows. Using ensemble correlation averaging helps one maximize the utility of ultrasound until attenuation takes over.

5.1. Introduction and scope

Particle Image Velocimetry (PIV) is a matured measurement technique and has become an integral part of the experimental fluid mechanics lexicon over the past three decades. At the heart of PIV algorithms lie spatial cross-correlation analyses, whose results are translated to velocity fields. Since the cross-correlation analysis can quantify motion in general, techniques developed for PIV have been used in several other contexts as well. One notable example is its application to ultrasound images, commonly referred to Ultrasound Imaging Velocimetry (UIV) or echo-PIV (Poelma, 2017).

Unlike the technology developed for PIV, commercially available ultrasound imaging systems are developed for medical imaging on the scale of human bodies, and not for fluid mechanics research. Thus, unsurprisingly, UIV finds its foremost applications in cardiovascular research. Nevertheless, UIV can be extended to study other forms of flows as well. In particular, the potential to study multiphase flows is a well-acknowledged advantage of ultrasonic techniques (Powell, 2008; Takeda, 2012; Poelma, 2020). This work is geared towards the application of UIV to particle-laden flows.

Owing to differences in the instrumentation and working principles, there is a key difference between the "illumination" in UIV for particle-laden flows and conventional PIV. PIV is typically used to study single-phase flows seeded with tracer particles, and the laser pulses used therein are extremely powerful. Partially owing to this, the effect of illumination intensity variation across the field-of-view, along the direction of propagation, can often be safely neglected. Of course, this assumption may break down if excessive seeding is used or if a high concentration of fluorescent dye is additionally present in the flow (Crimaldi, 2008). The above assumption of uniform "illumination" intensity is also usually valid when UIV is applied to a single-phase flow which has been seeded with tracer particles. However, when applying UIV to particle-laden flows with moderate/high particle loading (where particles are the dispersed phase and not tracers), this assumption might not hold true any more, as acoustical energy can vary strongly with imaging depth due to attenuation (absorption and/or scattering of sound). Several studies have acknowledged the negative effect of ultrasound attenuation on velocimetry of suspensions, but few have discussed it in detail (Wiklund and Stading, 2008; Kotzé, Haldenwang, and Slatter, 2008; Ricci *et al.*, 2012; Kotzé, Wiklund, and Haldenwang, 2016; Kupsch *et al.*, 2019).

Here, we take a closer look at the performance of UIV for particle-laden flows, especially how attenuation appears in the processing chain. We do so by considering two distinct particle-laden pipe flows: one at laboratory scale with the flow of neutrally buoyant suspensions, wherein particle sizes are comparable to the ultrasonic wavelength; the other at industrial scale with the flow of a non-Newtonian slurry, wherein particles are far smaller than the ultrasonic wavelength. Experimental observations are complemented and supported by a modified cross-correlation theory for UIV in particle-laden flows. This modified theory is obtained by incorporating a lumped model of ultrasonic scattering in a suspension (Dash, Hogendoorn, and Poelma, 2021) in the cross-correlation theory developed for PIV by Keane and Adrian (1992). This allows us to form heuristic arguments on the performance of UIV for particle-laden flows.

This work is aimed at researchers who consider using UIV to study particle-laden flows. We intend to convince the reader on the existence of ceilings for particle loading,

imaging depths, and temporal resolutions that can be accessed confidently using UIV. Using the modified cross-correlation theory and two experimental case studies, we provide a template on how one can assess UIV results in particle-laden flows. Specifically, we wish to show why and how ensemble correlation averaging is the best way to compute time-averaged velocity profiles. Being aware of the extents to which UIV returns acceptable results ensures that one can possess foresight on the accessible parameter space, prior to planning an extensive measurement campaign.

The chapter is arranged as follows: In Section 5.2, we modify theoretical formulations for spatial cross-correlation analysis developed for PIV, by including characteristics of ultrasonic scattering induced by the presence of particles. After describing the two distinct experimental flow configurations in Section 5.3, we discuss the quality of the experimental results in Section 5.4. In Section 5.5, we present case studies illustrating the extents to which UIV can diagnose academically and industrially relevant flows. The quality of the results in the case studies are discussed in the framework of the foregoing sections. We end by summarizing our main findings in Section 5.6.

5.2. Extending cross-correlation theory to UIV for particle-laden flows

In this section, we incorporate a simple, lumped model of ultrasonic backscattering in a suspension, which we evaluated in an earlier study (Dash, Hogendoorn, and Poelma, 2021), into the cross-correlation theory developed for single-exposure, double-frame PIV systems (Keane and Adrian, 1992). The reader interested in an extensive discussion on the theory of PIV cross-correlation in Section 5.2.1 is directed to sections 3.4 and 8.2 in Adrian and Westerweel (2011).

5.2.1. Cross-correlation theory for single-exposure, double-frame PIV

Over its history, PIV has been operated in several modes. Here, we consider single-exposure, double-frame PIV, as it is most relevant from the perspective of UIV. While performing spatial cross-correlation of two single-exposure images, one is interested in the location of the peak that represents the particle displacement. The height of this signal peak, $\mathscr{R}$, should ideally stand out compared to random correlations, which are commonly referred to as noise peaks.

Under the assumption of homogeneous distribution of tracer particles, no local variation of mean image intensities, as well as no local presence of strong velocity gradients, the ensemble average of the correlation of the intensity fluctuations, $\mathscr{R}$, for a given fixed flow field, can be given by Equation (5.1).

$$\mathscr{R} = P\, \mathscr{I}^2\, N_I\, F_I\, F_O\, \tau_{00}^2 F_\tau \tag{5.1}$$

There are several terms on the right hand side which contribute to the signal peak.

1. P is the number of correlation planes added. Conventionally, it is unity. This is a special term and its significance will be explained later in this section.

2. $\mathcal{I}$ is the intensity of illumination. The exponent of two appears since two images are cross-correlated.

3. N_I is the image density and is directly proportional to the number density of tracers. This number is typically optimized. Very low values would lead to poor PIV results while very high values might bring about speckle and/or multiphase flow effects.

4. F_I is the in-plane loss of correlation, and is inversely proportional to the in-plane displacement of particles. Values close to unity can be achieved with advanced interrogation techniques.

5. F_O is the out-of-plane loss of correlation, and is inversely proportional to the the out-of-plane displacement. These losses are caused by particles leaving the measurement volume and thus cannot be accounted for in the data-processing stage.

6. $\tau_{00}^2 F_\tau$ represents the particle image self-correlation. It is also known as Optical Transfer Function and is related to the shape of the particle image. In short, the shape of the displacement-correlation plane will be the convolution between the displacement distribution and this term.

Thus, in conventional planar PIV, based on Equation (5.1), rules of thumb have been defined for $N_I F_I F_O$, posing constraints on three of the terms (see Scharnowski and Kähler, 2020, for a recent review). Westerweel (2008) has extended the above theoretical formulation to include the effect of velocity gradients in an additional term F_Δ. Similarly, Scharnowski and Kähler (2016) have extended it to include the effect of spatially-invariant image noise in F_σ. The latter is relevant for the present study, and we shall discuss this in more detail later.

Time-averaged velocity results from PIV measurements can be obtained in several ways (see Meinhart, Wereley, and Santiago, 2000, Figure 1 therein). Vector averaging (average of instantaneous velocity measurements) is commonly used in turbulent flows. An alternative is the correlation averaging technique wherein all the displacement-correlation planes are summed prior to obtaining the time-averaged velocity field. Correlation averaging was primarily introduced to improve velocity estimation in case of poorer signal-to-noise ratios (Santiago *et al.*, 1998; Delnoij *et al.*, 1999). Basically, by adding several correlation planes, the desired signal peak continues to add up and grow, while the undesired noise peaks cancel out. The presence of turbulence will result in broadening of the correlation peak (Kähler, Scholz, and Ortmanns, 2006). The term P in Equation (5.1) represents the ensemble size to obtain correlation averaged results.

5.2.2. Interaction between ultrasonic waves and suspensions

While the theory of cross-correlation for PIV has been derived from first principles, we only consider a lumped model which encapsulates the nature of ultrasonic backscatter in a suspension. There are more rigorous models that express the interaction between acoustic waves and suspensions (Thorne and Hanes, 2002), but these have been primarily derived for dilute suspensions of sediment being probed by a single-element ultrasonic transducer. The lumped model allows one to evaluate arbitrary suspensions using linear array transducers (arbitrary beamforms).

This lumped model consists of two terms: the peak backscatter amplitude, $\mathcal{I}_0$, and the amplitude attenuation rate, $\Delta.\mathcal{I}$. The first term represents the acoustic energy backscattered by the initial layer of particles of a uniform suspension. The second term represents the decay of acoustic energy per unit length in the axial direction, for waves propagating through a uniform suspension. The magnitude of these two terms typically increases with increasing volume fraction, ϕ, of the suspension. For simplicity, we do not consider multiple scattering (Tourin, Fink, and Derode, 2000; Snieder and Page, 2007). This phenomenon nullifies the assumption that the time of a received signal can be converted to a corresponding depth. Moreover, we do not include propagation in the acoustic coupling medium, the wall materials, and specular reflections at walls (Wang *et al.*, 2003). Including the role of other factors such as measurement volume, image pre-processing (envelope detection, log-compression), electronic time gain compensation would require a detailed, quantitative description of the fundamentals of acoustics and ultrasound imaging electronics.

Assuming a general, heterogeneous distribution of particles, $\phi(z)$, across the imaging depth axis, z, the generalized backscatter profile can be defined by Equation (5.2). The ultrasound transducer is located at $z = 0$. This is analogous to equations 7, 8 in Thorne and Hanes (2002) and equation 5 in Saint-Michel *et al.* (2017). See Figure 5.1(a) for the corresponding coordinate system.

$$\mathcal{I}(z) = \mathcal{I}_0(\phi(z)) \cdot \exp\left(- \int_0^z \Delta.\mathcal{I}(\phi(z'))\mathrm{d}z' \right) \tag{5.2}$$

This means that the intensity of the ultrasonic wave corresponding to the depth z is composed of two parts. The prefactor is directly related to the volume fraction of particles at depth z. The exponential term, on the other hand, is related to the distribution of particles between the transducer and depth z.

The above equation resembles a Beer-Lambert law, but with one difference: the prefactor is not a constant. Typical Beer-Lambert laws are based solely on attenuation of beams between a separate transmitter and receiver. In such cases, the prefactor is the initial energy deposited. On the other hand, ultrasound imaging (pulse-echo) is based on backscatter, with the same instrument functioning as a transmitter and receiver. Thus, the prefactor is a depth-dependent variable.

5.2.3. Cross-correlation theory for UIV of particle-laden flows

Due to the many differences between UIV for particle-laden flows and conventional PIV, several changes can arise in Equation (5.1) by incorporating Equation (5.2).

1. $\mathcal{I}^2$: This term needs to be adapted in the axial direction of imaging based on Equation (5.2).

2. N_I: This term is now dictated by the particle-laden flow itself. In particle-laden flows, the dispersed phase is generally used for velocimetry and no additional tracer particles are introduced.

3. $\tau_{00}^2 F_\tau$: Ultrasound images of particles are sensitive to several factors. For example, the image of a point target is sensitive to its location in the insonified region (see Ortiz, Chiu, and Fox, 2012, Figure 2 therein). Particle image shapes can also be sensitive to the relative wavelength defined as $2\pi a/\lambda$, where a is the particle radius and λ is the ultrasonic wavelength (see Baddour et al., 2005, Figure 4 therein).

4. P, F_I, F_O: There is no major change.

For the following discussion only, we assume ϕ to be invariant in z such that particles are uniformly distributed with a bulk volume fraction ϕ_b. Moreover, we introduce the exponent α for ensemble size P, whose significance will be shown later. Typically, α is unity. Combining all of the above yields Equation (5.3).

$$\mathscr{R} = P^\alpha \, \mathscr{J}_0(\phi_b)^2 \exp(-2\Delta\mathscr{J}(\phi_b) z) \, N_I \, F_I \, F_O \, \tau_{00}^2 F_\tau \tag{5.3}$$

As a next step, we take a logarithm on both sides of the above equation, and assume F_I and F_O to be unity, aiding its physical interpretation. This yields:

$$\begin{aligned} \log \mathscr{R} = \underbrace{\alpha \log P}_{\text{A}} + \underbrace{2 \log \mathscr{J}_0(\phi_b)}_{\text{B}} - \underbrace{2\Delta\mathscr{J}(\phi_b) z}_{\text{C}} \\ + \underbrace{\log N_I}_{\text{D}} + \underbrace{\log \tau_{00}^2 F_\tau}_{\text{E}} \end{aligned} \tag{5.4}$$

The contribution of the different factors on the displacement-correlation peak ($\mathscr{R}$) can thus be segregated as follows:

1. $P \uparrow \implies \mathscr{R} \uparrow$: By summing more correlation planes (term A), the height of the peak should rise.

2. $z \uparrow \implies \mathscr{R} \downarrow$: By going deeper into the imaging plane, more acoustic energy is lost due to attenuation. As a result, the signal-to-noise ratio of the displacement-correlation plane may drop (term C). In flows with low image density (term D), the particle self-correlation term (term E) may also be dependent on z.

3. $\phi_b \uparrow \implies \mathscr{R} \updownarrow$: The effect of adding particles into the flow is ambiguous. Increasing ϕ_b usually increases the magnitudes of $\mathscr{J}_0$ and $\Delta\mathscr{J}$, which have opposing effects on $\mathscr{R}$ (terms B, C). Since term C also includes z, increasing ϕ_b is likely to create a stronger gradient in the quality of the cross-correlation planes along the imaging depth. Increasing ϕ_b also increases N_I (term D) which contributes positively to $\mathscr{R}$. Thus, for a fixed a and λ, there shall be a critical ϕ_b wherein the imaging will switch from particle-image to speckle mode (term E).

4. a (for fixed λ, either fix ϕ_b or N_I): The effect of modifying the particle size on $\mathscr{R}$ is difficult to generalize. Increasing a increases the relative wavelength, $2\pi a/\lambda$, which can have a strong effect on $\mathscr{J}_0$, $\Delta\mathscr{J}$, and the particle image shape (terms B, C, E). The magnitude of both $\mathscr{J}_0$ and $\Delta\mathscr{J}$ are expected to rise with increasing a, especially when N_I is held constant. When a is increased while holding ϕ_b constant,

N_I reduces (term D) in addition to effects on other terms as well (terms B, C, E). In such a scenario, there will be a critical a wherein the imaging will switch from speckle to particle-image mode.

5. λ: The ultrasonic wavelength primarily influences the displacement-correlation plane via $\mathcal{J}_0$, $\Delta\mathcal{J}$, and the particle image shape (terms B, C, E). Since the imaging resolution is dependent on λ, it could also affect N_I (term D) and thus the imaging (particle-image/speckle mode). Generally, a larger wavelength leads to better penetration (reduced attenuation).

The above discussion serves as a starting point for explaining the quality of the experimental data.

Scharnowski and Kähler (2016) investigated the effect of spatially-invariant image noise on PIV results. They do so by introducing a new term, F_σ, and formulating a general approach to quantify the effect of image noise from autocorrelation planes. To simulate the effect of image noise in experiments, the authors reduce the power contained in the laser pulses. In comparison to the above work, there are a couple of differences in our approach. For starters, the illumination intensity in UIV is non-uniform and depth-variant. Moreover, we directly incorporate the effect of noise into the intensity illumination term already present in Equation (5.1), instead of using the autocorrelation.

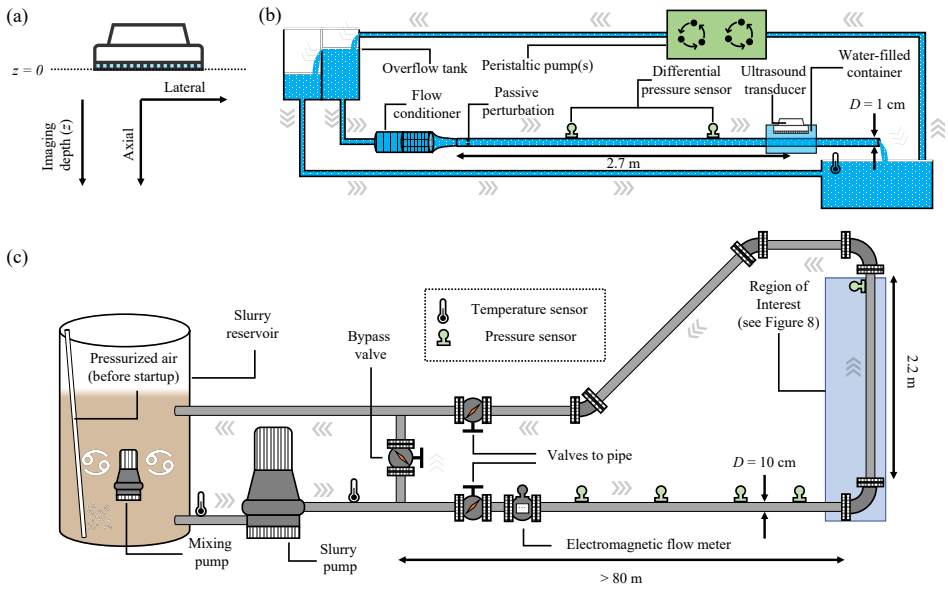

Figure 5.1: (a) Coordinate system for ultrasound imaging and global overview of experimental setups: (b) Laboratory scale (c) Industrial scale.

5.3. Experimental datasets: particle-laden pipe flows

With the modified cross-correlation theory for UIV in particle-laden flows being established in Section 5.2, we now consider two experiments. One of the experiments is at a laboratory scale (total system volume ~10 litres, pipe length ~3 meters) focusing on fundamental aspects of particle-laden pipe flows, while the other is at an industrial scale (total system volume ~4000 litres, pipe length ~85 meters) focusing on an applied aspect of particle-laden pipe flows. Shown in Figure 5.1 are schematics of the experimental facilities, while key differences are presented in Table 5.1.

Table 5.1: Key differences between the experiments.

Characteristic	Laboratory	Industrial
Particle	Polystyrene	Kaolinite
Shape	Spherical	Irregular
a	265 μm	2.5 μm
Particles per cm^3	100 – 2000	$\mathcal{O}(10^{10})$
Pipe wall	PMMA	PVC
Wall thickness	1 mm	5 mm
Imaging system	Parallel	Sequential
λ	143 μm	148 or 296 μm
$2\pi a/\lambda$	11.6	0.10 or 0.05

While these two examples represent two distinct scales of experimental setups, the examples also represent two distinct scales from the perspective of interaction between ultrasonic waves and suspensions. The relative wavelength ($2\pi a/\lambda$) in acoustics is analogous to that in optics with three regimes: long-wavelength / Rayleigh scattering ($2\pi a/\lambda \ll 1$), intermediate-wavelength / Mie scattering ($2\pi a/\lambda \approx 1$), short-wavelength / geometrical scattering ($2\pi a/\lambda \gg 1$).

5.3.1. UIV at laboratory scale

An open question in fundamental fluid mechanics is how the addition of particles affects the laminar-turbulent transition in a pipe flow. To be specific, the particles are rigid, spherical, and their mass density is equal to that of the carrier fluid. A pipe flow facility was constructed for investigating this question. The measurements herein were performed to extend on the findings of Hogendoorn and Poelma (2018), with the goal to extract turbulence intensity profiles in these suspension flows (using the technique reported by Hogendoorn and Poelma, 2019).

In short, a precision glass pipe with an internal diameter of 10.00 mm is laden with suspensions of varying bulk volume fractions. The carrier liquid is a saline water mixture and the dispersed solids are polystyrene spheres with diameters of $530 \pm 75\mu$m. An ultrasound imaging system (Verasonics Vantage 128) collects raw data for UIV at high temporal resolution (400-4000 frames per second). The system is coupled to a linear array transducer (L11-5v) of 128 elements with a pitch of 0.3 mm and an elevation focus at 18 mm. Ultrasound frequencies of 10.5 MHz are used. Data are sampled at 62.5 MHz with a 14-bit resolution. Image acquisition is performed in parallel, meaning all elements transmit ultrasonic pulses and later receive echoes simultaneously. Four sets of 10000 images are collected. At the location where ultrasound images are recorded (270 pipe diameters downstream of the pipe inlet), the glass pipe is replaced by a plexiglass pipe (internal diameter = 10 mm) to reduce reflection losses caused by the higher acoustic impedance difference between glass and water. Acoustic coupling between the transducer and the pipe is obtained via a water filled container surrounding the pipe.

5.3.2. UIV at industrial scale

To move towards a new generation of sustainable sanitation systems, one of the proposed ideas is to transport domestic wastewater without the conventional technique of dilution with excessive water. Due to the concentrated nature of the domestic slurry, it often is non-Newtonian in nature, for which hydraulic design data is sparse. To this end, a pipe flow facility was commissioned at Deltares ('β-loop') to study the flow of non-Newtonian slurries. The slurry in the facility mimics the non-Newtonian behaviour of concentrated wastewater. The measurements herein extend upon the work of Thota Radhakrishnan *et al.* (2021). Based on figures 7(b), 15(a) of Pullum, Boger, and Sofra (2018), pipe flows with bulk velocities between 1.5–5 m/s and pipe diameters ≥10 cm can be categorized as industrially relevant.

In short, a PVC pipe with an internal diameter of 100 mm is laden with a non-Newtonian slurry. A long horizontal pipe section (>800 pipe diameters) is followed by a 90° bend, after which the pipe is vertical for a length of 22 pipe diameters. This is followed by another 90° bend after which the slurry returns to the reservoir. In the reservoir, pressurized air is released to resuspend the settled slurry prior to the startup of the flow loop. During measurements, a mixing pump is used to prevent any settling of particles in the reservoir. Kaolin(ite), a form of clay, is mixed in tap water to form the slurry (21% w/w or 9% v/v). The particles are fine with a median size of 5.18 μm. The slurry has a mass density of 1152.1 kg/m^3 and its non-Newtonian behaviour can be characterized by the Herschel-Bulkley model ($\tau = \tau_y + K\dot{\gamma}^n$). The parameters for the model are determined via a rheogram between the shear stress, τ, and the shear rate, $\dot{\gamma}$. The slurry has a yield stress of $\tau_y = 0.8889$ Pa, a consistency index of $K = 0.1579$ Pa·s$^{0.4579}$, and a behaviour index of $n = 0.4579$ at 18°C. In the present study, we focus on the flow near the first 90° bend. The ratio between inner radius of the pipe and radius of curvature of bend is approximately 0.23. Further details are provided in Section 5.5.2.

Raw data for UIV was acquired using sequential beamforming techniques with a SonixTOUCH Research (Ultrasonix/BK Ultrasound). This imaging system is coupled to a linear array transducer (L14-5/38) of 128 elements with a pitch of 0.3 mm and an elevation

focus at 16 mm. Acoustic coupling between the ultrasound sensor and the pipe is achieved with Aquasonic 100 gel (Parker laboratories, Fairfield, NJ, USA). A custom "aligner" is 3D-printed, which allows for an accurate placement and alignment of the ultrasound transducer with respect to the pipe wall. The transducer is placed in the backward sweep mode (beam sweep direction opposite to flow direction). This is chosen over the forward sweep mode to obtain reduced particle displacements (Zhou *et al.*, 2013). Images are acquired until depths of 60 mm with a single transmit focus set at 45 mm. Measurements are performed in the 'Penetration' mode (ultrasound pulses with central frequency of 5 MHz and 2 cycles long) or 'Resolution' mode (ultrasound pulses with central frequency of 10 MHz and 1 cycle long). Moreover, a sector of 50% and line density of 64 was used to obtain imaging rates of 287 frames per second. Data are sampled at 40 MHz with a 16-bit resolution. Five sets of 2503 images are collected.

5.3.3. Data processing

For both sets of experiments, B-mode images are generated from the raw data. For the industrial scale experiments, the time-averaged RF image is subtracted prior to envelope detection and log-compression to generate B-mode images. In the laboratory scale experiments, the B-mode images are first generated following which the time-averaged B-mode image is subtracted. For the laboratory scale experiments, image sizes are 128×200 pixels (lateral × axial direction), whereas for the industrial scale experiments typical sizes are 33×812 pixels.

The B-mode images are processed using a slightly modified version of PIVware (Matlab script based on Westerweel, 1993). We perform single-pass processing without any advanced techniques such as window offsets (Westerweel, Dabiri, and Gharib, 1997) or iterative image deformation (Scarano, 2001). This simplicity is maintained so that results can be directly compared, without influence of these steps. For the laboratory scale experiments, a grid of interrogation windows with sizes of 32×8 pixels are used with 50% overlap in both directions, resulting in six columns of velocity vectors. This grid is generated only between the pipe walls. For the industrial scale experiments, window sizes of either 16×24 or 32×24 pixels are used, resulting in three columns of velocity vectors. An overlap of 50% is used in the axial direction and 85% in the lateral direction. The 85% overlap is a practical necessity, given that the image size is 33 pixels in the lateral direction while the window size is 24 pixels. Doing so ensures three columns of vectors, one of which is not at the edge. The displacement-correlation peak is estimated with subpixel accuracy by fitting a 2D Gaussian function in a 5×5 pixel neighbourhood of the maximum. This choice is warranted due to peak broadening, as shall be shown later. Moreover, for the industrial scale experiments, sweep correction is warranted (Zhou *et al.*, 2013). While UIV is a 2D2C technique, for the purpose of this paper, we focus solely on the variation of the streamwise velocity along the wall-normal direction (axial direction of ultrasound images). In both cases, we pick a single column of vectors for further analysis.

Examples of instantaneous B-mode images from both experiments are shown in Figure 5.2. To obtain the mean intensity profile, the total ensemble of images (three dimensional array - lateral direction, axial direction, time) is averaged along time and lateral direction. Even though the volume fraction of the dispersed phase is 0.09 in both examples

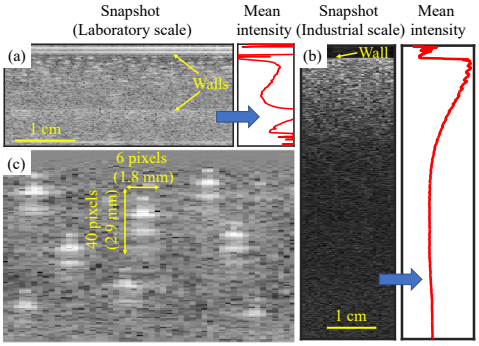

Figure 5.2: Exemplary B-mode images for a homogeneous suspension with ϕ_b = 0.09 in (a) Laboratory scale experiments and (b) Industrial scale experiments; (c) Individual particle features in the laboratory scale experiments under dilute conditions. In (a) and (b), mean B-mode image intensity profiles are also shown. The mean intensities increase to the right. In (a), the mean intensity profile is zoomed in on to show attenuation.

(Figure 5.2(a,b)), the source density in (b) is several orders of magnitude higher than in (a), owing to the finer particle sizes. In both examples, attenuation of the ultrasound signal from top to bottom is evident. Due to the differences in the relative wavelengths, it can be expected that attenuation of the ultrasonic waves is dominated by scattering processes for the laboratory scale experiments and by absorption processes for the industrial scale experiments (Dukhin and Goetz, 2001). Another visible difference is the imaging mode itself. In the laboratory scale experiments, features of individual particles are discernible at smaller imaging depths, before the image devolves into speckle-like patterns at larger imaging depths due to a mix of attenuation and multiple scattering. In contrast, for the industrial scale experiments, the slurry is visible as speckle, due to high source density.

For the laboratory scale experiments, individual particle images are rather peculiar and the spatial extent of a single particle image far exceeds its physical dimensions (Figure 5.2(c)). The shape of the particle images has clear artefacts. The topmost reflection likely corresponds to the top of the particle, whereas the others are "copies" of the same particle. For the single particle highlighted in Figure 5.2(b), the spatial dimensions of the particle image are approximately 1.8 mm × 2.9 mm. Similar observations have been made in the past, and the interested reader is directed to Section V.A. of Baddour and Kolios (2005), wherein this observation is discussed in depth. One of the explanations offered for such behaviour is the scattering regime (high relative wavelength). A negative consequence of such particle images is that it may lead to inaccuracies in the UIV analysis (via term E in Equation (5.4)).

5.4. Quality of cross-correlation results

Next, we view the quality of the cross-correlation results in the experiments through the lens of Equation (5.4).

5.4.1. Effect of ensemble size and imaging depth with fixed bulk volume fraction

We first consider a single example from the industrial scale experiments wherein the loop is operated at at a bulk velocity of U_b = 1.48 m/s. This corresponds to the turbulent flow regime and the slurry is homogeneous, i.e. ϕ is not a function of z. Moreover, the experiments are performed for a single ϕ_b. It must be noted that this velocity is higher than what is typically studied using UIV (~ 0.5–1.0 m/s). Measurements are performed in the horizontal pipe section, approximately 17 pipe diameters upstream of the 90° bend. The flow can be safely considered to be fully developed since the flow has been transported over 800 pipe diameters.

Corresponding correlation planes as a function of P and z are shown in Figure 5.3. Expectations on the basis of Equation (5.4) are qualitatively visible here. For example, the clarity of the displacement-correlation peak increases with increasing ensemble sizes and decreasing imaging depths. At the same time, this hints at the need for tens of thousands of images in order to quantify the time-averaged velocity at the pipe axis (around imaging depths of 55 mm). Moreover, with increasing imaging depths, the influence of noise grows, and can impact the accurate subpixel estimation of the displacement peak. Furthermore, if it is desired to extract Reynolds stresses from ensemble correlation averaging of UIV data (Scharnowski, Hain, and Kähler, 2012), the effect of noise would also need to be considered.

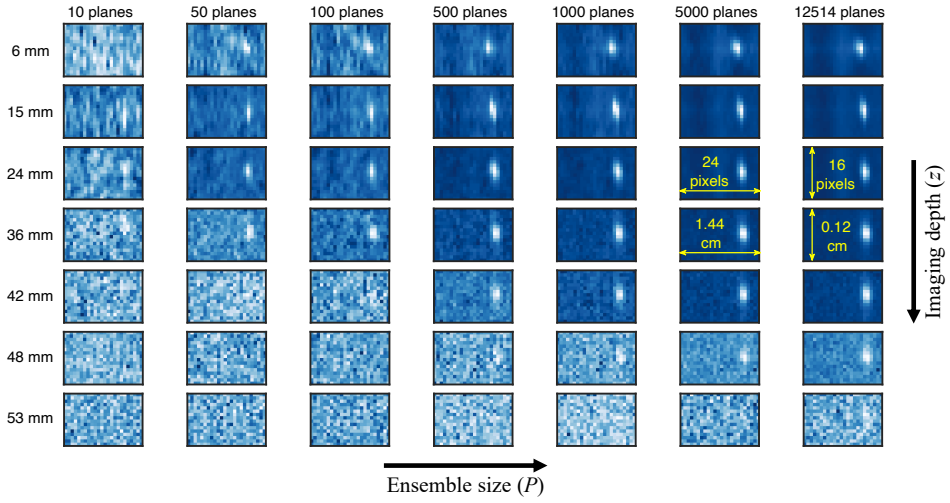

Figure 5.3: Evolution of correlation maps for the industrial scale experiments as function of P and z.

For the purpose of quantifying the quality of the correlation result, we use the metric "peak to root-mean-square ratio". We refer to this as "signal-to-noise ratio (SNR)" henceforth. While PIV traditionally relies on ratio between the two tallest peaks, a change is warranted for the present study. For starters, the peak ratio is considered an *ad-hoc* measure (Xue, Charonko, and Vlachos, 2014), and is best applicable for cross-correlation

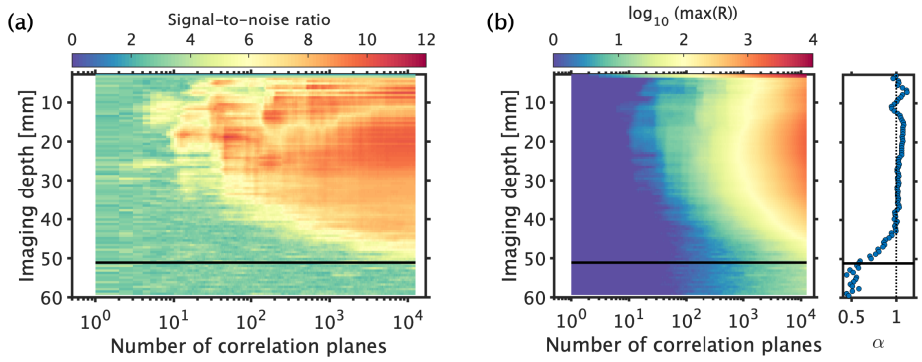

Figure 5.4: (a) SNR of summed correlation planes as function of P and z. (b) Maximum peak height as function of P and z. The panel on the right shows α as a function of z. Horizontal black lines represent the critical penetration depth for the maximum number of images analysed.

of two images (as in vector averaging). Moreover, since quality of ultrasound images is inherently low, typical peak ratio values are <2. Since we add several planes, SNR, as defined above, provides a better insight on its quality.

In Figure 5.4(a), we plot the SNR of the correlation planes as a function of P and z. This serves as a quantitative counterpart to Figure 5.3. Thus, it confirms that the quality of the cross-correlation plane improves with increasing ensemble size and decreasing imaging depths. The SNR seems to be best around imaging depths of 20 mm, while one would expect it to be better at small imaging depths. There could be a few reasons for this. The region close to the transducer falls in the "near-field" of the transducer (transmit focus is at 45 mm), where pressure amplitude characteristics of the ultrasonic waves are complex and unfavourable (see Bushberg *et al.*, 2012, Figure 14-14 therein). From the perspective of the flow, the presence of velocity gradients could also be detrimental to the SNR at imaging depths close to the pipe wall.

This plot, however, also allows one to judge whether time-resolved measurements are possible using sliding averaging (discussed later). For example, at an imaging depth of 20 mm, about 10 correlation planes are needed to obtain a SNR of approximately 6. In comparison, at an imaging depth of 40 mm, nearly 200 correlation planes are needed to obtain a SNR of approximately 6. This implies that in order to obtain identical quality of correlation planes, about 20 times more images would be required at 40 mm than at 20 mm. This is an important factor to consider prior to planning time-resolved measurements in unsteady flows.

Previously, in Equation (5.3), we introduced the exponent α for the ensemble size, P. For a stochastically stationary flow and with low levels of image noise, the exponent should be unity (see Adrian and Westerweel, 2011, Figure 8.27 therein). This would mean that adding ten correlation planes would increase the peak height tenfold. In Figure 5.4(b) we investigate whether this indeed holds true for experimental data. The contour plot therein shows the logarithm of the maximum value of $\mathscr{R}$. As expected, this value increases with increasing P (Equation (5.4)). To estimate α at each imaging depth, a linear fit is performed between $\log_{10}(\max(\mathscr{R}))$ and $\log_{10} P$. The slope of the linear fit is α.

The exponent α is the growth rate of the maximum value of the correlation plane, which is also plotted. For imaging depths up to approximately 40 mm, α is nearly unity, as expected. However, its value then gradually drops to a value of 0.5 with increasing imaging depths, after which it stays nearly constant. We speculate that the value of 0.5 is associated with additive properties of random noise. This speculation is also supported by Figure 8.27 in Adrian and Westerweel (2011), wherein the noise peak grows with an exponent of 0.65 (a value lower than unity). The depth at which the exponent becomes constant also coincides with the depth where no velocimetry results can be derived. This critical penetration depth is indicated by a horizontal black line in Figure 5.4. The short region where the exponent is $0.5 < \alpha < 1$ might represent regions where noise starts playing an increasing role. For example, the received ultrasonic backscatter corresponding to these imaging depths could be pushing close to the resolving power of the electronics, subsequently leading to lower "pixel fill ratios" and quantization errors. As a result, increasingly lower fractions of correlation planes would contribute constructively. This might represent a region where the situation is salvageable, by simply recording even more images.

As mentioned previously in Section 5.2.1, there are numerous ways to quantify the time-averaged velocity profile. Here, we consider three different ways: vector averaging, sliding correlation averaging and ensemble correlation averaging. Sliding correlation averaging represents a hybrid of the other two techniques, which allows attaining reasonably good signal-to-noise ratio while having a certain temporal resolution (Samarage *et al.*, 2012). In this example, a total of 12514 cross-correlation planes are available. The ensemble correlation average is thus based on the sum of all planes. Vector averaging is based on taking the average of instantaneous velocities evaluated by interrogating images 1-2, 2-3, 3-4 ···. Sliding correlation averaging is based on taking the average of "instantaneous" velocities evaluated by summing correlation planes 1-10, 6-15, 11-20 ···. This selection of summing 10 planes is based on the trade-off between obtaining acceptable temporal resolution and acceptable signal-to-noise ratios. Please note that 10 is not the optimal value but a typical one.

We compare the results of time-averaging from the above three techniques in Figure 5.5(a). We expect that correlation averaging yields the most accurate results on basis of Figure 5.3 (since the peak on the correlation plane begins to stand out as more planes are used). Evaluating the integral $\int_0^1 2(u(r/R)/U_b)(r/R)d(r/R)$ returns the value of 0.964 (expected value = 1), ascertaining the good performance of the correlation averaging technique. It can be seen that vector averaging as well as sliding averaging under-predict the velocity. Vector averaging, especially, performs poorly and is unreliable. Sliding correlation averaging returns lot more satisfactory results until about 33 mm deep, beyond which it fails. Correlation averaging works well until imaging depths of approximately 50 mm before failing. Of course, collecting even more images might push the penetration depth a bit further. Results for sliding averaging in Figure 5.5(a) have been improved by neglecting detected outliers while computing the temporal mean. Further explanation is provided in Section 5.A.

Thus, one must resort to ensemble correlation averaging rather than sliding averaging or vector averaging to compute time-averaged velocity profiles in particle-laden flows. The more correlation planes used, the deeper one can obtain time-averaged velocities.

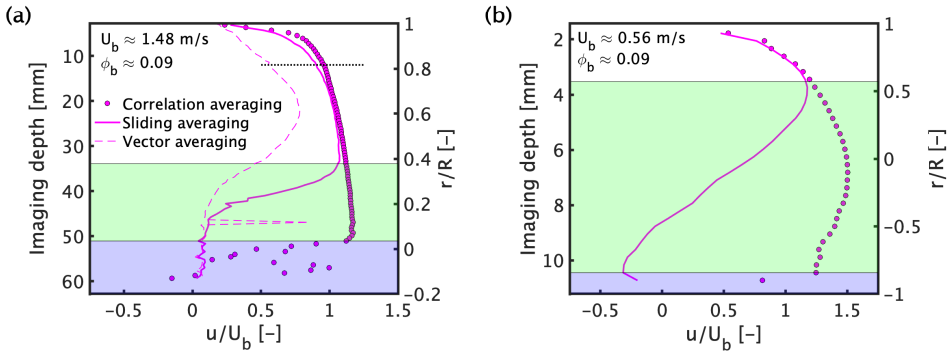

Figure 5.5: Effect of averaging techniques on time-averaged velocity profiles for homogeneous suspensions in (a) Industrial scale and (b) Laboratory scale experiments. The green and blue patches indicate depths at which sliding averaging and correlation averaging fail, respectively. The dotted black line in (a) is relevant for Figure 5.11(d).

Sliding averaging can be used to retrieve time-resolved velocity profiles, albeit until smaller imaging depths.

5.4.2. Effect of bulk volume fraction

In order to investigate the effect of particle loading, we consider data corresponding to the laboratory scale experiments, where ϕ_b was varied from 0 to 0.20. For $\phi_b \geq 0.175$, we were unable to extract any kind of useful velocity information, effectively restricting our analysis to $0 \leq \phi_b \leq 0.15$.

In Figure 5.5(b), we plot time-averaged velocity profiles for a laboratory scale experiment in a manner similar to Figure 5.5(a). The profiles are also based on 12515 images. Sliding averaging already fails at imaging depths of approximately 3 mm, implying that any time-resolved measurements will be restricted to the near-wall region. Correlation averaging is able to salvage time-averaged velocities until depths of 9 mm. Even though the volume fractions in Figure 5.5(b) and Figure 5.5(a) are similar, the limiting penetration depths are strikingly different.

Several factors contribute to the vastly differing penetration depths (based on Table 5.1). For example, the degree of specular reflection will be different because of different materials of the pipe wall, and will be dependent on the acoustic impedances. Differing materials and thickness' of the pipe wall would lead to different degrees of acoustic energy losses by absorption. Similarly, when using a parallel acquisition system, as compared to a sequential one, relatively inferior quality images are obtained in exchange for higher frame rates. Lastly, the different relative wavelengths result in different attenuation rates. Based on Figure 1(b)-(c) in Thorne and Hurther (2014), it can be expected that $\mathcal{I}_0$ and $\Delta\mathcal{I}$ are higher for higher relative wavelengths. Thus, it can be expected that if all other factors remain unchanged, performing UIV on particle-laden flows with finer particles would return better results.

In Figure 5.6, we plot the signal-to-noise ratio of the correlation planes as well as α for a range of particle volume fractions. Figure 5.6(d) is a low velocity measurement

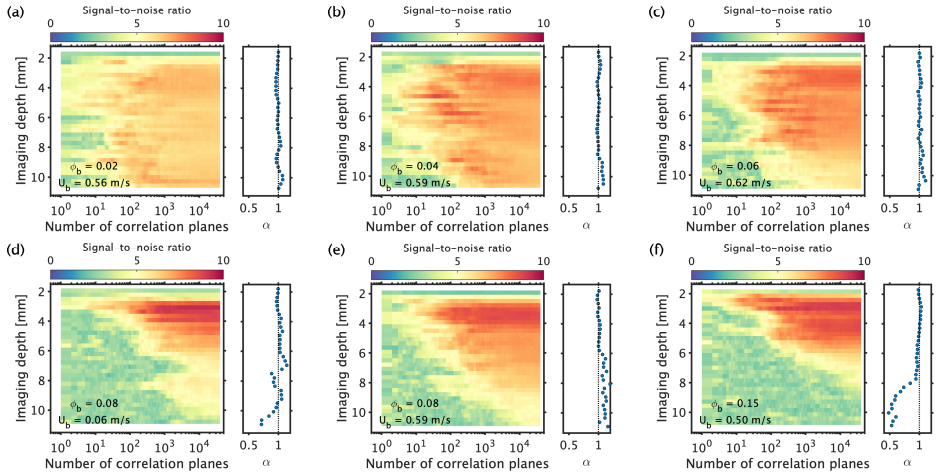

Figure 5.6: SNR of cross-correlation planes and α as function of P and z for laboratory scale experiments.

(laminar conditions) wherein radial migration of particles is expected, leading to a non-uniform distribution of particles (see Dash, Hogendoorn, and Poelma, 2021, Figure 13 therein). The remaining cases have higher velocities and it can be assumed that particles are relatively uniformly dispersed. To facilitate a fair comparison, an attempt was made to hold F_I constant, which is directly related to the particle displacements. For example, Figure 5.6(d) corresponds to measurements in a flow with U_b = 0.06 m/s and images were recorded at 1000 frames per second, while for Figure 5.6(e), U_b = 0.59 m/s and images were recorded at 4000 frames per second. Thus, for the former, image 1 is correlated with image 10, image 2 with image 11, image 3 with image 12 and so on. For the latter, image 1 is correlated with image 5, image 2 with image 6, image 3 with image 7 and so on.

The effect of varying bulk volume fractions is visible in Figure 5.6(a-c, e-f) For ϕ_b = 0.02, the SNR is nearly uniform across the entire $P-z$ plane, suggesting that time-resolved measurements with depth-invariant quality can be made, implying that attenuation, $\Delta\mathcal{I}z$, does not play a role yet (term C, Equation (5.4)). When ϕ_b is increased to 0.04, the SNR *improves* uniformly due to increase in $\mathcal{I}_0$ (term B, Equation (5.4)). Upon increasing ϕ_b to 0.06, the SNR improves slightly, at least for $z < 8$ mm due to $\mathcal{I}_0$, but beyond this, there is a drop in SNR due to the growing dominance of $\Delta\mathcal{I}z$. For ϕ_b = 0.08, 0.15, the conflicting roles of $\mathcal{I}_0$ and $\Delta\mathcal{I}z$ cause a starker contrast between smaller and larger imaging depths. Only for ϕ_b = 0.15, the exponent α shows a gradual decline from 1 to 0.5, like Figure 5.4(b).

For simplifying the interpretation of Equation (5.4), it was assumed that the particles were uniformly distributed throughout the flow. An example where this might not hold true is when particle migration occurs. At low Reynolds numbers for semi-dilute suspensions, inertial migration has been reported previously (Ardekani *et al.*, 2018; Dash, Hogendoorn, and Poelma, 2021; Yousefi *et al.*, 2021). We compare SNR patterns in Figure 5.6(d-e) with respect to the presence/absence of radial migration for constant ϕ_b. When radial migration occurs, there is locally higher particle volume fraction between the

pipe axis and wall, leading to high $\mathcal{I}_0$ and increased SNR. However, this is also accompanied by increasing influence of $\Delta\mathcal{I}$, leading to a quicker decay in SNR values. Interestingly, the signature of inertial migration, with reduced volume fraction at the pipe axis, is weakly reflected in the SNR contour plots as well.

5.5. Case studies

In this section, we consider two case studies corresponding to the two experimental facilities. The case studies illustrate how one can use the foregoing discussion to get the most out of UIV. Conversely, we also demonstrate how one can use information about the flow to reason the performance of UIV. Collectively, the case studies illustrate scenarios when UIV succeeds or fails.

5.5.1. Laminar-turbulent transition of non-Brownian suspensions

We first consider the laboratory scale experiments. In Figure 5.7, time-averaged velocity measurements (of the dispersed phase) are presented for $\phi_b = 0, 0.05, 0.10, 0.15$, while covering a broad range of suspension Reynolds numbers (Re_{susp}). The Reynolds number is based on an effective suspension viscosity (Eilers, 1941). All results shown are based on ensemble correlation averaging of 40000 images. The values of SNR in Figure 5.7 are strongly reflective of Figure 5.6 and Equation (5.4).

We use the example of $\phi_b = 0$ to show the validity of UIV measurements. For these measurements, Vestosint spheres (Degussa-Hüls, Frankfurt, Germany) with a mean diameter of 56 μm and mass density of 1016 kg/m^3 were added to the flow to generate acoustic contrast. Under laminar flow conditions, there is a good agreement between the UIV measurements and the analytical, Poiseuille solution ($u/U_b = 2(1 - (r/R)^2)$), for $Re_{\text{susp}} \leq 1740$, in the bulk region away from of the walls. At low velocities, tracer particles are not dispersed all the way to the upper pipe wall since the system is not entirely neutrally buoyant. This creates a void near the upper pipe wall, leading to inaccurate velocity estimations.

Hereafter, in the transitional region, with increasing Reynolds number, the mean velocity slowly deviates from the Poiseuille solution and becomes blunter, as would be expected. At $Re_{\text{susp}} = 5300$, our estimates compare well with the results of Eggels *et al.* (1994). The mean absolute deviation from the results of Eggels *et al.* (1994) is 4.1% between $-0.85 \leq r/R \leq 0.85$. Moreover, it can be seen that the SNR of the correlation planes is high and uniform. Of course, the tracer particles used to generate acoustical contrast have much different properties compared to the particles used in the suspension. Thus, care must be taken while comparing SNR with the forthcoming examples.

Next, we consider the example of $\phi_b = 0.05$. Under laminar conditions, a clear asymmetry in the velocity profile is visible with respect to the analytical solution for single-phase flows. This asymmetry is characterized by "underestimation" of velocities in the top half of the pipe and "overestimation" in the bottom half. This asymmetry is likely to have been caused by the features that are visible at an individual particle level (Figure 5.2(b)). It is likely that the centroid of a particle image is offset from the centroid of the particle itself. Thus, it could be expected that velocity gradients might get smoothed out in the

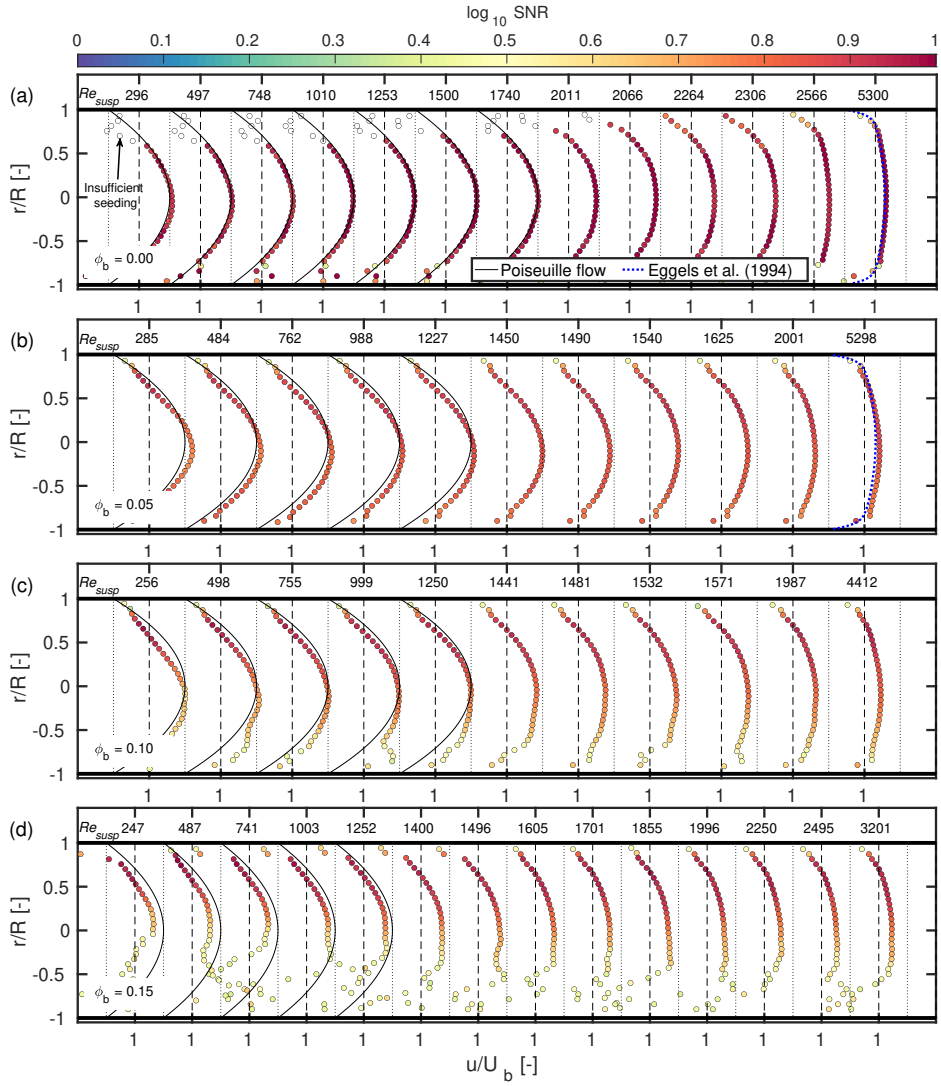

Figure 5.7: Time-averaged, normalized streamwise velocity profiles as function of ϕ_b and Re_{susp}.

direction away from the ultrasound transducer (term E in Equation (5.4)). The extent of smoothing in the velocity profiles is about 1 mm, which is in the same order of magnitude as the particle image sizes (Figure 5.2(b)). This smoothing of the velocity profile is also present under turbulent conditions when the suspension would be homogeneous.

In contrast to the smoothing of the velocity profile, it is difficult to conclusively comment on the degree of under/overestimation. The presence of radial migration of particles can also affect the velocity profiles. Thus, two factors play a role in the under/overestimation of the velocity profiles - particle distribution and the particle image

self-correlation. For example, when particles undergo inertial migration, a ring of particles is formed at a radial location between the pipe wall and the pipe axis. There are very few particles at the pipe axis. The degree of migration increases with decreasing Reynolds numbers. Clear visualizations of this phenomenon under extremely dilute conditions can be found in Matas, Morris, and Guazzelli (2004), whereas ultrasonic observations of this phenomenon under (semi-)dilute conditions can be found in Dash, Hogendoorn, and Poelma (2021). The presence of inertial migration means that the effective viscosity of the suspension is low at the pipe axis, and thus the fluid would experience less resistance. This is weakly visible in the velocimetry results for $\phi_b = 0.05$. For example, in the laminar regime, as the Reynolds number decreases, the maximum velocity slowly increases. However the above is speculative and needs to be conclusively verified.Beyond the laminar regime, the velocity profiles slowly flatten out with increasing Reynolds numbers.

At $Re_{\text{susp}} = 5298$, we compare the velocity profiles against the single-phase flow profiles from Eggels *et al.* (1994). The measured particle velocities seem to be slightly higher than in single-phase flows, but it is difficult to draw a concrete conclusion due to the role of the particle image shapes. The SNR values for this volume fraction are nearly uniform and acceptable, implying that attenuation is not yet significant, in line with Figure 5.6.

Interpreting the physics of the flow at higher volume fractions becomes challenging, partly due to the dominance of attenuation. For $\phi_b = 0.10$, the quality of the velocity profile begins to deteriorate close to the pipe axis, while for $\phi_b = 0.15$, the deterioration begins even sooner. For example, it is thus ambiguous whether the mismatch between the UIV measurement and the theoretical profile for $\phi_b = 0.15$ is physical or is also caused by the features of an individual particle image (similar to $\phi_b = 0.05$). This limits us to interpreting the effect of Re_{susp} and one can see the flattening of the velocity profiles with increasing Re_{susp}. The spatial variation of SNR, or lack thereof, can indicate the presence or absence of uniform particle distributions.

In short, this example implies that quantitative estimates of the time-averaged velocities of the dispersed phase can be extracted until $\phi_b \leq 0.15$, for limited depths. Limitations are partially caused by the relatively large particle sizes. Performing UIV on smaller particles is likelier to yield better quality results, aiding a better physical understanding of the flow.

5.5.2. Effect of a 90° bend on slurry flow

We next consider the effect of a 90° bend corresponding to the industrial scale experiments. The incoming flow is in a horizontal pipe and the outgoing flow is upwards in a vertical pipe (H→V↑). For an extensive overview of single-phase flows through curved pipes, the reader is directed to Kalpakli Vester, Örlü, and Alfredsson (2016). Shown in Figure 5.8 is a schematic of the experiments.

Unlike the previous case study, ϕ_b is fixed in the present one. This restricts the extent to which the results in this section can be evaluated in the framework of Equation (5.4). However, the flow in this case study is not quasi-1D which allows us to demonstrate the role of factors that were not included in Equation (5.4).

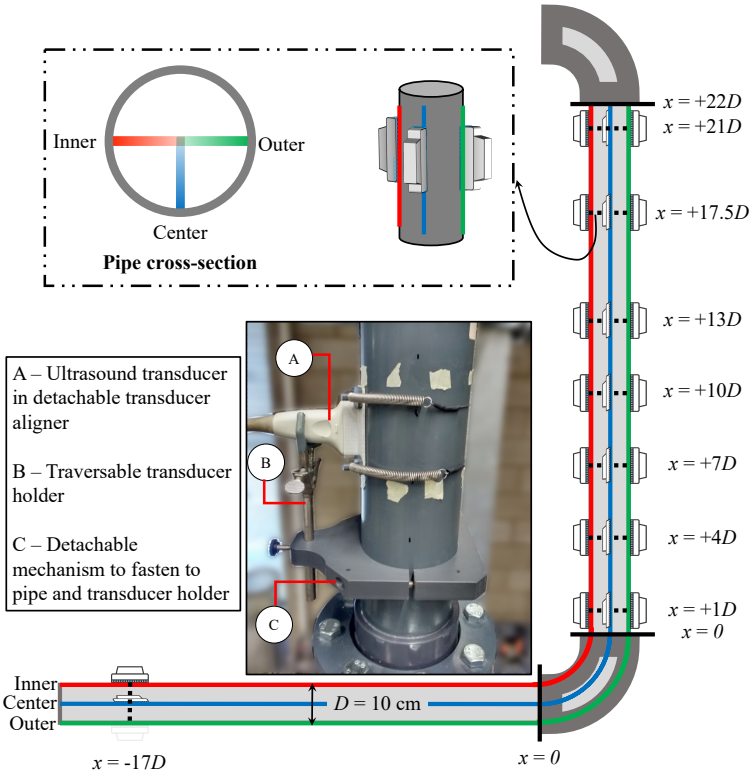

Figure 5.8: Schematic for the case study of the 90° bend.

Measurement procedure

At the beginning of a measurement day, the entire system was well mixed at high flow rates for a minimum of thirty minutes. Thereafter, the flow rate is reduced to its desired value. UIV measurements are performed at eight streamwise locations. The location $+21D$ is only one pipe diameter upstream of the following 90° bend, but we do not expect this to have a major influence on the results (on basis of Sudo, Sumida, and Hibara, 1998, Figure 5a therein). At each streamwise location, velocity profiles are measured at three azimuthal locations. Only at $-17D$, no measurement is made at the "outer" location due to restricted access (due to presence of supporting structures). Having three measurements at a single streamwise location allows for a robust judgement on the symmetry and recovery of the flow downstream of the bend. Measurements were first performed at the most downstream location, $+21D$, and then gradually moved upstream, until the final measurements are performed at the horizontal pipe, $-17D$. All results shown here are based on ensemble correlation averaging of 12515 images captured at each location.

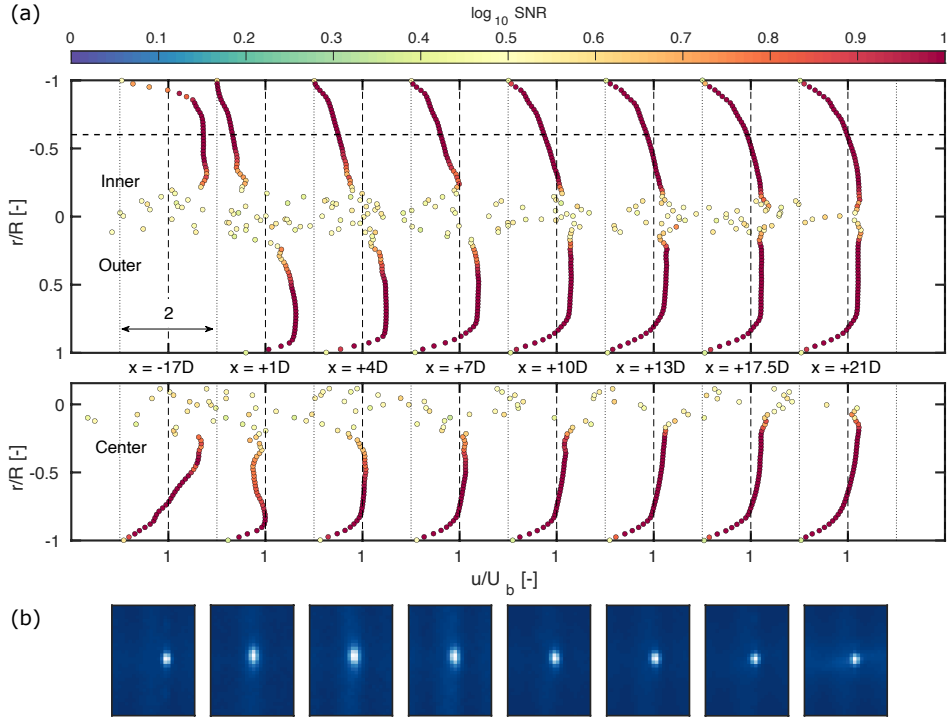

Figure 5.9: (a) Time-averaged streamwise velocity profiles under laminar conditions. The bulk velocity reduces from U_b = 0.60 m/s to U_b = 0.51 m/s over the course of the measurement day. (b) Correlation maps corresponding to the dashed line at $r/R = -0.60$ at "Inner".

Laminar conditions

We first consider the example of the flow of the slurry under laminar conditions in Figure 5.9. The effect of the bend is best visible at streamwise locations $+1D \leq x \leq +10D$, wherein the velocities along the "inner" location are far more subdued compared to that at the "outer" location. This asymmetry is known to be caused by a combination of centrifugal forces in the bend and associated pressure gradients. This leads to the maximum velocity shifting outside while also setting up secondary flows (see Miller, 1978, Section 5.4.2 therein, for a clear explanation). Sample displacement-correlation planes at a fixed location (indicated by the horizontal dashed line) are shown, whose significance shall be explained at a later stage.

Upon moving further downstream ($+13D \leq x \leq +21D$), two things can be observed. One is that the flow gradually regains symmetry. However, it can be seen that the flow is not yet fully symmetric, suggesting the need for long development lengths under laminar conditions. Another observation is that further away from the bend, the penetration depth until which results with acceptable SNR are obtained, increases. We do no think this is a coincidence and is related to the decreasing unsteadiness in the flow (visible in sliding averaging results). At larger imaging depths, unsteadiness in the flow could exacerbate the

already low signal-to-noise ratios of UIV (as a consequence of attenuation).

Upstream of the bend ($x = -17D$), it is evident from the UIV measurements that the flow is not axisymmetric. During the course of the day, we also observe a significant drop in the measured volumetric flow rate. The bulk velocity gradually reduces from 0.60 m/s to 0.51 m/s over the course of several hours. Based on the above two observations, we suspect the presence of particle settling in the horizontal pipe section, which was verified in separate tests. This in turn poses a few issues. For starters, this prevents us from comparing the UIV measurements in the horizontal pipe against analytical solutions of velocity profiles for a non-Newtonian fluid. It is also not possible to directly compare the measurements downstream of the bend against those upstream in the context of flow "recovery", as there would be no settling issues in the vertical section. Thus, under fully-developed conditions, the flow profile in the vertical section would be expected to be axisymmetric. Another consequence of settling is that the mass fraction of the slurry varies across the day and affects both the measurement quality and the flow itself. Lastly, the results presented herein are likely to be sensitive to the initial conditions as well as when the UIV measurements took place. This would make the results not easily reproducible.

Turbulent conditions

We next consider the example of the flow of the slurry under turbulent conditions in Figure 5.10, with a bulk velocity of 1.88 m/s. Before interpreting the results, we discuss factors that affect the signal-to-noise ratio for this specific example due to high velocities and turbulent conditions. Even a cursory glance at the correlation maps in Figure 5.9 and Figure 5.10 suggests that the SNR at higher velocities is inferior, when compared to lower velocities, due to the following factors:

- The in-plane displacements become comparable to the field-of-view itself. This would bring about reduced values of F_I. The effect of F_I is best visible while comparing the correlation maps in Figure 5.9 and Figure 5.10. Due to reduced values of F_I, the correlation maps at higher flow rates have more pronounced background features (see Section 5.A). Multi-pass techniques will be challenging to execute here, given that the total image width is only 33 pixels and particle displacements are about 10 pixels.

- Turbulence and secondary flows, coupled with higher absolute velocities will exacerbate out-of-plane motions, reducing the values of F_O. This can be best visualized by comparing the correlation maps in Figure 5.9 and Figure 5.10, especially along the "inner" side at $+1D$ and $+4D$. Under laminar conditions and lower velocities, secondary flows will be present, but it seems that the out-of-plane motions are not severe enough to worsen the correlation plane. However, under turbulent conditions, coupled with higher velocities, the out-of-plane motion is strong enough to generate ambiguity. We have intentionally chosen to show correlation planes along a location on the "inner" profile (indicated by the horizontal dashed line), since there is a higher probability of flow separation occurring at the inner pipe wall than at any other circumferential location, resulting in a higher degree of unsteadiness.

- The near-wall velocity gradients will be much higher, leading to reduced quality of velocimetry near the pipe walls via F_Δ. While no concrete example of a correlation map is presented here, the high velocity gradients near the wall are not well-resolved for the turbulent conditions, resulting in apparent "slip" velocities. Under laminar conditions, the gradients in the near-wall region are well-resolved, and the velocities near the pipe wall are almost zero. Advanced interrogation techniques can help resolve the near-wall region better for higher velocities.

- At $x = +1D$, along the inner side, the correlation map is completely inconclusive and there is simply no hope in recovering any useful time-averaged information. This is in part due to the presence of secondary motions and high degree of turbulence. In figure 6e of Sudo, Sumida, and Hibara (1998), it can be seen that turbulence intensities of about 15% are present along the inner side, while it is only about 5% along the outer side. This could be further exacerbated in the presence of flow separation and vortex shedding. At $x = +4D$, a displacement peak is visible, but the background features, which are leftover even after background subtraction, are equally dominant. Since the algorithm works by identifying the highest peak, a peak corresponding to the background features can also be incorrectly identified as the displacement peak. Further downstream, the displacement peak regains its dominance, due to diminishing unsteadiness. The background features can be suppressed by slightly modifying the cross-correlation technique (see Section 5.A). Doing so removes the ambiguity, but also reduces penetration depths by a few interrogation windows (shown for "Inner" profile at $+4D$).

Despite the challenges posed by $F_I F_O F_\Delta$, the quality of the results is sufficient to comment on the flow physics. For starters, the flow upstream of the bend ($-17D$) is rather symmetric in comparison to the laminar case, implying that the slurry is homogeneously suspended. While the "inner" velocity measurements at $+1D$ are not very convincing, the "outer" and "center" measurements do suggest the presence of flow asymmetry. From $+4D$ onwards, it can be clearly seen that the flow slowly regains its symmetry as well as streamwise momentum, implying a diminishing role of secondary motions. This is accompanied with a simultaneous increase in SNR values as well as penetration depths, implying reduced unsteadiness in the flow. The increasing penetration depth suggests the weakening influence of peak broadening caused by unsteadiness with respect to attenuation. In the correlation maps until $+10D$, it can also be seen that there is radially outward flow (upward shift in the peak location). Such behaviour has also been observed in time-averaged measurements of single-phase flows as the effect of secondary flows has been observed even until $+10D$ (see Sudo, Sumida, and Hibara, 1998, Figures 5, 9 therein). Even at our most downstream measurement location, $+21D$, it can be seen that there is a deficit in the streamwise velocity when compared to the upstream conditions, $-17D$. This, combined with the presence of weak asymmetry, means that the flow has not fully recovered yet. In light of the pressure drop measurements of single-phase turbulent flows, albeit for a bend with a slightly different geometry, nearly 50 pipe diameters are required for a full recovery (see Ito, 1960, Figure 3 therein). The degree of asymmetry and recovery measured by UIV is valuable information for validation of numerical studies.

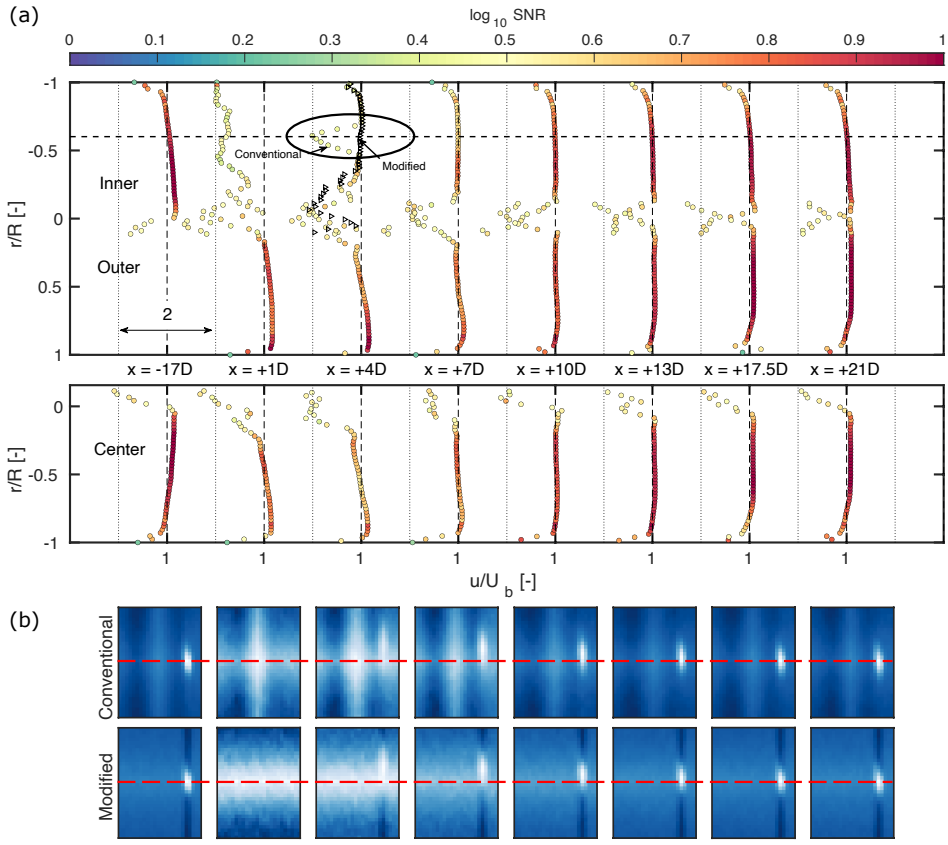

Figure 5.10: (a) Time-averaged streamwise velocity profiles under turbulent conditions (U_b = 1.88 m/s). (b) Correlation maps corresponding to the dashed line at $r/R = -0.60$ at "Inner". All velocity profiles in (a), except the one with open markers, are based on the conventional cross-correlation technique. The red dashed line in (b) indicates zero displacement along the vertical direction of the images. Also see Section 5.A.

5.6. Conclusions and Outlook

In this paper, we elaborated upon the differences that arise between UIV for particle-laden flows and conventional PIV. Cross-correlation theory developed for PIV is modified to include ultrasonic backscatter behaviour in suspensions. This allows us to heuristically argue how different factors propagate into the cross-correlation plane of UIV measurements. This modified theory sufficiently explains the experimental data and can be seen as a step towards a complete understanding of the role of ultrasound imaging in UIV for particle-laden flows. The experimental case studies herein highlight scenarios wherein UIV succeeds or fails.

The key takeaway message is that while applying UIV to particle-laden flows, one must be aware of the presence of a ceiling for particle volume fraction, imaging depth, as well as achievable (depth-variant) temporal resolutions. These ceilings are mainly imposed due

to the attenuation of ultrasound waves. For obtaining time-averaged velocities, ensemble correlation averaging is strongly advised. It is strongly recommended to work at the level of correlation planes while assessing the quality of velocimetry results. Determining α (growth rate of correlation peak height as function of number of images) on a preliminary measurement can help one assess whether recording even more ultrasound images will be beneficial or not. The imaging depth to which sliding correlation averaging helps with time-resolved measurements is lower than that for which ensemble correlation averaging helps with time-averaged measurements. From a practical perspective, combining UIV with finer particles is likely to be more rewarding than with coarser particles.

Our study highlights the need for one to perform preliminary tests in an ex-situ mock-up prior to an exhaustive and resource intensive measurement campaign. Even though there is no harm in performing measurements and realizing the limitations *a posteriori*, valuable time and labour can be saved while possessing realistic expectations of the feasibility *a priori*. This is especially valid when large volumes of suspensions need to be prepared. If the generation of realistic, synthetic ultrasound images for particle-laden flows can be realised (similar to Monte Carlo simulations for PIV), it will greatly help assess the performance of UIV in a controlled manner. As an example, Swillens, Segers, and Lovstakken (2010) as well as Swillens *et al.* (2010) perform speckle tracking on synthetic ultrasound images of cardiovascular flows.

In conclusion, we provide a methodology and framework (for example, Equation (5.4), SNR, α) for one to evaluate particle-laden flows with UIV. Despite the few limitations of UIV in the context of particle-laden flows, we demonstrate its ability in acquiring unique and useful experimental data, which cannot otherwise be readily obtained.

Acknowledgements

Experiments and curation of B-mode images corresponding to the laboratory scale experiments were performed by W. Hogendoorn. The industrial scale experiments were made possible in a collaboration involving G. Oldenziel, F. Clemens, A. Zubova, M. Verhoek and M. Tukker. The industrial scale experiments were successfully executed thanks to the technical support offered by the Department of Experimental Facility Support at Deltares. J. de Schipper (equipment for fastening to pipe), W. Taal (data acquisition), F. de Vreede (sensor calibration), R. Boele (safety), and G. Mulder (technical assistance with the Ultrasonix apparatus as well as conceptualizing and 3D-printing the aligner for the ultrasound transducer) are gratefully acknowledged. The work also benefited from a fruitful discussion with J. Westerweel.

5.A. Additional explanation for PIV processing

Here, we elaborate on two matters in the main text. One is related to the quality of sliding averaged velocity profiles (Figure 5.5(a)). The other is related to the suppression of the vertical stripes observed in correlation maps (Figure 5.10).

Shown in Figure 5.11(a)-(c) is an example wherein the detection of outliers for sliding averaging technique is demonstrated. While typical outlier detection / replacement tech-

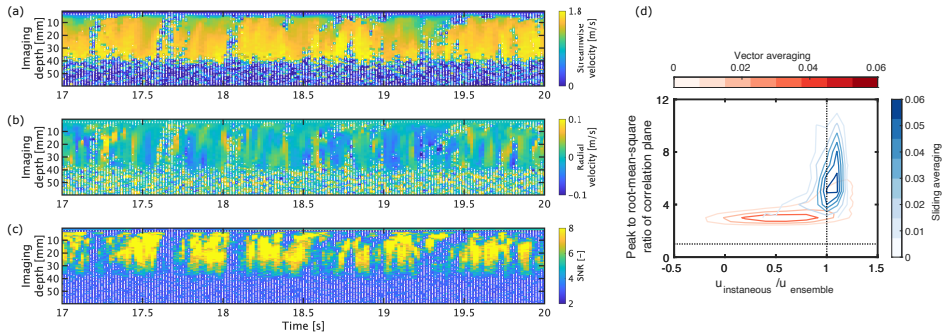

Figure 5.11: Space-time plots of (a) streamwise velocity, (b) radial velocity, (c) SNR corresponding to Figure 5.5(a). The white dots indicate points where SNR < 3. (d) Joint probability distribution function between signal-to-noise ratios of displacement-correlation planes and "instantaneous" streamwise velocity measurements at imaging depth of approximately 12 mm (horizontal dotted line in Figure 5.5(a)).

niques take place in spatial coordinates (Westerweel and Scarano, 2005; Garcia, 2011), in Figure 5.5(a) we have performed this analysis on spatio-temporal coordinates. Such a change is necessary since only three columns of velocity vectors are computed, with only the middle one being reliable, ruling out post-processing in spatial coordinates. In short, for each point on the spatio-temporal plot, the SNR of the corresponding correlation plane is evaluated. If this SNR < 3, we do not include it while computing the mean. For imaging depths > 35 mm, it can be seen that the SNR based on 10 planes is simply unacceptable. We do not attempt to replace the detected outliers. Replacement strategies will function well at low velocities, as long as outliers are not clustered together. At higher velocities, the higher fraction of outliers coupled with clustering of outliers will overwhelm any correction procedure. For example, at 19.9 s between depths of 30-40 mm, the few detected outliers may be replaced without much problems. However, the cluster of outliers around 17.6 s stretching from depths of 5-35 mm would prove challenging to replace. In case the identified clusters strongly correlate to turbulent structures, this filtering process might result in a bias by neglecting these structures.

Previously, in Figure 5.5(a), it was shown that there was an underestimation of the time-averaged velocity profiles by vector and sliding averaging. In order to have a closer look at this underestimation, we consider a single interrogation window at an imaging depth of approximately 12 mm (dashed line in Figure 5.5(a)). In Figure 5.11(d), the joint probability distribution function between the SNR of correlation planes and the "instantaneous" velocity normalized by the time-averaged velocity computed by correlation averaging is shown. For vector averaging, several outliers are present. These outliers are asymmetric about the expected value, which leads to an underestimation in time-averaged velocities. The fraction of outliers is too high to be detected and replaced by conventional techniques. For sliding averaging, the distribution of "instantaneous" velocities is a lot more favourable with a far smaller fraction of outliers. Thus, sliding averaging outperforms vector averaging.

Choosing an appropriate threshold for SNR will eliminate a fraction of the outliers. To show the effect of the choice of threshold on the time-averaged velocity computed by

sliding averaging, we consider Figure 5.12. Basically, we consider a relatively favourable and adverse situation of the flow. The favourable situation is at a lower velocity (0.51 m/s) and laminar conditions, while the adverse situation is at a higher velocity (1.88 m/s) and turbulent conditions. The experimental dataset corresponds to the "Inner" location at $-17D$ in Figure 5.9 and Figure 5.10.

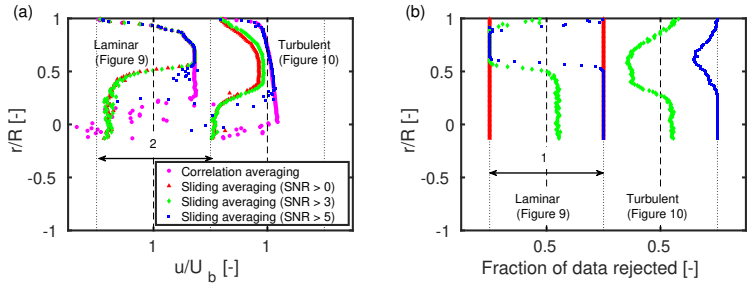

Figure 5.12: (a) The role of SNR threshold on time-averaged velocity results computed by sliding averaging (b) Corresponding fraction of data rejected.

In the more favourable scenario, the choice of the SNR threshold has virtually no effect on the time-averaged velocity profile. Moreover, there is good agreement between the velocity profiles obtained by sliding averaging and correlation averaging. As expected, the penetration depth by sliding averaging is lower than that by correlation averaging. The imposition of a SNR threshold would reject a fraction of data at each imaging depth (for example, the white dots in Figure 5.11(a)-(c)). However, for the laminar flow, virtually no data is rejected at the imaging depths where sliding averaging performs well (Figure 5.12(b)).

In the more adverse scenario, the choice of the SNR threshold has a major effect on the time-averaged velocity profile. When the SNR threshold is 0, the sliding averaging results grossly underpredict the results obtained by correlation averaging, presumably because of excessive outliers. Increasing the SNR threshold to 3, improves the situation slightly. From Figure 5.12(b), it can be seen that 25-60% of data is rejected. Increasing the SNR threshold to 5 greatly improves the estimation of the time-averaged velocity, and it agrees well with the results obtained by correlation averaging. However, in order to achieve this, about 80-95% of the data is rejected. As expected, the penetration depth by sliding averaging is lower than that by correlation averaging.

At higher velocities, another challenge we encounter is the dominant role played by background features in the correlation planes, as was mentioned during the case studies. Shown in Figure 5.13 is a more detailed example, corresponding to the measurements at "Inner" and -17D in Figure 5.10. In the time-averaged B-mode image intensities, there is a clear variation in the intensities laterally and axially. The axial variation is due to attenuation of ultrasonic waves. It is unclear where the lateral variation originates from, but we speculate that it may be related to the beamforming process. The lateral variation across the interrogation windows is evident at small imaging depths and is absent at large imaging depths. Conventionally, while performing spatial cross-correlation analysis, the mean image intensity of each interrogation window is subtracted. As can be seen in the top

row of correlation windows in Figure 5.10, this conventional technique results in trends in the mean B-mode image intensities being propagated into the cross-correlation plane. Moreover, we observe that the strength of these stripe like features is more dominant at higher velocities. In order to tackle this, we subtract a columnwise mean image intensity of the interrogation windows before performing the cross-correlation analysis. We refer to this as the modified technique. This helps suppress the stripe like features. While the modified technique helps suppress the effect of lateral intensity variation, we also observe that the penetration depth is reduced by a few interrogation windows (see Figure 5.10, "inner" profile and $+4D$).

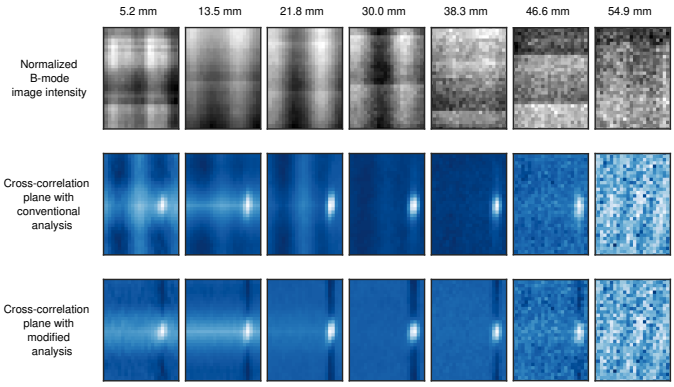

Figure 5.13: Time-averaged B-mode image intensities at several imaging depths. Corresponding correlation planes obtained by the conventional and modified cross-correlation analysis are also shown.

Long-time-scale transients in an industrial scale slurry pipeline near the laminar-turbulent transition

It takes time for new technologies to be adopted as common practice … There may be many reasons for this, such as challenges to conventional wisdom, resistance to change, scepticism of claims and finally, proof of success that takes time to filter through, due to a slow uptake of the technology. This is typical of the well known technology diffusion curve …

Paterson (2012)

We revisit laminar-turbulent transition of a fine-grained slurry in a large pipe. The combination of long measurement times in an industrial scale facility and ultrasound imaging allows us to observe and address anomalous trends. Under turbulent conditions, the flow is homogeneous and steady. However, under laminar conditions, two types of long-time-scale transient behaviours are captured. In the first scenario, the system has been homogenized, following which the flow rate is reduced to laminar conditions. The flow rate continues to gradually drop, while particles settle and form a stationary bed. In the second scenario, the system has been shutdown for a prolonged period and the flow rate is slowly increased. The flow rate continues to rise while particles are slowly resuspended from the gradually eroding bed. Near the laminar-turbulent transition point, two types of intermittent structures are responsible for resuspension. The equilibrium phase, with steady flow rate, coincides with complete resuspension. These two long-time-scale transients correspond to the phenomena of "slow settling" and "self-equilibration",

This chapter has been published in Dash and Poelma (2022). The appendices of this chapter appear as online supplementary material for the corresponding publication. 'We' in this chapter refers to the two authors - Amitosh Dash and Christian Poelma.

respectively. While the former can lead to shutdowns, the latter generates a stable system. Being aware of these phenomena is of relevance while operating slurry pipelines near the favourable operating point of laminar-turbulent transition.

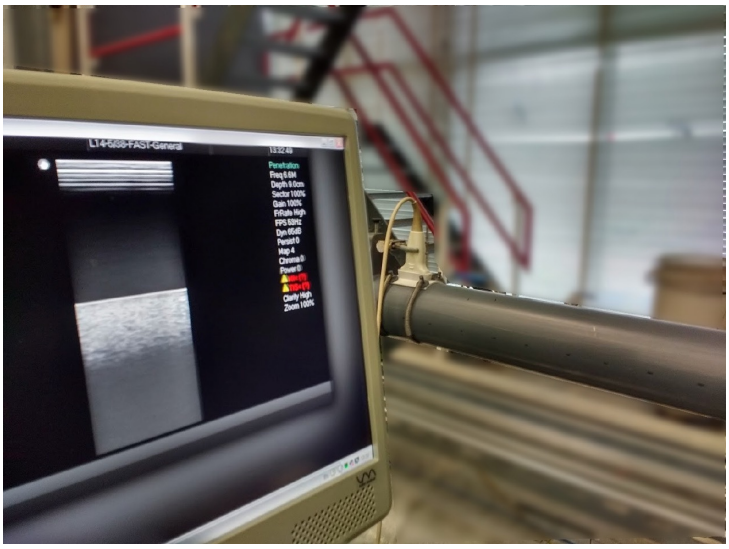

Ultrasound imaging can be deployed outside medical clinics as well. Above is an example wherein it is used to study the flow of a slurry in an industrial scale pipe. The pipe was behaving peculiarly. With ultrasound imaging, the root causes could be diagnosed.

Impact Statement

Pipeline transport of slurries is an applied field wherein decision-making is driven by guidelines, rules-of-thumb, and models derived from fundamental fluid mechanics. We demonstrate how ultrasound imaging can complement measurements of integral quantities, offering an avenue to reassess our fundamental understanding of established applied processes. We advocate for *slowly settling* slurries to gain mainstream recognition, next to the present dichotomy of settling and non-settling ones. This is related to the settling of conventionally non-settling slurries over long distances/times, foreshadowing shutdown. Similarly, laminar-to-turbulent transition is often boiled down to a critical velocity, touted as the most efficient operating point. Targeting this critical velocity via *self-equilibrating* behaviour is demonstrated while starting up a pipe. Particles initially in the bed are slowly entrained into the flow. The final stage involves an equilibrium, with all particles suspended and the flow having visible intermittency. This can serve as an alternative approach for starting up a pipeline.

6.1. Introduction

Pipeline transport of slurries is a matured field (Wasp, 1983; Paterson, 2012; Thomas and Cowper, 2017) where solids ('payload') are transported in a carrier liquid ('vehicle'). Owing to the intrinsic breadth of slurry flows, distinctions are made to allocate slurries to categories. A major classification factor is whether the slurry is *settling* or *non-settling*, depending on the settling tendency of the particles. Accordingly, the slurry is either treated as pseudo-homogeneous (non-settling) or heterogeneous (settling). Commonly, classification is based on particle size, a typical threshold being 40 μm. For non-settling slurries, varying the volume fraction of the particles additionally influences its rheology. Non-settling slurries offer a convenient avenue for simplification, with the option to model the two-phase system as an effectively single-phase, homogeneous, non-Newtonian fluid.

Even though flows of Newtonian fluids are almost always turbulent in practice, slurry flows can be laminar due to the significantly enhanced effective viscosity caused by the presence of particles. A key benchmark of a slurry pipeline (for a non-settling slurry) is the *critical velocity* at which laminar-turbulent transition occurs. This serves two major roles: (1) to determine an appropriate model to predict total pressure drops, and (2) to establish an operation point where the *specific energy consumption* (energy imparted to slurry divided by product of pipeline length and dry solids throughput) is minimized (Pullum, Boger, and Sofra, 2018). The latter aspect is relevant economically. For a non-settling slurry, the most favourable operation point would be just below the critical velocity. In contrast, for a settling slurry, it would be just above the critical velocity, so that turbulence would counter settling (Wilson *et al.*, 2006). From Newtonian fluid mechanics, transition is known to occur over a range of velocities and is accompanied by rich phenomena (Barkley, 2016). However, the slurry community typically reduce transition to a single point. This might be driven by pragmatism, since only pressure gradients are needed to design pipelines (Güzel *et al.*, 2009). Furthermore, a *minimum allowable transport velocity* is determined by applying a safety margin to the critical velocity (Javadi, Pirouz, and Slatter, 2020).

While slurry flows in pipelines have been studied extensively, experimental work for laminar-turbulent transition in non-settling slurries is often restricted to time-averaged pressure drop measurements. Occasionally, pressure fluctuations (standard deviation or time series) are also used to detect laminar-turbulent transition (Vlasak and Chara, 2004; El-Nahhas *et al.*, 2004; Slatter, 2005). Only a handful of studies consider local features of the flow using ultrasonic techniques (Benslimane *et al.*, 2016; Thota Radhakrishnan *et al.*, 2021).

We take a close look at the laminar-turbulent transition of a common model slurry, a Kaolin-water mixture (21% w/w or 9% v/v). Based on rules of thumb, this slurry is non-settling (median size = 5.18 μm, measured settling velocity = 342 nm/s). It flows in a pipe loop with an inner diameter of 0.1 m, generally considered as a lower threshold for industrial scale pipelines (Pullum, Boger, and Sofra, 2018). This slurry is dense enough to possess non-Newtonian properties (yield-pseudoplastic fluid). The flow is probed with time-averaged pressure drop measurements as well as ultrasound imaging. Using cross-correlation techniques, ultrasound imaging velocimetry (UIV) returns velocity profiles (Poelma, 2017). The ultrasound image intensities furthermore reveal the spatial distribution of the solids in the slurry. Typically, brighter intensities suggests more particles.

However, one must be aware of the role of attenuation, which leads to reduced intensities away from the transducer. We perform experiments with two trajectories: one wherein the flow velocity is increased in time (system not homogenized prior to setting desired flow conditions) and another wherein the flow velocity is reduced in time (system homogenized prior to setting desired flow conditions). We aim to illustrate two types of long-time-scale transients, which are dependent on the experimental trajectory. The usage of long measurement times in an industrial scale facility and ultrasound imaging help unearth and explain observations which would have otherwise been missed. Knowledge of these transients could be relevant when operating pipelines close to the favourable point of laminar-turbulent transition.

In Section 6.2, we describe the experimental facility and the various experiments considered. Two types of experiments are performed: "unaltered inflow" (Section 6.3) and "ramped inflow" (Section 6.4). From these experiments, two types of transient behaviours are captured, which we refer to as "slowly settling" (Section 6.5) and "self-equilibration" (Section 6.6). The key conclusions are summarized in Section 6.7.

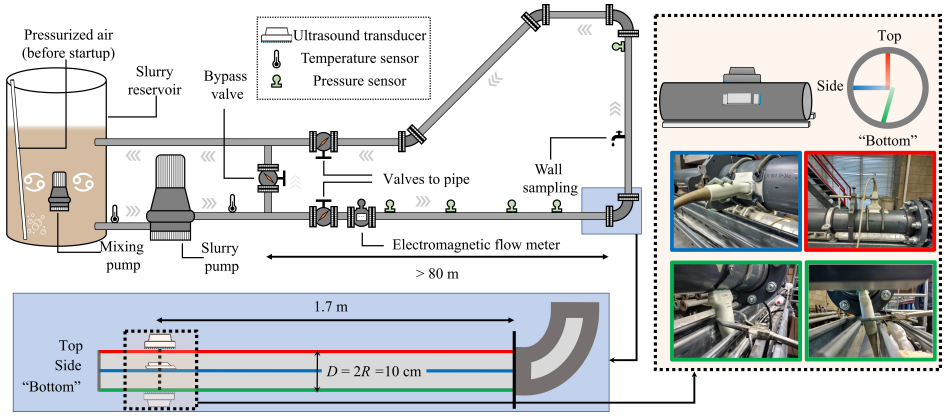

Figure 6.1: Schematic of the experimental facility and the region of interest (not to scale).

6.2. Experimental setup and procedures

The experiments are performed in a facility specifically designed for slurry flows ('β-loop', Deltares, Delft, The Netherlands), the schematic of which is shown in Figure 6.1. The facility contains more than 4 m^3 of slurry. A slurry reservoir contains the bulk of the slurry. The pipes are made of Polyvinyl Chloride (PVC) with an internal diameter of $D = 10$ cm. The flow is driven by a variable frequency centrifugal slurry pump (NT 3153, Xylem). The pump frequency can be controlled manually up to a maximum of 50 Hz. Three valves in the facility (bypass valve and two valves to pipe) can be regulated manually to alter the flow. The volumetric flow rate is monitored by an electromagnetic flow meter (Optiflux 2300C, Krohne). Submersible pressure transducers (PDCR5031, GE) and temperature sensors (STS-PT100, Ametek) are installed at several locations to measure the absolute

pressure and temperature, respectively. Pressures, temperatures, and the volumetric flow rate are logged at 50 Hz over a working day (~8 hours).

Ultrasound images were recorded using a SonixTOUCH Research (Ultrasonix/BK Ultrasound) coupled to a linear array transducer (L14-5/38). While setting up an ultrasound imaging measurement, a balance needs to be struck between imaging frame rate, field-of-view, line density (see Chapter 14 in Bushberg *et al.*, 2012). In our experiments, we achieve imaging depths of 6 cm, and an imaging rate of 287 frames per second by reducing the sector to 50% and line density to 64. The imaging resolutions in the axial direction (direction parallel to beam propagation) and lateral direction (direction perpendicular to beam propagation) are 0.6 mm and 0.3 mm respectively. Velocity results were generated using PIVware (Matlab script based on Westerweel, 1993) followed by sweep correction (Zhou *et al.*, 2013). Further technical details surrounding ultrasound imaging (velocimetry) measurements and the corresponding post-processing can be found in Sections 3.2-3.3 of Dash *et al.* (2022). The axial spatial resolution of the velocimetry measurements is 0.6 mm while the temporal resolution is 182 ms. The performance of ultrasound imaging (velocimetry) in particle-laden flows is reduced due to attenuation. In several of the results presented herein, it is evident that the quality of the velocimetry results is inferior farther away from the ultrasound transducer.

For a detailed overview of the slurry characterization, the interested reader is directed to the supplementary material. Only a short summary is provided here. In brief, the slurry has a mass density of ρ = 1152.1 kg/m^3 and contains fine particles with a median size of 5.18 μm. Its non-Newtonian behaviour can be characterized by the Herschel-Bulkley model ($\tau = \tau_y + K\dot{\gamma}^n$), whose parameters are determined via a rheogram between the shear stress, τ, and the shear rate, $\dot{\gamma}$. The slurry has a yield stress, τ_y = 0.8889 Pa, a consistency index, K = 0.1579 Pa·s$^{0.4579}$, and a behaviour index, n = 0.4579 at 18°C.

The slurry settles overnight (~16 hours) during a prolonged period of shutdown, and the system is stratified (all particles in a stationary bed and clear liquid atop). Two types of experimental 'trajectories' are considered: one wherein the system is homogenized before setting the desired flow rate, and another wherein the system is not homogenized. The two trajectories are denoted by ↓ and ↑ respectively, and symbolize the approach employed to arrive at the desired flow velocities. In both cases, prior to measurements, pressurized air is released at the bottom of the reservoir to resuspend the settled particles. Hereafter, a mixing pump suspended in the reservoir reduces particle settling. These actions are necessary for the reservoir and do not affect the pipe.

The ↑ experiments require a certain degree of care. Even before resuspending the settled slurry in the reservoir, the valves to the pipe are slowly opened completely to equalize the pressure across it. This step needs to be done carefully, failing which the stationary bed may get disturbed. With the bypass valve completely open and the valves to the pipe completely closed, the slurry pump is turned on at a frequency of 20 Hz and the flow occurs exclusively in the bypass loop between the reservoir and the bypass valve. Then, the bypass valve is closed gradually until the desired flow rate is achieved. Using the bypass valve, bulk velocities up to U_b = 1.48 m/s can be attained. To obtain even higher velocities, the pump frequency needs to be increased.

For the ↓ experiments, the procedure requires less care. With the bypass valve completely open and the valves to the pipe completely closed, the slurry pump is turned on

at a frequency of 20 Hz and the flow occurs exclusively in the bypass loop. The valves to the pipe are then fully opened and then the bypass valve is completely closed. The pump frequency is then increased to 50 Hz and a bulk velocity > 3.5 m/s is achieved. The system is maintained in this state for at least thirty minutes. To achieve a target volumetric flow rate ≥ 1.48 m/s, the pump frequency is lowered to an appropriate value. To achieve bulk velocities < 1.48 m/s, the pump frequency is brought down to 20 Hz and the bypass valve is gradually opened until the desired volumetric flow rate is reached.

Two types of experiments (not to be confused with the two trajectories) are considered here. The first are experiments wherein the system settings (pump and valves) are left untouched once the desired flow rate has been achieved, until shutdown. The only time the system is perturbed is midway through the experiments while *wall sampling* (tapping a slurry sample from a port on the wall). This tap is present along the inner curvature of the 90° bend, 5.5 pipe diameters downstream of it. The second set of experiments are experiments wherein the bulk velocity is either gradually increased (↑) from a fully stratified state, or decreased (↓) following homogenization at the highest flow rate, over the course of a working day. No wall sampling is performed here. These are referred to as "unaltered inflow" and "ramped inflow" experiments respectively.

A total of nine "unaltered inflow" experiments are considered: [1.87, 1.47, 1.46, 1.30, 1.15, 0.99, 0.80, 0.63] m/s ↓, 0.60 m/s ↑. The velocities in the above list are the target bulk velocities and the pump/valves are left untouched once the conditions are achieved. Ultrasound images are recorded in the horizontal pipe section (top and side) as well, towards the end of the working day. The streamwise location on the horizontal pipe is 17 pipe diameters upstream of the bend and nearly 800 pipe diameters downstream of the entrance.

In contrast, four "ramped inflow" experiments are performed with a combination of the two trajectories (↑ and ↓) and two ultrasound imaging locations (top and "bottom"). Underneath the horizontal pipe lie support structures preventing us from achieving a normal contact angle between the pipe and the ultrasound transducer. Thus, the "bottom" measurements must be inferred in a semi-quantitative manner. Decisions to alter the flow rate had to be made on the fly depending on what was observed in real-time, given the constraint of the working day. Since the facility is not computer-controlled, the rate of ramping is arbitrary. By observing the trends in measured pressure drops and ultrasound images, as well as remaining time in the day, decisions to alter the flow conditions were made. Since flow rates are altered manually and arbitrarily, it would be difficult to reproduce the experiments in a one-to-one manner. The aim of these experiments was to have a close look at the laminar-turbulent transition in this flow loop.

6.3. Results: unaltered inflow experiments

6.3.1. Global characteristics: pressure drop and bulk velocity

The volumetric flow rates and pressure drops in the horizontal pipe section measured during the unaltered inflow experiments for several initial settings are shown in Figure 6.2(a)-(b), wherein each time series is normalized with its initial value. After the desired initial condition was attained (time = 0 minutes), the pump/valves were left untouched until

shutdown (sharp drops in bulk velocity or pressure drop). Since each experiment in this measurement campaign lasted over a working day, it allowed us to record global system behaviour over the course of several hours.

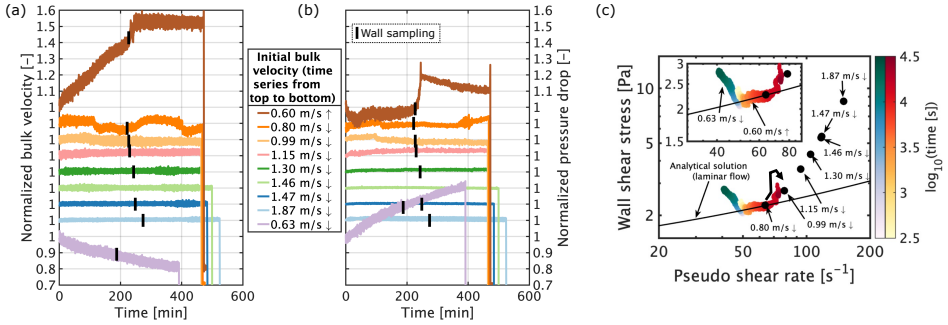

Figure 6.2: (a) Bulk velocity and (b) pressure drop in the horizontal pipe section for different initial conditions. Normalization performed with corresponding value at 0 min. Each experimental dataset is vertically offset by 0.1 in both subplots. The black lines denote the moments when wall sampling was performed. (c) Corresponding pipe rheograms. The black circles correspond to experiments wherein no remarkable transient behaviour is observed, whereas for the other experiments, the transient behaviour is shown with the corresponding colorbar (left and right for 0.63 m/s ↓ and 0.60 m/s ↑ respectively). The curved arrow represents the trajectory of the wall shear stress for 0.60 m/s ↑. The analytical solution for laminar flow holds true for Herschel-Bulkley rheology, and the equation is reproduced in the supplementary material.

When the initial bulk velocity is high (≥ 0.99 m/s), the bulk velocity as well as the pressure drop remain steady and fairly constant over the entire day (fluctuations within 2%). For the example of 0.80 m/s ↓, there are visible long-time-scale fluctuations in the bulk velocity, the causes for which are unclear. The two most interesting examples are 0.63 m/s ↓ and 0.60 m/s ↑, whose behaviours are peculiar.

For 0.63 m/s ↓, the bulk velocity drops by 20% over 6.5 hours, while the pressure drop in the system rises by 30%. This is detrimental from a practical perspective. Were these trends to continue, a complete shutdown could occur, and no particles would get transported. This observation already hints that some form of settling is present in the system despite the slurry being "non-settling", which will be verified later in Section 6.5. Settling of particles would result in the formation of a stationary bed, which lead to an increased resistance (higher pressure drop), which causes a reduction in the flow rate. The reduced flow rate then further facilitates particle settling allowing this transient to sustain.

At the other end of the spectrum lies the example of 0.60 m/s ↑. Basically, the bulk velocity rises by 50% over four hours after which it attains some form of equilibrium. Based on the above example of 0.63 m/s ↓ where we suspect the presence of settling, the most obvious ansatz would be that there is gradual erosion of the bed accompanied with particle resuspension in 0.60 m/s ↑. This ansatz will be verified later in Section 6.6. Resuspension of particles would lead to an increased cross-sectional area, which would reduce resistance to the flow leading to an increased flow rate. The increased flow rate would trigger further resuspension. In the initial phase wherein the bulk velocity rises gradually, the pressure drop varies mildly. When there is a transition from a transient state to a steady state, there is a sharp rise in the pressure drop with the peak reaching

as high as 30%. However, during the steady state phase, we see that the pressure drop reduces gradually by 10% over the course of four hours.

One caveat in the observations for 0.60 m/s ↑ is that the causality behind equilibration might be influenced by wall sampling. From Figure 6.2(a)-(b), it is evident that wall sampling for 0.60 m/s ↑ is immediately followed by a jump in the pressure drop and volumetric flow rate. This is in contrast to all the other ↓ experiments, where wall sampling has no visible effect. In this scenario, we suspect that the equilibration process is triggered by an external perturbation rather than it being an intrinsic phenomenon. We conjecture how wall sampling may have influenced the flow in the ↑ experiments. The slurry loop is a pressurized system and the internal pressure near the wall sampling location is higher than the atmospheric pressure. When the tap is opened, this location is suddenly exposed to lower, atmospheric pressure. This leads to an increased pressure drop between the horizontal pipe and the wall sampling location, which would increase the bulk velocity in the system. If the system is already homogeneous and well-mixed (like in ↓ experiments), the increased velocity should not affect the distribution of particles. However, if particles are settled (like in ↑ experiments), the increased velocity would resuspend them and possibly homogenize the slurry. This might explain why wall sampling seemingly influences the ↑ experiments but not the ↓ experiments. The seemingly benign action of wall sampling appears to be more complicated and one must be aware of its potential implications.

In Figure 6.2(c), the corresponding pipe rheograms (wall shear stress versus pseudo shear rate (= $8U_b/D$)) are shown. To define the pseudo shear rate, the bulk velocity, U_b, and the pipe diameter, D, are required. We report pipe rheograms rather than Moody diagrams (skin friction factor versus Reynolds number) to avoid dealing with the selection of a model to define the Reynolds number for a non-Newtonian slurry. For experiments with relatively steady state conditions, the laminar-turbulent transition can be clearly seen. The analytical solution under laminar conditions is based on Equation 9 in van den Heever, Sutherland, and Haldenwang (2014). The pipe rheogram undergoes a gradual transition from laminar to turbulent conditions, typical of non-Newtonian fluids/slurries (unlike Newtonian fluids that show an abrupt transition). Based on this plot, one could conclude that 0.80 m/s ↓ has laminar conditions, while the remaining points are non-laminar. We later show via the results of the 'ramped inflow' experiments that the critical velocity for the present combination of the slurry and flow facility is between 0.85 and 0.89 m/s. The overlapping results of 1.47 m/s ↓ and 1.46 m/s ↓ (performed twelve days apart) suggest that experiments are repeatable in the turbulent regime.

For the plots demonstrating transient behaviour, a moving mean over 10 seconds is applied, and thereafter only data points at every 2 seconds are shown. For 0.63 m/s ↓, the initial condition agrees with the analytical solution for laminar flows. However, with increasing time, the wall shear stresses exceed the analytically expected value for a homogeneous system, suggesting loss of homogeneity. On the other hand, for 0.60 m/s ↑, the measured wall shear stress is initially slightly higher than the analytical solution, possibly due to the presence of a bed. With increasing time, the agreement with the analytical solution improves, before sharply deviating from the analytical solution. After reaching a maximal deviation from the analytical solution (denoted by curved arrow in Figure 6.2(c)), the wall shear stress slowly arrives at a value close to the measurement of 0.99 m/s ↓. As a whole, the pipe rheogram appears to have a minimum, which is commonplace for settling

slurries. This example shows that despite similar initial conditions in the volumetric flow rate, the end result could vary greatly depending on the initial conditions of the slurry homogeneity.

Seldom are pipe rheograms presented in this manner where the transient behaviour is evident. Observing these transients requires periods of several hours. Typically, measurements are presented in a manner which reflect that all measurements are performed at steady-state. This is especially true for slurries that are classified as non-settling. The results herein suggest that time can become a relevant factor in hydraulic design, especially when considering conventionally non-settling slurries in a large or long pipe. Studies in smaller pipes (laboratory scale) might miss this behaviour altogether as higher flow velocities compensate for the smaller diameters to achieve similar Reynolds numbers (thus, increased chance for particles to be resuspended).

6.3.2. Local characteristics: velocity profiles

Any deviation from homogeneity in the slurry mixture should affect the otherwise axisymmetric time-averaged velocity profiles in the horizontal pipe section. For this purpose, we present the time-averaged velocity plots from UIV in Figure 6.3(a). For each example, two plots are shown - one wherein images were taken from the top and another from the side. The overlap of the two velocity profiles, or lack thereof, can already serve as an indicator of homogeneity in the system. All these measurements were performed within thirty minutes prior to shutdown and are based on a total of 43.6 seconds (five discontinuous datasets spanning 8.72 seconds). At locations with low signal-to-noise ratio (as defined in Dash *et al.*, 2022), the velocity data is excluded. Data quality is typically low very close to the wall (due to high velocity gradients) and far away from the wall (due to attenuation of ultrasound waves).

For [1.87, 1.15] m/s ↓, the two velocity profiles overlap well, implying that the system should be homogeneous. Similar overlap also holds true for [1.47, 1.46, 1.30] m/s ↓ (data not shown). With decreasing bulk velocity, the region near the wall with a high velocity gradient becomes larger, resulting in a less flatter velocity profile. For 0.99 m/s ↓ and 0.80 m/s ↓, the loss of axisymmetry is visible but not severe. However, for the two peculiar cases, 0.63 m/s ↓ and 0.60 m/s ↑, the deviations from axisymmetry are much more emphatic - the velocity profiles measured from the top and side show poor overlap.

At least for 0.63 m/s ↓ where a stationary bed is expected to be present, the velocity profile from the top is expected to possess more momentum. Thus the loss of axisymmetry for 0.63 m/s ↓ is not too surprising. For the experiment 0.60 m/s ↑ (where 0.60 m/s is the *initial* velocity), the bulk velocity was already 0.92 m/s by the time the ultrasound images were recorded. However, the deviation from axisymmetry is much stronger than either 0.80 m/s ↓ or 0.99 m/s ↓. This observation, together with the example of the gradually dropping pressure gradient in Figure 6.2(b), might suggest that the homogenization process is perhaps incomplete.

Our velocity measurements imply that modelling two-phase fine-grained slurry flows as a homogeneous, effectively single-phase, non-Newtonian liquid under non-turbulent conditions must be done at one's peril. The additional possibility of inhomogeneity must not be neglected. Thus, it would be far-fetched for us to directly associate our observations

in the transitional regime to those observed in homogeneous systems. It is well known that in such homogeneous non-Newtonian systems, the time-averaged velocity profiles in the transitional regime are non-axisymmetric, unlike the laminar or the turbulent regime (Escudier and Presti, 1996; Escudier *et al.*, 2005; Peixinho *et al.*, 2005; Güzel *et al.*, 2009; Wen *et al.*, 2017).

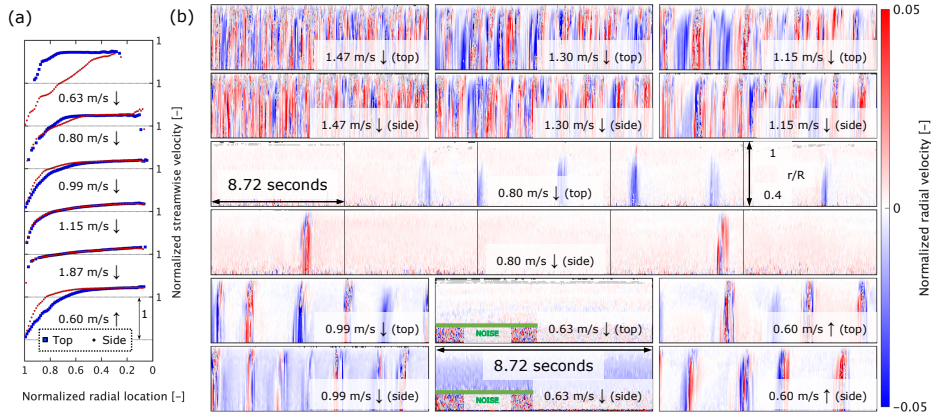

Figure 6.3: (a) Presence/absence of symmetry in time-averaged velocity profiles. (b) Spatio-temporal plots of radial velocity normalized by bulk velocity. At the time of measurement, for 0.63 m/s ↓, U_b = 0.51 m/s while for 0.60 m/s ↑, U_b = 0.92 m/s. The measurements from top and side are not simultaneous. The horizontal extent of each box is 8.72 seconds. The results of 0.63 m/s ↓ are afflicted by noise away from the wall (underneath the green line) and should not be mistaken for turbulence.

To have a closer look at the flow topology, instantaneous velocities are considered next. In Figure 6.3(b), spatio-temporal radial velocity profiles for seven of the nine experiments are shown. Basically, instantaneous radial velocity profiles are stacked together. To estimate the length of the structures, the temporal axis can be converted to a spatial axis using the bulk velocity. For 1.87 m/s ↓, capturing the instantaneous velocities becomes challenging due to the high velocities in the flow. The experiments of 1.46 m/s ↓ were a repeatability test for 1.47 m/s ↓, and hence are not presented.

For 1.47 m/s ↓, 1.30 m/s ↓ and 1.15 m/s ↓, the entire spatio-temporal plot is filled with fluctuations, and thus can be classified as turbulent. This is not unexpected based on the pipe rheogram in Figure 6.2(c). As a result, the system is well mixed and explains why the corresponding time-averaged velocity profiles are symmetric. For 0.63 m/s ↓, the flow topology is laminar at the time of measurement. It seems that the velocimetry results for 0.63 m/s ↓ are corrupted away from the wall, due to the domination of noise. We believe this is caused by ultrasonic attenuation which itself is a function of spatial particle distribution.Velocity results underneath the green line are unreliable. For the remaining cases of 0.99 m/s ↓, 0.80 m/s ↓ and 0.60 m/s ↑, the flow topology can be classified as intermittent or transitional. Of course, for 0.60 m/s ↑, the bulk velocity had risen significantly to 0.92 m/s by the time these measurements were performed. Of the three intermittent cases, the case of 0.80 m/s ↓ has the sparsest levels of intermittency. Across all the examples, the rms of the radial velocity fluctuations is approximately 2-3% of the bulk velocity, meaning that they are typically > 0.02 m/s (several orders of magnitude higher

than the measured settling velocity of 342 nm/s). While we only present the radial velocity profiles here, the passage of these intermittent structures also affect the corresponding streamwise velocity profiles. Since ultrasound images are recorded at arbitrary times, the time-averaged velocity profiles from top and side might differ, depending on the degree of intermittency present when the ultrasound images were recorded.

The combined insights from the global point of view (pipe rheogram) and the local point of view (spatio-temporal distribution of velocities), can help one classify the flow regime. In the slurry community, especially for pipes, there exists a dichotomy in the flow regimes - a laminar and a turbulent regime separated by a single critical velocity. This critical velocity for transition is the point at which the wall shear stress begins to deviate from the analytical solution for laminar flows. Our results show that the process has a lot more intricacies. The example of 0.80 m/s ↓ is sparsely intermittent but the corresponding wall shear stress lies on the analytical solution for laminar flows. The case of 0.99 m/s ↓ as well as the final state of 0.60 m/s ↑ (0.92 m/s) deviate visibly from the laminar solution and could possibly be considered as approximate critical velocities from the perspective of slurry system design. As explained in Section 6.1, operating the pipeline close to the laminar-turbulent transition is considered most favourable. However, even if sparse levels of intermittency are present at velocities lower than the conventional critical velocity, it might be an even more favourable operating point. Thus, it might be valuable to consider a range of transitional velocities instead of reducing it to a point.

While flows of slurries in pipes are broadly categorized into two regimes, transitional flows in open channel flows are recognized as a regime rather than an intermediate step. For example, Haldenwang (2003) achieves this by distinguishing between the onset of transition and the onset of full turbulence. Baas *et al.* (2009) use ultrasonic velocity profiling to extract time-averaged and time-resolved velocities, and identify five different flow regimes: turbulent flow, turbulence-enhanced transitional flow, lower and upper transitional flow, and quasi-laminar plug flow. This is not to say that slurry community is unfamiliar with the concept of intermittent flows in pipes. However, slurry flows in pipes could benefit from a more refined classification of the flow regimes.

6.4. Results: ramped inflow experiments

Four day-long ramped inflow experiments were performed, wherein two types of trajectories were followed: ramp-up (↑) and ramp-down (↓). Shown in Figure 6.4 are the pipe rheograms for both experimental trajectories. At lower pseudo shear rates (conversely, lower bulk velocities), the flow typically displays transient behaviour irrespective of the experimental trajectory (see the two examples that have been zoomed in on in Figure 6.4(a)). In a few instances, the transient behaviour is not as evident. However, our observations are limited to the time spent at each measurement point. At higher pseudo shear rates, the flow rates were altered after a few minutes (typically ranging between 3-10 minutes). At lower pseudo shear rates, where transient behaviour was evident, the observation times were long enough to capture transient behaviour but short enough so that the the entire range of velocities could be traversed across the working day.

From the global behaviour of the pipe rheograms in Figure 6.4(b), a few things can be clearly deduced. Under laminar conditions (transient behaviour), the measured wall shear

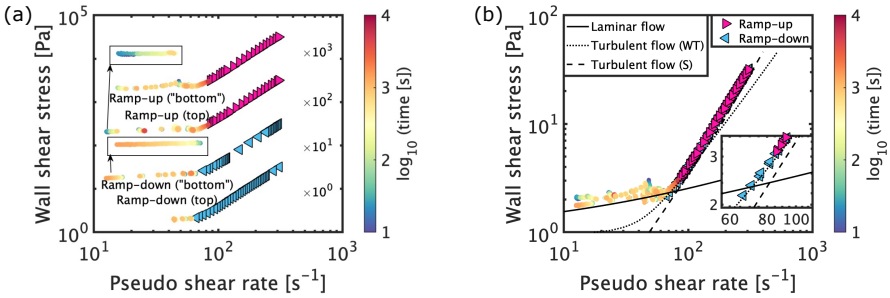

Figure 6.4: Pipe rheograms for the ramped inflow experiments. In (a) and (b), the four datasets are shown with and without an offset respectively. The identifiers "top" and "bottom" refer to the location of ultrasound imaging and are unrelated to the pressure drop measurements. Measurements wherein no transient behaviour was seen are plotted as triangular markers. Colour of the circular markers indicates the time passed since the flow rate had been set. In (b), a few relations popular in the slurry community are also plotted. "Laminar flow" = analytical solution for a laminar, pipe flow of a Herschel-Bulkley fluid. "Turbulent flow (WT)" = turbulent flow model of Wilson and Thomas (1985) and Thomas and Wilson (1987). "Turbulent flow (S)" = turbulent flow model of Slatter (1995). Equations for these relations are reproduced in the supplementary material. The inset in (b) zooms in on the beginning/end of observed steady-state behaviour.

stress slightly exceeds the analytically expected value. As the flow approaches the point of transition (when experimental data begins deviating from the analytical solution for laminar flows), the agreement between the experimental data and the analytical solution improves. This might be caused by the improved homogeneity in the system, as the analytical solution does not account for inhomogeneities.

There are a couple of subtle differences with respect to the pipe rheogram in Figure 6.2(c). In Figure 6.2(c), the results of 0.63 m/s ↓ deviate strongly from the laminar solution, as compared to the ramp-down results in Figure 6.4. One possible explanation for this is that in the ramped inflow experiments, the system is perturbed at irregular intervals by adjusting the bypass valve to attain a new flow rate. Another difference is related to how the ramp-up results differ from the unaltered inflow experiment of 0.60 m/s ↑. For 0.60 m/s ↑, the wall shear stress showed a small abrupt deviation from the laminar solution before gradually arriving closer to the trendline for non-laminar flows (see inset of Figure 6.2(c)). No such abrupt deviation is visible in the ramp-up experiments. This might provide further weight to the argument that the equilibration in that particular unaltered inflow experiment was indeed triggered by wall sampling.

In the slurry community, numerous criteria to detect laminar-turbulent transition point have been developed (Eshtiaghi, Markis, and Slatter, 2012). One of the simplest ways to determine a transitional velocity is by the so called intersection method, first used by Hedström (1952). Basically, a turbulent flow model needs to be selected, and its intersection with the analytical solution for laminar flow is considered to be the transitional velocity. According to the measurements, the transitional velocity is determined to lie between 0.85 and 0.89 m/s. In the present case, selecting the model of Wilson and Thomas (1985) (0.90 m/s) for the intersection method works better than selecting the model of Slatter (1995) (1.03 m/s). Finally, in the turbulent regime, the Slatter model performs better in predicting the wall shear stress. This also serves as a cautionary tale on directly

using various models. While these models are capable of providing a ballpark for pressure gradients or critical velocities, they need not necessarily work perfectly. For example, the models might be sensitive to the choice of the fitted parameters characterizing the rheology (Vlasak and Chara, 1999).

Based on relatively well overlapping curves in Figure 6.4(b), one might conclude that there are no hysteresis effects in the system (since data points collapse on one another irrespective of the protocol). However, this is not strictly true. In the inset of Figure 6.4(b), it can be seen that the pseudo shear rates below which transient effects are evident for the ramp-up experiments are higher than for ramp-down experiments. For clarity, only the non-transient data are shown in the inset of Fig. 4b, to highlight that the onset occurs at different pseudo shear rate. We identify these two critical pseudo shear rates (or velocities) as *suspending velocity* (ramp-up) and *deposit velocity* (ramp-down). The former is the critical velocity above which all particles are suspended, whereas the latter is the critical velocity below which particles begin to deposit. These concepts are well-established in the context of settling slurries (Carleson *et al.*, 1987). In our experiments, the suspending velocity exceeds the deposit velocity, subtly illustrating the presence of hysteresis.

6.5. Slowly settling behaviour

While discussing the unaltered inflow experiments, it was shown that if the system was homogenized at a very high velocity and then the flow rate was reduced to a desired value, a steady flow rate could be obtained under intermittent/turbulent conditions. However, under laminar conditions, the flow rate dropped continuously and gradually, while the pressure gradient rose. Spatio-temporal plots of ultrasound image intensities recorded from top, in Figure 6.5(a), show that the intensities are lower under laminar than turbulent conditions proving that the slurry is not homogenized under laminar conditions. All of this led us to hypothesize that this supposedly "non-settling" slurry experiences settling.

To verify this hypothesis, a separate experiment was performed. After operating the system at a relatively high velocity (albeit much lower than the maximum velocity), the flow rate was reduced to a value in the laminar regime. We capture ultrasound images from the bottom of the pipe. We concurrently log the flow meter readings, from which the bulk velocity can be determined. As expected, we observe a gradual decline in the measured bulk velocity as shown in Figure 6.5(b). However, the rate of decline (0.8 mm/s per minute) is higher than in Figure 6.2(a) for 0.63 m/s ↓ (0.3 mm/s per minute). This suggests that the transient behaviour is sensitive to the initial conditions.

The simultaneously recorded ultrasound images verify our hypothesis regarding the settling of particles and the formation of a stationary bed. This is shown in Figure 6.5(c), wherein the thickness of the stationary bed grows in time. Since the static background is subtracted from the images, the pipe wall and the stationary bed appear dark in Figure 6.5(c). Next to it is a thin, bright patch which we identify as mobile bed layer. Beyond that is the slurry which is still suspended. The effect of the growing stationary bed height is also visible on the intensity of the images. As the bed gets thicker with time, the attenuation of the ultrasonic waves grows. As a result, the image intensity of the sliding bed and the suspended slurry reduces. We can claim that the gradual reduction in measured volumetric flow rates is correlated to the settling of particles leading to a bed for-

mation. These observations seemingly contradict common rules-of-thumb wherein such fine-grained kaolin slurries are assumed to be non-settling.

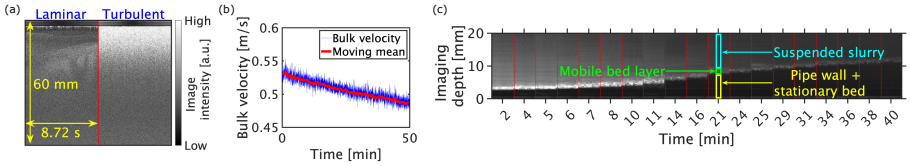

Figure 6.5: (a) Spatio-temporal evolution of ultrasound image intensities under laminar and turbulent conditions (ramp-down experiments), when viewed from top. (b) Measured volumetric flow rate. (c) Formation of stationary bed as imaged from bottom. Results in (b) and (c) are simultaneous.

Clarke and Charles (1997) too observed a slow accumulation of a stationary deposit, leading to a gradual reduction in flow rate (albeit for a slightly coarser kaolin slurry). In this context, we second Clarke and Charles (1997) in their statement *"While many slurries may be classified as either settling or non-settling, it is sometimes difficult to assign a slurry to one of these categories, and thus it is more appropriate to classify it as 'slowly-settling'."* Such a classification is yet to be acknowledged in mainstream literature. This is not to say that the slurry community is unfamiliar with this behaviour. Thomas (1961) has stated that the critical deposit velocity (the velocity below which a stationary bed forms) coincides with the transition from laminar to turbulent flow. While not shown, we do not observe any bed formation under turbulent flow conditions, in line with Thomas (1961). Javadi, Pirouz, and Slatter (2020) write *"for slow settling materials ... the laminar regime transportation can be adopted for relatively short distances since the likelihood of a density profile formation is expected to be relatively low"*. Subsequently, the authors also write about a maximum pipeline length which can be accepted, before blockage becomes an issue under laminar conditions. Similarly, Thomas, Pullum, and Wilson (2004) write *"There are a number of long distance slurry pipelines that have transported fine particle slurries under laminar flow conditions ... Aude, Derammelaere, and Wasp (1996) ... concluded that even fine particles settled slowly towards the bottom of the pipe under laminar flow conditions, although this might not occur for the first few kilometers of travel"*. The results presented here should not be confused with *stabilised laminar slurry flow*, Stab-flo(w). Stab-flo(w) involves transporting coarse particles in a suspension of carrier liquid and fine particles. The idea is that the fine particles introduce a yield stress, which would prevent settling of the coarse particles. All of this allows transporting the slurry under laminar conditions (more energy efficient) while maintaining stability (lack of settling). Nonetheless, several works have identified that Stab-flo(w) conditions are not as stable and settling of the coarse particles does occur. See Thomas, Pullum, and Wilson (2004) and Paterson (2012) for detailed overviews. In any case, the settling that is observed in our experiments is that of fine particles itself, which might also be of relevance for Stab-flo(w).

Experiments similar to those considered here (measuring global and local quantities) can be used to establish critical pipe lengths for which transport of slurries under laminar conditions can be executed without the danger of blockage (for example, by performing experiments in pipes of various lengths). This would also allow one to adjudge whether a pipeline transporting fines should be operated on the laminar side of the laminar-turbulent

transition, which is considered to be more efficient. While practitioners may be familiar slow settling, its obscurity in academic literature prevents the possibility for it to be thoroughly analysed to formulate/reassess guidelines.

6.6. Self-equilibrating behaviour

In this section, we take a closer look at the self-equilibrating behaviour. Such behaviour was evident in the two ramp-up experiments (ramped inflow experiments wherein the system is not initially homogenized; in one experiment ultrasound images are recorded from the top, and from the "bottom" in the other), whose results are reported here. Figure 6.6 compiles the key results from the ramp-up experiments. Please note that only results concerning the self-equilibration phenomenon from these measurement days are shown. These events span about 100 minutes, which is a fraction of the working day.

In Figure 6.6(a), we show the evolution of the bulk velocity in time on two separate days of ramp-up experiments. Sudden jumps in the bulk velocity indicate that the flow rate was altered manually (for example, far right side of the top left blue panel). In the ramp-up experiment wherein imaging was performed from the top, we observe a period wherein the bulk velocity gradually rises (red patch). After adjusting the flow rate by closing the bypass valve a bit (blue patch), this trend of increasing bulk velocity continues (albeit at a faster rate), before it attains a form of equilibrium with constant velocity. A similar observation was made while imaging from the bottom (magenta patch). Remarkably, the bulk velocity at which equilibrium is observed happens to be 1.04 m/s on both occasions. Given that the ↑ experiments require more care in starting up and might be sensitive to how the various valves were handled (which can affect the bed), it is remarkable that the equilibrium velocity is identical. This is higher than the equilibrium velocity of 0.92 m/s observed in the unaltered inflow experiment of 0.60 m/s ↑. The mismatch in the equilibrium velocities could be attributed to the role of wall sampling in affecting the flow during the unaltered inflow experiments. The rate at which the velocity rises in the final stages of these ramp-up experiments is 4.9 mm/s per minute (imaging from top) and 5.5 mm/s per minute (imaging from bottom), in contrast to 0.9 mm/s per minute in the unaltered inflow experiments. These rates are much higher than what we observed for slow settling.

Simultaneous evolution of pressure gradient is shown in Figure 6.6(b). In the self-equilibrating phase, the pressure gradient gradually rises over 30 minutes and appears to be steady thereafter (at least for the observed time period). Unlike the unaltered inflow experiment of 0.60 m/s ↑, no wall sampling was performed. Therefore, in these instances, we can claim that the equilibrating process occurs intrinsically.

On both days, simultaneously measured time-resolved radial velocities are shown in Figure 6.6(c) from top and bottom. Downward moving motions have negative values and vice versa. The quality of UIV is reduced from the bottom for two reasons: the presence of more settled particles (attenuation of sound waves) and poorer contact with the pipe wall (non-normal angle). Four instances of image intensities are shown in Figure 6.6(d), denoted by T1-4 and B1-4. The velocities considered here are close to the laminar-turbulent transition. At lower velocities, viscous resuspension (Zhang and Acrivos, 1994) probably governs the increasing flow rates.

The UIV results from the top offer insights on this process. Initially, the flow appears

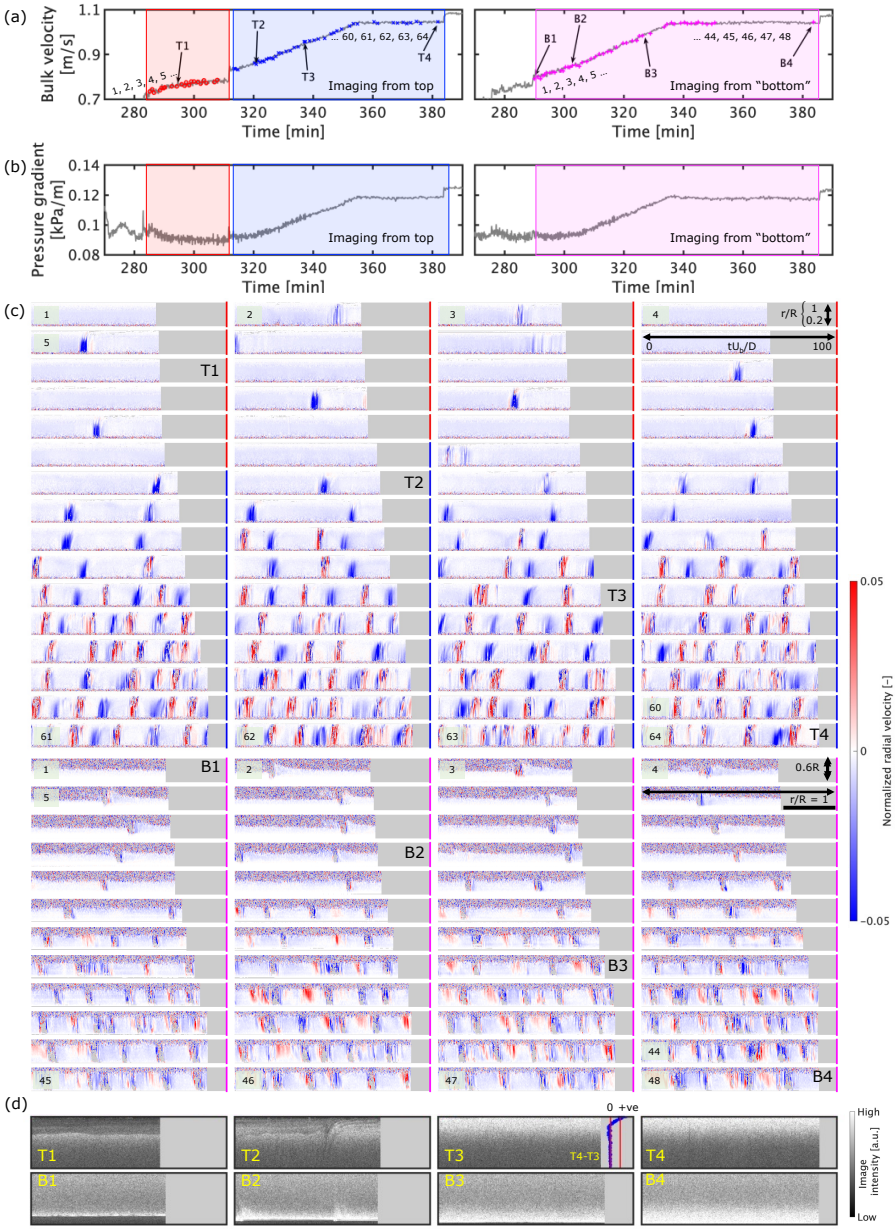

Figure 6.6: (a) Temporal evolution of bulk velocity during the self-equilibrating process on two separate days. The markers indicate moments at which ultrasound images were recorded. There are 64 markers in the left and 48 in the right panel. Coloured patches correspond to one setting of the slurry pump frequency and bypass valve opening fraction. (b) Corresponding temporal evolution of pressure gradient (c) Spatio-temporal features of the flow corresponding to the patches and markers in (a). The numbering in the panels gives an indication of how these panels are related to the markers in (a). All measurements based on 8.72 seconds. (d) Spatio-temporal features of the image intensity. Extents of axes same as (c). The plot of T4-T3 shows that the process of homogenization is incomplete at T3.

to be mainly free of disturbances (laminar) with very sporadic instances of downward moving intermittent structures passing by. As time passes, the frequency with which structures appear increases. Hereafter, another type of intermittent structure begins to appear, one that is moving upwards. These two types of intermittent structures then begin to appear regularly and alternately. In the final stage, these intermittent structures appear in a more random manner. From the bottom, two distinct types of structures can be seen as well, but there is some ambiguity surrounding their exact characteristics and the order in which they appear, due to the reduced quality of results. These structures likely promote the complete resuspension of the slurry, which is verified from the image intensities.

From the top, it can be seen that under laminar conditions (T1), the slurry is not homogeneous. When an intermittent structure passes by (T2), it is immediately followed by a region wherein slurry has been resuspended. Eventually, as more of these structures pass by, the more the slurry is resuspended (T3). The complete resuspension of the slurry coincides with the attainment in an equilibrium flow rate (T4). That the resuspension process is incomplete at T3 is visualized by the blue line plotting T4-T3. While T3 and T4 appear very similar, the difference can be highlighted by subtracting the time-averaged intensity profiles (blue line T4-T3 in Figure 6.6(d)). From the bottom, a similar trend is seen, except this time, the stationary bed is visualized (black region at the bottom). Under laminar conditions, a bed is present (B1). Upon the passage of intermittent structures, particles from the bed are entrained into the flow (B2). As more of these intermittent structures pass by, the bed gets thinner (B3). Eventually, when the equilibrium phase is attained, the bed is absent (B4).

The process of self-equilibration is facilitated by two types of intermittent structures, which appear in stages. We refer to the first type of intermittent structure as "downward moving" and the second type as "upward moving". We consciously do not refer to these structures as puffs as observed in Newtonian fluids. Typically, turbulent puffs contain a mixture of positive and negative fluctuations. In this context, the second type of intermittent structure resembles a turbulent puff. But, more measurements will be necessary for verification. That we observe the transition process to occur in two stages is something that was also reported by Peixinho *et al.* (2005) for a single-phase, non-Newtonian fluid with a yield stress. Esmael and Nouar (2008) suggest that in such non-Newtonian fluids, a robust nonlinear coherent structure characterized by two weakly modulated counter-rotating vortices mediates the transition to turbulence. However, we cannot directly place our results in the context of the works of Peixinho *et al.* (2005) or Esmael and Nouar (2008). The main reason is that we view our non-Newtonian slurry from the optics of two-phase flows, unlike the single-phase nature of the above studies.

To the best of our knowledge, this long-time-scale transient has not been reported previously. Most studies on non-settling slurry flows focus on steady state behaviour (possibly after the system has been well-mixed). However, we did find a handful of studies focusing on the start-up process commencing from an initial condition of settled solids.

Shook and Hubbard (1973) used a slowly-settling slurry (particle sizes slightly larger than present study) as well, to look into the first few seconds of the startup process. Using their experiments, they were able to demonstrate that the slurry could be fully suspended within a couple of seconds, even after several hours of shutdown (possibly under turbulent

conditions).

In a follow-up study, Peters, Salazar, and Shook (1977) performed similar experiments for a settling slurry and provided nice insights into this process by flow visualization. They look into the time needed for the bulk flow rate to reach 63.2% (1-1/e) of the final velocity for two different lengths of the bed and two different solids concentration. In their case, the timescales were in the order of seconds, which might be due to the smaller size of the facility (< 4 m). In fact, their findings and remarks might already explain our observations – that partially obstructed pipelines can be cleared of the solids with low pressure gradients, but the startup process would be prolonged. They report that the erosion of the bed occurs upstream followed by deposition downstream leading to an effective bed displacement velocity. If such behaviour occurs in our relatively larger pipe (> 80 m), the timescales could be much longer.

More recently, Goosen (2015) performed similar experiments with a settling slurry, where the system was ramped from a settled state to a fully suspended state in two minutes. The key findings were that the suspending velocity exceeded the deposit velocity, the suspending velocity increased with increasing length of the shutdown, and that there was a peak in the pressure gradient just before the bed is fully re-suspended. Only the first of the above three is observed by us.

The relevance of our findings lies in the fact that the equilibrium state corresponds to the intermittent regime, near the favourable operating point of the critical velocity. As a result, this is interesting from a practical perspective, especially while restarting a pipe. Over the course of a prolonged shutdown, the rheology of the mixture could undergo a change. This would necessitate reassessing the rheology to determine the new critical velocity. The self-equilibrating approach to starting up the pipe would, however, not require a reassessment of the rheology. In short, this approach will target the suspending velocity rather than the deposit velocity. Having the system achieve its own equilibrium point (albeit with a prolonged period of low throughput) rather than fully homogenizing it and seeking a point above the deposit velocity could serve as an alternate and a less uncertain approach to pipeline startups.

6.7. Conclusions and Outlook

We presented a case study taking a close look at laminar-turbulent transition for a conventionally non-settling Kaolin slurry. Thanks to the relatively large scale of the flow facility and long measurement times, we identified two long-time-scale transients - *slow settling* and *self-equilibration*. Signatures of these phenomena can be found in the flow meter readings (decreasing and increasing bulk velocities respectively) facilitating easy detection. These phenomena are dependent on the initial conditions. Slow settling requires the system to be in the laminar regime following homogenization, whereas self-equilibration requires the system to be in the laminar regime without any homogenization. For self-equilibration, the settled particles are gradually resuspended, and the final state of the flow is intermittent. Seemingly, two types of intermittent structures are responsible for self-equilbration. These structures appear in two stages, and the degree of intermittency increases as the slurry homogenizes.Signatures of these phenomena can be found in the flow meter readings (decreasing and increasing bulk velocities respectively) facilitating easy detection. In

Table 6.1, we summarize all the experiments and corresponding results.

We interpreted our observations in the context of slurry flow in a horizontal pipe. For completeness, it would be necessary to interpret the observations in the context of the system as a whole (for example, including the role of the bypass loop or 90° bend, in influencing the transients). Experiments with more slurries and in different facilities will help form a more complete picture. The fact that the transients have a long-time-scale is subjective to the present combination of slurry and facility. Different combinations could alter the time-scales for the transient behaviour, to the extent that it could be debated whether they can be classified as 'long-time-scale' to begin with.Moreover, our observations are primarily qualitative. This case study serves as a starting point to revisit these phenomena from a more quantitative viewpoint (for example, influence of flow history and ramping rates on transient behaviours, or the exact structure of the two types of intermittent structures responsible for self-equilibration).In the present study, based on flow meter readings, we observe different rates at which these transient phenomena occur. This obviously suggests that defining timescales for these transient phenomena unambiguously will not be trivial.

Our findings can be relevant from a practical perspective. The slow settling behaviour should gain more recognition in mainstream slurry literature, in contrast to the present dichotomy of settling and non-settling slurries. This is relevant, as slow settling is a precursor to shutdown. The self-equilibrating behaviour offers an alternate approach to starting up a pipeline following a shutdown, without necessarily having to possess knowledge of the slurry rheology. The significance of these transients necessitates that the dichotomy of laminar and turbulent regimes be altered to include the transitional regime.

From an experimental perspective, monitoring fine-grained slurries with ultrasound imaging (velocimetry) will help discover phenomena or, at the very least, generate unique experimental data to validate numerical/theoretical studies. Ultrasound imaging (velocimetry), which is relatively expensive, helped us link local and global features concerning the two long-time-scale transients. This measurement technique can be used to calibrate and benchmark signals obtained by differential pressure sensors and/or ultrasonic velocity profilers, which are cheaper. These cheaper alternatives can then be placed at multiple streamwise and circumferential locations to monitor the long-time-scale transients with more rigour (for example, decay/splitting/expansion of intermittent structures, bed profiles, and the interplay between the bed and the intermittent structures). Using numerical simulations could serve as an alternate modality for studying this phenomenon in more detail. Our work demonstrates that such fine-grained, non-Newtonian slurries may not simply be assumed to be homogeneous away from the turbulent regime. While discrete particle modelling of such systems would be infeasible with present day capabilities, two-fluid models might serve as a balance between affordability and scientific fidelity.

To conclude, the settling behaviour and the laminar-turbulent transition of slurries is more nuanced than the present rules-of-thumb or models used by slurry pipeline transport practitioners. A concerted attempt to translate these subtleties into decision-making (for example, maximum pipeline length for laminar transport or the minimum allowable transport velocity) can prove beneficial, since the critical velocity for laminar-turbulent transition is an optimal operating point.

Table 6.1: Overview of experiments and corresponding key results presented in this chapter.

Experiment - Section 6.2, Figure 6.1	Global flow features	Local flow features
(I) *Unaltered inflow experiments - Section 6.3, Figure 6.2, Figure 6.3*		
– [1.87, 1.47, 1.46, 1.15] m/s ↓ – System mixed at highest flow rate prior to setting target conditions	– Pressure drop and volumetric flow rate steady throughout working day – Rheogram suggests flow is turbulent	– Symmetric time-averaged velocity profile – Flow state turbulent
– [0.99, 0.80] m/s ↓ – System mixed at highest flow rate prior to setting target conditions	– Pressure drop and volumetric flow rate fairly steady throughout working day for 0.99 m/s ↓ – Peculiar fluctuations for 0.80 m/s ↓ – Rheogram suggests 0.99 m/s ↓ is turbulent while 0.80 m/s ↓ is laminar	– Mild loss of symmetry in time-averaged velocity profile – Spatio-temporal intermittency higher in 0.99 m/s ↓ than for 0.80 m/s ↓
– 0.63 m/s ↓ – System mixed at highest flow rate prior to setting target conditions	– Volumetric flow rate monotonically reduces by 20% over working day – Simultaneously, pressure drop rises by 30% – Rheogram initially in line with analytical solution for laminar flow, before slowly deviating from it	– At time of measurement, bulk velocity is 0.51 m/s – Remarkable absence of symmetry in time-averaged velocity profile – Flow topology laminar at time of measurement

Continued on next page ...

Table 6.1: ...continued from previous page

Experiment - Section 6.2, Figure 6.1	Global flow features	Local flow features
– 0.60 m/s ↑ – System started from stratified state (so no mixing)	– Volumetric flow rate monotonically rises by 50% while pressure drop stays constant until wall sampling – Following wall sampling, the pressure drop shows a sharp rise, while the flow rate equilibrates – Rheogram initially in line with analytical solution for laminar flow before wall sampling causes it to deviate and suggest the presence of turbulence	– At time of measurement, bulk velocity is 0.92 m/s – Mild loss of symmetry in time-averaged velocity profile – Spatio-temporal intermittency visible
(II) *Additional experiment to probe slow settling - Section 6.5, Figure 6.5*		
– System mixed at a high flow rate – Bulk velocity set to 0.55 m/s	– Volumetric flow rate drops monotonically	– Simultaneous imaging reveals bed formation, the height of which grows in time

Continued on next page ...

Table 6.1: ...continued from previous page

Experiment - Section 6.2, Figure 6.1	Global flow features	Local flow features
(III) *Ramped inflow experiments - Section 6.4, Section 6.6, Figure 6.4, Figure 6.5, Figure 6.6*		
– Ramp-down – Two separate days of experiments (one day imaging from top, other day from "bottom") – System mixed at highest flow rate following which flow rate is reduced in steps over course of the working day	– Rheogram close to analytical solution for laminar flow – Critical velocity (deposit velocity) below which transient behaviour of dropping flow rates is evident	– Clear reduction of slurry homogeneity in laminar conditions as compared to turbulent conditions
– Ramp-up – Two separate days of experiments (one day imaging from top, other day from "bottom") – System started from a stratified state following which flow rate is raised in steps over course of the working day	– Rheogram close to analytical solution for laminar flow – Critical velocity (suspending velocity) below which transient behaviour of rising flow rates is evident – Suspending velocity higher than deposit velocity – Self-equilibrating behaviour visible in flow rate (slow rise followed by equilibration) – Self-equilibration velocity is 1.04 m/s on both days	– Self-equilibrating behaviour captured via ultrasound imaging – Two types of intermittent structures seemingly appear in stages, which are found to be responsible for slurry resuspension – Increase in flow rate corresponds with increased frequency in the appearance of intermittent structures and increased homogeneity

Acknowledgements

The measurement campaign was hosted and facilitated by Deltares. Assistance from members of the Physical Laboratory (Deltares), especially A. Shakeel, aided the slurry characterization. The work also benefited from a fruitful discussion with A. Talmon.

6.A. Slurry characterization

The slurry sample is composed of Kaolin(ite) dispersed in tap water (electrical conductivity = 0.0635 S/m). In short, kaolin is a hydrophilic whitish powder with pseudo-hexagonal flakes (Murray, 1961, 2000). While there are several publications characterizing Kaolin, properties may vary from sample to sample and is likely to be dependent on the mineralogy as well. This makes characterization a necessary step.

We report information on particle sizing, mass density, rheology, zeta potential, and in-situ settling velocity of the slurry. The mass density and rheology measurements are based on slurry samples collected midway through an experimental day corresponding to the unaltered inflow experiments (wall sampling). All ex-situ tests presented here were performed at the Physical Laboratory located at Deltares.

6.A.1. Particle sizing

The particle size distribution of kaolin was determined using a Malvern Mastersizer 2000, which relies on a light scattering technique. A dilute sample of the slurry was stirred at 2000 rpm, strong enough to prevent agglomerates of clay particles. The results are presented in Figure 6.7(a). We show the distribution of samples from the pipeline (dispersed) and of the dry clay powder (undispersed). For the latter, measurements were made after one hour of continuous stirring in the measurement device. It is evident that the particles in the dispersed sample are finer than in the undispersed sample. There could be a couple of explanations for these: particles in the undispersed sample might still be stuck due to cohesive forces, while particles in the dispersed sample might have experienced attrition in the slurry pump. Of course, the dispersed sample is of higher interest, for which d_{10} = 1.18 μm, d_{50} = 5.18 μm, d_{90} = 20.76 μm. The particles are relatively fine by the standards of the slurry transport community (Pullum, Boger, and Sofra, 2018).

6.A.2. Mass density

The mass density of the slurry samples was estimated by three different techniques: drying-weighing, 25 ml glass beaker pycnometer, and a handheld density meter (Anton Paar DMA-35). We report results from all three techniques in Figure 6.7(b), but the drying-weighing technique is least prone to errors. The results of the handheld density meter were typically close to that from the drying-weighing method (except one instance). The mass densities estimated using the beaker pycnometer technique systematically overestimated densities by 2%. For the drying-weighing technique, a slurry sample is allowed to dry in an oven at 105 $^{\circ}$C for > 24 hours. By knowing the weights of the slurry sample before and after drying, the mass fraction can be determined. To convert the mass

fraction of the slurry to mass density of the slurry, the mass density of individual Kaolin particles is necessary. This was determined to be 2695.2 kg/m^3 by an AccuPyc 1330 pycnometer. The density of the slurry is approximately 1152.1 kg/m^3. The measured mass densities across the samples collected during the "unaltered inflow" experiments reflect the (in)homogeneity of the flow when wall sampling was performed. The biggest deviations in the measured mass densities occur for 0.83 m/s ↓, 0.63 m/s ↓, and 0.60 m/s ↑, which are also the cases where peculiarities in the measured bulk velocities were observed Figure 6.2(a).

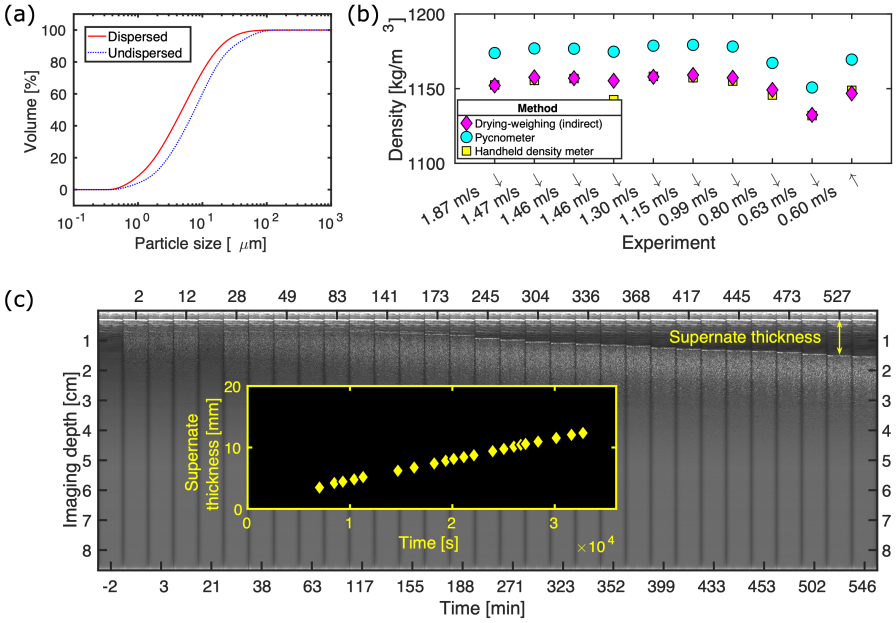

Figure 6.7: (a) Cumulative particle size distribution of the kaolin particles (b) Mass density for samples collected for the unaltered inflow experiments (c) In-situ settling of the slurry under quiescent conditions.

6.A.3. Rheology

In our case, this slurry is specifically used in order to mimic the rheological properties of wastewater, which is typically non-Newtonian, can exhibit a yield stress, and is shear thinning (Eshtiaghi *et al.*, 2013). Of course, in reality, actual wastewater will have even more complex properties such as thixotropy (history-dependent rheology).

For the purpose of this work, we describe the rheology of the slurry using a Herschel-Bulkley equation, $\tau = \tau_y + K\dot{\gamma}^n$. Here, τ is the shear stress and $\dot{\gamma}$ is the shear rate, which together determine the rheogram. To characterize the slurry, the following are needed: τ_y (yield stress), K (consistency index), and n (behaviour index). The apparent viscosity of the slurry, η, can then be determined as $\eta = \tau/\dot{\gamma}$.

Typically, two yield stresses are quantifiable - a static and a dynamic yield stress. The

former would be the minimum stress needed to start a flow whereas the latter would be the minimum stress necessary to sustain a flow. For the present work, knowing the dynamic yield stress is more relevant. The static yield stress can be determined from steady shear rate measurements in which the shear rate is increased in time and the dynamic yield stress can be determined from steady shear rate measurements wherein the shear rate is decreased (Dinkgreve *et al.*, 2016).

Rheological characterization is performed using a HAAKE MARS I rheometer (Thermo Scientific, Germany) with a conventional bob-cup geometry. This simple geometry is sufficient as the slurry is thin and fluid-like. The temperature is set at 18°C.

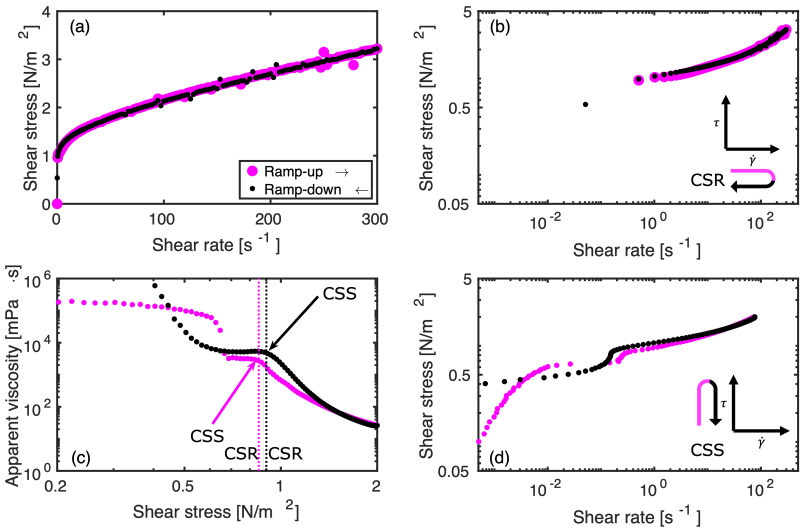

Figure 6.8: Rheology of the sample collected under turbulent conditions. (a), (b) CSR rheogram on linear and log scales (c) Apparent viscosity from CSS measurement (d) CSS rheogram on log scale.

Two different protocols were followed: one with controlled shear stress (CSS) followed by one with controlled shear rate (CSR). In CSS experiments, torque on the bob is controlled while in CSR experiments, torque on the bob is measured. Prior to performing each protocol, a fresh sample was agitated manually and added to a new cup.

In the CSS measurements, the shear stress is slowly ramped up from 0-2 N/m^2 over the course of 200 s in a linear, stepwise manner. Data is sampled every 2 s returning 100 points. The shear rate and apparent viscosity are measured. After the maximum shear stress is reached, the ramp direction is reversed immediately from 2-0 N/m^2 in a similar manner.

In the CSR measurements, the shear rate is slowly ramped up from 0-25 s^{-1} over 100 s in a linear, stepwise manner. Hereafter, the shear rate is ramped up from 25-300 s^{-1} over 200 s in a linear, stepwise manner. Data is sampled every 2 s returning 150 points. The shear stress and apparent viscosity are measured. After the maximum shear rate is reached, the ramp direction is immediately reversed from 300-0 s^{-1} in a similar manner.

Given the relatively low volumetric concentration of kaolin, the slurry has a low yield stress. Fitting the Herschel-Bulkley equation directly to CSR measurements will yield an "apparent" yield stress. Hence, a CSS measurement allows for an accurate estimation of a "true" yield stress, due to an improved resolution of shear stresses. This τ_y is then used in a recast Herschel-Bulkley equation, $\log(\tau - \tau_y) = \log K + n \log \dot{\gamma}$, in combination with CSR measurements to recover K, n.

In Figure 6.8, we present the rheology of the slurry sample collected during the turbulent flow measurements. Based on the rheograms in Figure 6.8(a, b), corresponding to the CSR protocols, it can be seen that the apparent yield stress is in the order of 1 Pa. Moreover, there are no discernible differences between the ramp-up and ramp-down portions of the protocol, suggesting the absence of any significant thixotropic behaviour. However, on the logarithmic scale, it is evident that there are not enough data points for the low shear rates, that would be necessary for one to confidently estimate the yield stress.

The CSS measurements, thus, solve this issue, as is evident in Figure 6.8(d). The rheogram can be reformulated to plot the apparent viscosity as a function of shear stress, like in Figure 6.8(c). For the ramp-up measurements, there are two shear stresses at which a sharp drop in the apparent viscosity is observed, at approximately 0.6 Pa and 0.85 Pa. The former might be related to slip between the slurry and the bob and is not of physical interest. The latter represents the desired yield stress that can be used to characterize the slurry. Similar two-step yielding behaviour has been observed for mud suspensions (see Shakeel, Kirichek, and Chassagne, 2020, Figure 4 therein). For the ramp-down measurement, there is only a single shear stress at which there is a sharp change in viscosity, at approximately 0.9 Pa. We use the ramp-down segment to estimate τ_y. Using this value from the CSS measurement, we use the ramp-down portion of the CSR rheogram to determine K, n. In short, we determine the following properties for this slurry: $\tau_y = 0.8889$ Pa, $K = 0.1579$ Pa·s$^{0.4579}$, $n = 0.4579$.

6.A.4. Zeta potential

Kaolin is also considered to have "relatively weak cohesive properties" (Baas, Best, and Peakall, 2016). We confirm this by measuring the zeta potential with a Malvern ZetaNano device. In short, this measurement indicates the surface charge of the particles and their ability to attract/repel each other. Prior to measuring the zeta potential, the slurry was diluted with supernatant (carrier fluid) from the flow facility. The zeta potential was measured to be -18.7 ± 0.469 mV. This value suggests that flocculation should not occur readily, and that the slurry is relatively stable. If flocculation is present, settling velocities would be enhanced.

6.A.5. Settling test

Another common test to characterize sediment/slurry is to perform a batch settling test, in order to estimate a settling velocity. We perform this in-situ in the horizontal pipe section of the industrial scale facility. After homogenizing the flow, the flow is stopped, and ultrasound images of the slurry are taken from the upper section of the horizontal pipe

section, similar as those shown in Figure 6.7(c). Images are taken at irregular intervals. When no images are being recorded, the ultrasound power is reduced to a minimum to minimize its influence on the slurry. Based on the slurry "blanket" height or thickness of the supernate measured under quiescent conditions over several hours (similar to Locatelli *et al.*, 2015), the settling velocity of this slurry is estimated to be 342 nm/s or 1.2 mm/hour. These values might be affected by the polydispersity of the slurry. Imaging from top will likely capture the finer particles, while imaging from the bottom will focus on the coarser particles.

6.B. Relevant equations for laminar and turbulent flows of a non-Newtonian slurry

We reproduce a few relevant equations/models from the summary compiled by van den Heever, Sutherland, and Haldenwang (2014). Please note that we only reproduce those equations/models that are used in the main text to compare with our measured data. Typically, relations are obtained between the bulk velocity, U_b, the wall shear stress, τ_w, the pipe diameter, D, and the slurry rheology, τ_y, K, n.

6.B.1. Laminar flow calculations

Under the absence of slip, the equation for volumetric flow rate can be combined with the Herschel-Bulkley rheological model to yield Equation (6.1). This equation provides a relation between the pseudo shear rate, the wall shear stress and the slurry rheology. This equation is analytically accurate and does not involve any major assumptions.

$$\frac{8U_b}{D} = \left(\frac{1}{K}\right)^{1/n} \frac{4}{\tau_w^3}(\tau_w - \tau_y)^{(n+1)/n} \times \left[\frac{n\tau_w^2}{(n+1)} - \frac{2n^2\tau_y(\tau_w - \tau_y)}{(n+1)(2n+1)} - \frac{2n^2(\tau_w - \tau_y)^2}{(n+1)(3n+1)}\right] \quad (6.1)$$

6.B.2. Turbulent flow model of Wilson and Thomas

A model to predict the turbulent flow of a non-Newtonian fluid was developed by Wilson and Thomas (1985) and Thomas and Wilson (1987). While the model was first presented in Wilson and Thomas (1985), a plus sign was incorrectly written as a minus sign (Thomas, 2018). This was rectified in Thomas and Wilson (1987). This model focuses on the change of the velocity profile in the wall region ("viscous layer thickening"). Equation (6.2) shows how the bulk velocity can be estimated.

$$U_b = 2.5u_* \ln\left(\frac{D\rho u_*}{\mu'}\right) + u_*[11.6(\alpha - 1) - 2.5\ln(\alpha) - \Omega] \quad (6.2)$$

The term u_* is the shear velocity ($= \sqrt{\tau_w/\rho}$). The term α is the ratio of areas under the non-Newtonian and assumed Newtonian flow curves at a given wall shear stress. The term μ' is the apparent viscosity at the wall shear stress. The term Ω accounts for blunting

of the velocity profile near the pipe centerline. The equations for α and Ω are given in Equation (6.3) and Equation (6.4) respectively.

$$\alpha = 2\left[\frac{1 + n\left(\frac{\tau_y}{\tau_w}\right)}{(1+n)}\right] \tag{6.3}$$

$$\Omega = -2.5 \ln\left[1 - \left(\frac{\tau_y}{\tau_w}\right)\right] - 2.5\left(\frac{\tau_y}{\tau_w}\right)\left[1 + 0.5\left(\frac{\tau_y}{\tau_w}\right)\right] \tag{6.4}$$

6.B.3. Turbulent flow model of Slatter

Another model was developed by Slatter (1995) for turbulent flow of non-Newtonian slurries. Basically, it relies on the classical roughness function utilized for Newtonian flows. But, it replaces the roughness with a characteristic particle size, d_{85}. Using this, a roughness Reynolds number, R_r. Equation (6.5) shows how this is defined for a Herschel-Bulkley fluid.

$$R_r = \frac{8\rho u_*^2}{\tau_y + K\left(\frac{8u_*}{d_{85}}\right)^n} \tag{6.5}$$

Depending on the value of the roughness Reynolds number, the flow can be classified as either "smooth wall turbulent flow" or "rough wall turbulent flow". The critical roughness Reynolds number is 3.32. According to the scenario, the appropriate relation can be used: Equation (6.6) for smooth or Equation (6.7) for rough.

$$U_b = u_*\left[2.5 \ln\left(\frac{D}{2d_{85}}\right) + 2.5 \ln R_r + 1.75\right] \quad \text{for} \quad R_r \le 3.32 \tag{6.6}$$

$$U_b = u_*\left[2.5 \ln\left(\frac{D}{2d_{85}}\right) + 4.75\right] \quad \text{for} \quad R_r > 3.32 \tag{6.7}$$

7

Meten is weten - Conclusions, outlook, and impact

…For the purpose of discovering new phenomena, experiments remain the most economical tool for fluid mechanics, while simulations, once they have been verified against experiments, are more suitable for producing comprehensive flow databases.
The computation of physical phenomena without developing a physical understanding can often produce misleading results. On the other hand, misguided experiments can equally contribute to the generation of more questions than answers. These somewhat orthogonal approaches have created two cultures of fluid mechanicians. The continuation of this two-culture mentality, namely experimentalists and numerical analysts who conduct experiments and simulations in isolation, would delay reaching the goals of understanding, modeling and predicting turbulence. To solve this problem, we need to include provisions in our university and government/industrial research policies to accommodate and encourage a new generation of scientists and engineers who understand and appreciate both simulations and experiments.

Gharib (1996)

Researchers occasionally go to great lengths to perform experiments or gather data, even if it is 1.5 meters above the ground.

7.1. Conclusions: what is new in this dissertation

In this section, key findings from the various chapters of this thesis are summarized. As a reminder, the key objective of this dissertation is: **How and to what extent can state-of-the-art measurement techniques be leveraged, in particular ultrasound imaging, to gain novel insights into the fluid mechanics of opaque inertial suspensions?** Research questions for individual chapters stated in Section 1.3 are repeated in bold text below.

7.1.1. Fundamental Fluid Mechanics

In the Taylor-Couette geometry, the effect of particle loading and Reynolds number on the different flow regimes was investigated with flow visualization. High suspension Reynolds numbers in dense suspensions of relatively large particles were investigated. Like other previous studies, an increased appearance of non-axisymmetric flow structures between circular Couette flow and wavy vortices was observed, with increased particle loading. Moreover, when experiments are performed where Reynolds number is increased with time, the likelihood of axially segregated, coexisting flow structures increases. A novel flow structure discovered during these experiments was the "azimuthally localized wavy vortex flow" - a structure which is a hybrid of axisymmetric Taylor vortices and non-axisymmetric wavy Taylor vortices. This structure could be sustained for as long as five hours (**Can new structures be discovered in suspension Taylor-Couette flows?**)!

Beyond the appearance of wavy vortices, the analysis was mainly restricted to frequency spectra. For low particle loading, the route to chaos appears similar to single-phase flows, that a second incommensurate frequency appears in the spectrum, before fine-scale structure is visible. In contrast, for high particle loading, the appearance of a second, incommensurate frequency was not observed (at least for the range of Reynolds numbers investigated). This could mean that at higher Reynolds numbers, the route to chaos is altered, without any appearance of modulated wavy vortices. At intermediate particle loadings, the presence/absence of a second, incommensurate frequency was found to be protocol dependent (**What is the characteristic of the flow structures beyond the appearance of wavy Taylor vortices, particularly with an eye on the route to chaos?**). Simultaneous torque measurements on the inner cylinder suggest that the exponent relating torque and Reynolds number is independent of particle loading (**What additional information do the torque measurements provide?**).

In the pipe geometry, experimental data corresponding to the flow of (semi-)dilute suspensions of relatively large particles were analysed. The range of suspension Reynolds numbers covered the laminar-turbulent transition. In these studies, ultrasound imaging was deployed to gain information on the microstructure of the flow, with all measurements being performed at a single streamwise location. For volume fractions up to 0.08, inertial migration of particles was detected. The strength of this migration became weaker with increasing Reynolds number, and the signature of migration was also evident at the beginning of transitional flows. With increasing turbulence in the flow, the signature of migration disappears. (**Can inertial migration of particles in a pipe flow be detected at optically inaccessible volume fractions?**). Time-averaged velocity profiles of the particulate phase were also extracted, for volume fractions up to 0.15. However, the sole insight

that could be gained is that the velocity profile became flatter with increasing Reynolds numbers. For lower Reynolds numbers and low particle volume fractions, weak evidence for the velocity profiles being affected by particle migration was also presented (**To what extent can ultrasound imaging tackle flows in academic ... backdrops?**).

7.1.2. Applied Fluid Mechanics

Measurements of the flow of a non-Newtonian kaolin slurry affected by a 90° bend were performed. The slurry is meant as a proxy for concentrated wastewater. These experiments were performed in an industrial scale facility with an initially well-mixed system. The main aim was to measure the recovery of the flow following the bend. Two examples are presented - one for a turbulent flow, and another for a laminar flow. In both cases, 21 pipe diameters was found to be insufficient for the flow to completely recover its streamwise momentum as well as axisymmetry. Under turbulent conditions, the recovery is faster than laminar conditions though. Results from these unique measurements can be used to validate numerical simulations or hydraulic design software (**To what extent can ultrasound imaging tackle flows in ... industrial backdrops?**).

In the above experiments, a peculiar observation was made in the form of long-time-scale transients of the bulk velocity and the pressure drop, under laminar conditions. When a target flow rate is achieved in the laminar regime after homogenizing the system at a high flow rate, the flow rate continues to drop gradually. In contrast, if a similar target flow rate is achieved in the laminar regime without homogenization, the flow rate continues to rise gradually, before it attains a constant value. Separate ramp experiments offer similar insights. There is no significant hysteresis based on pipe rheograms, but there are differences in the critical velocity at which steady-state behaviour is seen (**What is the role of the experimental protocol in the context of slurry pipe flows?**). With the aid of ultrasound imaging, it was shown that the gradual reduction in the flow rate appears simultaneously with formation of a stationary bed as the particles slowly settle out. Similarly, the gradual rise in the flow rate appears simultaneously with the gradual erosion of the bed. The constant flow rate is achieved once there is enough (intermittent) turbulence in the system to prevent any settling. These two transients are referred to as "slow settling" and "self-equilibration" respectively (**What additional information does ultrasound imaging offer to the measurement of global quantities of slurry flows?**).

Despite laminar-turbulent transition of non-Newtonian, non-settling slurries being treated as a trivial subject in literature, the results herein demonstrate that there are several, critical nuances. For example, there is a need for "slowly settling" slurries to be recognized as a category next to the present dichotomy of settling and non-settling slurries. The self-equilibrating behaviour offers an alternate way to start up a pipeline following a shutdown and attain a favourable operating point close to the critical velocity of laminar-turbulent transition (**Can understanding the underlying fluid mechanical processes provide inputs on practical guidelines to operate a slurry pipeline?**).

7.1.3. Experimental Fluid Mechanics

Ultrasonic techniques are considered to be niche in the Fluid Mechanics community, when compared to optical techniques. While ultrasound based velocimetry has been often rec-

ognized as a tool to tackle opaque flowing suspensions, there have not been many efforts in extracting particle distribution from ultrasonic data. This warranted a thorough scan of literature from other communities wherein acoustics/ultrasonics are used to profile flows. Based on the literature study and a few preliminary experiments, an empirical approach was formulated. Basically, two parameters were defined: peak backscatter amplitude and the amplitude attenuation rate. For a suspension with fixed particle size, both of these are functions of the particle volume fraction. Both these parameters represent two distinct processes of ultrasonic (back)scattering in a suspension. Calibration in uniform suspensions is necessary to obtain these two parameters, which can later be exploited to reconstruct particle volume fraction profiles in non-uniform suspensions (**How can one profit from ultrasonic backscatter data to reconstruct particle volume fraction profiles?**).

Of course, there are limitations as well, one of the major ones being the presence of multiple scattering. This phenomenon is only characterized in this thesis but no solution is offered to tackle it. The empirical approach, however, was successful in detecting inertial migration of non-Brownian suspensions in a pipe flow which was optically inaccessible. In a related example, ultrasound image intensities (albeit without any translation to volume fraction profiles) proved key in demonstrating how dropping flow meter readings correspond to settling of fine-grained particles (**What are the possibilities and limitations in the context of ultrasonic particle volume fraction profiling?**).

A direct consequence of attenuation of ultrasonic waves in suspensions is the loss of signal strength with increasing imaging depth. To this end, existing cross-correlation theory for Particle Image Velocimetry was combined with a lumped model characterizing the behaviour of ultrasonic backscattering in suspensions. This allows one to dissect the role of different parameters (such as particle volume fraction, particle size, imaging depth, number of images) on the quality of the velocimetry data. From the perspective of time-averaged velocities, lower imaging depths and larger number of images are more favourable. As a result, there is an upper limit in particle volume fraction, size, and imaging depth that can be accessed using ultrasound. This also limits the application of ultrasound for time-resolved flows (**What is the role of particles in the quality of velocimetry data?**). Ensemble correlation averaging is shown to be the best way to extract time-averaged velocity profiles. Assessing the quality of the velocimetry results at the level of the correlation planes is recommended. The rate at which the peak height on the correlation plane grows as a function of ensemble size can serve as an indicator whether recording more images would be useful or not (**How can one gain the maximum out of the recorded images in the context of velocimetry?**).

As discussed in the preceding two subsections, ultrasound is still a useful tool to study the fluid mechanics of suspensions. In this thesis, several examples of ultrasound imaging being applied to address problems related to fundamental and applied fluid mechanics have been shown (**To what extent can ultrasound imaging tackle flows in academic or industrial backdrops?**).

7.2. Outlook: how to build on this dissertation

This thesis is a product of finite time, finite ability, and finite resources. Needless to say, this thesis can be built up on. In this section, a few ideas for future research are pitched.

7.2.1. Fundamental Fluid Mechanics

In the Taylor-Couette geometry, flow visualization was used in this thesis - mainly to classify flow topologies. Since the occurrence of non-axisymmetric flows and defects increases with particle loading, one project that has been conceived is to use multiple cameras and visualize the entire circumference of the Taylor-Couette system. Using such an experimental setup will facilitate visualizing the onset and spatio-temporal development of non-axisymmetric structures and defects. Moreover, such a setup can also help study modulations on wavy vortices, if present.

Detection of inertial migration in pipe flows with ultrasound was shown to be feasible. In a similar vein, inertial migration in Taylor-Couette systems can be investigated for higher volume fractions. Unfortunately, this cannot be done in tandem with flow visualization, as ultrasonic scattering from visualization flakes would interfere with that from the inertial particles leading to cross-talk.

One parameter that is yet untouched is the influence of the outer cylinder rotation on the flow patterns. As Morris (2020) writes *"Examination of the suspension TC flow under conditions of both cylinders rotating is rather obviously expected to be enlightening."* The very recent work of Singh, Ghosh, and Alam (2022) is a first exploration in this direction.

From the perspective of pipe flows, the detection of inertial migration and its effect on the velocity profile can be taken into account while explaining the laminar-turbulent transition phenomenon for suspensions. Matas, Morris, and Guazzelli (2003) state *"A more refined analysis should take into account the influence of particles on the velocity and concentration profile in the pipe flow. In conditions of very low Reynolds number and high concentration, particles migrate towards the center of the pipe and blunt the velocity profile ... This effect which would tend to reduce the effective viscosity in the pipe ... There exists a second type of migration, the so-called "tubular pinch effect", which is inertial and causes a single particle to move to a position at a distance of 0.3D from the axis.This effect is observed with the larger particles in both pipes. The present study seems to suggest that the particles alter the threshold of the subcritical transition through coupling of the base flow to velocity fluctuations rather than the base flow itself through their migration but this requires confirmation."* Present literature in particle-laden pipe flows focuses primarily on the *"particles alter ...coupling of the base flow to velocity fluctuations"*. The option of *"particles alter ...the base flow itself through migration"* is yet to be properly accounted for.

Lastly, the Taylor-Couette can be operated with only the outer cylinder rotating to mimic the direct laminar-to-turbulent transition observed in pipe flows. If the two compare well qualitatively, the Taylor-Couette flow can be used as a simple way to track puff splitting and decay events in suspension flows.

7.2.2. Applied Fluid Mechanics

The measurement of time-averaged velocity profiles of a fine-grained slurry about a 90° bend was successful. This opens up opportunities to perform further flow characterizations for a range of pipe appendages and fittings, in addition to the pipe itself. Hydraulic design data for non-Newtonian slurries is scarce. Of course, there will be limitations to the slurry concentrations, imaging depths, or particle sizes that can be successfully tackled. The experimental data will undoubtedly offer useful reference data for validating numeri-

cally computed velocity profiles. Advancements in ultrasonic instrumentation will further help assess the turbulent regime in more detail (turbulence intensity profiles and/or the near-wall region). Combining a high-frequency ultrasound transducer can be used to focus on near-wall features whereas a low-frequency transducer can be used to probe the bulk.

The discovery of the long-time-scale transients was interesting, yet the results presented were a concoction of multiple, separate experiments. Future experiments could simply focus on these transients. Benchmarking single-element ultrasound transducers and differential pressure sensors against ultrasound imaging, can help identify the signature of specific flow events. Using these cheaper single-element ultrasound transducers and differential pressure sensors at multiple streamwise locations of the pipe can shed further light on the interplay between these long-time-scale transients and any bed formation. In general, more focus can be put on transient phenomena such as sudden surges, ebbs, starts, shutdowns, or even pulsatile flows. It is likely that slurry flows in the real world are far from the ideal, steady-state, fully-developed horizontal pipe flow.

7.2.3. Experimental Fluid Mechanics

In this thesis, ultrasound is treated as means to an end. Therefore, the development of the measurement technique for volume fraction profiling is done in a top-down manner (starting from the scattering at the level of the ensemble of particles) than in a bottom-up manner (starting from scattering at the level of a single particle). A top-down approach is certainly pragmatic but approaching the problem from a bottom-up manner might yield refinements in the methodology. For instance, there are examples in literature wherein multiple scattering is treated as a diffusion process. A bottom-up approach is likely to be more theoretical though. Thus, such a task would require an intimate understanding of ultrasound imaging and acoustical scattering. The above discussion may also be extended to the development of velocimetry techniques.

Assessment of ultrasonic particle volume fraction profiling and ultrasound imaging velocimetry often relied on heuristic arguments and educated guesses of the flow. This was necessary as the experiments in this thesis did not possess any reference data. An intermediate step of evaluating the algorithms on synthetically generated ultrasound images would have been of great help. Therefore, the generation of thousands of such images using acoustic simulation software should be pursued in the near future. Needless to say, implementing this accurately will too require an intimate understanding of ultrasound imaging and acoustical scattering.

This thesis only uses ultrasound to study the flow in a non-invasive fashion. It would be intriguing to perform experiments combining high intensity ultrasound (to manipulate the flow of suspensions) and low intensity ultrasound (to monitor the manipulated flow). Specific examples would be to generate intermittent disturbances or manipulate the flow around a bend. This combination will create a beautiful 'echosystem'.

Ultrasound is commonly used as the first line of diagnosis in the field of medicine. The same can be applicable to the study of particle-laden flows, to identify major trends and irregularities. When ultrasonic data is inconclusive or if extremely accurate information is desired, relatively expensive and time-consuming alternatives such as X-ray Computed Tomography or Magnetic Resonance Imaging can be brought in for further analysis.

7.3. Impact: who benefits from this dissertation

A question that often arises while assessing the quality of research is its impact. Previously in the dissertation, the topics covered in this dissertation were classified under three themes: fundamental fluid mechanics, applied fluid mechanics, and experimental fluid mechanics. In this section, an attempt is made to philosophize the impact of the work herein, with respect to the above classification. After all, this is a dissertation to earn the degree of Doctor of "Philosophy".

For the purpose of this discussion, three distinct sectors are identified wherein a typical dissertation from the engineering sciences can be relevant: academia, industry, and society/environment. Shown in Figure 7.1 is a graphical visualization summarizing the relevance of this thesis with respect to the three sectors. Furthermore, impact can also be at a local (direct collaborators) or a non-local level (non-collaborators).

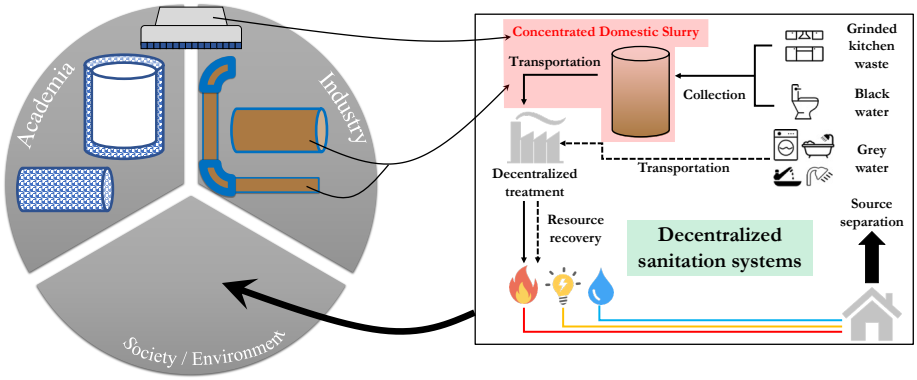

Figure 7.1: The author's opinion on where the research in this dissertation will be of interest

Fundamental Fluid Mechanics → Academia

Fundamental research is, more often than not, relevant to the confines of academia. With that regard, it is natural that the work classified under fundamental fluid mechanics will mostly be of interest to academic researchers. At a non-local level, the work on the transitions of suspensions in a Taylor-Couette will mainly serve as reference experimental data (flow regimes and torque measurements) for validation of numerical works as well as experiments. The parameters traversed here are in the pre-turbulent regime. Nevertheless, the data can serve as a stepping stone towards a more complete understanding of how the onset of turbulence is affected by the presence of particles. The azimuthally localized wavy vortex flow, on the other hand, is an intriguing anomaly. It is likely that this flow regime will be considered an "interesting observation" rather than it receiving a detailed treatment. When it comes to suspension flows in pipes, it is the same story as above - that the data will mainly be relevant for validating numerical works (velocity and volume fraction profiles of particles). That (weak) inertial migration is present in semi-dilute suspensions, even at the onset of turbulence, suggests that particle distributions and their

consequences on the velocity profiles should not be neglected (especially when attempting theoretically). In short, the above work is a small contribution to the burgeoning field of "Fluid Mechanics of Suspensions".

At a local level, the work in this thesis serves can spawn a line of research targeting the flow of suspensions in the Taylor-Couette geometry. Previous research focussed on turbulent flows and/or the role of surface modification. Presently, another participant in the OpaqueFlows project is already extending on the work herein. In contrast, the contributions of this thesis to the pipe flows of non-Brownian suspensions will play a relatively diminished role. Other participants in the OpaqueFlows project have explored this system more extensively, by means of multiple other imaging modalities (Hogendoorn, 2021). An attempt to directly compare the experimental results from ultrasound imaging to Direct Numerical Simulations in the laminar regime was attempted, but fell short. Nonetheless, insights from ultrasound imaging herein will serve as a piece of the puzzle.

Applied Fluid Mechanics → Industry

Research in this thesis concerning applied fluid mechanics will mainly be of industrial interest. The recovery of the flow downstream of the bend (velocity profiles) can be used validate numerical works or simpler hydraulic models. This is a crucial step prior to building a "digital twin" of a real-world set up. In a similar vein, the work on long-time-scale transients offers an avenue for the slurry community to revisit/reassess existing guidelines and rules-of-thumb. For example, extrapolating results from the flows of homogeneous, single-phase non-Newtonian fluids to two-phase slurries is non-trivial, especially if the slurry is inhomogeneous. En route to simplifying fundamental fluid mechanics to rules-of-thumb, subtleties might disappear. The results herein can trigger the slurry community to reconsider two "false dichotomies" for slurry flows in pipes: settling/non-settling slurries and laminar/turbulent regimes. Of course, the author realizes that the previous sentence is a bit outlandish, given that the author has written this thesis at a university and is not a practitioner.

Locally, the experimental data concerning the 90° bend are already being used for validation of numerical simulations of a non-Newtonian fluid with external collaborators. Upon successful validation, these simulations can be expanded to curate an accurate but small database of hydraulic design data for turbulent flow of non-Newtonian slurries. This can be used to validate simpler one-dimensional models popular in industry which can then generate a much larger database. Moreover, previous experimental work on this project (identical slurry, facility, imaging system) assumed that the slurry was homogeneously distributed and that no settling occurred, which was found to be invalid. Thus, in future experiments, assumptions will be made more cautiously and, hopefully, the experimental protocols will be carefully reported.

Experimental Fluid Mechanics → Academia/Industry

The final leg of the research in this thesis involves experimental fluid mechanics, namely development and application of ultrasound imaging to flowing suspensions. The corresponding work can possibly be of interest to researchers in academia and industry. Researchers in academia can use ultrasound imaging to extract velocity and volume fraction

profiles in suspension flows. The work in this thesis offers guidelines on how to include physical aspects of ultrasound imaging in assessing fluid mechanics of suspensions. Unfortunately though, ultrasound will only play a limited role and will fail in dense suspensions or systems where particles are much larger than the ultrasonic wavelength. In academia, thus, ultrasound imaging will have to share its place in the sun with numerous other experimental techniques. In industry, single-element ultrasound sensors are already used for flow monitoring. Using ultrasound imaging is a viable but more expensive alternative, and would require at least one well-trained expert to operate an apparatus which is not plug-and-play. Nevertheless, if ultrasonic flow monitoring is being used for crucial research and development purposes, investing in ultrasound imaging is worthwhile.

Locally, the ultrasound imaging experiments add depth to previous work carried out. In the past, concentration profiling as well as velocimetry in non-Brownian suspensions and non-Newtonian slurries have been executed. This thesis adds depth by understanding the "means" before applying it "to an end". The collaboration on measuring non-Newtonian slurries was a fruitful endeavour while also serving as a proof-of-concept and proof-of-value of ultrasound imaging (velocimetry). Depending on the perceived success of ultrasound imaging by the external collaborator, an opportunity exists for translating this to proof-of-commerce (for example, by offering ultrasound imaging flow diagnostics as a service).

? → Society/Environment

It would be challenging for the author to give a convincing elevator pitch to a layperson to convey how this thesis directly tackles a societally/environmentally relevant problem. This is because the research performed as part of this thesis occurs at much lower technological readiness levels, TRL 1-3 (NASA, 2012). For example, the flow of neutrally buoyant suspensions in a Taylor-Couette or a pipe is rather abstract and translating its usefulness to immediate societal/environmental needs would require mental gymnastics. The question mark in "? → Society/Environment" reflects the author's doubts on whether the work in this thesis will contribute to a greater good.

This thesis' benefit to society/environment can, at best, come to fruition in a trickle-down fashion. Decentralized Sanitation Systems, illustrated in Figure 7.1, have been proposed as a step to move from a linear to a circular economy. One less understood, yet crucial, aspect is the optimization of the concentrated domestic slurry transportation. The experiments combining ultrasound imaging and the non-Newtonian slurry were sanctioned due to a dearth of knowledge on these systems. Experiments in this thesis are rather unique which can inspire future ultrasound imaging experiments. These subsequent experiments can play a role in validation of digital twins, whose results will eventually be translated to hydraulic design guidelines. The hydraulic design would serve as one of numerous factors a sanitary engineer would have to contemplate before building an actual system. From the perspective of the sanitary engineer, measurements like those herein would be a minor detail. Nevertheless, it could also be reassuring for the sanitary engineer to know that months were invested to understand a certain flow. If in the future, sustainable sanitation systems transporting concentrated slurries come to fruition, the work in thesis might have had an infinitesimal impact on society/environment after all.

References

Abbott, J. R., Tetlow, N., Graham, A. L., Altobelli, S. A., Fukushima, E., Mondy, L. A., and Stephens, T. S., *"Experimental observations of particle migration in concentrated suspensions: Couette flow,"* Journal of Rheology **35**, 773–795 (1991).

Abshagen, J., von Stamm, J., Heise, M., Will, C., and Pfister, G., *"Localized modulation of rotating waves in Taylor-Couette flow,"* Physical Review E **85**, 056307 (2012).

Admiraal, D., and García, M. H., *"Laboratory measurement of suspended sediment concentration using an Acoustic Concentration Profiler (ACP),"* Experiments in Fluids **28**, 116–127 (2000).

Adrian, R. J., *"Scattering particle characteristics and their effect on pulsed laser measurements of fluid flow: speckle velocimetry vs particle image velocimetry,"* Applied Optics **23**, 1690–1691 (1984).

Adrian, R. J., and Westerweel, J., *Particle Image Velocimetry* (Cambridge University Press, 2011).

Agrawal, N., Choueiri, G. H., and Hof, B., *"Transition to Turbulence in Particle Laden Flows,"* Physical Review Letters **122**, 114502 (2019).

Albion, K. J., Briens, L., Briens, C., and Berruti, F., *"Multiphase Flow Measurement Techniques for Slurry Transport,"* International Journal of Chemical Reactor Engineering **9** (2011).

Ali, M. E., Mitra, D., Schwille, J. A., and Lueptow, R. M., *"Hydrodynamic stability of a suspension in cylindrical Couette flow,"* Physics of Fluids **14**, 1236–1243 (2002).

Alidai, A., Greidanus, A. J., Delfos, R., and Westerweel, J., *"Turbulent Spot in Linearly Stable Taylor Couette Flow,"* Flow, Turbulence and Combustion **96**, 609–619 (2016).

Allegra, J., and Hawley, S., *"Attenuation of Sound in Suspensions and Emulsions: Theory and Experiments,"* The Journal of the Acoustical Society of America **51**, 1545–1564 (1972).

Altmeyer, S., and Hoffmann, C., *"Secondary bifurcation of mixed-cross-spirals connecting travelling wave solutions,"* New Journal of Physics **12**, 113035 (2010).

Anantharaman, A., *Suspension Taylor–Couette flow: Investigation of particle loading effects on transitions between flow regimes*, Master's thesis, Delft University of Technology (2019).

Andereck, C. D., Liu, S. S., and Swinney, H. L., *"Flow regimes in a circular Couette system with independently rotating cylinders,"* Journal of Fluid Mechanics **164**, 155–183 (1986).

Anugonda, P., Wiehn, J. S., and Turner, J. A., *"Diffusion of ultrasound in concrete,"* Ultrasonics **39**, 429–435 (2001).

Ardekani, M. N., Al Asmar, L., Picano, F., and Brandt, L., *"Numerical study of heat transfer in laminar and turbulent pipe flow with finite-size spherical particles,"* International Journal of Heat and Fluid Flow **71**, 189–199 (2018).

Aubry, A., and Derode, A., *"Detection and imaging in a random medium: A matrix method to overcome multiple scattering and aberration,"* Journal of Applied Physics **106**, 044903 (2009).

Aude, T. C., Derammelaere, R. H., and Wasp, E. J., *"Instability of laminar flow in long distance pipelines and solutions,"* in *21st International Technical Conference on Coal Utilization and Fuel Systems* (Clearwater, FL, USA, 1996).

Avila, K., Moxey, D., de Lozar, A., Avila, M., Barkley, D., and Hof, B., *"The Onset of Turbulence in Pipe Flow,"* Science **333**, 192–196 (2011).

Awad, T., Moharram, H., Shaltout, O., Asker, D., and Youssef, M., *"Applications of ultrasound in analysis, processing and quality control of food: A review,"* Food Research International **48**, 410–427 (2012).

Baas, J. H., Best, J. L., and Peakall, J., *"Comparing the transitional behaviour of kaolinite and bentonite suspension flows,"* Earth Surface Processes and Landforms **41**, 1911–1921 (2016).

Baas, J. H., Best, J. L., Peakall, J., and Wang, M., *"A Phase Diagram for Turbulent, Transitional, and Laminar Clay Suspension Flows,"* Journal of Sedimentary Research **79**, 162–183 (2009).

Baddour, R. E., and Kolios, M. C., *"The effect of volume fraction on the backscatter from nucleated cells at high frequencies,"* in *IEEE Ultrasonics Symposium, 2005.*, Vol. 3 (2005) pp. 1672–1674.

Baddour, R. E., Sherar, M. D., Hunt, J. W., Czarnota, G. J., and Kolios, M. C., *"High-frequency ultrasound scattering from microspheres and single cells,"* The Journal of the Acoustical Society of America **117**, 934–943 (2005).

Bagnold, R. A., *"Experiments on a gravity-free dispersion of large solid spheres in a Newtonian fluid under shear,"* Proceedings of the Royal Society of London. Series A. Mathematical and Physical Sciences **225**, 49–63 (1954).

Bakhuis, D., Verschoof, R. A., Mathai, V., Huisman, S. G., Lohse, D., and Sun, C., *"Finite-sized rigid spheres in turbulent Taylor–Couette flow: effect on the overall drag,"* Journal of Fluid Mechanics **850**, 246–261 (2018).

Bamberger, J. A., and Greenwood, M. S., *"Measuring fluid and slurry density and solids concentration non-invasively,"* Ultrasonics **42**, 563–567 (2004).

Barkley, D., *"Theoretical perspective on the route to turbulence in a pipe,"* Journal of Fluid Mechanics **803**, P1 (2016).

Barkley, D., Song, B., Mukund, V., Lemoult, G., Avila, M., and Hof, B., *"The rise of fully turbulent flow,"* Nature **526**, 550–553 (2015).

Baroudi, L., Majji, M. V., and Morris, J. F., *"Effect of inertial migration of particles on flow transitions of a suspension Taylor-Couette flow,"* Physical Review Fluids **5**, 114303 (2020).

Benschop, H. O. G., Guerin, A. J., Brinkmann, A., Dale, M. L., Finnie, A. A., Breugem, W.-P., Clare, A. S., Stübing, D., Price, C., and Reynolds, K. J., *"Drag-reducing riblets with fouling-release properties: development and testing,"* Biofouling **34**, 532–544 (2018).

Benslimane, A., Bekkour, K., François, P., and Bechir, H., *"Laminar and turbulent pipe flow of bentonite suspensions,"* Journal of Petroleum Science and Engineering **139**, 85–93 (2016).

Bilson, M., and Bremhorst, K., *"Direct numerical simulation of turbulent Taylor–Couette flow,"* Journal of Fluid Mechanics **579**, 227–270 (2007).

Bjørnø, L., *Applied Underwater Acoustics* (Elsevier, 2017).

Bohs, L. N., Geiman, B. J., Anderson, M. E., Gebhart, S. C., and Trahey, G. E., *"Speckle tracking for multi-dimensional flow estimation,"* Ultrasonics **38**, 369–375 (2000).

Borrero-Echeverry, D., Crowley, C. J., and Riddick, T. P., *"Rheoscopic fluids in a post-Kalliroscope world,"* Physics of Fluids **30**, 087103 (2018).

Borrero-Echeverry, D., Schatz, M. F., and Tagg, R., *"Transient turbulence in Taylor–Couette flow,"* Physical Review E **81**, 025301(R) (2010).

Borup, D. D., Elkins, C. J., and Eaton, J. K., *"Development and validation of an MRI-based method for 3D particle concentration measurement,"* International Journal of Heat and Fluid Flow **71**, 275–287 (2018).

Brandt, L., and Coletti, F., *"Particle-Laden Turbulence: Progress and Perspectives,"* Annual Review of Fluid Mechanics **54** (2022).

Bude, R. O., and Adler, R. S., *"An Easily Made, Low-Cost, Tissue-Like Ultrasound Phantom Material,"* Journal of Clinical Ultrasound **23**, 271–273 (1995).

Burin, M. J., Schartman, E., and Ji, H., *"Local measurements of turbulent angular momentum transport in circular Couette flow,"* Experiments in Fluids **48**, 763–769 (2010).

Bushberg, J. T., Seibert, A. J., Leidholt Jr, E. M., and Boone, J. M., *The Essential Physics of Medical Imaging* (Lippincott Williams & Wilkins, 2012).

Butler, J. E., and Bonnecaze, R. T., *"Imaging of particle shear migration with electrical impedance tomography,"* Physics of Fluids **11**, 1982–1994 (1999).

Büttner, L., Nauber, R., Burger, M., Räbiger, D., Franke, S., Eckert, S., and Czarske, J., *"Dual-plane ultrasound flow measurements in liquid metals,"* Measurement Science and Technology **24**, 055302 (2013).

Bux, J., Peakall, J., Biggs, S., and Hunter, T. N., *"In situ characterisation of a concentrated colloidal titanium dioxide settling suspension and associated bed development: Application of an acoustic backscatter system,"* Powder Technology **284**, 530–540 (2015).

Cagney, N., and Balabani, S., *"Taylor–Couette flow of shear-thinning fluids,"* Physics of Fluids **31**, 053102 (2019).

Caporaloni, M., Tampieri, F., Trombetti, F., and Vittori, O., *"Transfer of Particles in Nonisotropic Air Turbulence,"* Journal of the Atmospheric Sciences **32**, 565–568 (1975).

Carey, C. S., Schlender, A. B., and Andereck, C. D., *"Localized intermittent short-wavelength bursts in the high-radius ratio limit of the Taylor–Couette system,"* Physical Review E **75**, 016303 (2007).

Carleson, T., Drown, D. C., Hart, R. E., and Peterson, M. E., "Evaluation of the transport and resuspension of a simulated nuclear waste slurry: Nuclear Waste Treatment Program," Tech. Rep. (Pacific Northwest Lab., Richland, WA (USA), 1987).

Carlson, J., and Ing, R., *"Ultrasonic speckle correlation imaging of 2D particle velocity profiles in multiphase flows,"* Flow Measurement and Instrumentation **14**, 193–200 (2003).

Challis, R., Povey, M., Mather, M., and Holmes, A., *"Ultrasound techniques for characterizing colloidal dispersions,"* Reports on Progress in Physics **68**, 1541 (2005).

Chemloul, N. S., Chaib, K., and Mostefa, K., *"Simultaneous measurements of the solid particles velocity and concentration profiles in two phase flow by pulsed ultrasonic doppler velocimetry,"* Journal of the Brazilian Society of Mechanical Sciences and Engineering **31**, 333–343 (2009).

Chen, J.-F., and Zagzebski, J. A., *"Frequency dependence of backscatter coefficient versus scatterer volume fraction,"* IEEE Transactions on Ultrasonics, Ferroelectrics, and Frequency Control **43**, 345–353 (1996).

Cheng, N.-S., *"Formula for the Viscosity of a Glycerol–Water Mixture,"* Industrial & Engineering Chemistry Research **47**, 3285–3288 (2008).

Chossat, P., and Iooss, G., *The Couette-Taylor Problem*, 1st ed. (Springer, New York, NY, 1994).

Chow, A. W., Sinton, S. W., Iwamiya, J. H., and Stephens, T. S., *"Shear-induced particle migration in Couette and parallel-plate viscometers: NMR imaging and stress measurements,"* Physics of Fluids **6**, 2561–2576 (1994).

Clarke, P. F., and Charles, M. E., *"Experimental test of a model for laminar slurry flow with sedimentation,"* The Canadian Journal of Chemical Engineering **75**, 692–703 (1997).

Coghe, A., and Cossali, G., *"Quantitative optical techniques for dense sprays investigation: A survey,"* Optics and Lasers in Engineering **50**, 46–56 (2012).

Cole, J. A., *"Taylor-vortex instability and annulus-length effects,"* Journal of Fluid Mechanics **75**, 1–15 (1976).

Coles, D., *"Transition in circular Couette flow,"* Journal of Fluid Mechanics **21**, 385–425 (1965).

Costa, P., Picano, F., Brandt, L., and Breugem, W.-P., *"Universal Scaling Laws for Dense Particle Suspensions in Turbulent Wall-Bounded Flows,"* Physical Review Letters **117**, 134501 (2016).

Couette, M., *"Études sur le frottement des liquides,"* Annales de chimie et de physique **6**, 433–510 (1890).

Cowan, M. L., Jones, I. P., Page, J. H., and Weitz, D. A., *"Diffusing acoustic wave spectroscopy,"* Physical Review E **65**, 066605 (2002).

Cowan, M. L., Page, J. H., Norisuye, T., and Weitz, D. A., *"Dynamic sound scattering: Field fluctuation spectroscopy with singly scattered ultrasound in the near and far fields,"* The Journal of the Acoustical Society of America **140**, 1992–2001 (2016).

Cowan, M. L., Page, J. H., and Weitz, D. A., *"Velocity Fluctuations in Fluidized Suspensions Probed by Ultrasonic Correlation Spectroscopy,"* Physical Review Letters **85**, 453 (2000).

Cox, R. G., and Mason, S. G., *"Suspended Particles in Fluid Flow Through Tubes,"* Annual Review of Fluid Mechanics **3**, 291–316 (1971).

Crapper, M., Bruce, T., and Gouble, C., *"Flow field visualization of sediment-laden flow using ultrasonic imaging,"* Dynamics of Atmospheres and Oceans **31**, 233–245 (2000).

Crimaldi, J. P., *"Planar laser induced fluorescence in aqueous flows,"* Experiments in Fluids **44**, 851–863 (2008).

Culjat, M. O., Goldenberg, D., Tewari, P., and Singh, R. S., *"A review of tissue substitutes for ultrasound imaging,"* Ultrasound in Medicine & Biology **36**, 861–873 (2010).

Czarny, O., and Lueptow, R. M., *"Time scales for transition in Taylor–Couette flow,"* Physics of Fluids **19**, 054103 (2007).

Darcy, H., *Recherches expérimentales relatives au mouvement de l'eau dans les tuyaux*, Vol. 1 (Mallet-Bachelier, 1857).

Dash, A., Anantharaman, A., Greidanus, A., and Poelma, C., *"Simultaneous Ultrasound Imaging Velocimetry (UIV) and Flow Visualization in Taylor-Couette flows: Validation of UIV in single-phase flows,"* in *Proceedings of the 13th International Symposium on Particle Image Velocimetry (Munich, Germany, 22-24 July 2019)*, edited by C. J. Kähler, R. Hain, S. Scharnowski, and T. Fuchs (Universität der Bundeswehr München, 2019) pp. 980–989.

Dash, A., Anantharaman, A., and Poelma, C., *"Particle-laden Taylor–Couette flows: higher-order transitions and evidence for azimuthally localized wavy vortices,"* Journal of Fluid Mechanics **903**, A20 (2020).

Dash, A., Hogendoorn, W., Oldenziel, G., and Poelma, C., *"Ultrasound imaging velocimetry in particle-laden flows: counteracting attenuation with correlation averaging,"* Experiments in Fluids **63** (2022).

Dash, A., Hogendoorn, W., and Poelma, C., *"Ultrasonic particle volume fraction profiling: an evaluation of empirical approaches,"* Experiments in Fluids **62** (2021).

Dash, A., and Poelma, C., *"Long-time-scale transients in an industrial-scale slurry pipeline near the laminar–turbulent transition,"* Flow **2**, E25 (2022).

Davis, C. E., and Oakes, E. T., *"Further studies of the physical characteristics of gelatin solutions,"* Journal of the American Chemical Society **44**, 464–479 (1922).

Deen, N. G., Westerweel, J., and Delnoij, E., *"Two-phase PIV in Bubbly Flows: Status and Trends,"* Chemical Engineering & Technology **25**, 97–101 (2002).

Delnoij, E., Westerweel, J., Deen, N. G., Kuipers, J. A. M., and van Swaaij, W. P. M., *"Ensemble correlation PIV applied to bubble plumes rising in a bubble column,"* Chemical Engineering Science **54**, 5159–5171 (1999).

Dessup, T., Tuckerman, L. S., Wesfreid, J. E., Barkley, D., and Willis, A. P., *"Self-sustaining process in Taylor–Couette flow,"* Physical Review Fluids **3**, 123902 (2018).

Dherbécourt, D., Charton, S., Lamadie, F., Cazin, S., and Climent, E., *"Experimental study of enhanced mixing induced by particles in Taylor–Couette flows,"* Chemical Engineering Research and Design **108**, 109–117 (2016).

Di Prima, R. C., and Swinney, H. L., *"Instabilities and transition in flow between concentric rotating cylinders,"* in *Hydrodynamic instabilities and the transition to turbulence* (Springer-Verlag, 1985) pp. 139–180.

Dinkgreve, M., Paredes, J., Denn, M. M., and Bonn, D., *"On different ways of measuring "the" yield stress,"* Journal of Non-Newtonian Fluid Mechanics **238**, 233–241 (2016).

Divoux, T., Fardin, M. A., Manneville, S., and Lerouge, S., *"Shear banding of complex fluids,"* Annual Review of Fluid Mechanics **48**, 81–103 (2016).

Donnelly, R. J., *"Taylor–Couette flow: the early days,"* Physics Today **44**, 32–39 (1991).

Donnelly, R. J., Park, K., Shaw, R., and Walden, R. W., *"Early nonperiodic transitions in Couette flow,"* Physical Review Letters **44**, 987 (1980).

Dukhin, A. S., and Goetz, P. J., *"Acoustic and electroacoustic spectroscopy for characterizing concentrated dispersions and emulsions,"* Advances in Colloid and Interface Science **92**, 73–132 (2001).

Dukhin, A. S., and Goetz, P. J., *"Ultrasound for characterizing colloids: Particle sizing, Zeta Potential, Rheology,"* in *Studies in Interface Science*, Vol. 15 (Elsevier, San Diego, CA, 2002) pp. 1–372.

Dutcher, C. S., and Muller, S. J., *"Spatio-temporal mode dynamics and higher order transitions in high aspect ratio Newtonian Taylor–Couette flows,"* Journal of Fluid Mechanics **641**, 85–113 (2009).

Eckhardt, B., Grossmann, S., and Lohse, D., *"Torque scaling in turbulent Taylor–Couette flow between independently rotating cylinders,"* Journal of Fluid Mechanics **581**, 221–250 (2007).

Eckhardt, B., Schneider, T. M., Hof, B., and Westerweel, J., *"Turbulence transition in pipe flow,"* Annual Review of Fluid Mechanics **39**, 447–468 (2007).

Eggels, J. G. M., Unger, F., Weiss, M. H., Westerweel, J., Adrian, R. J., Friedrich, R., and Nieuwstadt, F. T. M., *"Fully developed turbulent pipe flow: a comparison between direct numerical simulation and experiment,"* Journal of Fluid Mechanics **268**, 175–210 (1994).

Eilers, H., *"Die viskosität von emulsionen hochviskoser stoffe als funktion der konzentration,"* Kolloid-Zeitschrift **97**, 313–321 (1941).

El-Nahhas, K., El-Hak, N. G., Rayan, M. A., Vlasak, P., and El-Sawaf, I. A., *"The laminar/turbulent transitional condition of non-newtonian slurries flow in pipes,"* (BHR Group, 2004) pp. 47–60.

Epstein, P. S., and Carhart, R. R., *"The absorption of sound in suspensions and emulsions. I. Water fog in air,"* The Journal of the Acoustical Society of America **25**, 553–565 (1953).

Escudier, M. P., Poole, R. J., Presti, F., Dales, C., Nouar, C., Desaubry, C., Graham, L., and Pullum, L., *"Observations of asymmetrical flow behaviour in transitional pipe flow of yield-stress and other shear-thinning liquids,"* Journal of Non-Newtonian Fluid Mechanics **127**, 143–155 (2005).

Escudier, M. P., and Presti, F., *"Pipe flow of a thixotropic liquid,"* Journal of Non-Newtonian Fluid Mechanics **62**, 291–306 (1996).

Eshtiaghi, N., Markis, F., and Slatter, P., *"The laminar/turbulent transition in a sludge pipeline,"* Water Science and Technology **65**, 697–702 (2012).

Eshtiaghi, N., Markis, F., Yap, S. D., Baudez, J.-C., and Slatter, P., *"Rheological characterisation of municipal sludge: a review,"* Water Research **47**, 5493–5510 (2013).

Esmael, A., and Nouar, C., *"Transitional flow of a yield-stress fluid in a pipe: Evidence of a robust coherent structure,"* Physical Review E **77**, 057302 (2008).

Esser, A., and Grossmann, S., *"Analytic expression for Taylor–Couette stability boundary,"* Physics of Fluids **8**, 1814–1819 (1996).

Faisst, H., and Eckhardt, B., *"Traveling waves in pipe flow,"* Physical Review Letters **91**, 224502 (2003).

Faran Jr, J. J., *"Sound scattering by solid cylinders and spheres,"* The Journal of the Acoustical Society of America **23**, 405–418 (1951).

Fardin, M. A., Perge, C., and Taberlet, N., *""The hydrogen atom of fluid dynamics"–introduction to the Taylor–Couette flow for soft matter scientists,"* Soft Matter **10**, 3523–3535 (2014).

Fardin, M. A., Perge, C., Taberlet, N., and Manneville, S., *"Flow-induced structures versus flow instabilities,"* Physical Review E **89**, 011001(R) (2014).

Fay, B., Brendel, K., and Ludwig, G., *"Studies of inhomogeneous substances by ultrasonic back-scattering,"* Ultrasound in Medicine & Biology **2**, 195–198 (1976).

Fenstermacher, P. R., Swinney, H. L., and Gollub, J. P., *"Dynamical instabilities and the transition to chaotic Taylor vortex flow,"* Journal of Fluid Mechanics **94**, 103–128 (1979).

Fiabane, L., Zimmermann, R., Volk, R., Pinton, J.-F., and Bourgoin, M., *"Clustering of finite-size particles in turbulence,"* Physical Review E **86**, 035301(R) (2012).

Franceschini, E., and Guillermin, R., *"Experimental assessment of four ultrasound scattering models for characterizing concentrated tissue-mimicking phantoms,"* The Journal of the Acoustical Society of America **132**, 3735–3747 (2012).

Franke, S., Lieske, H., Fischer, A., Büttner, L., Czarske, J., Räbiger, D., and Eckert, S., *"Two-dimensional ultrasound Doppler velocimeter for flow mapping of unsteady liquid metal flows,"* Ultrasonics **53**, 691–700 (2013).

Fromant, G., Hurther, D., Le Dantec, N., Lebourges-Dhaussy, A., Jourdin, F., Vergnes, A., Le Coz, J., Fisher, S., and Pierrefeu, G., "Hydrac, an inversion software for SPM quantification," in *River Flow 2020: Proceedings of the 10th Conference on Fluvial Hydraulics (Delft, The Netherlands, 7-10 July 2020)* (2020) p. 340.

Furlan, J. M., Mundla, V., Kadambi, J., Hoyt, N., Visintainer, R., and Addie, G., *"Development of A-scan ultrasound technique for measuring local particle concentration in slurry flows,"* Powder Technology **215**, 174–184 (2012).

Gadala-Maria, F., and Acrivos, A., *"Shear-induced structure in a concentrated suspension of solid spheres,"* Journal of Rheology **24**, 799–814 (1980).

Gallot, T., Perge, C., Grenard, V., Fardin, M.-A., Taberlet, N., and Manneville, S., *"Ultrafast ultrasonic imaging coupled to rheometry: Principle and illustration,"* Review of Scientific Instruments **84**, 045107 (2013).

Garcia, D., *"A fast all-in-one method for automated post-processing of PIV data,"* Experiments in Fluids **50**, 1247–1259 (2011).

Gauthier, G., Gondret, P., and Rabaud, M., *"Motions of anisotropic particles: application to visualization of three-dimensional flows,"* Physics of Fluids **10**, 2147–2154 (1998).

Gharib, M., *"Perspective: The Experimentalist and the Problem of Turbulence in the Age of Supercomputers,"* Journal of Fluids Engineering **118**, 233–242 (1996).

Gibson Jr, R. L., and Toksöz, M. N., *"Viscous attenuation of acoustic waves in suspensions,"* The Journal of the Acoustical Society of America **85**, 1925–1934 (1989).

Gillissen, J. J. J., and Wilson, H. J., *"Taylor–Couette instability in sphere suspensions,"* Physical Review Fluids **4**, 043301 (2019).

van Gils, D. P. M., Bruggert, G.-W., Lathrop, D. P., Sun, C., and Lohse, D., *"The Twente turbulent Taylor–Couette (T^3C) facility: strongly turbulent (multiphase) flow between two independently rotating cylinders,"* Review of Scientific Instruments **82**, 025105 (2011).

van Gils, D. P. M., Huisman, S. G., Grossmann, S., Sun, C., and Lohse, D., *"Optimal Taylor–Couette turbulence,"* Journal of Fluid Mechanics **706**, 118–149 (2012).

Goharzadeh, A., and Mutabazi, I., *"Measurement of coefficients of the Ginzburg-Landau equation for patterns of Taylor spirals,"* Physical Review E **82**, 016306 (2010).

Gollub, J. P., and Swinney, H. L., *"Onset of turbulence in a rotating fluid,"* Physical Review Letters **35**, 927–930 (1975).

Goosen, P., *"Analysis of friction pressure gradients during slurry pipeline restart,"* in *Proceedings, 17th International Conference on Transport and Sedimentation of Solid Particles (Delft, The Netherlands, 22-25 September 2015)* (2015).

Gorman, M., Reith, L. A., and Swinney, H. L., *"Modulation patterns, multiple frequencies, and other phenomena in circular Couette flow,"* Annals of the New York Academy of Sciences **357**, 10–21 (1980).

Gorman, M., and Swinney, H., "A retrospective on Modulated Wavy Vortex Flow," (2009).

Gorman, M., and Swinney, H. L., *"Spatial and temporal characteristics of modulated waves in the circular Couette system,"* Journal of Fluid Mechanics **117**, 123–142 (1982).

Greidanus, A. J., Delfos, R., Tokgoz, S., and Westerweel, J., *"Turbulent Taylor–Couette flow over riblets: drag reduction and the effect of bulk fluid rotation,"* Experiments in Fluids **56**, 107 (2015).

Grossmann, S., Lohse, D., and Sun, C., *"High–Reynolds number Taylor–Couette turbulence,"* Annual Review of Fluid Mechanics **48**, 53–80 (2016).

Guazzelli, É., and Morris, J. F., *A physical introduction to suspension dynamics* (Cambridge University Press, 2011).

Guazzelli, É., and Pouliquen, O., *"Rheology of dense granular suspensions,"* Journal of Fluid Mechanics **852**, P1 (2018).

Gul, M., Elsinga, G. E., and Westerweel, J., *"Experimental investigation of torque hysteresis behaviour of Taylor–Couette flow,"* Journal of Fluid Mechanics **836**, 635–648 (2018).

Gunning, P. A., Hibberd, D. J., Howe, A. M., and Robins, M. M., *"Gravitational destabilization of emulsions flocculated by non-adsorbed xanthan,"* Food Hydrocolloids **2**, 119–129 (1988).

Gurung, A., Haverkort, J. W., Drost, S., Norder, B., Westerweel, J., and Poelma, C., *"Ultrasound image velocimetry for rheological measurements,"* Measurement Science and Technology **27**, 094008 (2016).

Gurung, A., and Poelma, C., *"Measurement of turbulence statistics in single-phase and two-phase flows using ultrasound imaging velocimetry,"* Experiments in Fluids **57**, 171 (2016).

Güzel, B., Burghelea, T., Frigaard, I., and Martinez, D., *"Observation of laminar–turbulent transition of a yield stress fluid in Hagen–Poiseuille flow,"* Journal of Fluid Mechanics **627**, 97–128 (2009).

Güzel, B., Frigaard, I., and Martinez, D., *"Predicting laminar–turbulent transition in Poiseuille pipe flow for non-Newtonian fluids,"* Chemical Engineering Science **64**, 254–264 (2009).

Haavisto, S., Cardona, M. J., Salmela, J., Powell, R. L., McCarthy, M. J., Kataja, M., and Koponen, A. I., *"Experimental investigation of the flow dynamics and rheology of complex fluids in pipe flow by hybrid multi-scale velocimetry,"* Experiments in Fluids **58**, 1–13 (2017).

Hagen, G., *"Ueber die bewegung des wassers in engen cylindrischen röhren,"* Annalen der Physik **122**, 423–442 (1839).

Hagen, G. H. L., *"Über den einfluss der temperatur auf die bewegung des wassers in röhren,"* Abhandlungen der koniglichen preussischen Akademie der Wissenschaften zu Berlin. Physikalisch - mathematische Classe. Berlin **17**, 17–98 (1854).

Haldenwang, R., *Flow of non-Newtonian fluids in open channels*, Ph.D. thesis, Cape Technikon (2003).

Hall, C. S., Marsh, J. N., Hughes, M. S., Mobley, J., Wallace, K. D., Miller, J. G., and Brandenburger, G. H., *"Broadband measurements of the attenuation coefficient and backscatter coefficient for suspensions: A potential calibration tool,"* The Journal of the Acoustical Society of America **101**, 1162–1171 (1997).

Halow, J. S., and Wills, G. B., *"Experimental observations of sphere migration in Couette systems,"* Industrial & Engineering Chemistry Fundamentals **9**, 603–607 (1970a).

Halow, J. S., and Wills, G. B., *"Radial migration of spherical particles in Couette systems,"* AIChE Journal **16**, 281–286 (1970b).

Hampton, R. E., Mammoli, A. A., Graham, A. L., Tetlow, N., and Altobelli, S. A., *"Migration of particles undergoing pressure-driven flow in a circular conduit,"* Journal of Rheology **41**, 621–640 (1997).

Han, E., Peters, I. R., and Jaeger, H. M., *"High-speed ultrasound imaging in dense suspensions reveals impact-activated solidification due to dynamic shear jamming,"* Nature Communications **7**, 1–8 (2016).

Han, E., Zhao, L., Van Ha, N., Hsieh, S. T., Szyld, D. B., and Jaeger, H. M., *"Dynamic jamming of dense suspensions under tilted impact,"* Physical Review Fluids **4**, 063304 (2019).

Han, M., Kim, C., Kim, M., and Lee, S., *"Particle migration in tube flow of suspensions,"* Journal of Rheology **43**, 1157–1174 (1999).

Harker, A. H., and Temple, J. A. G., *"Velocity and attenuation of ultrasound in suspensions of particles in fluids,"* Journal of Physics D: Applied Physics **21**, 1576 (1988).

Hedström, B. O., *"Flow of plastic materials in pipes,"* Industrial & Engineering Chemistry **44**, 651–656 (1952).

van den Heever, E. M., Sutherland, A. P. N., and Haldenwang, R., *"Influence of the rheological model used in pipe-flow prediction techniques for homogeneous non-Newtonian fluids,"* Journal of Hydraulic Engineering **140**, 04014059 (2014).

Henderson, K. L., and Gwynllyw, D. R., *"Limiting behaviour of particles in Taylor–Couette flow,"* Journal of Engineering Mathematics **67**, 85–94 (2010).

Hitomi, J., Nomura, S., De Cesare, G., Takeda, Y., Park, H. J., Tasaka, Y., and Murai, Y., *"Flow monitoring of particle-laden flows combining ultrasonic doppler and echo intensity profiling techniques,"* in *Proceedings of the 11th International Symposium on Ultrasonic Doppler Methods for Fluid Mechanics and Fluid Engineering (Berlin, Germany, 5-7 September 2018)*, edited by M. Juling and N. Furuichi (2018) pp. 75–78.

Hof, B., "Resolving Reynolds Riddle," (2011), The Nature of Turbulence (Feb 7 - Jun 3, 2011).

Hof, B., van Doorne, C. W. H., Westerweel, J., Nieuwstadt, F. T. M., Faisst, H., Eckhardt, B., Wedin, H., Kerswell, R. R., and Waleffe, F., *"Experimental observation of nonlinear traveling waves in turbulent pipe flow,"* Science **305**, 1594–1598 (2004).

Hof, B., Westerweel, J., Schneider, T. M., and Eckhardt, B., *"Finite lifetime of turbulence in shear flows,"* Nature **443**, 59–62 (2006).

Hoffmann, C., Lücke, M., and Pinter, A., *"Spiral vortices traveling between two rotating defects in the Taylor–Couette system,"* Physical Review E **72**, 056311 (2005).

Hogendoorn, W., Chandra, B., and Poelma, C., *"Suspension dynamics in transitional pipe flow,"* Physical Review Fluids **6**, 064301 (2021).

Hogendoorn, W., Chandra, B., and Poelma, C., *"Onset of turbulence in particle-laden pipe flows,"* Physical Review Fluids **7**, L042301 (2022).

Hogendoorn, W., and Poelma, C., *"Particle-Laden Pipe Flows at High Volume Fractions Show Transition Without Puffs,"* Physical Review Letters **121**, 194501 (2018).

Hogendoorn, W., and Poelma, C., *"High frame rate flow measurement using Ultrasound Imaging Velocimetry,"* in *Proceedings of the 13th International Symposium on Particle Image Velocimetry (Munich, Germany, 22-24 July 2019)*, edited by C. J. Kähler, R. Hain, S. Scharnowski, and T. Fuchs (Universität der Bundeswehr München, 2019) pp. 972–979.

Hogendoorn, W. J., *Suspension dynamics in transitional pipe flow*, Ph.D. thesis, Delft University of Technology (2021).

Hoyle, B. S., *"Process tomography using ultrasonic sensors,"* Measurement Science and Technology **7**, 272 (1996).

Hoyos, M., Bacri, J. C., Martin, J., and Salin, D., *"A study of the sedimentation of noncolloidal bidisperse, concentrated suspensions by an acoustic technique,"* Physics of Fluids **6**, 3809–3817 (1994).

Huisman, S. G., Scharnowski, S., Cierpka, C., Kähler, C. J., Lohse, D., and Sun, C., *"Logarithmic boundary layers in strong Taylor–Couette turbulence,"* Physical Review Letters **110**, 264501 (2013).

Hunt, M. L., Zenit, R., Campbell, C. S., and Brennen, C. E., *"Revisiting the 1954 suspension experiments of R. A. Bagnold,"* Journal of Fluid Mechanics **452**, 1–24 (2002).

Hunter, T. N., Darlison, L., Peakall, J., and Biggs, S., *"Using a multi-frequency acoustic backscatter system as an in situ high concentration dispersion monitor,"* Chemical Engineering Science **80**, 409–418 (2012).

Hunter, T. N., Peakall, J., and Biggs, S., *"An acoustic backscatter system for in situ concentration profiling of settling flocculated dispersions,"* Minerals Engineering **27**, 20–27 (2012).

Hunter, T. N., Peakall, J., Egarr, D., Cowell, D. M., Freear, S., Tonge, A. S., Horton, L., Rice, H. P., Smith, I., Malone, K., Burt, D., Barnes, M., Randall, G., Biggs, S., and Fairweather, M., *"Concentration profiling of a horizontal sedimentation tank utilising a bespoke acoustic backscatter array and CFD simulations,"* Chemical Engineering Science **218**, 115560 (2020).

Hurther, D., Thorne, P. D., Bricault, M., Lemmin, U., and Barnoud, J.-M., *"A multi-frequency Acoustic Concentration and Velocity Profiler (ACVP) for boundary layer measurements of fine-scale flow and sediment transport processes,"* Coastal Engineering **58**, 594–605 (2011).

Imomoh, E., Dusting, J., and Balabani, S., *"On the quasiperiodic state in a moderate aspect ratio Taylor–Couette flow,"* Physics of Fluids **22**, 044103 (2010).

Ito, H., *"Pressure losses in smooth pipe bends,"* Journal of Basic Engineering **82**, 131–140 (1960).

Javadi, S., Pirouz, B., and Slatter, P., *"Paste and Thickened Tailings Transportation Design Aspects Overview,"* in *Paste 2020: 23rd International Conference on Paste, Thickened and Filtered Tailings*, edited by H. Quelopana (Gecamin Publications, 2020).

Javanaud, C., and Thomas, A., *"Multiple scattering using the Foldy-Twersky integral equation,"* Ultrasonics **26**, 341–343 (1988).

Jensen, J. A., *"Field: A program for Simulating Ultrasound Systems,"* Medical & Biological Engineering & Computing **34**, 351–353 (1997).

Jia, X., *"Codalike multiple scattering of elastic waves in dense granular media,"* Physical Review Letters **93**, 154303 (2004).

Jones, C. A., *"The transition to wavy Taylor vortices,"* Journal of Fluid Mechanics **157**, 135–162 (1985).

Kähler, C. J., Scholz, U., and Ortmanns, J., *"Wall-shear-stress and near-wall turbulence measurements up to single pixel resolution by means of long-distance micro-PIV,"* Experiments in Fluids **41**, 327–341 (2006).

Kalpakli Vester, A., Örlü, R., and Alfredsson, P. H., *"Turbulent flows in curved pipes: recent advances in experiments and simulations,"* Applied Mechanics Reviews **68**, 050802 (2016).

Kang, C., and Mirbod, P., *"Flow instability and transitions in Taylor–Couette flow of a semidilute non-colloidal suspension,"* Journal of Fluid Mechanics **916**, A12 (2021).

Karnis, A., Goldsmith, H. L., and Mason, S. G., *"The flow of suspensions through tubes: V. Inertial effects,"* The Canadian Journal of Chemical Engineering **44**, 181–193 (1966a).

Karnis, A., Goldsmith, H. L., and Mason, S. G., *"The kinetics of flowing dispersions: I. Concentrated suspensions of rigid particles,"* Journal of Colloid and Interface Science **22**, 531–553 (1966b).

Kazerooni, H. T., Fornari, W., Hussong, J., and Brandt, L., *"Inertial migration in dilute and semidilute suspensions of rigid particles in laminar square duct flow,"* Physical Review Fluids **2**, 084301 (2017).

Keane, R. D., and Adrian, R. J., *"Theory of cross-correlation analysis of PIV images,"* Applied Scientific Research **49**, 191–215 (1992).

King, G. P., Li, Y., Lee, W., Swinney, H. L., and Marcus, P. S., *"Wave speeds in wavy Taylor-vortex flow,"* Journal of Fluid Mechanics **141**, 365–390 (1984).

King, G. P., and Swinney, H. L., *"Limits of stability and irregular flow patterns in wavy vortex flow,"* Physical Review A **27**, 1240–1243 (1983).

Knowles, P. L., and Kiger, K. T., *"Quantification of dispersed phase concentration using light sheet imaging methods,"* Experiments in Fluids **52**, 697–708 (2012).

Koeltzsch, K., Qi, Y., Brodkey, R. S., and Zakin, J. L., *"Drag reduction using surfactants in a rotating cylinder geometry,"* Experiments in Fluids **34**, 515–530 (2003).

Koh, C. J., Hookham, P., and Leal, L. G., *"An experimental investigation of concentrated suspension flows in a rectangular channel,"* Journal of Fluid Mechanics **266**, 1–32 (1994).

Kohyama, M., Norisuye, T., and Tran-Cong-Miyata, Q., *"Dynamics of microsphere suspensions probed by high-frequency dynamic ultrasound scattering,"* Macromolecules **42**, 752–759 (2009).

Koschmieder, E. L., *"Turbulent Taylor vortex flow,"* Journal of Fluid Mechanics **93**, 515–527 (1979).

Koschmieder, E. L., *Bénard cells and Taylor vortices* (Cambridge University Press, 1993).

Kotzé, R., Haldenwang, R., and Slatter, P., *"Rheological characterization of highly concentrated mineral suspensions using ultrasound velocity profiling with combined pressure difference method,"* Applied Rheology **18**, 62114–1 (2008).

Kotzé, R., Wiklund, J., and Haldenwang, R., *"Application of ultrasound Doppler technique for in-line rheological characterization and flow visualization of concentrated suspensions,"* The Canadian Journal of Chemical Engineering **94**, 1066–1075 (2016).

Krueger, E. R., Gross, A., and Di Prima, R. C., *"On the relative importance of Taylor-vortex and non-axisymmetric modes in flow between rotating cylinders,"* Journal of Fluid Mechanics **24**, 521–538 (1966).

Kundu, P. K., Cohen, I. M., and Dowling, D. R., *"Appendix C - Founders of Modern Fluid Dynamics,"* in *Fluid Mechanics* (Academic Press, Boston, 2012) 5th ed., pp. 869–871.

Kupsch, C., Feierabend, L., Nauber, R., Büttner, L., and Czarske, J., *"Ultrasound super-resolution flow measurement of suspensions in narrow channels,"* IEEE Transactions on Ultrasonics, Ferroelectrics, and Frequency Control **68**, 807–817 (2021).

Kupsch, C., Weik, D., Feierabend, L., Nauber, R., Büttner, L., and Czarske, J., *"Vector flow imaging of a highly laden suspension in a zinc-air flow battery model,"* IEEE Transactions on Ultrasonics, Ferroelectrics, and Frequency Control **66**, 761–771 (2019).

Kuster, G. T., and Toksöz, M. N., *"Velocity and attenuation of seismic waves in two-phase media: Part II. Experimental results,"* Geophysics **39**, 607–618 (1974).

Landau, L. D., *"On the problem of turbulence,"* *Doklady Akademii Nauk SSSR.*, **44**, 311–314 (1944), reprinted in *Collected Papers of L. D. Landau*, edited by D. ter Haar (Pergamon Press, 1965).

Lareo, C., Branch, C. A., and Fryer, P. J., *"Particle velocity profiles for solid-liquid food flows in vertical pipes part I. Single particles,"* Powder Technology **93**, 23–34 (1997).

Lareo, C., Nedderman, R. M., and Fryer, P. J., *"Particle velocity profiles for solid-liquid food flows in vertical pipes part II. Multiple particles,"* Powder Technology **93**, 35–45 (1997).

Lashgari, I., Picano, F., Breugem, W.-P., and Brandt, L., *"Laminar, turbulent, and inertial shear-thickening regimes in channel flow of neutrally buoyant particle suspensions,"* Physical Review Letters **113**, 254502 (2014).

Lathrop, D. P., Fineberg, J., and Swinney, H. L., *"Transition to shear-driven turbulence in Couette–Taylor flow,"* Physical Review A **46**, 6390–6405 (1992).

Leal, L. G., *"Particle motions in a viscous fluid,"* Annual Review of Fluid Mechanics **12**, 435–476 (1980).

Lee, J. H., Boning, D. S., and Anthony, B. W., *"Measuring the Absolute Concentration of Microparticles in Suspension Using High-Frequency B-Mode Ultrasound Imaging,"* Ultrasound in Medicine & Biology **44**, 1086–1099 (2018).

Leibovich, S., *"Preface by S. Leibovich and The Editors,"* Annual Review of Fluid Mechanics **35**, null (2003).

Leighton, D., and Acrivos, A., *"The shear-induced migration of particles in concentrated suspensions,"* Journal of Fluid Mechanics **181**, 415–439 (1987).

Leskovec, M., Lundell, F., and Innings, F., *"Pipe flow with large particles and their impact on the transition to turbulence,"* Physical Review Fluids **5**, 112301 (2020).

Lewis, G. S., and Swinney, H. L., *"Velocity structure functions, scaling, and transitions in high-Reynolds-number Couette-Taylor flow,"* Physical Review E **59**, 5457–5467 (1999).

Liu, C., and Kiger, K. T., *"Multi-camera PIV imaging in two-phase flow for improved dispersed-phase concentration and velocity calculation,"* in *Proceedings of the 18th International Symposium on Application of Laser and Imaging Techniques to Fluid Mechanics* (Instituto Superior Técnico, 2016).

Locatelli, F., François, P., Laurent, J., Lawniczak, F., Dufresne, M., Vazquez, J., and Bekkour, K., *"Detailed velocity and concentration profiles measurement during activated sludge batch settling using an ultrasonic transducer,"* Separation Science and Technology **50**, 1059–1065 (2015).

Lohse, D., "Turbulent Taylor Vortex Flow," (2011), The Nature of Turbulence (Feb 7 - Jun 3, 2011).

Lueptow, R. M., Docter, A., and Min, K., *"Stability of axial flow in an annulus with a rotating inner cylinder,"* Physics of Fluids A: Fluid Dynamics **4**, 2446–2455 (1992).

Majji, M. V., Banerjee, S., and Morris, J. F., *"Inertial flow transitions of a suspension in Taylor–Couette geometry,"* Journal of Fluid Mechanics **835**, 936–969 (2018).

Majji, M. V., and Morris, J. F., *"Inertial migration of particles in Taylor-Couette flows,"* Physics of Fluids **30**, 033303 (2018).

Majumdar, S., Peters, I. R., Han, E., and Jaeger, H. M., *"Dynamic shear jamming in dense granular suspensions under extension,"* Physical Review E **95**, 012603 (2017).

Mallock, A., *"III. Experiments on fluid viscosity,"* Philosophical Transactions of the Royal Society of London. Series A, Containing Papers of a Mathematical or Physical Character **187**, 41–56 (1896).

Manneville, S., *"Recent experimental probes of shear banding,"* Rheologica Acta **47**, 301–318 (2008).

Manneville, S., Bécu, L., and Colin, A., *"High-frequency ultrasonic speckle velocimetry in sheared complex fluids,"* The European Physical Journal-Applied Physics **28**, 361–373 (2004).

Manneville, S., Sandrin, L., and Fink, M., *"Investigating a stretched vortex with ultrafast two-dimensional ultrasonic speckle velocimetry,"* Physics of Fluids **13**, 1683–1690 (2001).

Marcus, P. S., *"Simulation of Taylor-Couette flow. part 2. Numerical results for wavy-vortex flow with one travelling wave,"* Journal of Fluid Mechanics **146**, 65–113 (1984).

Martinand, D., Serre, E., and Lueptow, R. M., *"Mechanisms for the transition to waviness for Taylor vortices,"* Physics of Fluids **26**, 094102 (2014).

Matas, J.-P., Glezer, V., Guazzelli, É., and Morris, J. F., *"Trains of particles in finite-Reynolds-number pipe flow,"* Physics of Fluids **16**, 4192–4195 (2004).

Matas, J.-P., Morris, J. F., and Guazzelli, É., *"Transition to turbulence in particulate pipe flow,"* Physical Review Letters **90**, 014501 (2003).

Matas, J.-P., Morris, J. F., and Guazzelli, É., *"Inertial migration of rigid spherical particles in Poiseuille flow,"* Journal of Fluid Mechanics **515**, 171–195 (2004).

Maude, A. D., and Yearn, J. A., *"Particle migrations in suspension flows,"* Journal of Fluid Mechanics **30**, 601–621 (1967).

Mehta, D., Thota Radhakrishnan, A. K., van Lier, J. B., and Clemens, F. H., *"Assessment of numerical methods for estimating the wall shear stress in turbulent Herschel–Bulkley slurries in circular pipes,"* Journal of Hydraulic Research **59**, 196–213 (2021).

Meinhart, C. D., Wereley, S. T., and Santiago, J. G., *"A PIV algorithm for estimating time-averaged velocity fields,"* Journal of Fluids Engineering **122**, 285–289 (2000).

Metzner, A., and Reed, J., *"Flow of non-Newtonian fluids—correlation of the laminar, transition, and turbulent-flow regions,"* AIChE Journal **1**, 434–440 (1955).

Miller, D. S., *Internal flow systems* (BHRA Fluid Engineering, 1978).

Moazzen, M., Lacassagne, T., Thomy, V., and Bahrani, S. A., *"Torque scaling at primary and secondary bifurcations in a Taylor–Couette flow of suspensions,"* Journal of Fluid Mechanics **937**, A2 (2022).

Morita, Y., Itano, T., and Sugihara-Seki, M., *"Equilibrium radial positions of neutrally buoyant spherical particles over the circular cross-section in Poiseuille flow,"* Journal of Fluid Mechanics **813**, 750–767 (2017).

Morris, J. F., *"Toward a fluid mechanics of suspensions,"* Physical Review Fluids **5**, 110519 (2020).

de Motta, J. C. B., Costa, P., Derksen, J. J., Peng, C., Wang, L.-P., Breugem, W.-P., Estivalezes, J. L., Vincent, S., Climent, E., Fede, P., Barbaresco, P., and Renon, N., *"Assessment of numerical methods for fully resolved simulations of particle-laden turbulent flows,"* Computers & Fluids **179**, 1–14 (2019).

Mudde, R. F., *"Gravity-driven bubbly flows,"* Annual Review of Fluid Mechanics **37**, 393–423 (2005).

Mullin, T., *"Experimental studies of transition to turbulence in a pipe,"* Annual Review of Fluid Mechanics **43**, 1–24 (2011).

Murai, Y., Ohta, S., Shigetomi, A., Tasaka, Y., and Takeda, Y., *"Development of an ultrasonic void fraction profiler,"* Measurement Science and Technology **20**, 114003 (2009).

Murray, H. H., *"Industrial applications of kaolin,"* Clays and Clay Minerals **10**, 291–298 (1961).

Murray, H. H., *"Traditional and new applications for kaolin, smectite, and palygorskite: a general overview,"* Applied Clay Science **17**, 207–221 (2000).

Nadeem, H., and Heindel, T. J., *"Review of noninvasive methods to characterize granular mixing,"* Powder Technology **332**, 331–350 (2018).

Najjari, M. R., Zhang, K., and Rival, D. E., *"Capturing both carrier and disperse phases in dense suspensions using harmonic Ultrasound Imaging Velocimetry,"* Measurement Science and Technology (2021).

Nakayama, S., Yamashita, H., Yabu, T., Itano, T., and Sugihara-Seki, M., *"Three regimes of inertial focusing for spherical particles suspended in circular tube flows,"* Journal of Fluid Mechanics **871**, 952–969 (2019).

NASA„ "Technological Readiness Level," (2012).

Nauber, R., Thieme, N., Radner, H., Beyer, H., Büttner, L., Dadzis, K., Pätzold, O., and Czarske, J., *"Ultrasound flow mapping of complex liquid metal flows with spatial self-calibration,"* Flow Measurement and Instrumentation **48**, 59–63 (2016).

Nguyen, C. V., Nguyen, T. D., Wells, J. C., and Nakayama, A., *"Interfacial PIV to resolve flows in the vicinity of curved surfaces,"* Experiments in Fluids **48**, 577–587 (2010).

van Ommen, J. R., and Mudde, R. F., *"Measuring the gas-solids distribution in fluidized beds–a review,"* International Journal of Chemical Reactor Engineering **6**, R3 (2008).

Ortiz, S. H. C., Chiu, T., and Fox, M. D., *"Ultrasound image enhancement: A review,"* Biomedical Signal Processing and Control **7**, 419–428 (2012).

Ostilla, R., Stevens, R. J. A. M., Grossmann, S., Verzicco, R., and Lohse, D., *"Optimal Taylor–Couette flow: direct numerical simulations,"* Journal of Fluid Mechanics **719**, 14–46 (2013).

Ostilla-Mónico, R., Huisman, S. G., Jannink, T. J. G., van Gils, D. P. M., Verzicco, R., Grossmann, S., Sun, C., and Lohse, D., *"Optimal Taylor–Couette flow: radius ratio dependence,"* Journal of Fluid Mechanics **747**, 1–29 (2014).

Ovarlez, G., Bertrand, F., and Rodts, S., *"Local determination of the constitutive law of a dense suspension of noncolloidal particles through magnetic resonance imaging,"* Journal of Rheology **50**, 259–292 (2006).

Park, J., Im, S., Sung, H. J., and Park, J. S., *"PIV measurements of flow around an arbitrarily moving free surface,"* Experiments in Fluids **56**, 56 (2015).

Parker, N. G., and Povey, M. J. W., *"Ultrasonic study of the gelation of gelatin: phase diagram, hysteresis and kinetics,"* Food Hydrocolloids **26**, 99–107 (2012).

Paterson, A. J. C., *"Pipeline transport of high density slurries: a historical review of past mistakes, lessons learned and current technologies,"* Mining Technology **121**, 37–45 (2012).

Peixinho, J., Nouar, C., Desaubry, C., and Théron, B., *"Laminar transitional and turbulent flow of yield stress fluid in a pipe,"* Journal of Non-Newtonian Fluid Mechanics **128**, 172–184 (2005).

Perge, C., Fardin, M.-A., and Manneville, S., *"Inertio-elastic instability of non shear-banding wormlike micelles,"* Soft Matter **10**, 1450–1454 (2014).

Peters, J., Salazar, A., and Shook, C. A., *"Startup of a pipeline containing settled solid particles,"* The Canadian Journal of Chemical Engineering **55**, 506–509 (1977).

Picano, F., Breugem, W.-P., Mitra, D., and Brandt, L., *"Shear thickening in non-Brownian suspensions: an excluded volume effect,"* Physical Review Letters **111**, 098302 (2013).

Pinfield, V. J., Povey, M. J., and Dickinson, E., *"Interpretation of ultrasound velocity creaming profiles,"* Ultrasonics **34**, 695–698 (1996).

Poelma, C., *"Ultrasound Imaging Velocimetry: a review,"* Experiments in Fluids **58**, 3 (2017).

Poelma, C., "Ondoorzichtige stromingen doorzien," (2018), Inaugural Lecture.

Poelma, C., *"Measurement in opaque flows: a review of measurement techniques for dispersed multiphase flows,"* Acta Mechanica **231**, 2089–2111 (2020).

Poelma, C., Westerweel, J., and Ooms, G., *"Turbulence statistics from optical whole-field measurements in particle-laden turbulence,"* Experiments in Fluids **40**, 347–363 (2006).

Poiseuille, J. L., "Recherches expérimentales sur le mouvement des liquides dans les tubes de très-petits diamètres," (Mémoires present'es par divers savants à l'Académie Royale des Sciences de l'Institut de France, 1846) pp. 433–544.

Powell, R. L., *"Experimental techniques for multiphase flows,"* Physics of Fluids **20**, 040605 (2008).

Prigent, A., and Dauchot, O., *"Visualization of a Taylor–Couette flow avoiding parasitic reflections,"* Physics of Fluids **12**, 2688–2690 (2000).

Prigent, A., Dubrulle, B., Dauchot, O., and Mutabazi, I., "The Taylor-Couette flow: The hydrodynamic twin of Rayleigh-Bénard convection," in *Dynamics of Spatio-Temporal Cellular Structures: Henri Bénard Centenary Review*, edited by I. Mutabazi, J. E. Wesfreid, and E. Guyon (Springer New York, New York, NY, 2006) pp. 225–242.

Pullum, L., Boger, D. V., and Sofra, F., *"Hydraulic mineral waste transport and storage,"* Annual Review of Fluid Mechanics **58**, 157–185 (2018).

Qin, Z., Durand, L.-G., and Cloutier, G., *"Kinetics of the "black hole" phenomenon in ultrasound backscattering measurements with red blood cell aggregation,"* Ultrasound in Medicine & Biology **24**, 245–256 (1998).

Ramesh, P., and Alam, M., *"Interpenetrating spiral vortices and other coexisting states in suspension Taylor–Couette flow,"* Physical Review Fluids **5**, 042301 (2020).

Ramesh, P., Bharadwaj, S., and Alam, M., *"Suspension Taylor–Couette flow: co-existence of stationary and travelling waves, and the characteristics of Taylor vortices and spirals,"* Journal of Fluid Mechanics **870**, 901–940 (2019).

Ramotowski, T. S., "Method for improving acoustic impedance of epoxy resins," (2012), US Patent 8,299,187 B1.

Ravelet, F., Delfos, R., and Westerweel, J., *"Influence of global rotation and Reynolds number on the large-scale features of a turbulent Taylor–Couette flow,"* Physics of Fluids **22**, 055103 (2010).

Rayleigh, J. W. S., *The theory of sound*, Vol. 2 (Macmillan, 1877).

Rayleigh, L., *"On the dynamics of revolving fluids,"* Proceedings of the Royal Society of London. Series A, Containing Papers of a Mathematical and Physical Character **93**, 148–154 (1917).

Reeks, M., *"The transport of discrete particles in inhomogeneous turbulence,"* Journal of Aerosol Science **14**, 729–739 (1983).

Reynolds, O., *"III. An experimental investigation of the circumstances which determine whether the motion of water shall be direct or sinuous, and of the law of resistance in parallel channels,"* Proceedings of the Royal Society of London **35**, 84–99 (1883a).

Reynolds, O., *"XXIX. An experimental investigation of the circumstances which determine whether the motion of water shall be direct or sinuous, and of the law of resistance in parallel channels,"* Philosophical Transactions of the Royal Society of London **174**, 935–982 (1883b).

Ricci, S., Liard, M., Birkhofer, B., Lootens, D., Brühwiler, A., and Tortoli, P., *"Embedded Doppler system for industrial in-line rheometry,"* IEEE Transactions on Ultrasonics, Ferroelectrics, and Frequency Control **59**, 1395–1401 (2012).

Rice, H. P., Fairweather, M., Hunter, T. N., Mahmoud, B., Biggs, S., and Peakall, J., *"Measuring particle concentration in multiphase pipe flow using acoustic backscatter: Generalization of the dual-frequency inversion method,"* The Journal of the Acoustical Society of America **136**, 156–169 (2014).

Rice, H. P., Fairweather, M., Peakall, J., Hunter, T. N., Mahmoud, B., and Biggs, S. R., *"Measurement of particle concentration in horizontal, multiphase pipe flow using acoustic methods: Limiting concentration and the effect of attenuation,"* Chemical Engineering Science **126**, 745–758 (2015).

Richardson, J. F., and Zaki, W. N., *"The sedimentation of a suspension of uniform spheres under conditions of viscous flow,"* Chemical Engineering Science **3**, 65–73 (1954).

Rida, Z., Cazin, S., Lamadie, F., Dherbécourt, D., Charton, S., and Climent, E., *"Experimental investigation of mixing efficiency in particle-laden Taylor–Couette flows,"* Experiments in Fluids **60**, 61 (2019).

Ridout, R., *"On a new copying process,"* Nature **21**, 155–156 (1879).

Rott, N., *"Note on the History of the Reynolds Number,"* Annual Review of Fluid Mechanics **22**, 1–12 (1990).

Rudtsch, S., and Hammerschmidt, U., *"Intercomparison of measurements of the thermophysical properties of polymethyl methacrylate,"* International Journal of Thermophysics **25**, 1475–1482 (2004).

Ruelle, D., and Takens, F., *"On the nature of turbulence,"* Communications in Mathematical Physics **20**, 167–192 (1971).

Saint-Michel, B., Bodiguel, H., Meeker, S., and Manneville, S., *"Simultaneous concentration and velocity maps in particle suspensions under shear from rheo-ultrasonic imaging,"* Physical Review Applied **8**, 014023 (2017).

Saint-Michel, B., Gibaud, T., and Manneville, S., *"Uncovering instabilities in the spatiotemporal dynamics of a shear-thickening cornstarch suspension,"* Physical Review X **8**, 031006 (2018).

Salewski, M., Gibson, J. F., and Schneider, T. M., *"Origin of localized snakes-and-ladders solutions of plane Couette flow,"* Physical Review E **100**, 031102 (2019).

Samarage, C. R., Carberry, J., Hourigan, K., and Fouras, A., *"Optimisation of temporal averaging processes in PIV,"* Experiments in Fluids **52**, 617–631 (2012).

Sandrin, L., Manneville, S., and Fink, M., *"Ultrafast two-dimensional ultrasonic speckle velocimetry: A tool in flow imaging,"* Applied Physics Letters **78**, 1155–1157 (2001).

Santiago, J. G., Wereley, S. T., Meinhart, C. D., Beebe, D., and Adrian, R. J., *"A particle image velocimetry system for microfluidics,"* Experiments in Fluids **25**, 316–319 (1998).

Sarabian, M., Firouznia, M., Metzger, B., and Hormozi, S., *"Fully developed and transient concentration profiles of particulate suspensions sheared in a cylindrical Couette cell,"* Journal of Fluid Mechanics **862**, 659–671 (2019).

Savage, S. B., and McKeown, S., *"Shear stresses developed during rapid shear of concentrated suspensions of large spherical particles between concentric cylinders,"* Journal of Fluid Mechanics **127**, 453–472 (1983).

Savaş, Ö., *"On flow visualization using reflective flakes,"* Journal of Fluid Mechanics **152**, 235–248 (1985).

Scarano, F., *"Iterative image deformation methods in PIV,"* Measurement Science and Technology **13**, R1 (2001).

Scharnowski, S., Hain, R., and Kähler, C. J., *"Reynolds stress estimation up to single-pixel resolution using PIV-measurements,"* Experiments in Fluids **52**, 985–1002 (2012).

Scharnowski, S., and Kähler, C. J., *"On the loss-of-correlation due to PIV image noise,"* Experiments in Fluids **57** (2016).

Scharnowski, S., and Kähler, C. J., *"Particle image velocimetry - Classical operating rules from today's perspective,"* Optics and Lasers in Engineering , 106185 (2020).

Schrimpf, M., Esteban, J., Warmeling, H., Färber, T., Behr, A., and Vorholt, A. J., *"Taylor–Couette reactor: Principles, design, and applications,"* AIChE Journal **67**, e17228 (2021).

Sciacchitano, A., and Scarano, F., *"Elimination of PIV light reflections via a temporal high pass filter,"* Measurement Science and Technology **25**, 084009 (2014).

Segré, G., and Silberberg, A., *"Radial particle displacements in Poiseuille flow of suspensions,"* Nature **189**, 209–210 (1961).

Segré, G., and Silberberg, A., *"Behaviour of macroscopic rigid spheres in Poiseuille flow Part 2. Experimental results and interpretation,"* Journal of Fluid Mechanics **14**, 136–157 (1962).

Shakeel, A., Kirichek, A., and Chassagne, C., *"Rheological analysis of natural and diluted mud suspensions,"* Journal of Non-Newtonian Fluid Mechanics **286**, 104434 (2020).

Shook, C. A., and Hubbard, L. T., *"An experimental study of transient slurry flow,"* The Canadian Journal of Chemical Engineering **51**, 607–612 (1973).

Shook, C. A., and Roco, M. C., *Slurry flow: principles and practice* (Elsevier, 1991).

Singh, S. P., Ghosh, M., and Alam, M., *"Counter-rotating suspension taylor–couette flow: pattern transition, flow multiplicity and the spectral evolution,"* Journal of Fluid Mechanics **944**, A18 (2022).

Sinton, S. W., and Chow, A. W., *"NMR flow imaging of fluids and solid suspensions in Poiseuille flow,"* Journal of Rheology **35**, 735–772 (1991).

Slatter, P. T., *Transitional and turbulent flow of non-Newtonian slurries in pipes*, Ph.D. thesis, University of Cape Town (1995).

Slatter, P. T., *"Tailings transport – back to basics!"* in *Paste 2005: Proceedings of the International Seminar on Paste and Thickened Tailings*, edited by R. Jewell and S. Barrera (Australian Centre for Geomechanics, 2005) pp. 165–176.

Smith, G. P., and Townsend, A. A., *"Turbulent Couette flow between concentric cylinders at large Taylor numbers,"* Journal of Fluid Mechanics **123**, 187–217 (1982).

Snieder, R., and Page, J., *"Multiple scattering in evolving media,"* Physics Today **60**, 49 (2007).

Stener, J. F., Carlson, J. E., Sand, A., and Pålsson, B. I., *"Towards the measurement of local particle mass fractions in magnetite suspensions,"* in *2014 IEEE International Ultrasonics Symposium* (IEEE, 2014) pp. 939–942.

Stener, J. F., Carlson, J. E., Sand, A., and Pålsson, B. I., *"Monitoring mineral slurry flow using pulse-echo ultrasound,"* Flow Measurement and Instrumentation **50**, 135–146 (2016).

Stewart, I., *In pursuit of the unknown: 17 equations that changed the world* (Basic Books, 2012).

Stolojanu, V., and Prakash, A., *"Characterization of slurry systems by ultrasonic techniques,"* Chemical Engineering Journal **84**, 215–222 (2001).

Strybulevych, A., Norisuye, T., Hasselfield, M., and Page, J. H., *"Particle dynamics in sheared particulate suspensions,"* AIChE Journal **65**, 840–849 (2019).

Sudo, K., Sumida, M., and Hibara, H., *"Experimental investigation on turbulent flow in a circular-sectioned 90-degree bend,"* Experiments in Fluids **25**, 42–49 (1998).

Sutera, S. P., and Skalak, R., *"The History of Poiseuille's Law,"* Annual Review of Fluid Mechanics **25**, 1–20 (1993).

Swillens, A., Segers, P., and Lovstakken, L., *"Two-dimensional flow imaging in the carotid bifurcation using a combined speckle tracking and phase-shift estimator: A study based on ultrasound simulations and in vivo analysis,"* Ultrasound in Medicine & Biology **36**, 1722–1735 (2010).

Swillens, A., Segers, P., Torp, H., and Lovstakken, L., *"Two-dimensional blood velocity estimation with ultrasound: Speckle tracking versus crossed-beam vector Doppler based on flow simulations in a carotid bifurcation model,"* IEEE transactions on Ultrasonics, Ferroelectrics, and Frequency Control **57**, 327–339 (2010).

Swinney, H. L., and Gollub, J. P., *"The transition to turbulence,"* Physics Today **31**, 41–49 (1978).

Szabo, T. L., *Diagnostic ultrasound imaging: inside out* (Academic Press, 2004).

Szasz, T., *Advanced beamforming techniques in ultrasound imaging and the associated inverse problems*, Ph.D. thesis, Toulouse 3 (2016).

Tagg, R., *"The Couette–Taylor problem,"* Nonlinear Science Today **4**, 1–25 (1994).

Takeda, Y., *"Velocity profile measurement by ultrasound Doppler shift method,"* International Journal of Heat and Fluid Flow **7**, 313–318 (1986).

Takeda, Y., *"Quasi-periodic state and transition to turbulence in a rotating Couette system,"* Journal of Fluid Mechanics **389**, 81–99 (1999).

Takeda, Y., *Ultrasonic Doppler Velocity Profiler for Fluid Flow*, 1st ed., Fluid Mechanics and Its Applications (Springer, Tokyo, 2012).

Takeda, Y., Fischer, W. E., Sakakibara, J., and Ohmura, K., *"Experimental observation of the quasiperiodic modes in a rotating Couette system,"* Physical Review E **47**, 4130–4134 (1993).

Tan, C., Murai, Y., Liu, W., Tasaka, Y., Dong, F., and Takeda, Y., *"Ultrasonic doppler technique for application to multiphase flows: A review,"* International Journal of Multiphase Flow **144**, 103811 (2021).

Tanter, M., and Fink, M., *"Ultrafast imaging in biomedical ultrasound,"* IEEE Transactions on Ultrasonics, Ferroelectrics, and Frequency Control **61**, 102–119 (2014).

Taylor, G. I., *"VIII. Stability of a viscous liquid contained between two rotating cylinders,"* Philosophical Transactions of the Royal Society of London. Series A, Containing Papers of a Mathematical or Physical Character **223**, 289–343 (1923).

Tetlow, N., Graham, A. L., Ingber, M. S., Subia, S. R., Mondy, L. A., and Altobelli, S. A., *"Particle migration in a Couette apparatus: Experiment and modeling,"* Journal of Rheology **42**, 307–327 (1998).

Thiel, M., Kurths, J., Romano, M. C., Moura, A., and Károlyi, G., "How did you get into chaos?" in *Nonlinear Dynamics and Chaos: Advances and Perspectives*, edited by M. Thiel, J. Kurths, M. C. Romano, G. Károlyi, and A. Moura (Springer Berlin Heidelberg, Berlin, Heidelberg, 2010) pp. 1–12.

Thomas, A., Pullum, L., and Wilson, K., *"Stabilised laminar slurry flow: Review, trends and prognosis,"* in *Hydrotransport 16th International Conference* (2004).

Thomas, A. D., *"Some observations regarding non-Newtonian turbulent flow and transition, especially in relation to the Wilson–Thomas (1985) theory,"* in *Paste 2018: Proceedings of the 21st International Seminar on Paste and Thickened Tailings* (Australian Centre for Geomechanics, 2018) pp. 205–216.

Thomas, A. D., and Cowper, N. T., *"The design of slurry pipelines–historical aspects,"* in *Hydrotransport 20th International Conference* (2017).

Thomas, A. D., and Wilson, K. C., *"New analysis of non-Newtonian turbulent flow – yield-power-law fluids,"* The Canadian Journal of Chemical Engineering **65**, 335–338 (1987).

Thomas, D. G., *"Transport characteristics of suspensions: II. Minimum transport velocity for flocculated suspensions in horizontal pipes,"* AIChE Journal **7**, 423–430 (1961).

Thorne, P. D., and Hanes, D. M., *"A review of acoustic measurement of small-scale sediment processes,"* Continental Shelf Research **22**, 603–632 (2002).

Thorne, P. D., and Hurther, D., *"An overview on the use of backscattered sound for measuring suspended particle size and concentration profiles in non-cohesive inorganic sediment transport studies,"* Continental Shelf Research **73**, 97–118 (2014).

Thorne, P. D., Hurther, D., and Moate, B. D., *"Acoustic inversions for measuring boundary layer suspended sediment processes,"* The Journal of the Acoustical Society of America **130**, 1188–1200 (2011).

Thota Radhakrishnan, A. K., Poelma, C., van Lier, J., and Clemens, F., *"Laminar-turbulent transition of a non-Newtonian fluid flow,"* Journal of Hydraulic Research **59**, 235–249 (2021).

Tokgöz, S., *Coherent structures in Taylor-Couette flow: Experimental investigation*, Ph.D. thesis, Delft University of Technology (2014).

Tokgoz, S., Elsinga, G. E., Delfos, R., and Westerweel, J., *"Spatial resolution and dissipation rate estimation in Taylor–Couette flow for tomographic PIV,"* Experiments in Fluids **53**, 561–583 (2012).

Tourin, A., Fink, M., and Derode, A., *"Multiple scattering of sound,"* Waves in Random Media **10**, R31–R60 (2000).

Treeby, B. E., and Cox, B. T., *"k-Wave: MATLAB toolbox for the simulation and reconstruction of photoacoustic wave fields,"* Journal of Biomedical Optics **15**, 021314 (2010).

Utomo, M., Warsito, W., Sakai, T., and Uchida, S., *"Analysis of distributions of gas and TiO_2 particles in slurry bubble column using ultrasonic computed tomography,"* Chemical Engineering Science **56**, 6073–6079 (2001).

Vatanakul, M., Zheng, Y., and Couturier, M., *"Application of ultrasonic technique in multiphase flows,"* Industrial & Engineering Chemistry Research **43**, 5681–5691 (2004).

Verschoof, R. A., te Nijenhuis, A. K., Huisman, S. G., Sun, C., and Lohse, D., *"Periodically driven Taylor–Couette turbulence,"* Journal of Fluid Mechanics **846**, 834–845 (2018).

Vlasak, P., and Chara, Z., *"Laminar and turbulent flow experiments with yield-power law slurries,"* Powder Technology **104**, 200–206 (1999).

Vlasak, P., and Chara, Z., *"Laminar and turbulent transition of fine-grained slurries,"* Particulate Science and Technology **22**, 189–200 (2004).

Volk, A., and Kähler, C. J., *"Density model for aqueous glycerol solutions,"* Experiments in Fluids **59**, 75 (2018).

Walden, R. W., and Donnelly, R. J., *"Reemergent order of chaotic circular Couette flow,"* Physical Review Letters **42**, 301 (1979).

Wang, G., Abbas, M., and Climent, E., *"Modulation of the regeneration cycle by neutrally buoyant finite-size particles,"* Journal of Fluid Mechanics **852**, 257–282 (2018).

Wang, S.-H., and Shung, K. K., *"An approach for measuring ultrasonic backscattering from biological tissues with focused transducers,"* IEEE Transactions on Biomedical Engineering **44**, 549–554 (1997).

Wang, T., Wang, J., Ren, F., and Jin, Y., *"Application of Doppler ultrasound velocimetry in multiphase flow,"* Chemical Engineering Journal **92**, 111–122 (2003).

Warsito„ Ohkawa, M., Kawata, N., and Uchida, S., *"Cross-sectional distributions of gas and solid holdups in slurry bubble column investigated by ultrasonic computed tomography,"* Chemical Engineering Science **54**, 4711–4728 (1999).

Warsito„ Uchida, S., Maezawa, A., and Okamura, S., *"Radial solid concentration profiles in a slurry bubble column measured by ultrasonic method,"* Journal of Chemical Engineering of Japan **30**, 786–792 (1997).

Wasp, E. J., *"Slurry pipelines,"* Scientific American **249**, 48–55 (1983).

Wedlock, D. J., McConaghy, C. J., and Hawksworth, S., *"Automation of ultrasound velocity scanning for concentrated dispersions,"* Colloids and Surfaces A: Physicochemical and Engineering Aspects **77**, 49–54 (1993).

Weik, D., Nauber, R., Kupsch, C., Büttner, L., and Czarske, J., *"Uncertainty Quantification of Ultrasound Image Velocimetry for Liquid Metal Flow Mapping,"* IEEE Transactions on Instrumentation and Measurement **70**, 1–11 (2021).

Wen, C., Poole, R. J., Willis, A. P., and Dennis, D. J. C., *"Experimental evidence of symmetry-breaking supercritical transition in pipe flow of shear-thinning fluids,"* Physical Review Fluids **2**, 031901 (2017).

Wendt, F., *"Turbulente Strömungen zwischen zwei rotierenden konaxialen Zylindern,"* Ingenieur-Archiv **4**, 577–595 (1933).

Wereley, S. T., and Lueptow, R. M., *"Azimuthal velocity in supercritical circular Couette flow,"* Experiments in Fluids **18**, 1–9 (1994).

Wereley, S. T., and Lueptow, R. M., *"Spatio-temporal character of non-wavy and wavy Taylor–Couette flow,"* Journal of Fluid Mechanics **364**, 59–80 (1998).

Weser, R., Wöckel, S., Hempel, U., Wessely, B., and Auge, J., *"Particle characterization in highly concentrated suspensions by ultrasound scattering method,"* Sensors and Actuators A: Physical **202**, 30–36 (2013a).

Weser, R., Wöckel, S., Wessely, B., and Hempel, U., *"Particle characterisation in highly concentrated dispersions using ultrasonic backscattering method,"* Ultrasonics **53**, 706–716 (2013b).

Weser, R., Woeckel, S., Wessely, B., Steinmann, U., Babick, F., and Stintz, M., *"Ultrasonic backscattering method for in-situ characterisation of concentrated dispersions,"* Powder Technology **268**, 177–190 (2014).

Westerweel, J., *Digital particle image velocimetry: Theory and application*, Ph.D. thesis, Delft University of Technology (1993).

Westerweel, J., *"On velocity gradients in PIV interrogation,"* Experiments in Fluids **44**, 831–842 (2008).

Westerweel, J., Dabiri, D., and Gharib, M., *"The effect of a discrete window offset on the accuracy of cross-correlation analysis of digital PIV recordings,"* Experiments in Fluids **23**, 20–28 (1997).

Westerweel, J., and Scarano, F., *"Universal outlier detection for PIV data,"* Experiments in Fluids **39**, 1096–1100 (2005).

Wiederseiner, S., *Rheophysics of concentrated particle suspensions in a Couette cell using a refractive index matching technique*, Ph.D. thesis, EPFL (2010).

Wiener, R. J., and McAlister, D. F., *"Parity breaking and solitary waves in axisymmetric Taylor vortex flow,"* Physical Review Letters **69**, 2915–2918 (1992).

Wiklund, J., and Stading, M., *"Application of in-line ultrasound Doppler-based UVP–PD rheometry method to concentrated model and industrial suspensions,"* Flow Measurement and Instrumentation **19**, 171–179 (2008).

Wilson, K. C., Addie, G. R., Sellgren, A., and Clift, R., *Slurry transport using centrifugal pumps*, 3rd ed. (Springer, Boston, MA, 2006).

Wilson, K. C., and Thomas, A. D., *"A new analysis of the turbulent flow of non-newtonian fluids,"* The Canadian Journal of Chemical Engineering **63**, 539–546 (1985).

Xiao, Q., Lim, T. T., and Chew, Y. T., *"Effect of acceleration on the wavy Taylor vortex flow,"* Experiments in Fluids **32**, 639–644 (2002).

Xue, Z., Charonko, J. J., and Vlachos, P. P., *"Particle image velocimetry correlation signal-to-noise ratio metrics and measurement uncertainty quantification,"* Measurement Science and Technology **25**, 115301 (2014).

Young, D. L., McFall, B. C., and Bryant, D. B., *"Bubble image velocimetry with a field-deployable acoustic camera,"* Measurement Science and Technology **29**, 125302 (2018).

Yousefi, A., Ardekani, M. N., Picano, F., and Brandt, L., *"Regimes of heat transfer in finite-size particle suspensions,"* International Journal of Heat and Mass Transfer **177**, 121514 (2021).

Yuan, Y.-W., and Shung, K. K., *"Echoicity of whole blood."* Journal of Ultrasound in Medicine **8**, 425–434 (1989).

Zhang, K., and Acrivos, A., *"Viscous resuspension in fully developed laminar pipe flows,"* International Journal of Multiphase Flow **20**, 579–591 (1994).

Zhang, L.-H., and Swinney, H. L., *"Nonpropagating oscillatory modes in Couette–Taylor flow,"* Physical Review A **31**, 1006–1009 (1985).

Zhou, B., Fraser, K. H., Poelma, C., Mari, J.-M., Eckersley, R. J., Weinberg, P. D., and Tang, M.-X., *"Ultrasound imaging velocimetry: Effect of beam sweeping on velocity estimation,"* Ultrasound in Medicine & Biology **39**, 1672–1681 (2013).

Zhu, X., and Vigil, R. D., *"Banded liquid–liquid Taylor–Couette–Poiseuille flow,"* AIChE Journal **47**, 1932–1940 (2001).

Zou, X.-J., Ma, Z.-M., Zhao, X.-H., Hu, X.-Y., and Tao, W.-L., *"B-scan ultrasound imaging measurement of suspended sediment concentration and its vertical distribution,"* Measurement Science and Technology **25**, 115303 (2014).

Propositions

accompanying the dissertation

Opaque Inertial Suspensions

by

Amitosh DASH

1. "Neutrally buoyant suspensions" exist on paper and in computers. Experimental works should refer to these as "nearly neutrally buoyant suspensions". (Chapter 3)
2. An empirical approach for ultrasonic particle volume fraction profiling will be appreciated more by an engineering scientist than a natural scientist. (Chapter 4)
3. Ultrasound imaging velocimetry will not be to suspension flows as particle image velocimetry has been to single-phase flows. (Chapter 5)
4. Wall sampling appears benign. However, given its intrusive nature, it is important to thoroughly reflect on its effect on the flow. (Chapter 6)
5. Scientific projects which are strongly multidisciplinary should have participants who are experts in the multiple disciplines that constitute said project.
6. Regular inclusion of anecdotes in one-way communications (presentations, theses, lectures, articles etc.) greatly enriches the engagement of the reader/listener.
7. Recency bias causes certain (dated) works to get buried in the rubble of literature. Unearthing obscure works is as valuable as reinventing the wheel.
8. Web search engines for scholarly literature should incorporate how a work has been cited to give a truer picture of the impact of said work.
9. A multiscale approach is necessary to reduce car dependency. At societal levels, the dissociation of driving a car from a status symbol. At city levels, better urban planning to increase opportunities for non-motorized and/or public transit. At provincial/national levels, ensuring that public transport infrastructure is attractive enough to possess the majority modal share.
10. In fluid mechanics research, extracting the essence of a real-world problem and abstractification thereof is approached carefully. Before proclaiming the usefulness of the research, a sincere attempt should be made by the researcher(s) in translating the conclusions of the abstract research back to the real-world problem.

These propositions are regarded as opposable and defendable, and have been approved as such by the promotors Prof. dr. ir. C. Poelma and Dr. ir. W.-P. Breugem.

Stellingen

behorende bij het proefschrift

Opaque Inertial Suspensions

door

Amitosh DASH

1. "Neutrally buoyant suspensions" bestaan op papier en in computers. In experimentele werken zouden deze moeten worden aangeduid als "nearly neutrally buoyant suspensions". (Hoofdstuk 3)
2. Een empirische aanpak voor ultrasone deeltjesconcentratie profielering zal meer gewardeerd worden door een ingenieurswetenschapper dan door een natuurwetenschapper. (Hoofdstuk 4)
3. Ultrasound imaging velocimetry zal voor suspensiestromingen niet betekenen wat particle image velocimetry voor eenfase stromingen heeft betekend. (Hoofdstuk 5)
4. Het afnemen van monsters door de wand lijkt goedaardig. Gezien de invasieve aard ervan is het echter van belang grondig na te denken over het effect ervan op de stroom. (Hoofdstuk 6)
5. Wetenschappelijke projecten die sterk multidisciplinair zijn, moeten deelnemers hebben die deskundig zijn in de verschillende disciplines waaruit het project bestaat.
6. Het regelmatig opnemen van anekdotes in eenrichtingscommunicatie (presentaties, scripties, lezingen, artikelen, enz.) verhoogt de betrokkenheid van de lezer/luisteraar aanzienlijk.
7. Door *recency bias* raken bepaalde (gedateerde) werken onder het puin van de literatuur bedolven. Het opgraven van obscure werken is even waardevol als het wiel opnieuw uitvinden.
8. Zoekmachines voor wetenschappelijke literatuur op het web moeten rekening houden met de mate waarin een werk is geciteerd om een getrouwer beeld te geven van de impact van dat werk.
9. Om de afhankelijkheid van de auto te verminderen is een multischalige aanpak nodig. Op maatschappelijk niveau, het loskoppelen van autorijden van een statussymbool. Op stadsniveau, een betere stadsplanning om de mogelijkheden voor niet-gemotoriseerd en/of openbaar vervoer te vergroten. Op provinciaal/nationaal niveau, ervoor zorgen dat de infrastructuur voor openbaar vervoer aantrekkelijk genoeg is om de meerderheid van de vervoerswijzen te vormen.
10. In vloeistofmechanica onderzoek wordt het extraheren van de essentie van een reëel probleem en de abstrahering daarvan zorgvuldig benaderd. Alvorens het nut van het onderzoek te verkondigen, moet door de onderzoeker(s) een oprechte poging worden ondernomen om de conclusies van het abstracte onderzoek terug te vertalen naar het reële probleem.

Deze stellingen worden opponeerbaar en verdedigbaar geacht en zijn als zodanig goedgekeurd door de promotors Prof. dr. ir. C. Poelma and Dr. ir. W.-P. Breugem.

Suspensions are of interest for curiosity-driven as well as applied research. From a fundamental perspective, inertia of the particles or the system triggers different behaviour in suspension flows. From an experimental perspective, analyzing suspensions is challenging due to their inherent opacity. This dissertation details the author's experience with **opaque inertial suspensions**. This book touches upon diverse subjects, including influence of non-Brownian suspensions on Taylor-Couette and pipe flows as well as the flow of a non-Newtonian slurry in an industrial-scale pipeline. This thesis also demonstrates the extents to which ultrasound imaging is useful for suspension fluid mechanics.

Read here
(scroll to date)

Watch here
(scroll to date)

laboratory for Aero & Hydro Dynamics

TU Delft

OPAQUE INERTIAL SUSPENSIONS

AMITOSH DASH

OPAQUE INERTIAL SUSPENSIONS

Amitosh Dash

You are invited to the public doctoral defence ceremony of my dissertation

OPAQUE INERTIAL SUSPENSIONS

08 September 2022
(Thursday)

Presentation: 1430
Defence: 1500 - 1600
Reception thereafter

Follow it physically at

Senaatzaal, Aula Conference Center,
Delft University of Technology
Mekelweg 5, Delft, The Netherlands

or digitally
by scanning
the QR-code
(scroll to date)

Amitosh Dash